

UAV-basierte Fernerkundungsmethoden der Aerogeophysik für die hochauflösende Beobachtung von alpinen Rutschhängen

Von der Fakultät für Bau- und Umweltingenieurwissenschaften
der Universität Stuttgart zur Erlangung der Würde eines
Doktor-Ingenieurs (Dr.-Ing.) genehmigte Abhandlung

Vorgelegt von
Uwe Niethammer
aus Stuttgart

Hauptberichter: Prof. Dr. rer. nat. Manfred Joswig

Mitberichter: Prof. Dr. J.A. Sander Huisman

Tag der mündlichen Prüfung: 27.09.2013

Institut für Geophysik der Universität Stuttgart

2013

Erklärung

Hiermit versichere ich, dass ich die vorliegende Arbeit selbstständig angefertigt und keine anderen als die angegebenen Quellen und Hilfsmittel verwendet habe. Die wissenschaftlichen Anteile an den zugehörigen Publikationen werden in Kapitel 2.1 aufgeschlüsselt.

Stuttgart, den 8. Juli 2013

Uwe Niethammer

Danksagung

An dieser Stelle möchte ich allen danken, die durch ihre Unterstützung zur Entstehung dieser Arbeit beigetragen haben. Herrn Prof. Dr. Joswig danke ich für die interessante Aufgabenstellung und die Übernahme des Erstgutachtens. Herrn Prof. Dr. J.A. Sander Huisman danke ich für die Übernahme des Zweitgutachtens. Außerdem bedanke ich mich bei Herrn Claar für die tatkräftigen, feinmechanischen Arbeiten zur Erstellung der Flugplattformen. Johannes Zeman möchte ich für die hervorragende Betreuung und Wartung der UAV-Systeme danken. Marco Walter danke ich für die Unterstützung während der Flugkampagnen in Frankreich und Österreich. Ulrich Schwaderer danke ich für die Durchführung der Studien zum multispektralen UAV-Einsatz einer Thermalkamera. Sabrina Rothmund möchte ich für die Einmessung der zahlreichen Passpunktdaten und für erste morphologische Analysen der Hangrutschung in Südfrankreich danken.

Allen weiteren Mitarbeitern des Instituts für Geophysik der Universität Stuttgart danke ich für die angenehme Arbeitsatmosphäre. Thom Bogaard und Jean-Philippe Malet möchte herzlich ich für die Einladung and die Super-Sauze Hangrutschung in Südfrankreich danken. Mike James danke ich für photogrammetrische Bearbeitungen mittels Methoden der Nahbereichsphotogrammetrie. Martin Weis danke ich für die Wandlung der Literaturdaten ins BibTeX-Format und für die Hilfe zur Lösung von diffizilen LaTeX-Problemstellungen. Der deutschen Forschungsgemeinschaft danke ich für die finanzielle Unterstützung im Rahmen des Forschungsprojekts „FOR 581 Natural Slopes“.

Kurzfassung

Massenbewegungen von Boden- und Felsmassen führen weltweit zu großen wirtschaftlichen Schäden mit zahlreichen menschlichen Opfern. Ein wichtiges wissenschaftliches Ziel ist daher die Erforschung der Ursachen, Mechanismen und Auslöser von Massenbewegungen. Am Institut für Geophysik der Universität Stuttgart werden hochempfindliche, seismische Verfahren (*Nanoseismic-Monitoring*) zur Detektion von kleinskaligen Bruchereignissen eingesetzt (Joswig, 2008).

Diese Verfahren kommen sowohl zur Registrierung natürlicher Seismizität, als auch zur Überwachung von induzierter Seismizität zum Einsatz. In aktuellen Forschungen (Walter et al., 2012) wurden Bruchereignisse in Lockersedimenten von Hangrutschungen registriert. Mit Hilfe dieser Bruchsignaturen eröffnen sich neue Einblicke in die bisher schwer fassbaren Triggermechanismen, zusätzlich können hieraus Hinweise zur Frühwarnung abgeleitet werden. Eine genaue räumliche Lokalisierung ist jedoch sehr schwierig, und die Mechanismen, welche zu Brüchen in Lockersedimenten führen, sind bisher unklar.

Sichtbare, oberflächennahe Phänomene von Hangrutschungen versprechen zusätzliche Informationen über die Prozessdynamik und sollen durch eine integrative Interpretation mit geophysikalischen Untergrunderkundungen zur Anwendung kommen. Zur Erfassung dieser Phänomene können zeitlich und räumlich hochauflösende Fernerkundungsdaten genutzt werden. Konventionelle Fernerkundungsverfahren mit Bodenauflösungen von wenigen Metern liefern jedoch nur unzureichende Informationen für detaillierte Untersuchungen. Anhand von unbemannten Flugzeugen (UAV) können seit wenigen Jahren kostengünstige Luftaufnahmen angefertigt werden, und Luftbilder mit geometrischen Auflösungen im Zentimeterbereich gewonnen werden. Regelmäßige Befliegungen beliebiger Wiederholraten in zeitlich kurzen Abständen sind möglich.

In der vorliegenden Arbeit werden aktuelle Fernerkundungsverfahren und UAV-Systeme des zivilen Bereichs der Fernerkundung vorgestellt. Sowohl die Vorzüge als auch die Einschränkungen der unterschiedlichen UAV-Systeme zur zeitlich und räumlich hochauflösenden Hang-Beobachtung im alpinen Raum werden erörtert. Am Beispiel mehrerer UAV-Pilotstudien kommen speziell zur Beobachtung von Hangrutschungen entwickelte Multi-Rotor UAV-Systeme mit optischen Sensoren zum Einsatz. Weiter werden notwendige Verfahren zur Prozessierung der optischen Luftbilder und unterschiedliche Methoden der fernerkundlichen Hangrutschungs-Analyse vorgestellt.

Zwei Hangrutschungen (Heumöser Hang, Österreich Vorarlberg und Super-Sauze Hangrutschung, Südfrankreich) werden fernerkundlich untersucht. Beide Hangrutschungen un-

terscheiden sich in wesentlichen Merkmalen. Während die Rutschung am Heumöser Hang nahezu vollständig mit Vegetation bedeckt ist und durch minimale Verschiebungsraten weniger Zentimeter im Jahr charakterisiert ist, weist die Super-Sauze Hangrutschung eine annähernd unbewachsene Oberfläche mit maximalen Bewegungsraten von bis zu mehreren Zentimetern pro Tag auf.

Im Zuge von zahlreichen UAV-basierten Fernerkundungs-Kampagnen kann auf eine große Zahl Luftbilder der Hangrutschungen zurückgegriffen werden. Diese hochauflösenden Luftbilder werden zur Erstellung von Ortho-Mosaiken und digitalen Geländemodellen herangezogen. Mit perspektivischen Einzelbild-Entzerrungsverfahren werden Ortho-Mosaik erstellt. Anhand dieser Mosaik sind Verschiebungsraten an der Oberfläche der Hangrutschungen ermittelbar. Zusätzlich können Deformations-Bereiche der Hangrutschungen identifiziert und analysiert werden.

Aus den UAV-basierten Luftaufnahmen werden in weiteren Studien hochauflösende digitale Modelle prozessiert. Die erstellten Oberflächenmodelle eignen sich gut für dreidimensionale, morphologische Analysen, zusätzlich können anhand der 3D-Modelle präzise Orthofotos erzeugt werden. Zwei verschiedene photogrammetrische Methoden zur Modell-Prozessierung werden untersucht. Während ein Verfahren der Nahbereichs-Photogrammetrie vor allem eine präzise Modell-Erstellung erlaubt, ermöglicht ein neuer Ansatz aus dem Bereich der *Computer Vision* eine vollautomatische Prozessierung der Bilddaten. Hierfür werden weder *a priori* Passpunkte, noch Verknüpfungspunkte im Bildmaterial benötigt. In ersten Studien werden diese neuen Verfahren auf systembedingte Abweichungen untersucht.

In weiteren Studien werden am Beispiel der Super-Sauze Hangrutschung neue Verfahren zur Kartierung von Oberflächenrissen anhand des hochauflösenden Bildmaterials vorgestellt. Diese semiautomatischen Verfahren ermöglichen erstmals großflächige Rissanalysen der Rutschungsoberfläche. Die Genauigkeit der resultierenden Karten wird durch Vergleiche mit verschiedenen manuellen Experten-Kartierungen beurteilt. Die Risskartierungen liefern ausreichende Details, um Rückschlüsse auf mechanische Prozesse in der Größenordnung der Hang-Skala ziehen zu können, und um interessante Bereiche für vertiefende Bodenuntersuchungen oder Überwachung festlegen zu können.

Am Beispiel der Super-Sauze Hangrutschung (Südfrankreich) wird eine kombinierte Hangrutschungsanalyse anhand von passiven seismischen Verfahren und räumlich hochauflösenden UAV-Erkundungen vorgestellt. Gemeinsame Beobachtungen von Bruchprozessen im Untergrund und hochauflösenden fernerkundlichen Oberflächen-Informationen ermöglichen eine Interpretation der komplexen Hangdynamik; die lokalisierten Brüche werden vor allem in den Grenzbereichen zwischen Rutschungsmaterial und bedeckten Festgesteinskämmen im Untergrund generiert.

Abstract

Mass movements such as landslides are leading to large economic damage and numerous human casualties world-wide. Hence, an important scientific aim is the investigation of the causes, mechanisms and triggers of such hazardous mass movements. At the Institute for Geophysics of the University of Stuttgart, highly sensitive, passive seismic methods (*Nanoseismic-Monitoring*) are in use for the detection of small fracture events (Joswig, 2008).

These methods have been used to record natural seismicity and to monitor induced seismicity. In landslide research (Walter et al., 2012) these techniques have detected fracture events in loose landslides sediments. New insights into the trigger mechanisms of landslides can be gained from these fracture signatures. In addition, early warning indications for landslide activity can be derived by detecting this kind of fracture events. Nevertheless, an exact spatial localisation of these fractures in the body of the landslide is very difficult, and the mechanisms which lead to fractures in loose sediments are, up to now, unclear.

Observations of the visible characteristics of landslides surfaces are a promising source of additional information about the process dynamics, and an integrative interpretation with geophysical underground investigations is planned for further studies. High temporal and spatial resolution remote sensing data can be used to determine such surface characteristics. However, conventional remote sensing methods, with spatial resolutions of several metres, deliver insufficient information for detailed landslide investigations. For some time now airborne photographs from unmanned airborne vehicles (UAV) can be used for landslides analysis, with spatial resolutions in the centimetre range and flexible temporal resolution.

This work introduces common remote sensing methods in comparison to new UAV-based remote sensing approaches for landslide studies. The advantages, as well as the restrictions of UAV systems for high-resolution landslide observations in alpine terrain are discussed. Specially developed multi-rotor UAV systems for work in alpine terrain are used for several remote sensing campaigns of different landslides. These UAV systems are equipped with optical sensors. The required procedures for image processing of airborne photographs, as well as different remote sensing methods for landslide analysis are introduced.

Two landslides (the Heumöser slope, Austria Vorarlberg and the Super-Sauze landslide, Southern France Alps) are examined. Both landslides differ in essential features. While

the Heumöser slope is characterized by a completely vegetated surface and maximum displacement rates of several centimetres per year, the Super-Sauze landslide shows a mainly uncovered surface with maximum displacement rates of up to some centimetres per day.

Numerous UAV-based remote sensing campaigns led to a large number of airborne photographs of the landslide surfaces. These high-resolution airborne photographs are used for ortho-mosaic and digital terrain model generation. Single image rectification procedures are applied for straightforward ortho-mosaic generation of the entire Super-Sauze landslide. The resulting ortho-mosaic is used for superficial displacement rate analysis and for the identification of different deformation areas of the landslide surface.

In addition, digital surface models of the Super-Sauze landslide are generated from the high-resolution UAV-based imagery. The resulting surface models are usable for three-dimensional, morphometric analyses. In addition, more accurate orthophotos can be generated with the help of precise 3D models.

Two different approaches are examined for photogrammetric 3D-model processing. While procedures of a close-range photogrammetric approach permit more precise models, newly developed *computer-vision*-based methods are useful for a fully automated processing of the UAV-based imagery. This approach neither requires *a priori* ground control points (GCP), nor manual tie points between the single photographs. In first studies these photogrammetric procedures are examined for system-conditioned distortions.

In further studies, a largely automated technique for the mapping of landslide surface fissures from the UAV-based images is proposed. The processing chain includes the usage of global filtering algorithms, post-processing procedures and an object-oriented analysis of the filtered imagery. The accuracy of the resulting maps is assessed by comparison with several expert-derived maps in terms of the affected area, fissure density and fissure orientation. The resulting fissure maps provide sufficient detail to infer mechanical processes at the slope scale and to prioritize areas for more detailed ground investigations or monitoring.

For the Super-Sauze landslide, a joint observation of subsurface fractures and the mapping of mass dynamics at the surface is introduced. During a field campaign in July 2008, different detected seismic signals of the landslide are analysed in combination with a UAV-borne ortho-mosaic. The joint analysis assists the estimation of seismic source areas and possible source mechanisms and vice versa. The observations of fracture processes in the subsoil and high-resolution remote sensing of surface information allow for a common interpretation of the complex slope dynamics; the localised fractures are mainly generated in the border areas between the landslide material and buried crests in the subsoil.

Inhaltsverzeichnis

1 Thematische Einführung	15
1.1 Hangrutschungen	15
1.1.1 Heumöser Hang Österreich	15
1.1.2 Super-Sauze Südfrankreich	15
1.1.3 Hangrutschungs-Forschung	17
1.2 Fernerkundung und Aerogeophysik	18
1.2.1 Verfahren	20
1.2.2 Beobachtung von Hangrutschungen	29
1.3 Unbemannte Flugzeuge: UAV	29
1.3.1 UAV-Systeme	31
1.3.2 UAV-basierte Hangbeobachtungen	36
1.3.3 UAV Flugrecht in Deutschland	40
2 Synopsis der Forschungsarbeiten	41
2.1 Eigenanteil an Publikationen	41
2.2 UAV-System und Software	43
2.2.1 Open-Source Komponenten	43
2.2.2 UAV-basierte Fernerkundung mittels SfM-MVS	44
2.2.3 Ergänzungen zur SfM-MVS Prozessierung	46
2.2.4 Ergänzungen zur Orthofoto-Erstellung	48
2.3 Befliegungen	50
2.3.1 Heumöser Hang	50
2.3.2 Super-Sauze	51
2.4 Pilotstudien der Hangbeobachtung	52
2.4.1 Morphologische Untersuchungen	52
2.4.2 Semiautomatische Risskartierung	53
2.4.3 Kombinierte Hangrutschungsanalyse	55
3 Diskussion und Ausblick	57
Literaturverzeichnis	60

A	Anhang	73
A.1	Publikationen Niethammer	73
A.1.1	Niethammer et al. (2011)	74
A.1.2	Niethammer et al. (2010)	80
A.1.3	Niethammer et al. (2012)	86
A.1.4	Stumpf et al. (2013)	104
A.1.5	Walter et al. (2009)	132
A.2	Entwickelte UAV-Systeme	143
A.2.1	Flugplattform	143
A.2.2	Steuerung (Flight-Ctrl)	143
A.2.3	Fernsteuerung	143
A.2.4	Kamera	147
A.3	Photogrammetrische Verfahren und Berechnungen	148
A.3.1	3D-Helmert-Transformation	148
A.3.2	Photogrammetrische Abbildungsgleichungen	149
A.3.3	Projektive Entzerrung	152
A.3.4	Projektionsmatrix	154
A.3.5	Differenzielle Entzerrung	156
A.3.6	Parametrisierbare Glättungsfilter	157
A.4	Lebenslauf	159

Abbildungsverzeichnis

1.1	Hangrutschungs-Typen	16
1.2	Spektralbereiche der Fernerkundung	19
1.3	Quickbird Multispektralaufnahmen	23
1.4	Reflexionseigenschaften verschiedener Materialien	24
1.5	LiDAR-basierte 3D-Modelle	25
1.6	Luftgestützte SAR Erkundung	26
1.7	Satellitengestützte dInSAR Erkundung	27
1.8	AEM Ausrüstung des BGR	28
1.9	Helikopter UAV-System	31
1.10	Multikopter UAV-Systeme	32

1.11	Coaxial UAV-System	32
1.12	Starrflügel UAV-System	33
1.13	Delta UAV-System	33
1.14	Ballon UAV-System	35
1.15	Luftschiff UAV-System	35
1.16	Gleitschirm UAV-System	37
1.17	Drachen UAV-System	37
1.18	Flugschema konventioneller photogrammetrischer Verfahren.	39
2.1	Open-Source UAV-System	44
2.2	SfM-MVS-basiertes 3D-Modell der Super-Sauze Hangrutschung	45
2.3	SfM Verfahren	46
2.4	MVS Verfahren	47
2.5	Projektive Luftbildentzerrung	48
2.6	Differenzielle Luftbildentzerrung	48
2.7	Ortho-Mosaik Erstellung	49
2.8	Befliegungen des Heumöser Hangs	50
2.9	Befliegungen der Super-Sauze Hangrutschung	51
2.10	Verschiebungsvektoren der Super-Sauze Hangrutschung	52
2.11	Riss-Kartierung der Super-Sauze Hangrutschung	54
2.12	Kombinierte Hangrutschungsanalyse	56
A.1	Quadrotor-UAV	144
A.2	Oktokopter UAV-System	144
A.3	Rahmenkonstruktion des Quadrotor-Systems	145
A.4	Steuerungselektronik	146
A.5	Fernsteuerungsanlage	146
A.6	Kamera	147
A.7	Koordinatensysteme des Bild- und Objektraums	149
A.8	Parallelprojektion zur Luftbildentzerrung.	156
A.9	Beispiel Filterung 3D-Punktwolke	157

Abkürzungen und Formelzeichen

Zeichen	Beschreibung
a_0	Parameter ($a_0 \in \mathbb{R}$)
a_1	Parameter ($a_1 \in \mathbb{R}$)
a_2	Parameter ($a_2 \in \mathbb{R}$)
A	$n \times 3$ Matrix der Ausgangs-Koordinatenvektoren \mathbf{X}_s
α	Winkelauflösung [rad]
b_0	Parameter ($b_0 \in \mathbb{R}$)
b_1	Parameter ($b_1 \in \mathbb{R}$)
b_2	Parameter ($b_2 \in \mathbb{R}$)
B	$n \times 3$ Matrix der Ziel-Koordinatenvektoren \mathbf{X}_d
c	Brennweite [m]
c_1	Parameter ($c_1 \in \mathbb{R}$)
c_2	Parameter ($c_2 \in \mathbb{R}$)
C	3×3 Hilfsmatrix
DGM	Digitales Geländemodell
dGPS	differential Global Positioning System
dInSAR	Differential Interferometric Synthetic Aperture Radar
δ	Skintiefe, Eindringtiefe
E	$n \times n$ Einheitsmatrix, Diagonalelemente 1, alle anderen Elemente 0
EP	Eintrittspupille, Eintrittsöffnung, Blendendurchmesser [m]
f	Frequenz [s^{-1}]
F	$n \times n$ Hilfsmatrix, alle Elemente 1
FIR	Fernes Infrarot
G	Hilfsvektor, alle Elemente 1, ($\mathbf{G} \in \mathbb{R}^n$)
i, j	Ganzzahlige Variablen
IMU	Inertial Measurement Unit
InSAR	Interferometric Synthetic Aperture Radar
INS	Inertial Navigation System
GIS	Geo-Informationen-System
GPS	Global-Positioning-System
GSD	Ground-Sampling-Distance [m]
GSI	Ground-projected Sample Interval [m]
h	Flughöhe über Grund [m]
K	$n \times n$ Hilfsmatrix

LiDAR	Light Detecting and Ranging
λ	Wellenlänge [m]
m	Ganzzahlige Variable
MIR	Mittleres Infrarot
MVS	Multi-View-Stereo
μ	Magnetische Feldkonstante, $\mu = 4\pi 10^{-7} [\frac{N}{A^2}]$
n_x, n_y	Anzahl der Bildpixel in x- und y-Richtung (Spalten, Zeilen)
NIR	Nahes Infrarot
n	Ganzzahlige Variable
p	Pixelrastermaß im Sensor [m]
p_{nm}	Element einer Projektionsmatrix P
ω	Kreisfrequenz, $\omega = 2\pi f$
PAN	Panchromatisch
r_{nm}	Element einer Rotationsmatrix R
R	3×3 Rotationsmatrix
RAR	Real Aperture Radar
RGB	Spektralkanäle rot, grün und blau
RTK	Real-Time-Kinematic
s	Skalierungsfaktor ($s \in \mathbb{R}$)
ρ	Spezifischer Widerstand [Ωm]
S	3×3 Diagonalmatrix mit Singulärwerten
SAR	Synthetic Aperture Radar
SfM	Structure-from-Motion
Δs	Räumliches Auflösungsvermögen [m]
S_X	Aufnahmedistanz in Flugrichtung [m]
S_Y	Aufnahmedistanz zwischen zwei Flugbahnen [m]
σ	Spezifische Leitfähigkeit [$\frac{S}{m}$]
T	Translationsvektor ($\mathbf{T} \in \mathbb{R}^3$)
U	3×3 Hilfsmatrix
UAV	Unmanned Aerial Vehicle
UV	Ultraviolett
V	3×3 Hilfsmatrix
VIS	Visual Light, Licht im sichtbaren Wellenlängen-Bereich
x	Bildkoordinatenvektor im Bildraum ($\mathbf{x} \in \mathbb{R}^3 \wedge x_z = 0$)
x₀	Koordinaten des Bildhauptpunktes im Bildraum ($\mathbf{x}_0 \in \mathbb{R}^3 \wedge x_{0z} = c$)
x	Bildkoordinate [m]

x_0	Koordinate des Bildhauptpunkts im Bildraum [m]
X	Koordinate im Objektraum [m]
X_0	Koordinate des Projektionszentrums im Objektraum [m]
X_b	Abgedeckter Bildbereich am Boden [m], in Flugrichtung
\mathbf{X}	Objektkoordinatenvektor ($\mathbf{X} \in \mathbb{R}^3$)
\mathbf{X}_0	Koordinaten des Projektionszentrums c im Objektraum ($\mathbf{X}_0 \in \mathbb{R}^3$)
\mathbf{X}_d	Vektor im Ziel-Koordinatensystem ($\mathbf{X}_d \in \mathbb{R}^3$)
\mathbf{X}_s	Vektor im Ausgangs-Koordinatensystem ($\mathbf{X}_s \in \mathbb{R}^3$)
y	Koordinate im Bildraum [m]
y_0	Koordinate des Bildhauptpunkts im Bildraum [m]
Y_b	Abgedeckter Bildbereich am Boden [m], quer zur Flugrichtung
Y	Koordinate im Objektraum [m]
Y_0	Koordinate des Projektionszentrums [m]
z	Bildkoordinate im Bildraum [m]
Z	Koordinate im Objektraum [m]
Z_0	Koordinate des Projektionszentrums [m]

1. Thematische Einführung

1.1. Hangrutschungen

Massenbewegungen von Boden- und Felsmassen treten an geneigten Oberflächen und senkrechten Grenzflächen auf. Sie führen weltweit zu großen wirtschaftlichen Schäden und zahlreichen menschlichen Opfern. Hangrutschungen entstehen als Wirkungskette von Ursachen und Auslösern, die zur Ausbildung von Scherbrüchen im Hangkörper und einer hangabwärts gerichteten Bewegung der Hangmasse führen (Damm, 2000). Nach Cruden und Varnes (1996) werden anhand von kinematischen Bewegungsmerkmalen sechs unterschiedliche Rutschungs-Typen klassifiziert (Abbildung 1.1). Sturzartige Hangrutschungen verursachen in der Regel die größten Schäden, jedoch kann die Dynamik abgegangener Rutschungen nicht mehr beobachtet werden. Im Bereich der Hangrutschungs-Forschung werden daher oftmals langsam gleitende oder kriechende Hänge beobachtet. In dieser Forschungsarbeit wurden eine kriechende und eine größtenteils fließende Hangrutschung untersucht.

1.1.1. Heumöser Hang Österreich

Am Heumöser Hang, Vorarlberg, Österreich erstreckt sich 25 km südlich von Bregenz eine kriechende Hangrutschung zwischen Höhen von 1360 m und 920 m ü.A. Der ca. 1800 m lange, und bis zu 30 m mächtige Rutschungskörper besteht aus Lockersedimenten wie verwittertem Hangschutt und Moränenmaterial. Er setzt sich aus teilweise sehr steilen Hangbereichen von bis zu 30° Hangneigung und relativ flachen Bereichen zusammen. Das anstehende Festgestein besteht hauptsächlich aus Mergeln. Das Volumen der Hangrutschung wird auf ca. 9.400.000 m³ geschätzt. Der Rutschungskörper ist nahezu vollständig bewachsen. Die Bewegungsraten des instabilen Hangbereichs erreichen maximal 0.1 m im Jahr (Lindenmaier, 2010).

1.1.2. Super-Sauze Südfrankreich

Die südfranzösische Super-Sauze Hangrutschung entwickelte sich seit den 60er Jahren am oberen Bereich der Sauze des Ubaye Tals an einem Nordhang des Barcelonnette Beckens.

1.1. Hangrutschungen

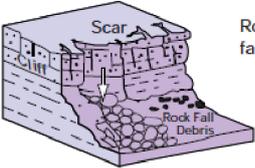
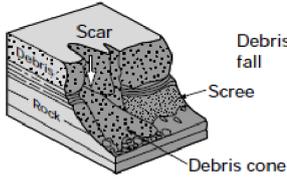
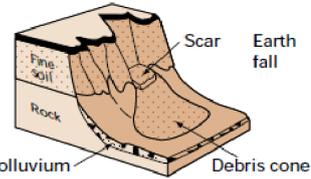
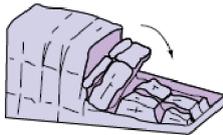
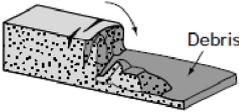
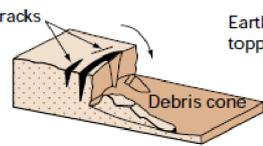
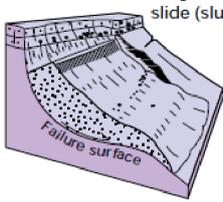
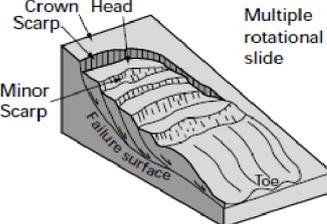
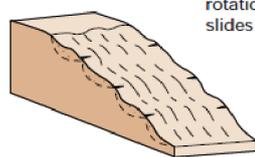
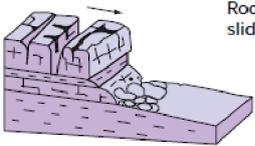
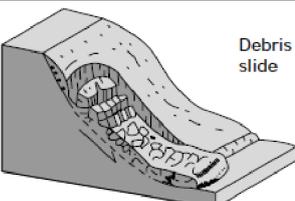
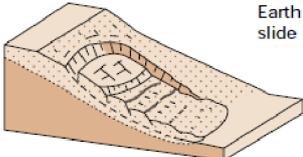
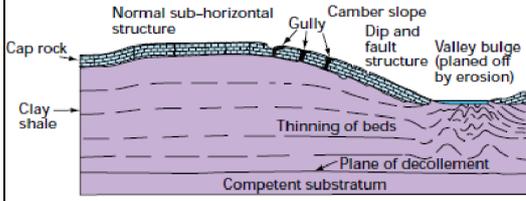
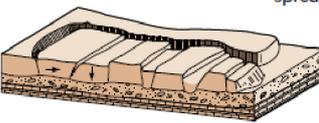
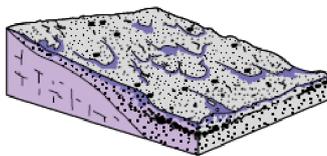
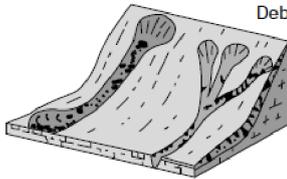
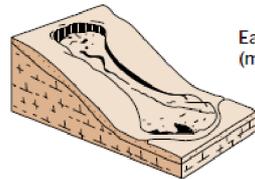
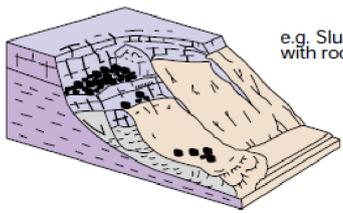
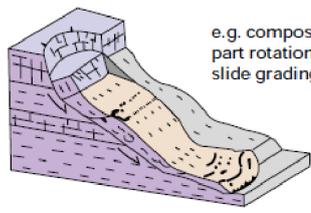
Material		ROCK	DEBRIS	EARTH
Movement type				
FALLS		 <p>Scar Rock fall Rock Fall Debris</p>	 <p>Scar Debris fall Scree Debris cone</p>	 <p>Scar Earth fall Fine soil Rock Colluvium Debris cone</p>
	TOPPLES	 <p>Rock topple</p>	 <p>Debris topple Debris cone</p>	 <p>Cracks Earth topple Debris cone</p>
SLIDES	Rotational	 <p>Single rotational slide (slump) Failure surface</p>	 <p>Crown Scarp Head Scarp Multiple rotational slide Minor Scarp Failure surface Toe</p>	 <p>Successive rotational slides</p>
	Translational (Planar)	 <p>Rock slide</p>	 <p>Debris slide</p>	 <p>Earth slide</p>
SPREADS	 <p>Cap rock Normal sub-horizontal structure Gully Camber slope Dip and fault structure Valley bulge (planed off by erosion) Thinning of beds Plane of decollement Competent substratum</p> <p>e.g. cambering and valley bulging</p>			 <p>Earth spread</p>
FLOWS	 <p>Solifluction flows (Periglacial debris flows)</p>	 <p>Debris flow</p>	 <p>Earth flow (mud flow)</p>	
COMPLEX	 <p>e.g. Slump-earthflow with rockfall debris</p>		 <p>e.g. composite, non-circular part rotational/part translational slide grading to earthflow at toe</p>	

Abbildung 1.1.: Hangrutschungs-Typen aus Cruden und Varnes (1996).

Die Rutschung erstreckt sich horizontal über eine Länge von 850 m in Höhen von 2105 m bis 1740 m mit einer durchschnittlichen Hangneigung von 25°. Die Rutschung besteht hauptsächlich aus schwarzen, jurassischen Mergeln, und wird auf ein Volumen von ca. 750,000 m³ geschätzt. Der Rutschungskörper ist nahezu unbewachsen. Die Bewegungsraten des instabilen, größtenteils fließenden Hangbereichs reichen von 0.01 m bis zu 0.4 m am Tag (Malet et al., 2005).

1.1.3. Hangrutschungs-Forschung

Die Erforschung von Hangrutschungen wird in übergeordnete Aufgaben wie Erkundung, Beobachtung, Analyse und Simulation eingeteilt. Erkundungen beinhalten das Auffinden und erstmalige Erfassen von aktiven und potenziellen Rutschungen. Eine gezielte Beobachtung liefert hingegen Informationen, welche für Analysen zu Trigger-Mechanismen und als Eingangsparameter zur computergestützten Simulation nutzbar sind. Mit Hilfe von Simulationen sollen Vorhersagen und Risikoabschätzungen ermöglicht werden. Zuverlässige Vorhersagen über Abgänge von Hangrutschungen sind nach dem aktuellen Stand der Forschung jedoch nicht möglich (van Asch et al., 2007). Im Bereich der Hangrutschungs-Forschung müssen fachübergreifende Forschungsansätze integriert werden. Die wichtigsten Bereiche werden im Folgenden kurz zusammengefasst:

- Geophysik
Die Geophysik befasst sich mit physikalischen Vorgängen auf sowie innerhalb der Erde. Auch der erdnahe, interplanetare Raum wird erforscht. Schwerpunkte der Geophysik sind Umweltgeophysik und Rohstoffexploration. Im Bereich der Hangrutschungs-Forschungen kommen hauptsächlich Verfahren der aktiven Seismik zur Untersuchung statischer Hangeigenschaften, sowie geoelektrische Verfahren zur Erfassung hydrologischer Parameter zum Einsatz.
- Geologie
Geologische Forschungen beschäftigen sich mit dem globalen Aufbau der Erde, mit ihrer Entstehungsgeschichte und mit erdgeschichtlichen Zusammenhängen. Es werden zahlreiche geowissenschaftliche Bereiche gegliedert. Vor allem geologische Kartierungen, aber auch geomorphologische Analysen sind für die Erforschung von Hangrutschungen von großer Bedeutung. Während geologische Kartierungen Informationen zu globalen Parametern beinhalten, beschreiben geomorphologische Parameter oftmals kleinste Oberflächendetails zu formbildenden Prozessen.
- Geodäsie
Im Bereich der Geodäsie werden Verfahren zur Bestimmung der Form und Lage

unserer Erde, sowie zur Bestimmung des Schwerefelds erforscht. Forschungsschwerpunkte sind sowohl die Vermessung der Erdoberfläche, als auch die Darstellung in Karten. Seit jüngerer Zeit wird der Bereich Geoinformatik gegliedert, welcher die geografische und raumbezogene Informationsverarbeitung beschreibt und Grundlage für alle digitalen Geoinformationssysteme (GIS) ist.

- Geotechnik

Die Geotechnik betreibt Forschungen zur lokalen Boden- und Felsmechanik. Forschungsschwerpunkt ist die Interaktion zwischen Baugrund und Bauwerk. Es werden die Bereiche Erdbau, Grundbau und Felsbau, sowie Tiefbau und Umweltgeotechnik unterschieden. Im Bereich der Hangrutschungs-Forschung kommen hauptsächlich Bohr-Verfahren zur Gewinnung von Bodenproben zum Einsatz.

- Hydrologie

Hydrologische Forschungen befassen sich mit den Eigenschaften des Wassers des festen Landes. Die unterschiedlichen Zustände auf und unter der Erdoberfläche, sowie physikalische, chemische und biologische Wechselwirkungen mit umgebenden Medien stehen im Vordergrund der Forschungen. Für Hangrutschungs-Forschungen sind vor allem die Wechselwirkungen mit dem Untergrund von Interesse, da diese oftmals den entscheidenden Triggermechanismus von Hangrutschungen darstellen.

- Kontinuumsmechanik

Die Kontinuumsmechanik beschreibt das Verformungsverhalten von kontinuierlichen Materialien und ist im Bereich der technischen Mechanik angesiedelt. Die Kontinuumsmechanik kann sowohl zur Analyse, als auch zur Simulation von Hangrutschungen herangezogen werden. Diskrete Materialien wie z. B. Sedimente werden als Kontinuum (kontinuierliches Material) modelliert.

- Mechanik diskreter Elemente

Kontinuumsmechanische Simulationen stoßen an ihre Grenze, wenn Bewegungsvorgänge von Hangrutschungen simuliert werden sollen. Für die Analyse von Bewegungsvorgängen lässt sich die Methode diskreter Elemente nutzen, mit welcher die Berechnung und Simulation von komplexen, bewegten Vorgängen gelöst werden kann.

1.2. Fernerkundung und Aerogeophysik

Fernerkundungsverfahren kommen für zahlreiche zivile und militärische Anwendungen zum Einsatz. Im Bereich der Geowissenschaften werden Fernerkundungsverfahren haupt-

sächlich zur Erforschung von planetaren Oberflächen und Atmosphären eingesetzt. Laut Definition nach Lillesand und Kiefer (1987) umfasst die Fernerkundung im Vergleich zu Erkundungsmethoden, die den direkten Zugang zum Objekt erfordern, ausschließlich berührungsfreie Verfahren. Als Informationsträger dienen reflektierte oder emittierte elektromagnetische Wellen (Abbildung 1.2). Die Fernerkundung wird übergeordnet in passive und aktive Verfahren eingeteilt, und anhand der verschiedenen technischen Methoden in die Bereiche optische Fernerkundung, multispektrale Fernerkundung, Laser-Fernerkundung und Mikrowellen-Fernerkundung unterteilt. Mit Hilfe von Mikrowellen sind selbst oberflächennahe Untergrunderkundungen durchführbar. Auch geophysikalische Feldmessungen wie Magnetfeldmessungen und Gravitationsmessungen können laut Definition zum Bereich der Fernerkundung gezählt werden. Jedoch sind nach Militzer und Weber (1985) luftgestützte geophysikalische Methoden der Aerogeophysik zuzuordnen. Aerogeophysikalische Verfahren werden in die Bereiche Aeromagnetik (AM), Aereoelktromagnetik (AEM), sowie Aeroradiometrie, Aero gravimetrie und Aero-Georadar gegliedert. Eine Abgrenzung zwischen geophysikalischen und fernerkundlichen Verfahren ist oftmals schwierig.

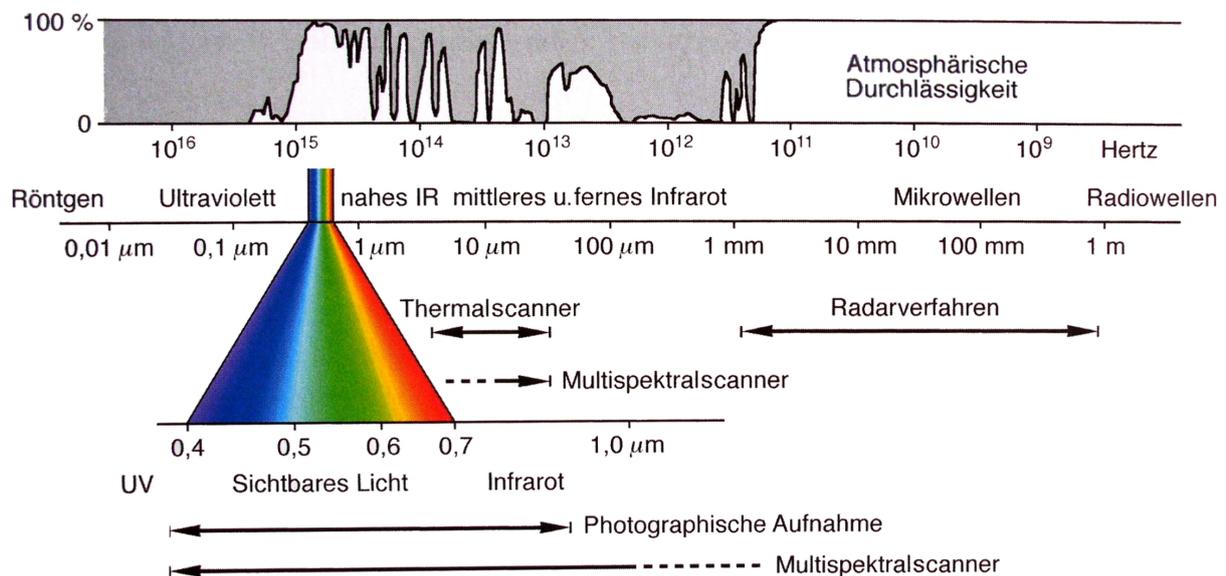


Abbildung 1.2.: Spektralbereiche der Fernerkundung, aus Albertz (2007).

1.2.1. Verfahren

Optische Erkundung

Optische Aufnahmen wurden erstmals 1839 von Joseph Nicéphore Niepce realisiert und waren die Grundlage für das älteste Fernerkundungs-Verfahren. Gaspar Felix Tournachon gelangen ca. 1858 von einem Ballon aus erste luftgestützte Fernerkundungs-Aufnahmen (Elachi, 1987). Luftaufnahmen werden im Allgemeinen als Senkrecht-Luftbilder (Nadir) aufgenommen. Das räumliche Auflösungsvermögen Δs eines fehlerfreien, optischen Systems ist durch die optische Beugung des Lichts begrenzt. Nach Löffler-Mang (2011) kann aus dem Rayleigh-Kriterium das räumliche Auflösungsvermögen nach Näherung (1.1) berechnet werden:

$$\Delta s \approx 1.22 \frac{\lambda \cdot h}{EP} \quad (1.1)$$

Δs = Räumliches Auflösungsvermögen λ = Wellenlänge
 EP = Eintrittspupille, Blendendurchmesser h = Flughöhe über Grund

Sofern optische Fehler, sowie atmosphärische Einflüsse vernachlässigt werden und das Auflösungsvermögen aus Näherung (1.1) gewährleistet ist, kann die räumliche Auflösung optischer Systeme vereinfacht berechnet werden. Die Bodenaufösung GSD (engl. *ground sampling distance*) oder auch GSI (*ground-projected sample interval*) ist für Nadir-Aufnahmen ebener Flächen folgendermaßen definiert (Schowengerdt, 2007):

$$GSD = \frac{h \cdot p}{c} \quad (1.2)$$

GSD = Bodenaufösung h = Flughöhe über Grund
 p = Pixelrastermaß im Sensor c = Brennweite der Optik

Moderne optische Verfahren nutzen den gesamten sichtbaren Wellenlängenbereich elektromagnetischer Wellen (Abbildung 1.2). Es werden zwei Daten-Typen unterschieden:

- PAN (panchromatisch), gesamter sichtbarer Spektralbereich (400–690 nm), Graustufenbild
- RGB Farbbild, sichtbares Licht (VIS) mit den Spektralkanälen rot (630–690 nm), grün (530–610 nm) und blau (450–520 nm),

Aufgrund der alltäglichen, visuellen Wahrnehmung des Menschen ermöglichen optische Fernerkundungsdaten intuitive Auswertungen. Optische Erkundungen der Erdoberfläche sind in der Regel nur während der Tageszeit durchführbar, da natürliches Sonnenlicht als Strahlungsquelle benötigt wird. Die Intensität und das Spektrum des reflektierten Lichts sind abhängig von Sonnenstand, Oberflächenmaterial und der Atmosphäre. Die Transmission durch die Atmosphäre wird durch Absorption und Streuung beeinflusst. Dies ist auf die enthaltenen Gase, Wolken, Regen und Staub zurückzuführen (Albertz, 2007). Eine deutlich wahrnehmbare, frequenzabhängige Streuung im blauen Spektralbereich wird von atmosphärischen Gasen wie Ozon und Aerosolen verursacht (de Bary und Bullrich, 1962). Dieser Effekt führt sowohl zur blauen Farbe des unbedeckten Himmels, als auch zu einer mit der Entfernung zunehmenden Blaufärbung der beobachteten Objekte. Optische Fernerkundungsdaten sind nur sehr aufwendig mit Hilfe einer photogrammetrischen Prozessierung in dreidimensionale Datensätze wandelbar, wobei die Genauigkeit stark von der Textur abhängig ist (Kraus, 1997). Die optische Fernerkundung ist den passiven Verfahren zugeordnet und kommt als terrestrisches, luftgestütztes und satellitengestütztes Verfahren zum Einsatz. Aktuelle satellitengestützte Aufnahmen erlauben Bodenauflösungen bis zu 0.41 m (PAN) und 1.65 m (RGB) (Sörgel et al., 2011). Flugzeuggetragene Systeme ermöglichen je nach Flughöhe Bodenauflösungen bis in den Submeter-Bereich (Gleichung 1.2).

Photogrammetrie

Die Photogrammetrie beschäftigt sich schon über 150 Jahre mit technischen und wissenschaftlichen Aspekten, die es ermöglichen, aus einzelnen oder mehreren optischen Aufnahmen Objekte in ihrer Lage und Form zu rekonstruieren (Luhman, 2010). Die grundlegenden mathematischen Forschungen zur projektiven Geometrie und der photogrammetrischen Rekonstruktion wurden im Jahre 1883 realisiert (Hauck, 1883). Diese Forschungen lieferten die Basis für die meisten photogrammetrischen Entwicklungen. Aktuelle photogrammetrische Grundlagenforschungen befassen sich mit Verfahren des *Image-Matching* zur vollautomatischen Erstellung von 3D-Modellen (Snavely et al., 2008) und mit der Beschleunigung von photogrammetrischen Prozessen (Gruen, 2012). Auch die Anwendung der perspektivischen Bildverzerrung für Kartographie und Luftbildvermessung ist im Bereich der Photogrammetrie schon seit mehr als 100 Jahre bekannt (Baltsavias, 1996).

Theodor Scheimpflug entwickelte um 1897 ein erstes Foto-basiertes Verfahren zur stückweisen Bildentzerrung. Seit ca. 1984 wird hauptsächlich die digitale Bildentzerrung eingesetzt (Goepfert, 1984; Wiesel, 1985). Sie hat im Laufe der Zeit aufwendige mechanische und optische Entzerrungs-Verfahren vollständig verdrängt. Mit aktuellen Verfahren der digitalen Entzerrung werden Luftbilder auf ein zugrunde liegendes 3D-Oberflächenmodell projiziert, diese 3D-Texturinformation des digitalen Modells kann dann in einem weiteren Schritt pixelweise mit Hilfe einer orthogonalen Parallel-Projektion in die Ebene der Höhe $Z = 0$ transformiert werden. Perspektivische Verzerrungen aufgrund von Schrägaufnahmen und unebener Oberflächen werden hierdurch effektiv beseitigt.

Multispektrale Erkundung

Multispektrale Fernerkundungsdaten setzen sich aus Informationen mehrerer Spektralkanäle zusammen. Hierzu lässt sich streng genommen auch die optische VIS-Fernerkundung mit den Spektralbändern RGB zählen, jedoch werden Datensätze erst ab mindestens vier Spektralkanälen als multispektral bezeichnet. Die Erfassung von multispektralen Daten erfolgt in der Regel mit optisch-mechanischen Scannern (Albertz, 2007). Je nach Fachbereich werden unterschiedliche Definitionen der Spektralbereiche vorgenommen. Die Spektralbänder der Satelliten-Fernerkundung setzen sich häufig nach Tabelle 1.3 zusammen. Mit multispektralen Informationen werden Differenzierungen unterschiedlicher Oberflächenmaterialien vorgenommen (Zillmann und Schnug, 2005). Analog hierzu bilden sich unterschiedliche Pflanzenarten und deren Zustand gut ab, da Chlorophyll im nahen Infrarot wesentlich stärker als im sichtbaren Bereich reflektiert (Curran, 1980). Multispektrale Bild-Daten sind mit Hilfe von sogenannten Falschfarben-Bildern visuell darstellbar, indem drei Spektralkanäle als RGB-Bild dargestellt werden (Abbildung 1.3).

Sollen mehr als drei Spektralkanäle zeitgleich visualisiert werden, lassen sich umfangreichen Datensätze mit Hilfe einer Hauptachsentransformation (auch: PCA, Karhunen-Loève-Transformation) vereinfachen (Jolliffe, 1986). Hierbei wird die gesamte Anzahl der Spektralkanäle durch eine geringere Zahl möglichst aussagekräftiger Hauptkomponenten genähert. Die gefundenen Hauptkomponenten werden dann mit den sichtbaren Kanälen RGB in einem Falschfarbenbild dargestellt. Diese Vorgehensweise erfordert jedoch erfahrene Auswerter bei der Interpretation (Canas und Barnett, 1985).

Multispektrale Sensorsysteme bestehen aus aufwendigen, technischen Komponenten, und die Kanäle des thermischen Infrarot liefern in der Regel gröbere Bodenauflösungen im Vergleich zu den restlichen multispektralen Kanälen (Albertz, 2007). Die multispektrale Fernerkundung ist den passiven Fernerkundungsmethoden zugeordnet, und kommt als satellitengestütztes und luftgestütztes Verfahren zum Einsatz. Satelliten-basierte Multispektraldaten weisen nach Sörgel et al. (2011) aktuell eine Bodenauflösung bis zu 1.65 m



Abbildung 1.3.: Multispektrale Quickbird-Aufnahmen zur großflächigen Hangrutschungs-Detektion (Falschfarben: Band 2-3-4); links: Zustand vor abgegangener Hangrutschung, rechts: sichtbare helle Bereiche der Rutschung, aus Casagli et al. (2005).

Bezeichnung	Spektralband	Wellenlänge
Blau	1	450 nm - 520 nm
Grün	2	530 nm - 610 nm
Rot	3	630 nm - 690 nm
Nahes Infrarot (NIR)	4	780 nm - 900 nm
Mittleres Infrarot (MIR)	5	1550 nm - 1750 nm
Thermisches Infrarot (TIR)	6	10.4 μm - 12.5 μm
Mittleres Infrarot (MIR)	7	2090 nm - 2350 nm
Panchromatisch (PAN)	8	520 nm - 900 nm

Tabelle 1.3.: Spektralbereiche am Beispiel Landsat 7, Quelle: USGS

auf, flugzeuggetragene Systeme ermöglichen je nach Flughöhe Bodenaufösungen bis in den Submeter-Bereich (Mumby et al., 1998).

Hyperspektrale Erkundung

Hyperspektrale Fernerkundungsverfahren stellen Datensätze mit mehr als 100 schmalbandigen Spektral-Kanälen bereit. Im Vergleich zu multispektralen Daten erlauben hyperspektrale Fernerkundungsdaten eine genauere Differenzierung unterschiedlicher Materialien (Abbildung 1.4). Sie eignen sich vor allem zur Analyse von Vegetation, da die breitbandigen Multispektralbänder signifikante Reflexionseigenschaften von Pflanzen nicht ausreichend auflösen (Darvishzadeh, 2008). Hyperspektrale Datensätze sind im Gesamten nicht

visuell darstellbar und die enorme Datenmenge erfordert einen großen Bearbeitungsaufwand.

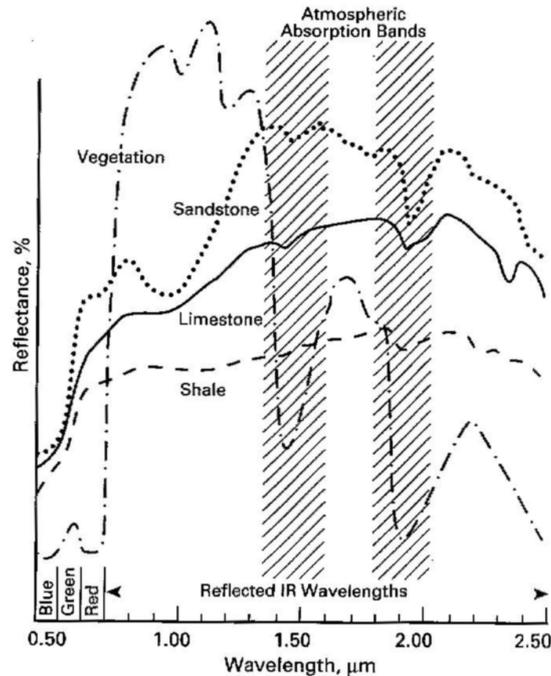


Abbildung 1.4.: Reflexionseigenschaften verschiedener Materialien, aus Sabins (1996).

Die hyperspektrale Fernerkundung kommt als passives Verfahren zum Einsatz und wird als terrestrische, luft- und satellitengestützte Methode genutzt. Nach einer Übersicht aus Sörgel et al. (2011) ist aktuell nur ein satellitengestützter Hyperspektralsensor mit einer Bodenauflösung von 30 m im Einsatz. Flugzeuggetragene Sensoren wie HyMap erzielen aus 2000 m Flughöhe geometrische Bodenauflösungen im Bereich von 4 m (Darvishzadeh, 2008).

Laser-Erkundung

Laserstrahlen des sichtbaren, ultravioletten und infraroten Spektralbereichs breiten sich räumlich sehr gerichtet aus und ermöglichen eine intensive Bestrahlung weit entfernter Objekte (Hecht, 1992). Die Erkundung von Fernerkundungs-Objekten ist daher auch mit selektiven Wellenlängen des elektromagnetischen Spektrums möglich. Messgrößen sind reflektierte Strahlungsintensitäten und Zeitdifferenzen zwischen Aussendezeitpunkten und Empfangszeitpunkten (Wehr und Lohr, 1999). Laser-basierte Fernerkundungsinstrumente werden auch als LiDAR (Light detection and ranging) bezeichnet (Lefsky et al., 2002). Für luftgestützte Erkundung müssen kontinuierliche, hochgenaue Positionsdaten des Flugzeuges zur Korrektur von Flugzeugbewegungen eingerechnet werden.

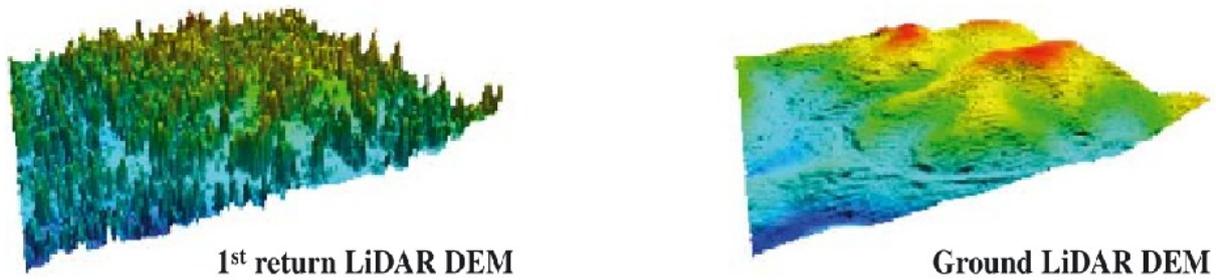


Abbildung 1.5.: Links: LiDAR-basiertes Oberflächenmodell, rechts: LiDAR-basiertes Geländemodell, aus Zimble et al. (2003).

Über bewaldeten Gebieten sind hochauflösende Oberflächen-Informationen erfassbar, indem das letzte Echo von den vorhergehenden Reflexionen der Vegetation separiert wird (Eeckhaut et al., 2007) (Abbildung 1.5). Auch atmosphärische Gase werden mit Hilfe von LiDAR erforscht (Killinger und Menyuk, 1987). Aktuelle geodätische Laser-Scanner ermöglichen eine luftgestützte Erhebung von dreidimensionalen Fernerkundungsdaten mit Bodenauflösungen im Submeter-Bereich (Wehr und Lohr, 1999). Die Laser-Fernerkundung wird hauptsächlich als terrestrisches und luftgestütztes Verfahren genutzt.

Mikrowellen-Erkundung

Während die passive Mikrowellen-Fernerkundung Erfassungen von Bodenparametern mittels natürlich emittierten Mikrowellen ermöglicht (Ulaby et al., 1982), werden mit aktiven Systemen, wie Real Apertur Radar (RAR), Synthetisch Apertur Radar (SAR) (Sherwin et al., 1962) und Scatterometer (Zoughi et al., 1985) Mikrowellen zur Geländeoberfläche gesendet. Messgrößen sind reflektierte Strahlungsintensitäten und Zeitdifferenzen zwischen Aussendezeitpunkten und den entsprechenden Empfangszeitpunkten. Eine SAR-Konfiguration benötigt im Gegensatz zur RAR-Konfiguration wesentlich kleinere Antennen, um identische Auflösungen zu erzielen (Albertz, 2007), und wird gegenwärtig bei nahezu allen abbildenden Satelliten- und Luftgestützten Erkundungen eingesetzt.

Die Transmission von Mikrowellen durch die Atmosphäre wird von Wolken und Regen kaum beeinflusst (Abbildung 1.2). Zuverlässige Erkundungen sind zu jeder Tageszeit und bei jeder Wetterlage durchführbar. Die Mikrowellen-Fernerkundung ist jedoch anfällig für Abbildungsfehler wie Verkürzung (Foreshortening), Überlagerung (Lay-Over), Abschattung (Shadowing) und Speckle (Frulla et al., 1998).

Mit Hilfe der aktiven Mikrowellen-Fernerkundung sind auch Informationen über oberflächennahe Bodenschichten erfassbar. Die Eindringtiefe ist abhängig von der Wellenlänge, der Einfallrichtung und des Materials (Davis und Annan, 1989), auch Informationen über

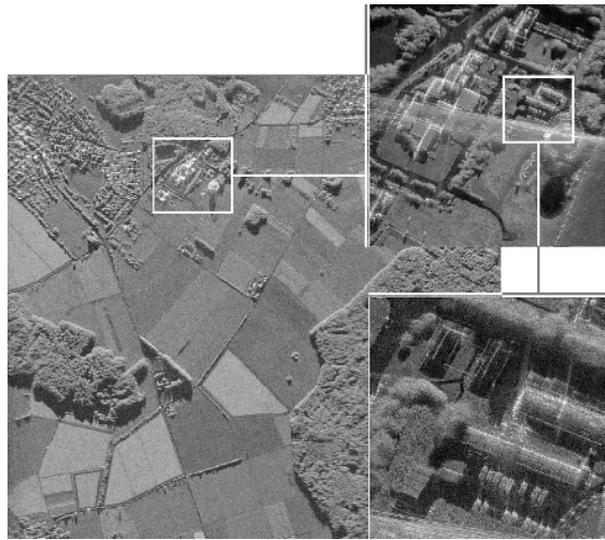


Abbildung 1.6.: Luftgestütztes SAR Intensitätsbild der Gebäude der Forschungsgesellschaft für Angewandte Naturwissenschaften e. V. in Werthhoven (10 cm Bodenaufösung), aus Brenner und Ender (2006).

den Wassergehalt des Bodens sind erfassbar (Dubois et al., 1995).

Die Mikrowellen-Fernerkundung wird sowohl am Boden, wie auch aus der Luft und vom Satellit aus betrieben. Das Spektrum von Mikrowellen erstreckt sich über einen Frequenzbereich von 1 GHz bis 325 GHz und ist standardisiert in mehrere Frequenzbänder unterteilt (Kraus und Schneider, 1988). Die derzeitig erreichbare Bodenaufösung Satellitenbasierter SAR-Systeme liegt im Meter-Bereich (Zhu und Bamler, 2010), flugzeuggetragene Systeme ermöglichen Bodenaufösungen im Submeter-Bereich (Brenner und Ender, 2006, Abbildung 1.6).

Mikrowellen-Interferometrie

Mit Hilfe der SAR Interferometrie (InSAR) und der differentiellen SAR Interferometrie (dInSAR) ist es möglich, hoch genaue Höheninformationen zu prozessieren. Interferometrische Auswertungen von SAR-Daten desselben Zeitpunktes aus unterschiedlichen Aufnahmepositionen ermöglichen die Generierung großflächiger, digitaler Gelände-Modelle (Graham, 1974; Catani et al., 2005). Die Verfahren des dInSAR nutzen hingegen Aufnahmen unterschiedlicher Zeiträume, woraus mittels Phasendifferenzen zwischen den verschiedenen Aufnahmen hoch genaue Höhenänderungen bestimmbar sind (Massonnet et al., 1993; Pepe et al., 2005). Eindeutige Höhenänderungen sind jedoch nur unterhalb der genutzten Wellenlänge bestimmbar, da mit jeder weiteren Periode Mehrdeutigkeiten im Bereich $n\lambda$ auftreten (Abbildung 1.7). Die Mikrowellen-Interferometrie erfordert kontinuierliche, hoch genaue Positionsinformationen über die bewegten Antennen.

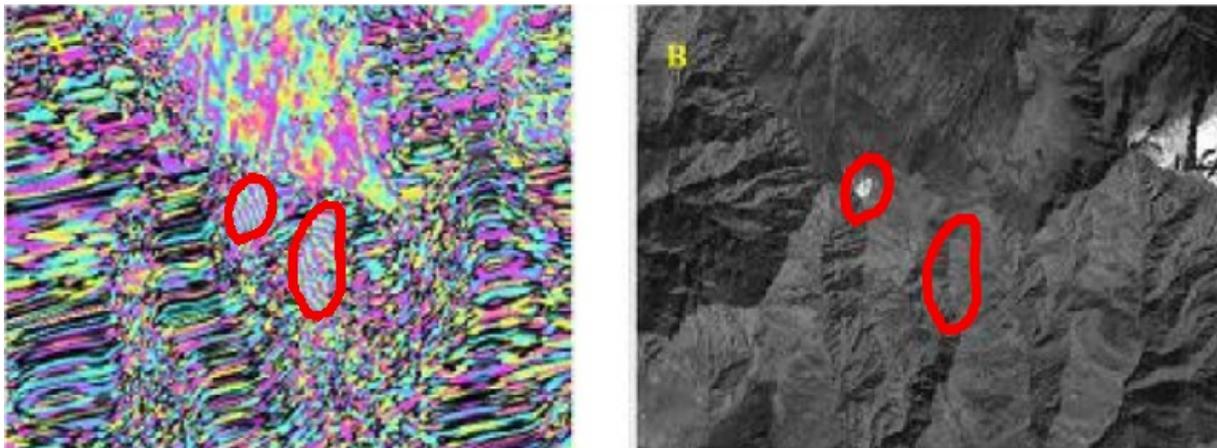


Abbildung 1.7.: Satellitengestützte ERS dInSAR Erkundungen von Rutschungen in Garhwal, Himalaya; links Interferogramm und rechts ETM Aufnahme, aus Singh und Ray (2009).

Aktuelle Satellitengestützte InSAR-Systeme wie TanDEM-X ermöglichen die Erstellung von 3D-Datensätzen mit 12 m Raster (Krieger et al., 2007), luftgestützte Erkundungen erlauben gegenwärtig eine Erfassung von 3D-Rasterdaten im Submeter-Bereich (Okada et al., 2007). InSAR-Erkundungen eignen sich im Vergleich zu luftgestütztem LiDAR eher für großflächige Erkundungen (Baran, 2009). Aktuelle Satelliten-basierte dInSAR-Erkundungen ermöglichen eine Erfassung von Höhenänderungen im Millimeterbereich (Onuma und Ohkawa, 2009), und werden zur Erkundung von Erdbeben, Vulkanen, Hangrutschungen oder Gletschern herangezogen ((Massonet und Feigl, 1998), (Belardinelli et al., 2003), (Refice et al., 2001)). Allerdings benötigen dInSAR Auswertungen konstante Phasenbeziehungen, welche aufgrund von Vegetation und aktiver Sedimentierung an Hangrutschungen selten gegeben sind. Hochauflösende dInSAR-Erkundungen sind dann nur punktuell mit Hilfe von Eckreflektoren erfassbar (McCardle et al., 2007).

Aerogeophysik

Analog zu den Fernerkundungsverfahren werden aerogeophysikalische Verfahren in aktive und passive Methoden unterteilt. Sowohl die Aeromagnetik und die Aeroradiometrie, als auch die Aerogravimetrie werden den passiven Methoden zugeordnet. Mit Hilfe der Aeromagnetik können großräumige Messungen des Erdmagnetfeldes durchgeführt werden (von Norbert, 1991). Auch magnetische Materialien im Untergrund sind mittels Aeromagnetik erfassbar (Yu et al., 2007). Zur Minimierung von magnetischen Störeinflüssen des Flugzeuges werden AM-Messungen oftmals mit geschleppten Messkonfigurationen durchgeführt. Verfahren der Aerogravimetrie kommen hauptsächlich zur Erkundung der Dichteverteilung des Untergrunds zum Einsatz. Hieraus lassen sich auch subglaziale Struk-

turen abschätzen (Studinger et al., 2004). Aeroradiometrische Verfahren erlauben eine flächendeckende Erfassung der Radioaktivität von oberflächennahen Gesteinsschichten und Böden. Diese Verfahren kommen hauptsächlich zur Erforschung des Aufbaus der Erdkruste und zur Rohstoffgewinnung zum Einsatz (Militzer und Weber, 1985).

Die aktiven Verfahren der Aeroelektromagnetik und des Aero-Georadars werden für oberflächennahe Bodenerkundungen eingesetzt. Die Eindringtiefe elektromagnetischer Wellen ist hauptsächlich von deren Frequenz und der Leitfähigkeit des Bodens abhängig. Nach Swift (1967) berechnet sich die Eindringtiefe elektromagnetischer Wellen nach folgender Gleichung:

$$\delta = \sqrt{\frac{2}{\mu\omega\sigma}} \approx 503,29 \sqrt{\frac{\rho}{f}} \quad (1.3)$$

δ = Eindringtiefe	μ = Permeabilitätskonstante
ω = Kreisfrequenz	σ = Spezifische Leitfähigkeit
ρ = Spezifischer Widerstand	f = Frequenz

Mit abnehmender Frequenz der Mikrowellen vergrößert sich die Eindringtiefe, jedoch werden dann größere Antennen benötigt, und der Energiebedarf zur Erzeugung von tieffrequenten elektromagnetischen Wellen steigt Görner und Hübner (2001).

Die Verfahren des Aero-Georadars eignen sich für großflächige Erkundungen von oberflächennahen geologischen Strukturen (Gundelach et al., 2010), auch luftgestützte Erkundungen von Schneetiefen sind realisierbar (Marchand et al., 2003). Jedoch muss im Falle von leitenden Bodenschichten mit einer starken Dämpfung gerechnet werden. In feuchten Tonschichten können z. B. nur Eindringtiefen <0,2 m erreicht werden. Im Bereich der Aero-Georadar Erkundung kommen Antennen außerhalb des Flugzeuges zum Einsatz.



Abbildung 1.8.: AEM Ausrüstung und Hubschrauber des BGR, Quelle: BGR.

Nach Görner und Hübner (2001) ist bei elektromagnetischen Erkundungen die Eindringtiefe zusätzlich von der Distanz zwischen Sende- und Empfangsantenne abhängig, und wird je nach Frequenz mit 40 - 80 % des Antennenabstandes angegeben. Mit den Verfahren der AEM werden Erkundungen von tektonischen Schichtungen (Jordan und Siemon, 2002), aber auch Grundwassererkundungen durchgeführt (Siemon, 2005). Zur Minimierung von elektromagnetischen Störeinflüssen des Flugzeuges kommen AEM-Verfahren hauptsächlich mit geschleppten Messkonfigurationen zum Einsatz (Abbildung 1.8).

1.2.2. Beobachtung von Hangrutschungen

Mit Hilfe von bodengestützten Fernerkundungsverfahren ist eine räumliche hochauflösende Datenerfassungen zu jeder Zeit realisierbar. Jedoch schränken Abschattungen die Nutzbarkeit aufgrund der schrägen Aufnahmeperspektive erheblich ein. Im Bereich der Hangrutschungs-Forschung kommen vor allem luft- und satellitengestützte Erkundungsmethoden zum Einsatz (Metternicht et al., 2005). Für räumlich hochauflösende Beobachtungen von Hangrutschungen sind folgende Methoden von besonderem Interesse:

- Luftgestützte, optische Beobachtungen aus niedrigen Flughöhen ermöglichen Bildaufnahmen mit Bodenauflösungen im Submeterbereich. Diese Daten können zur Generierung von digitalen Geländemodellen herangezogen werden. Anhand von hochauflösenden, dreidimensionalen Modellen und Texturinformationen sind morphologische Analysen durchführbar.
- Luftgestütztes geodätische LiDAR ermöglicht die direkte Erfassung von dreidimensionalen Oberflächeninformationen im Submeterbereich, selbst über bewaldeten Gebieten sind hochauflösende Oberflächeninformationen erfassbar.
- Satelliten-basierte dInSAR-Erkundungen eignen sich für eine großflächige, hoch genaue Dislokations-Erfassung im Millimeterbereich.

1.3. Unbemannte Flugzeuge: UAV

Die englische Abkürzung UAV (*unmanned aerial vehicle*) beschreibt unbemannten Fluggeräte, sowohl ferngelenkte, wie auch autonom fliegende Systeme (Eisenbeiss, 2009). Der fernerkundliche Einsatz von unbemannten Flugzeugen hat eine mehr als dreißigjährige Historie. Erste Bildflüge mit Modellflugzeugen wurden bereits im Jahre 1979 publiziert

(Przybilla und Wester-Ebbinghaus, 1979). Autonomes Fliegen war zu dieser Zeit technisch jedoch unmöglich und die notwendige, manuelle Navigation der Flugzeuge schränkte den Aktionsradius auf wenige hundert Meter ein. Erst seit wenigen Jahren ist eine zuverlässige Luftbilderfassung mittels UAV möglich (Eisenbeiss, 2009). Aufgrund von technischen Fortschritten wie der Miniaturisierung der Antriebs-, Sensor-, Akku- und Kamertechnik sind Luftbilderfassungen mittels autonom fliegenden Drohnen möglich. So kommt seit geraumer Zeit die UAV-basierte Fernerkundung immer häufiger zur Anwendung. Dies ist auch auf eine kostengünstige Verfügbarkeit von UAV- und Autopilot-Systemen zurückzuführen. Die Nutzung von UAV-Systemen als Fernerkundungsplattform verspricht wesentliche Vorteile gegenüber den herkömmlichen Fernerkundungs-Verfahren.

- Zeitlich unabhängige Datenerfassung (prompter Einsatz und beliebige Wiederholraten).
- Niedrige Flughöhen minimieren atmosphärische Störungen und störende Einflüsse von Wolken.
- Aufgrund beliebig niedriger Flughöhen sind sehr hochauflösende Datensätze erfassbar.
- Im Vergleich zu konventionellen Luftaufnahmen können kostengünstige Luftaufnahmen erfasst werden.

Obwohl die oben genannten Vorteile auf den ersten Blick überwiegen, müssen für den Einsatz von UAV-Systemen auch einige Nachteile in Betracht gezogen werden. Die wesentlichen Einschränkungen des fernerkundlichen Einsatzes von UAV-Systemen werden in folgenden Punkten zusammengefasst.

- Nur kleine Nutzlasten können getragen werden (Einschränkung bei der Sensorauswahl).
- Niedrige Flughöhen erfordern eine größere Anzahl von Luftaufnahmen.
- Autonome Flüge sind nach Luftrecht in vielen Ländern unzulässig.
- Die manuelle UAV-Navigation ist sehr schwierig und erfordert viel Flugerfahrung.

1.3.1. UAV-Systeme

Aktuell werden hauptsächlich Drehflügel- und Starrflügelsysteme, aber auch Ballone, Luftschiffe, Gleitschirme und Lenkdrachen zur zivilen fernerkundlichen Erfassung eingesetzt (Eisenbeiss, 2009). Die aktuell genutzten Systeme werden im folgenden Abschnitt vorgestellt.



Abbildung 1.9.: Helikopter UAV-System aus Eisenbeiss et al. (2005).

Drehflügel-UAV

Drehflügel-Systeme erlauben neben Schwebeflug sowohl Senkrechtstarts, als auch Senkrechtlandungen. Der gesamte Auftrieb muss mit Motorkraft erzeugt werden, und die mögliche Zuladung vermindert sich durch große Antriebskomponenten, Akkus und Treibstoff. Erste fernerkundliche Dokumentationen mittels ferngesteuerten Helikoptern wurden 1980 publiziert (Wester-Ebbinghaus, 1980). Eisenbeiss et al. (2005) publizierten erste großflächige photogrammetrische 3D Rekonstruktionen mittels Helikopter-UAVs (Abbildung 1.9). Seit Anfang des Jahres 2004 sind verschiedene Multikopter-Systeme am Markt. Multikopter Systeme verfügen über mehrere starre Rotoren, eine mechanische Pitch-Ansteuerung der Rotorblätter entfällt (Abbildung 1.10). Die Stabilisierung des Fluges wird mittels Inertial-Sensor-Systemen (INS) und einer PID-Regelung (Proportional Inte-

1.3. Unbemannte Flugzeuge: UAV

gral Differential Regelung) der einzelnen Rotoren realisiert (Bouabdallah et al., 2004). Im Bereich der UAV Forschung kommen seit einigen Jahren vereinzelt Koaxial-Systeme zum Einsatz. Zwei gegenläufige Pitch-Rotoren erzeugen den Auftrieb und ermöglichen sehr stabile Flugeigenschaften. Ein Heckrotor zur Kompensation des Drehmoments entfällt (Abbildung 1.11).



Abbildung 1.10.: Am IFG Universität Stuttgart entwickelte Multikopter.

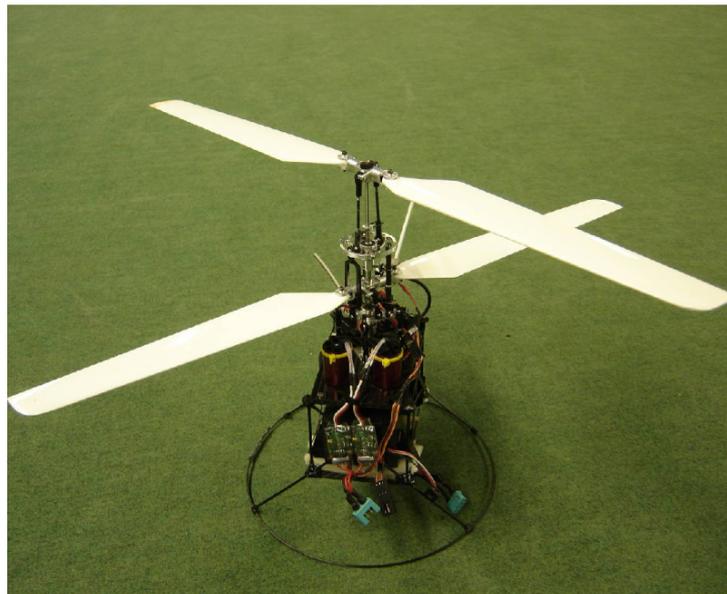


Abbildung 1.11.: Coaxial UAV-System aus Duranti et al. (2007).



Abbildung 1.12.: Starrflügel UAV-System, aus Haala et al. (2011).



Abbildung 1.13.: Starrflügel UAV-System aus Gülch (2012).

Starrflügel-UAV

Starrflügel-Systeme generieren den notwendigen Auftrieb aus ihrer Horizontalbewegung. Der Betrieb ist mit einem Bruchteil der aufzuwendenden Energie eines Drehflügelsystems möglich. Jedoch schränken größere Fluggeschwindigkeiten die Datenakquise aufgrund von Bewegungsunschärfe ein. Zusätzlich benötigen die meisten Starrflügel-Systeme zum Betrieb eine Start- und Landebahn. Erste Bildflüge mittels Starrflügel-System wurden 1979 durchgeführt (Przybilla und Wester-Ebbinghaus, 1979). Aktuell werden zahlreiche Starrflügel-UAVs für die unterschiedlichsten Anwendungen genutzt. Haala et al. (2011) verwendeten für photogrammetrische Tests zweimotorige Starrflügel-Systeme (Abbildung 1.12). In Studien zur photogrammetrischen Erfassung von Bodenerosion (d'Oleire Oltmanns et al., 2012) kommen einmotorige Systeme zum Einsatz. Selbst kleine ultra-leicht Deltaflügel-Systeme werden für photogrammetrische Erfassungen genutzt (Gülch, 2012). Mittlerweile steht eine Vielzahl von kommerziellen, autonom-fliegenden *Personal Aerial Mapping Systemen* (PAMS) für einfache fernerkundliche Erfassungen zur Verfügung (Abbildung 1.13).

Ballone

Ballone werden schon seit langer Zeit zur Luftbildakquise eingesetzt. So wurden schon die ersten Luftaufnahmen 1858 mit Hilfe eines Ballons durch G. F. Tournachon aufgenommen (Elachi, 1987). Der notwendige Auftrieb wird mit einem mitgeführten Gas, welches eine geringere Dichte als Luft besitzt, gewonnen. Heißluftballone sind im Bereich der UAV-Systeme bisher nicht bekannt. Die Handhabung eines Fesselballones gestaltet sich aus technischer Sicht relativ aufwendig, da gefüllte Ballone sehr große Abmessungen erreichen (siehe Abbildung 1.14) und aus Platzgründen nur im unbefüllten Zustand transportiert werden können. So muss ein Ballon vor jeder Erkundungs-Kampagne mit Gas befüllt- und nach jeder Nutzung wieder entleert werden. Die Positionierung (mittels Seilen) erfordert jedoch weniger Erfahrung im Vergleich zum ferngesteuerten Betrieb von Flugzeugen.

Aktuellere Erkundungen (Altan et al., 2004; Fotinopoulos, 2004; Scheritz et al., 2008) zeigen mögliche Anwendungen im Bereich der Photogrammetrie, aber auch die Einschränkungen von Fesselballon-Systemen auf: Das System ist sehr windempfindlich, und im Luftbild ist oft das fesselnde Seil sichtbar.

Luftschiffe

Luftschiffe erzeugen wie Ballone den notwendigen Auftrieb mit Hilfe eines mitgeführten Gases, welches eine geringere Dichte als Luft besitzt. Luftschiffe sind jedoch lenkbar und verfügen über einen eigenen Antrieb (Abbildung 1.15). Als wesentlicher Vorteil ist vor



Abbildung 1.14.: Ballon aus Altan et al. (2004).



Abbildung 1.15.: Luftschiff UAV-System aus Lanier (2011).

allen die Absturzsicherheit, sowie die Möglichkeit, im Schwebeflug über fixen Punkten zu verharren zu nennen. Nachteilig ist jedoch eine starke Windempfindlichkeit (Kawano, 2011). Aktuelle fernerkundliche Forschungen mit Luftschiffen beschäftigen sich mit der photogrammetrischen Erfassung von Wasserrinnen-Erosion (Ries und Marzloff, 2003), archäologischen 3D Rekonstruktionen (Gomez-Lahoz und Gonzalez-Aguilera, 2009) und aeromagnetischen Erkundungen (Grosser, 2009).

Gleitschirm-Systeme

UAV-Gleitschirme oder auch UAV-Paragliders werden seit jüngerer Zeit als motorisierte Fluggeräte für luftgestützte Erkundungen eingesetzt (Abbildung 1.16). Die Vorteile von Gleitschirm-UAVs zeigen sich vor allem in langen Flugzeiten (bis zu mehreren Stunden), geringen Fluggeschwindigkeiten und im Vergleich zum Eigengewicht relativ große Traglasten. Jedoch wird eine lange Aufstiegszeit benötigt, und die Systeme sind windanfällig und träge (Thamm und Judex, 2006). Gleitschirm-UAVs kommen aktuell eher selten zum Einsatz, Einsatzbereiche sind z. B. Kartierungen von Naturwäldern (Jütte, 2008), sowie Forschungen zur Verkehrsüberwachung (Clark et al., 2010).

Drachen-Systeme

Drachen gewinnen den notwendigen Auftrieb aus der kinetischen Energie der Luft. Wind wird über eine Segelfläche schräg nach unten abgelenkt, die resultierende vertikale Kraftkomponente erzeugt so den notwendigen Auftrieb. Die Auftriebskraft wird oftmals zusätzlich mit Hilfe von verschachtelten Segelflächen vergrößert (Abbildung 1.17). Die Vorteile von fernerkundlich genutzten Drachen liegen vor allem in einer einfachen Handhabung und schnellen Einsatzfähigkeit. Drachen-Systeme können je nach verwendeter Segelgröße innerhalb eines großen Windgeschwindigkeits-Bereiches genutzt werden, im Falle von Windstille ist jedoch kein Einsatz möglich. Drachen werden gegenwärtig für photogrammetrische Erfassungen und zur Erforschung der Atmosphäre eingesetzt (Aber et al., 2002; Balsley et al., 1998).

1.3.2. UAV-basierte Hangbeobachtungen

Die fernerkundliche UAV-Erfassung von alpinen Hängen ist mit windempfindlichen UAV Systemen wie Ballonen, Luftschiffen und Gleitschirmen nicht zuverlässig realisierbar, da zu jeder Zeit mit starken Hangwinden und Thermik zu rechnen ist. Drachensysteme eignen sich gut zur Anwendung bei Wind, sind jedoch aufgrund der Kontrolle mit Seilen weitgehend unflexibel und während Windstille nicht einsatzbereit. Im alpinen Gelände können



Abbildung 1.16.: Gleitschirm aus Clark et al. (2010).



Abbildung 1.17.: Drachen aus Reiche et al. (2012).

nur in seltenen Fällen geeigneten Start- und Landebahnen für den Betrieb von Starrflügelsystemen gefunden werden. Startkatapulte, sowie Fangnetze zur Landung müssen transportiert und aufgebaut werden, sie schränken die Flexibilität erheblich ein. Nach dem aktuellen Stand eignen sich Drehflügel UAV-Systeme für den alpinen Einsatz am besten. Eine robuste Technik zur Minimierung von Ausfällen ist mit herkömmlichen Helikoptern und Coaxial-Systemen aufgrund großer Rotoren und mechanischen Pitch-Ansteuerungen jedoch schwer umsetzbar. Im Falle von problematischen Landungen besteht ein großes Risiko, dass Rotoren den Boden streifen, beschädigt werden und ausgetauscht oder justiert werden müssen. Dieses Problem kann mit der Verwendung von Multi-Rotor-Systemen umgangen werden, da starre Luftschrauben nur kleine Durchmesser aufweisen und mit wenigen Handgriffen ersetzbar sind.

Seit Beginn dieser Forschungen im Jahre 2007 kann eine rasante Entwicklung im Bereich der Multi-Rotor UAV-Systeme beobachtet werden. Anfangs waren nur wenige kostengünstige Open-Source UAVs wie das verwendete Mikrokopter-System (Mikrokopter-Developer, 2013) verfügbar. Gegenwärtig werden Multi-Rotor UAVs für zahlreiche Forschungsprojekte genutzt, sie haben sich als kostengünstige, handhabbare Fernerkundungsplattform etabliert. Erste großflächige Erfassungen von Hangrutschungen mittels Open-Source Multikopter-System wurden 2009 publiziert (Niethammer et al., 2009). Diese, in der Kategorie der M-Klasse einzuordnenden Systeme (Eisenbeiss, 2009), werden hauptsächlich für optische und multispektrale Erfassungen genutzt. Aktuelle Forschungen im Bereich der UAV-gestützten LiDAR-Erkundung (Lin et al., 2011) kündigen erste Anwendungsmöglichkeiten mittels UAV-Systemen an. Für hochauflösende UAV-basierte LiDAR Erkundungen müssen jedoch weiterhin Probleme einer kontinuierlichen Positionserfassung der UAVs gelöst werden, da sich miniaturisierte GPS-INS und IMU-Systeme hierfür bisher als problematisch herausgestellt hatten (Eisenbeiss, 2009). Auch im Bereich der UAV-gestützten Mikrowellen Fernerkundung werden aktuell erste InSAR-Systeme entwickelt (Remy et al., 2012). Diese Systeme können bisher jedoch nicht in kleine UAV-Systeme integriert werden, da die notwendigen Sensor-Komponenten ein Gewicht von über 30 kg aufweisen.

UAV-Navigation

Konventionelle photogrammetrische Verfahren setzen eine vorgegebene Block-Konstellation der aufgenommenen Luftbilder voraus. In der Regel wird eine Bildüberlappung von mindestens 60 % in Flugrichtung und 30 % benachbarter Flugstreifen gefordert (Abbildung 1.18). Aus Gleichung (1.2) und der jeweiligen Pixelanzahl n_x und n_y können folgende Größen berechnet werden:

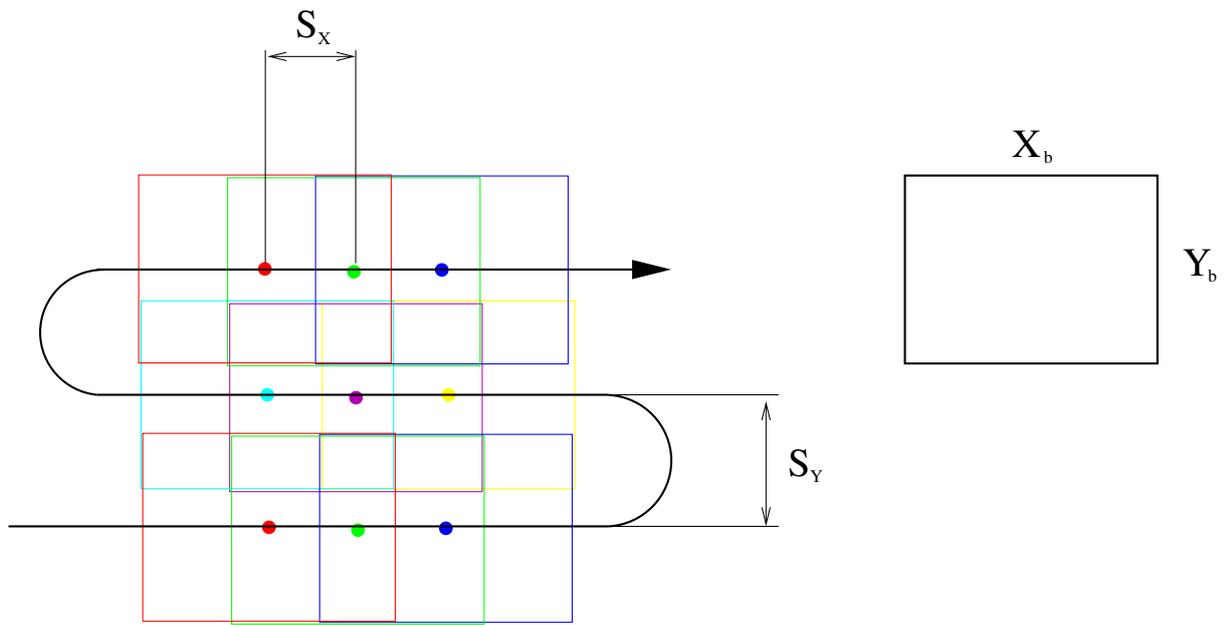


Abbildung 1.18.: Flugschema konventioneller photogrammetrischer Verfahren.

$$X_b = \frac{hpn_x}{c} \quad Y_b = \frac{hpn_y}{c} \quad (1.4)$$

Mit einer gewünschten Bildüberlappung von 60 % und 30 % ergeben sich Aufnahmestanzungen nach folgenden Gleichungen:

$$S_X = 0.4X_b \quad S_Y = 0.7Y_b \quad (1.5)$$

Parameter der Berechnung:

X_b Abgedeckter Bereich in Flugrichtung	Y_b Abgedeckter Bereich quer zur Flugrichtung
S_X Aufnahmedistanz in Flugrichtung	S_Y Distanz zwischen zwei Flugbahnen
n_x Pixelanzahl in x-Richtung, Spalten	n_y Pixelanzahl in y-Richtung, Zeilen
h Flughöhe über Grund	p Pixelrastermaß im Sensor
c Brennweite der Optik	

Einfache, GPS-gestützte Navigations-Systeme eignen sich nur unzureichend für direkte photogrammetrische Berechnungen. Die maximale Messgenauigkeit ist auf 5 m begrenzt. Weiterhin erschweren große Messabweichungen während schlechter Empfangskonstellationen (z. B. durch Abschattung im alpinen Raum) eine autonome Navigation für konventionelle Bildblock-Aufnahmen. Es können schnell Abweichungen bis zu 50 m auftreten. Neuste Entwicklung zur autonomen Navigation von UAV-Systemen erlauben nun eine 'GPS-freie' Navigation (Bry et al., 2012), diese Entwicklungen stehen jedoch am Anfang und sind für den praktischen Einsatz bisher ungeeignet. Eine zuverlässige Wegpunkt-Navigation im Submeterbereich ist nach dem aktuellen Stand der Technik nur mittels dGPS und Real-Time-Kinematik (RTK-dGPS) oder mit Hilfe einer Tachymeter-gestützter Navigation möglich (Bäumker und Przybilla, 2011). Zusätzlich schränken gesetzliche Vorschriften den autonomen Flugbetrieb ein. Eine großflächige Wegpunktnavigation kann somit nicht effektiv genutzt werden.

1.3.3. UAV Flugrecht in Deutschland

In der Vergangenheit unterlag in Deutschland der Betrieb von UAV-Systemen den gesetzlichen Regelungen für Flugmodelle (§ 1 Abs. 2 Nr. 9 LuftVG), sofern diese 5 kg Abfluggewicht nicht überschritten, und eine manuelle Kontrolle des Betreibers jederzeit gewährleistet war. Wurden diese Bedingungen erfüllt, so war keine spezielle Genehmigung durch Luftfahrtbehörden notwendig. Eine Genehmigungspflicht für Luftbildaufnahmen ist seit 1990 nach Artikel 37 des 3. Rechtsbereinigungsgesetzes entfallen, jedoch dürfen nach § 109g Abs. 5 Nr. 3 StGB Wehrmittel, Einrichtungen und Anlagen nicht fotografiert werden, wenn dadurch die Sicherheit der Bundesrepublik Deutschland oder die Schlagkraft der Truppe gefährdet wird. Nach einem BGH Urteil vom 9. Dezember 2003 (AZ: VI ZR 373/02, Luftbildaufnahmen vom Ferienhaus) ist das Eindringen in die geschützte Privatsphäre einer Person mittels Aufnahmen aus Flugzeugen unzulässig. Seit 2012 werden unbemannte Luftfahrtsysteme (UAVs) nach § 1 Abs. 2 folgendermaßen definiert: „... als Luftfahrzeuge gelten unbemannte Fluggeräte einschließlich ihrer Kontrollstation, die nicht zu Zwecken des Sports oder der Freizeitgestaltung betrieben werden“. Folglich bedarf die Nutzung des Luftraums zur Luftbilderfassung mit unbemannten Luftfahrtsystemen nach § 16 Abs. 1 Nr. 7 LuftVO, privat oder gewerblich, der Erlaubnis durch die örtlich zuständige Behörde des Landes. Diese Erlaubnis wird entsprechend gemeinsamer Grundsätze des Bundes und der Länder gemäß § 16 Abs. 3 LuftVO seit 2012 allgemein geregelt (NfL I 161/12). Für den Aufstieg von unbemannten Luftfahrtsystemen ohne Verbrennungsmotor bis 5 kg Gesamtmasse kann hiernach eine allgemeine Erlaubnis erteilt werden.

2. Synopsis der Forschungsarbeiten

Die vorliegende Dissertation wurde als kumulative Arbeit eingereicht. In diesem Kapitel werden Kurzformen der zugrundeliegenden Publikationen zusammen mit weiteren Informationen über die durchgeführten Befliegungen, sowie verschiedene Methoden der Photogrammetrie und Bildverarbeitung synoptisch dargestellt.

2.1. Eigenanteil an Publikationen

Grundlage dieser Arbeit sind fünf ausgewählte Publikationen (siehe auch Anhang A.4). Die wissenschaftlichen Arbeiten werden nach folgenden Anteilen aufgeschlüsselt:

1. Niethammer et al. (2011, Anhang A.1.1) Niethammer, U., Rothmund, S., Schwaderer, U., Zeman, J., und Joswig, M. (2011). **Open source image-processing tools for low-cost UAV-based landslide investigations.** *Int. Arch. Photogramm. Remote Sens. Spatial Inf. Sci.*, XXXVIII-1 C22:161–166.

Der Erstautor hat die UAV-Systeme entwickelt und die notwendigen Software-Komponenten erstellt, sowie sämtliche Befliegungen und Analysen durchgeführt. Alle weiteren Autoren haben unter Anleitung des Erstautors als Diplomanden und Hilfskräfte an kleineren Teilaufgaben mitgewirkt. M. Joswig ist als Betreuer beteiligt.

2. Niethammer et al. (2010, Anhang A.1.2) Niethammer, U., Rothmund, S., James, M., Travelletti, J. und Joswig, M. (2010). **UAV-based remote sensing of landslides.** *Int. Arch. Photogramm. Remote Sens. Spatial Inf. Sci.*, XXXVIII Part 5:496–501.

Der Erstautor hat alle notwendigen Befliegungen durchgeführt und die SfM-MVS-basierten 3D-Modelle erstellt und analysiert. S. Rothmund hat DGPS-Messungen von Passpunkten durchgeführt und unter Anleitung des Erstautors ein Orthomosaik der Super-Sauze Rutschung erstellt. M-R. James trägt ein zum Vergleich notwendiges DGM mittels Nahbereichs-Photogrammetrie bei. J. Travelletti trägt ergänzende Berechnungen zur Punktdichte bei. M. Joswig hat als Betreuer mitgewirkt.

3. Niethammer et al. (2012, Anhang A.1.3) Niethammer, U., James, M., Rothmund, S., Travelletti, J., und Joswig, M. (2012). **UAV-based remote sensing of the Super-Sauze landslide: Evaluation and results.** *Engineering Geology*, 128:2–11.

Der Erstautor ist für die Entwicklung der UAV-Systeme, die Durchführung aller UAV-Befliegungen, sowie die Entwicklung notwendiger Software-Komponenten und Analysen der Fernerkundungsdaten verantwortlich. M-R. James trägt photogrammetrische Vergleichs-Modelle bei. J. Travelletti trägt Vergleichsdaten mittels TLS bei. S. Rothmund verantwortet die geomorphologischen Analysen. M. Joswig ist als Betreuer beteiligt.

4. Stumpf et al. (2013, Anhang A.1.4) Stumpf, A., Malet, J.-P., Kerle, N., Niethammer, U., und Rothmund, S. (2013). **Image-based mapping of surface fissures for the investigation of landslide dynamics.** *Geomorphology*, 186:12–27.

A. Stumpf ist Erstautor und verantwortet die Entwicklung der notwendigen Algorithmen zur Riss-Detektion, sowie die Analysen der Daten. U. Niethammer ist Ko-Autor und trägt die Grund-Idee zur automatischen Riss-Detektion bei. U. Niethammer ist für die Erfassung und Erstellung aller UAV-gestützten Luftbild-Datensätze verantwortlich, S. Rothmund ist an der Zusammenstellung der Datensätze beteiligt. J-P. Malet und N. Kerle haben als Betreuer mitgewirkt.

5. Walter et al. (2009, Anhang A.1.5) Walter, M., Niethammer, U., Rothmund, S., und Joswig, M. (2009). **Joint analysis of the Super-Sauze (French Alps) mudslide by nanoseismic monitoring and UAV-based remote sensing.** *First Break, EAGE*, 27(8):53–60. European Association of Geoscientist & Engineers (EAGE).

M. Walter ist Erstautor und verantwortet die Teile der seismischen Analysen, sowie Teile der gemeinsamen Interpretation. U. Niethammer ist Ko-Autor und trägt die UAV-gestützten Luftbild-Datensätze, sowie Teile der gemeinsamen Interpretation bei. S. Rothmund ist an der Zusammenstellung der Datensätze und an der geomorphologischen Interpretation beteiligt. M. Joswig hat als Betreuer mitgewirkt.

2.2. UAV-System und Software

Als Fernerkundungsplattform wurden Multi-Rotor UAVs entwickelt. Die Verarbeitung der erfassten Daten wurde mit eigenen Softwarekomponenten durchgeführt. Rechenintensive Algorithmen konnten mittels der Programmiersprache C effektiv implementiert werden (Kernighan und Ritchie, 1990). Programme zur Bildentzerrung, Mosaik-Erstellung, 3D Helmert-Transformation, Interpolationsalgorithmen sowie Filteralgorithmen und zahlreiche Konvertierungsroutinen wurden erstellt.

2.2.1. Open-Source Komponenten

Publikation Niethammer et al. (2011, Anhang A.1.1) Niethammer, U., Rothmund, S., Schwaderer, U., Zeman, J., und Joswig, M. Open source image-processing tools for low-cost UAV-based landslide investigations. *Int. Arch. Photogramm. Remote Sens. Spatial Inf. Sci.*, XXXVIII-1 C22:161–166.

Am Institut für Geophysik der Universität Stuttgart wurden zur fernerkundlichen Beobachtung alpiner Hangrutschungen Multi-Rotor UAVs anhand von Open-Source Komponenten entwickelt (Abbildung 2.1).

Die Materialkosten dieser low-cost UAV-Systeme liegen je nach Ausstattung im Bereich zwischen 1000 und 1500 €. Die verwendeten Multi-Rotor Systeme eignen sich zur positionsgenauen Bildgewinnung und sind aufgrund einer robusten Technik für Flüge in schwierigem Gelände geeignet. Die Navigation der UAV-Systeme erfolgt in erster Linie manuell, wobei eine integrierte GPS-INS Prozessierung eine unterstützende, stabilisierende Funktion übernimmt. Das UAV-System wird zur Bilderfassung an der gewünschten Position ohne größeren Steuerungsaufwand vertikal in die gewünschte Aufnahmehöhe gebracht, um dann nach Vollendung der gewünschten Aufnahmen in gleicher Weise wieder vertikal zu landen.

Im Zuge zahlreicher UAV-basierter Fernerkundungs-Kampagnen von Hangrutschungen wurde eine große Zahl Luftbilder aufgenommen. Diese Bilder wurden dann zur Erstellung von Ortho-Mosaiken und digitalen Geländemodellen genutzt. Das entwickelte UAV-System und mehrere entwickelte Open-Source Bildverarbeitungswerkzeuge zur Erstellung von 3D-Geländemodellen, Orthofotos und Mosaiken erlauben einen kompletten Arbeitszyklus, ohne die Verwendung von kommerziellen UAV-Systemen oder Softwarekomponenten.

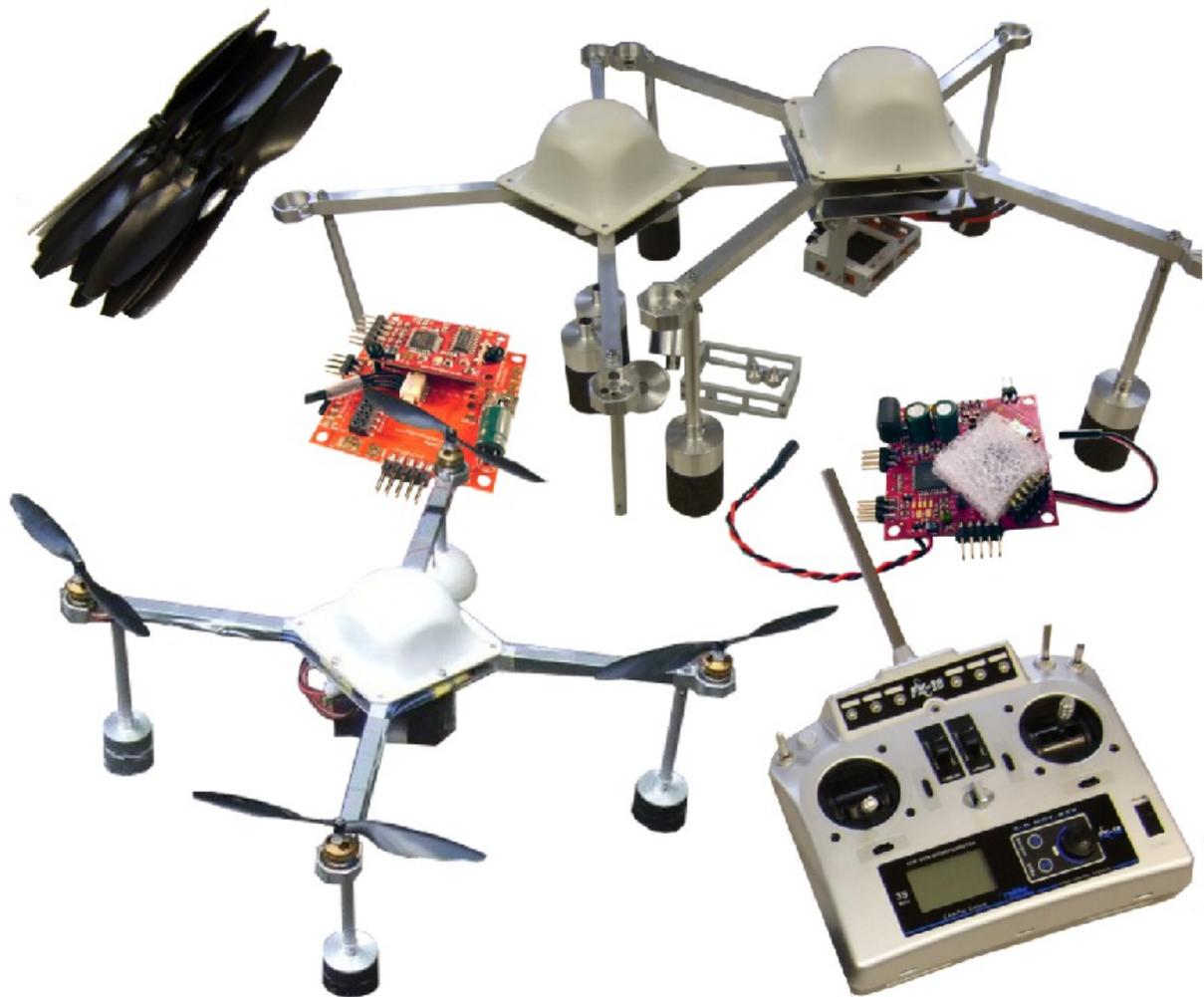


Abbildung 2.1.: Am Institut für Geophysik entwickelte Multi-Rotor UAV-Systeme.

2.2.2. UAV-basierte Fernerkundung mittels SfM-MVS

Publikation Niethammer et al. (2010, Anhang A.1.2) Niethammer, U., Rothmund, S., Joswig, M., James, M., und Travelletti, J. UAV-based remote sensing of landslides. *Int. Arch. Photogramm. Remote Sens. Spatial Inf. Sci.*, XXXVIII Part 5:496–501.

Während einer UAV-basierten Fernerkundungs-Kampagne im Jahre 2008 wurde eine große Zahl Luftbilder der Super-Sauze Hangrutschung aufgenommen. Anhand von 285 dieser Luftaufnahmen werden 3D-Oberflächenmodelle mit Hilfe aktueller *Structure-from-Motion* (SfM) und *Multi-View-Stereo* (MVS) Methoden aus dem Bereich der *Computer-Vision* erstellt. Ungeordnete und verkippte Luftbilder, welche mit einfachen digitalen Kompaktkameras aufgenommen wurden, sind nun mit Hilfe von SfM-MVS Methoden photogrammetrisch prozessierbar. Eine aufwendige Kalibrierung der Kamera entfällt.

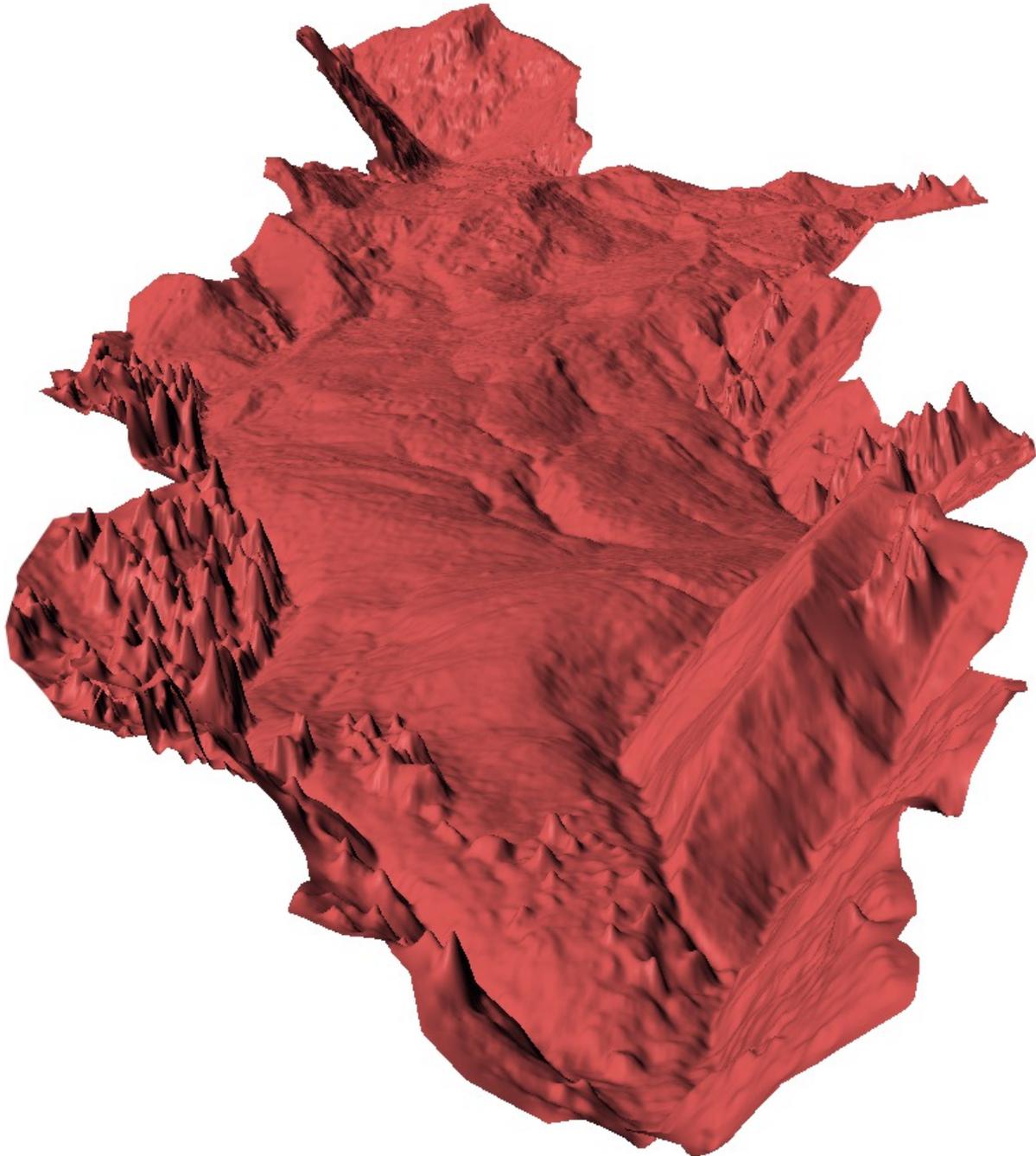


Abbildung 2.2.: SfM-MVS basiertes 3D-Modell der Super-Sauze Hangrutschung.

Diese neuen Verfahren versprechen im Gegensatz zu üblichen photogrammetrischen Verfahren eine effektive, automatische Erstellung von 3D-Modellen. Zur Prozessierung werden weder Passpunkt-, noch Verknüpfungs-Informationen benötigt, dies ermöglicht eine effektive, vollautomatische Verarbeitung großer Bildmengen. Jedoch muss in einem weiteren, manuellen Bearbeitungsschritt die Georeferenzierung mit Hilfe einer Transformation vorgenommen werden, welche die 3D-Punktwolke in das Koordinatensystem des realen Objektraums überführt. In dieser Studie werden erste geodätische Anwendungen und Genauigkeitsabschätzungen vorgestellt. Verschiedene Oberflächenmodelle der Super-Sauze Hangrutschung (Abbildung 2.2) werden in Bezug auf Punktdichte und Maßhaltigkeit untersucht. Analysen eines kleineren Modellbereichs zeigen brauchbare Ergebnisse, jedoch muss bei der SfM-basierten Bündel-Block-Prozessierung von großen Oberflächenmodellen mit signifikanten Abweichungen gerechnet werden.

2.2.3. Ergänzungen zur SfM-MVS Prozessierung

SfM-Algorithmen ermöglichen die Berechnung der jeweiligen inneren und äußeren Kamera-Orientierung anhand von gegebenen Bildsätzen (Abbildung 2.3). Zusätzlich wird eine grobe 3D-Rekonstruktion der Aufnahmeszene berechnet (Snavely et al., 2008). Für jedes Bild werden hierfür SIFT-Deskriptoren (Lowe, 2004) berechnet, deren Übereinstimmung dann mit Hilfe von ANN- und RANSAC-Algorithmen (Arya et al., 1998; Fischler und Bolles, 1981) abgeschätzt wird.



Abbildung 2.3.: Beispiel zu den SfM Verfahren, aus Snavely (2013).

In einem weiteren Bearbeitungsschritt kommt ein *Multi-View-Stereo Dense-Matching* Algorithmus zur Berechnung hochauflösender 3D-Punktwolken zum Einsatz (Furukawa und Ponce, 2007). Hierfür werden innerhalb kleiner Bildbereiche homologe Bildpunkte mittels eines *match-expand-filter* Algorithmus identifiziert und zu einer unskalierten 3D-Punktwolke vereinigt (Abbildung 2.4).



Abbildung 2.4.: MVS Verfahren, Beispiel einer 3D-Punktwolke, aus Furukawa und Ponce (2013).

Helmert Transformation

Die 3D-Punktwolken aus der SfM-MVS Prozessierung müssen mit einer 3D-Ähnlichkeits-
transformation in den Objektraum transformiert werden (Georeferenzierung). Hierfür
wurden Programme zur Transformation und Parameterbestimmung implementiert. Ver-
schiedene, teilweise sehr aufwendige Verfahren zur Parameterbestimmung sind bekannt
(Watson, 2006). Mittels einer Prokrustes-Transformation (Crosilla, 1999) kann die Pa-
rameterbestimmung jedoch sehr effektiv gelöst werden (siehe Anhang A.3.1).

Interpolation und Filterung

Die diskreten Punktwolken aus den berechneten 3d-Modellen setzen sich aus ungleich-
mäßig verteilten Punktkoordinaten $(x, y, z)^t$ zusammen. Für die weitere Nutzung dieser
diskreten Punktwolken müssen regelmäßige, zusammenhängende Rasterdaten erstellt wer-
den. Hierfür wurden anhand von frei verfügbaren *Natural-Neighbour-Algorithmen* (nnc,
2013) schnelle Softwarekomponenten implementiert. Die verwendeten Algorithmen zeigten
in Studien zur Performanz gute *Benchmarks* (Fan et al., 2005). Die *Natural-Neighbour-
Interpolation* basiert auf der *Voronoi-Tessellation* eines diskreten Punkte-Satzes (Sibson,
1981) und hat den Vorteil gegenüber einfacheren Interpolationsverfahren, dass es eine
gleichmäßige Annäherung an zugrunde liegende Stützpunkte erlaubt.

Zusätzlich können aus der photogrammetrischen Modell-Prozessierung Oberflächen-
modelle mit verbleibenden 3D-Rauschartefakten hervorgehen. Dies ist auf Ungenauigkei-
ten der Bildkorrespondenzanalyse zurückzuführen. Störende Rausch-Effekte können mit
digitalen Filteroperationen geglättet werden. Hierfür wurden parametrisierbare Filteral-
gorithmen implementiert (siehe Anhang A.3.6).

2.2.4. Ergänzungen zur Orthofoto-Erstellung

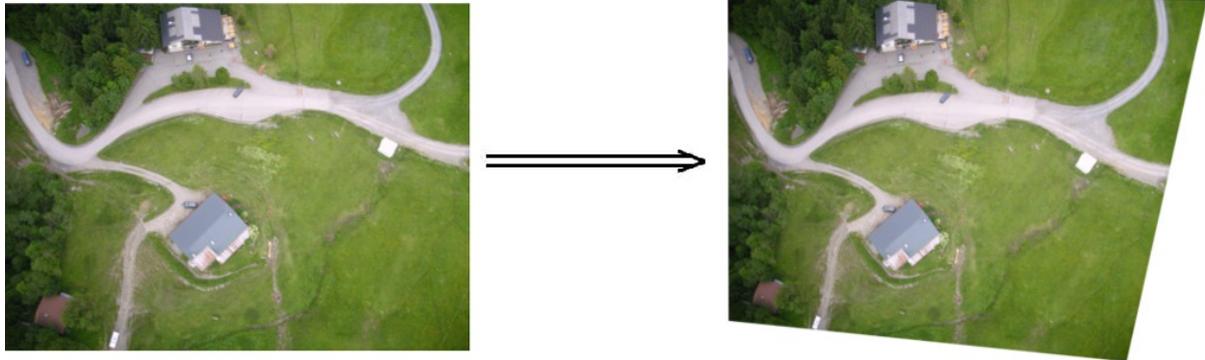


Abbildung 2.5.: Beispiel zur projektiven Luftbildentzerrung. Links: Luftbild des Heumöser Hangs, rechts: perspektivisch entzerrtes Bild.

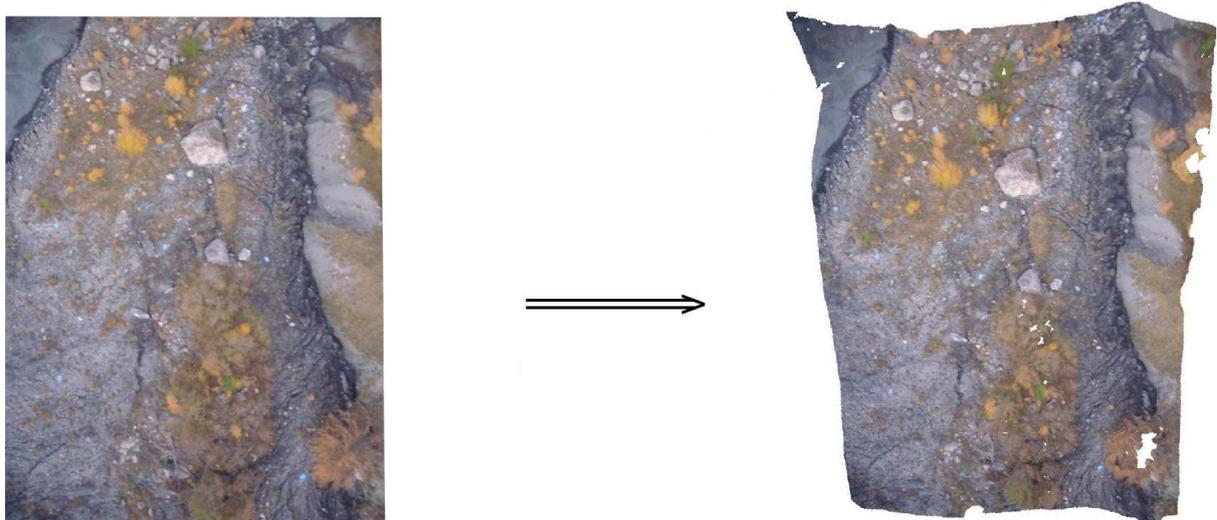


Abbildung 2.6.: Beispiel zur differentiellen Luftbildentzerrung. Links: Luftbild der Super-Sauze Hangrutschung, rechts: differentiell entzerrtes Bild.

Bildentzerrung

Mit Hilfe der projektiven Einzelbildentzerrung lassen sich Luftbilder anhand von minimal vier Passpunkt-Korrespondenzen entzerren. Zugrunde liegende 3D-Modelle werden hierfür nicht benötigt (Luhmann, 2002). Diese Methode (siehe Anhang A.3.3) erlaubt perspektivische Entzerrungen unter der Annahme einer eben Aufnahme­fläche (Abbildung 2.5). Die entwickelte Software unterstützt das *Portable Network Graphics* (PNG) Ausgabeform-

mat mit *Alpha-Blending* (Roelofs und Koman, 1999). undefinierte Bereiche am Bildrand werden mit diesem Format für eine anschließende Mosaikerstellung ausgeblendet.

Ein Verfahren zur präzisen Luftbild-Entzerrung wurde mittels der differentiellen Orthoprojektion (siehe Anhang A.3.5) umgesetzt. Die zur Erstellung der 3D-Modelle verwendeten SfM-Algorithmen (Snavely et al., 2008) stellen hierfür alle notwendigen Parameter der Projektionsmatrix bereit. Die implementierte Software erlaubt eine effektive Beseitigung perspektivischer Verzerrungen (Abbildung 2.6).

Mosaik-Prozessierung

Für die Erstellung von großflächigen, georeferenzierten Ortho-Mosaiken wurden weitere Software-Komponenten implementiert. Die entwickelte Software erlaubt eine vollautomatische Mosaik-Prozessierung der einzelnen entzerrten Luftbilder (Abbildung 2.7). undefinierte Bereiche werden mittels *Alpha-Blending* ausgeschlossen. Zusätzlich kommt ein effektiver *Image-Blending* Algorithmus zum Einsatz (Enblend, 2013). Das Softwarepaket wurde unter der GPL lizenziert (Jaeger und Metzger, 2011) und ist online verfügbar (BuildMosaic, 2013).

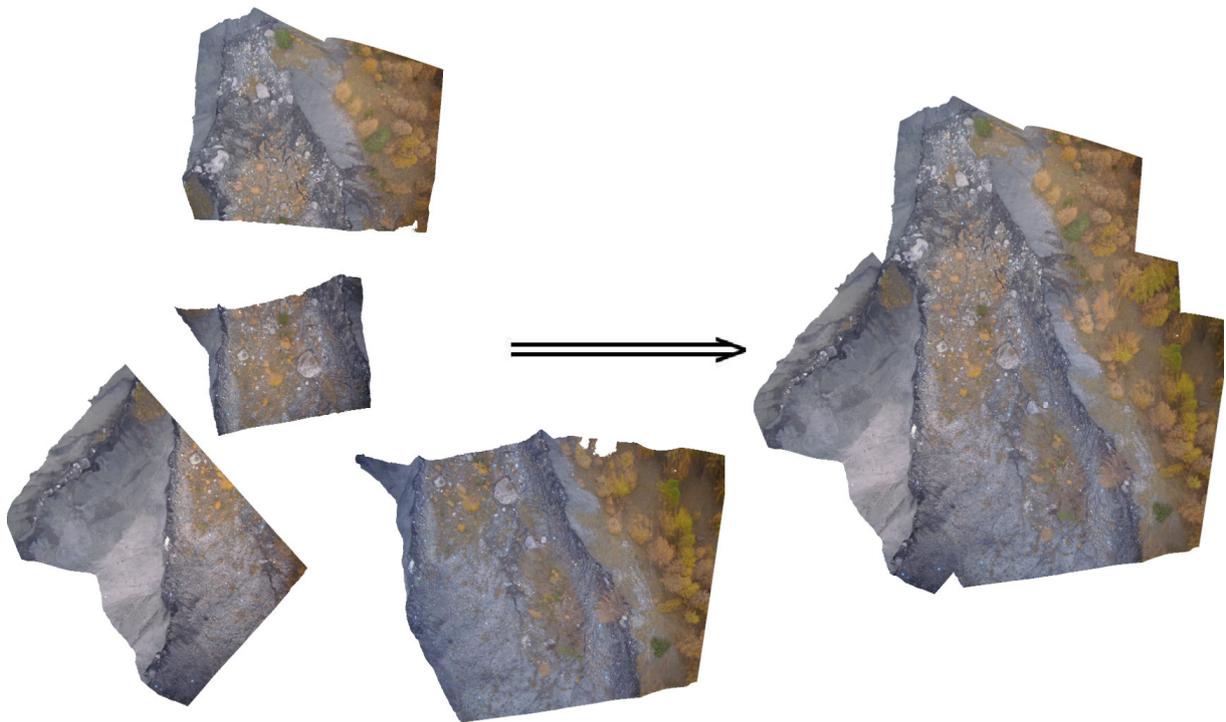


Abbildung 2.7.: Beispiel zur Erstellung eines Ortho-Mosaiks der Super-Sauze Hangrutschung aus mehreren differenziell entzerrten Bildern.

2.3. Befliegungen

Zwei Hangrutschungen (Heumöser Hang, Österreich Vorarlberg und Super-Sauze Südfrankreich) wurden im Rahmen der Forschungen mehrfach befliegen. Beide Hangrutschungen unterscheiden sich in wesentlichen Merkmalen. Während die Rutschung am Heumöser Hang nahezu vollständig mit Vegetation bedeckt ist und durch minimale Verschiebungsraten weniger Zentimeter im Jahr charakterisiert ist, weist die Super-Sauze Hangrutschung eine annähernd unbewachsene Oberfläche mit maximalen Bewegungsraten von bis zu mehreren Zentimetern pro Tag auf.

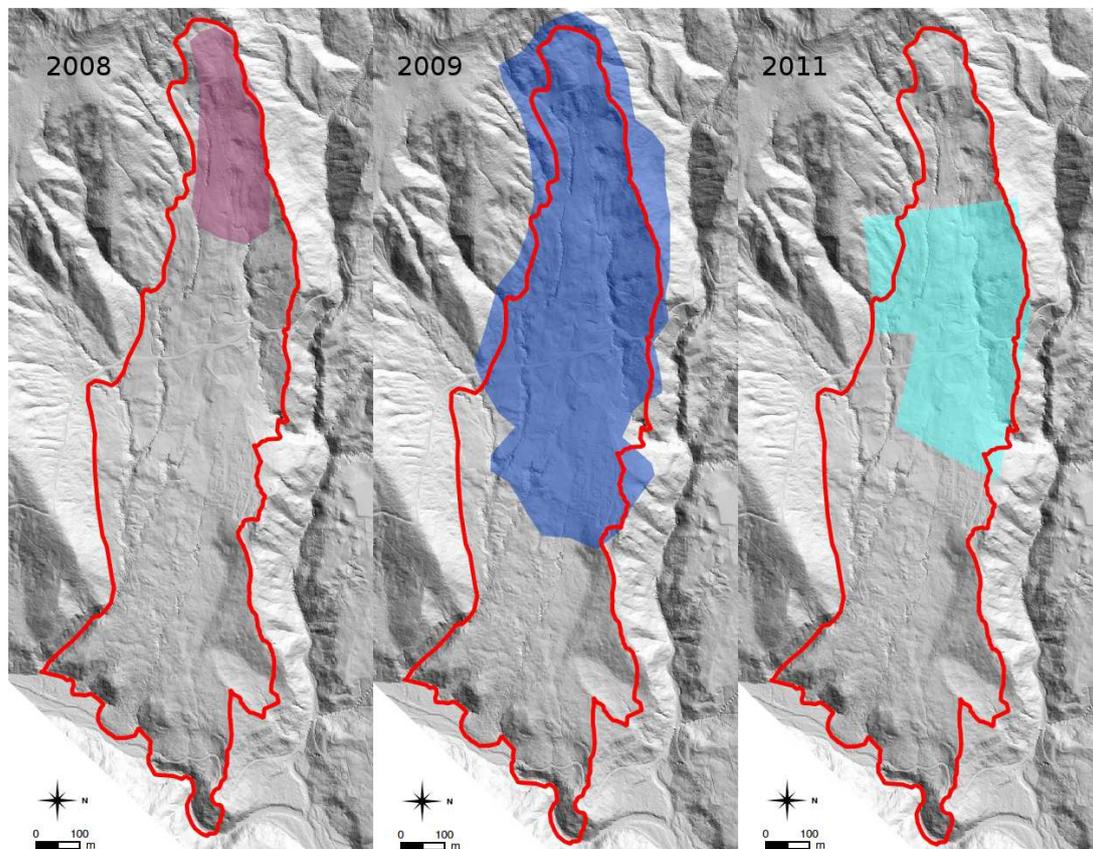


Abbildung 2.8.: Flächenabdeckung der Befliegungen des Heumöser Hangs. Links: Befliegung im Sommer 2008 des oberen Hangbereichs, Mitte: Befliegung des unbewaldeten Bereichs im Sommer 2009, rechts: Befliegung des mittleren Hangbereichs im Frühjahr 2011.

2.3.1. Heumöser Hang

Am Heumöser Hang, Österreich Vorarlberg, wurden drei Befliegungen durchgeführt (Abbildung 2.8). Hochauflösende, morphologische Analysen konnten aufgrund von Vegeta-

tion und geringer Bewegungsraten nicht durchgeführt werden. Multispektrale Analysen der Vegetation im VIS, NIR und thermischen Infrarotbereich (TIR) wurden durchgeführt (Schwaderer, 2010). Eine Luftbildakquise im nahen Infrarotbereich war gut durchführbar, jedoch konnten mit den gewonnenen Daten keine brauchbaren Informationen für die Hangrutschungs-Forschung erschlossen werden. Zusätzlich zeigte sich die ausgeprägte, teilweise meterhohe Vegetation auf dem Rutschungskörpers hinderlich für photogrammetrische Prozessierungen von 3D-Modellen.

2.3.2. Super-Sauze

Die südfranzösische Super-Sauze Hangrutschung wurde mit vier UAV-Kampagnen fernerkundlich erfasst (Abbildung 2.9). Zahlreiche Oberflächen-Parameter der Hangrutschung waren fernerkundlich erfassbar. Im Fokus stand die Beobachtung von Rissen und die Ermittlung von Verschiebungsraten an der Rutschungs-Oberfläche. Erste Versuche zur Ortho-Mosaik Erstellung wurden mittels Einzelbild Entzerrungsmethoden durchgeführt (Rothmund, 2009). In weiteren Studien wurde das Bildmaterial zur 3D-Modell Erstellung und für morphologische Studien genutzt.

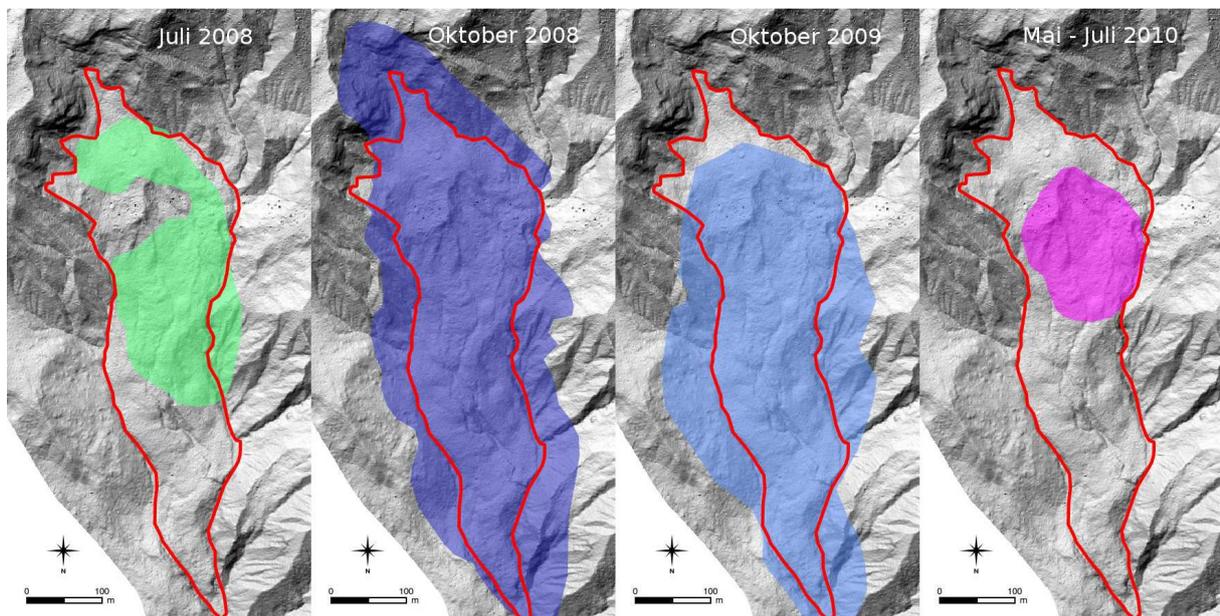


Abbildung 2.9.: Flächenabdeckung der Befliegungen der Super-Sauze Hangrutschung. Von links nach rechts: Befliegung Juli 2008, Befliegung Oktober 2008, Befliegung Oktober 2009, tägliche Befliegungen Mai - Juli 2010.

2.4. Pilotstudien der Hangbeobachtung

Ziel dieser Arbeit war es, UAV-basierte Fernerkundungsverfahren zur Hangbeobachtung anhand von unterschiedlichen Pilotstudien zu erproben. Drei Pilotstudien werden in den folgenden Abschnitten vorgestellt.

2.4.1. Morphologische Untersuchungen

Publikation Niethammer et al. (2012, Anhang A.1.3) Niethammer, U., James, M., Rothmund, S., Travelletti, J., und Joswig, M. UAV-based remote sensing of the Super-Sauze landslide: Evaluation and results. *Engineering Geology*, 128:2–11.

UAV-Systeme können zur schnellen, hochauflösenden Kartierung von Hangrutschungen eingesetzt werden. Zahlreiche Luftbilder der Super-Sauze Hangrutschung wurden im Oktober 2008 mit Hilfe von ferngesteuerten UAV-Systemen aufgenommen. Aus diesen Luftaufnahmen wurden hochauflösende Ortho-Mosaik der Rutschung und digitale Geländemodelle von mehreren Regionen der Rutschung erstellt. Das Potenzial der Datenerfassung und die Möglichkeiten verschiedener Bildverarbeitungsmethoden wie Entzerrung, Erfassung von Rissen, sowie Ermittlung von Verschiebungsraten an der Rutschungsoberfläche werden in dieser Studie untersucht. Horizontale Verschiebungen werden im direkten Vergleich anhand eines hochauflösenden, luftgestützten Orthofotos (Mai 2007) und des generierten Ortho-Mosaiks (Oktober 2008) ermittelt (Abbildung 2.10).

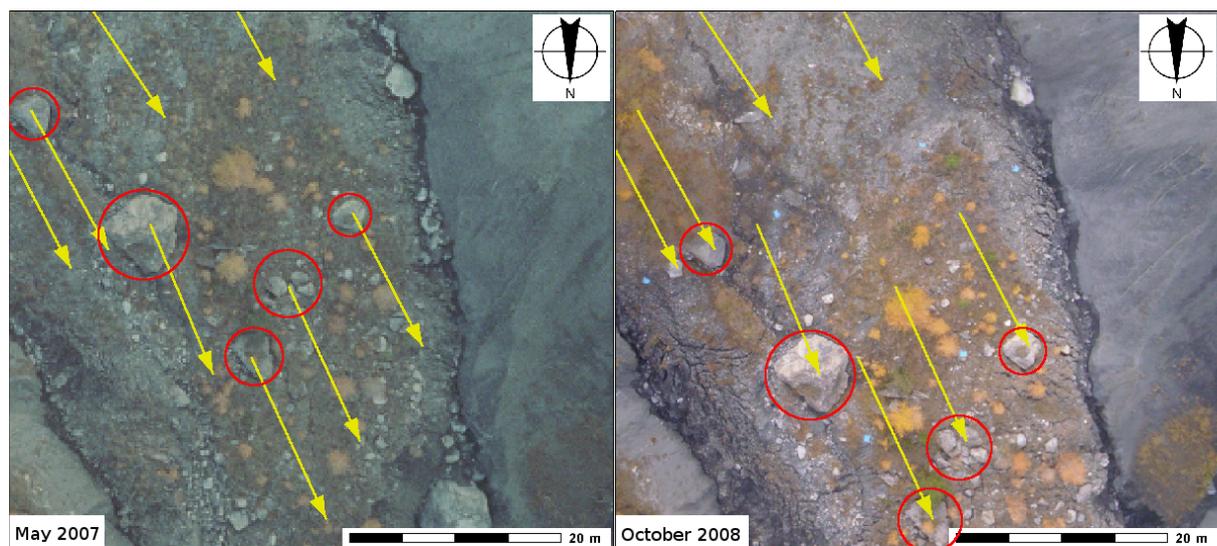


Abbildung 2.10.: Verschiebungsvektoren am Fuße der Super-Sauze Hangrutschung. Links Luftaufnahme im Mai 2007, rechts Orthomosaik im Oktober 2008.

Ortsfeste Bereiche mit konstanter Deformation sind anhand des Mosaiks gut identifizierbar. Diese Bereiche weisen unterschiedliche Riss-Strukturen mit verschiedenen Ausdehnungen und Orientierungen auf, und sind vergleichbar mit Gletscherspalten. Die identifizierten Spalten stehen in unmittelbarem Zusammenhang mit der Festgesteins-Topographie des Untergrunds. Die verwendeten UAV-Systeme zeigen eine wertvolle Möglichkeit der Datenerfassung auf, jedoch sind Verbesserungen zur effektiven Prozessierung von Orthofotos- und Oberflächenmodellen erforderlich: Um eine effiziente Bearbeitung zu ermöglichen und Fehler der Georeferenzierung zu minimieren, müssen differenzielle photogrammetrische Entzerrungsmethoden mit Hilfe von automatischen, Merkmals-basierten Verfahren zum Einsatz kommen.

2.4.2. Semiautomatische Risskartierung

Publikation Stumpf et al. (2013, Anhang A.1.4) Stumpf, A., Malet, J.-P., Kerle, N., Niethammer, U., und Rothmund, S. Image-based mapping of surface fissures for the investigation of landslide dynamics. *Geomorphology*, 186:12–27.

Risse in Hangoberflächen gelten als zuverlässiger Indikator für aktive Hangbewegungen. Eine Beobachtung der Rissentwicklung kann neue Informationen über Rutschungsmechanismen liefern und zur Vorhersage von Abgängen herangezogen werden. Untersuchungen von Hangrutschungen beinhalten daher häufig eine Kartierung der räumlichen Riss-Verteilung und deren Interpretation, welche typischerweise mit intensiver Feldarbeit und Instrumentierung verbunden sind. Erst seit kurzer Zeit kommen Luftbilder mit einer räumlichen Auflösung im sub-Dezimeter Bereich zum Einsatz. Aus der Fernerkundungsperspektive sind nun effektive Analysen kleinster Oberflächenmerkmale durchführbar. Obwohl diese Daten im Grundsatz zur Prozessierung mittels Bildverarbeitung geeignet sind, existieren noch keine automatischen Bildverarbeitungs-Methoden zur Extraktion dieser geomorphologischen Merkmale. Ein weitgehend automatisiertes Verfahren zur Kartierung von Oberflächenrissen aus hochauflösenden Luftbildern wird vorgestellt. Die Prozesskette beinhaltet sowohl Filteralgorithmen, als auch eine Nachbearbeitung der gefilterten Bilder mit Hilfe einer objektorientierten Analyse. Die Genauigkeit der resultierenden Karten wird in Bezug auf betroffenen Bereiche, Riss-Dichte und Riss-Orientierung durch Vergleiche mit verschiedenen manuellen Experten-Kartierungen beurteilt. Unter homogenen Ausleuchtungs-Bedingungen, werden richtig-positive Erkennungsraten von bis zu 65 % und falsch-positive Erkennungsraten in der Regel unter 10 % erreicht. Die resultierenden Risskartierungen liefern Details, um Rückschlüsse auf mechanische Prozesse in der Größenordnung der Hang-Skala ziehen zu können (Abbildung 2.11), und um interessante Bereiche für vertiefende Bodenuntersuchungen oder Überwachung festlegen zu können.

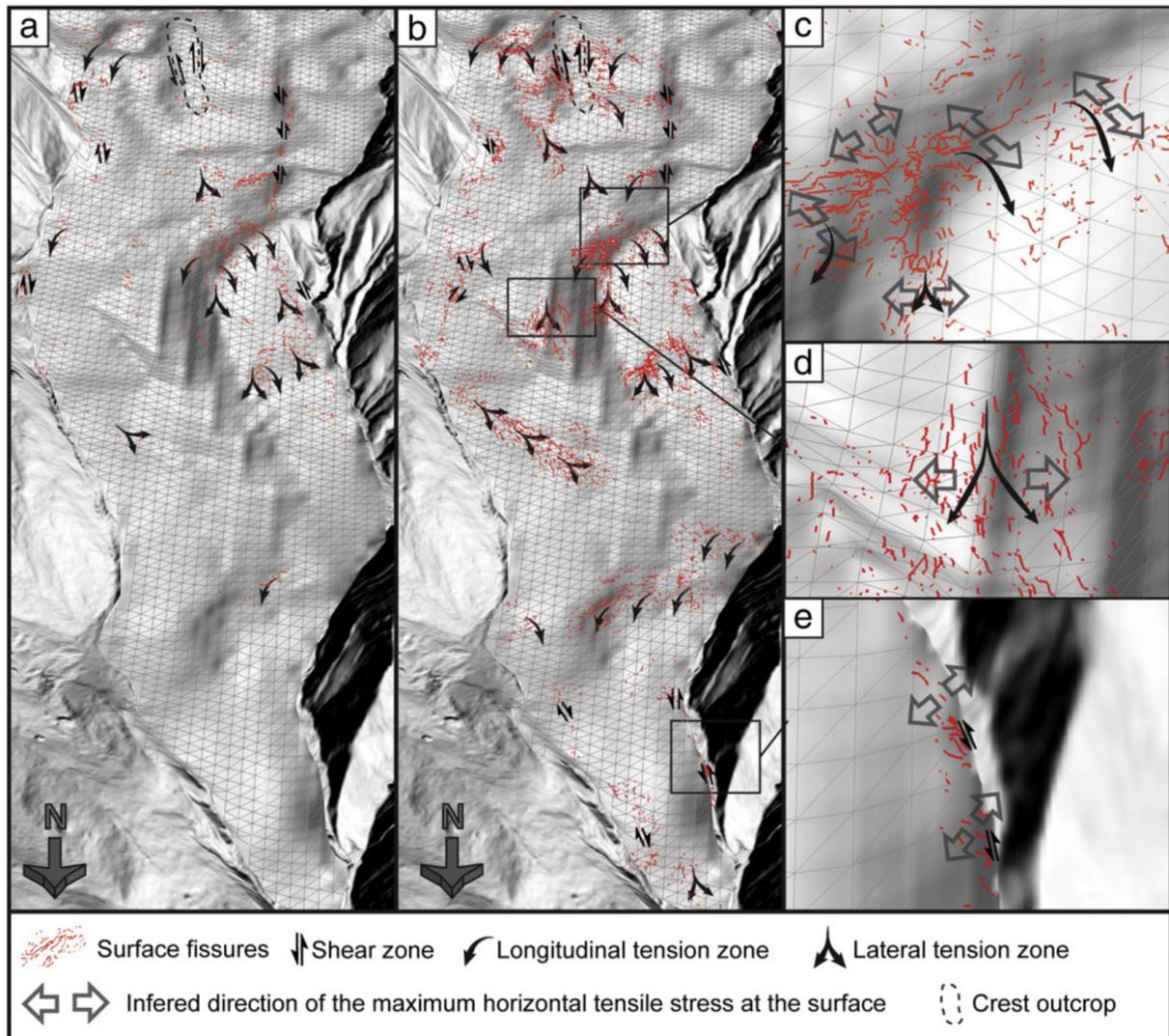


Abbildung 2.11.: Pseudo 3D-Ansicht der Super-Sauze Hangrutschung. Oberflächliche Riss-Formationen, Hangdynamik und Spannungs-Vektoren: (a) Mai 2007, (b) Oktober 2008. (c, d, und e) vergrößerte Ausschnitte Oktober 2008. Diese Ergebnisse wurden mit einem Modell der stabilen Untergrundtopographie aus Travelletti und Malet (2012) überlagert.

2.4.3. Kombinierte Hangrutschungsanalyse

Publikation Walter et al. (2009, Anhang A.1.5) Walter, M., Niethammer, U., Rothmund, S., und Joswig, M. Joint analysis of the Super-Sauze (French Alps) mudslide by nanoseismic monitoring and UAV-based remote sensing. *First Break, EAGE*, 27(8):53–60. European Association of Geoscientist & Engineers (EAGE).

Am Beispiel der Super-Sauze Hangrutschung (Südfrankreich) wird eine kombinierte Hangrutschungsanalyse mittels *Nanoseismic-Monitoring* und hochauflösender UAV-Erfassung vorgestellt. Gemeinsame Beobachtungen von Bruchprozessen im Untergrund und hochauflösenden fernerkundlichen Oberflächeninformationen ermöglichen eine Interpretation der komplexen Hangdynamik.

Während einer zehntägigen Messkampagne im Juli 2008 konnten verschiedene seismische Signale detektiert und lokalisiert werden. Neben sekundären Felssturz- und Stein Schlag Signalen vom Bereich der Abbruchkante und des Entstehungsbereiches der Hangrutschung konnten weitere Ereignisse detektiert werden, die auf ein Materialversagen im instabilen Teil der Hangrutschung zurückzuführen sind. Die räumliche Verteilung der Epizentren dieser Signale zeigt eine gute räumliche Übereinstimmung mit Hangbereichen, welche eine höhere Rutschungsgeschwindigkeit aufweisen (Abbildung 2.12).

Ergänzend zur seismischen Überwachung wurde eine Serie von UAV-gestützten Luftaufnahmen der Super-Sauze Hangrutschung aufgenommen. Die hochauflösenden Luftbilder erlaubten die Erstellung eines Ortho-Mosaiks der gesamten Hangrutschung mit einer resultierende Bodenauflösung im Bereich zwischen 3 - 8 cm. Aus dem erstellten Ortho-Mosaik konnten im direkten Vergleich mit einem Orthofoto einer Befliegung des Vorjahres horizontale Verschiebungen ermittelt werden. Zusätzlich wurden verschiedene Hang-Bereiche mit auffälligen Hangdeformationen und Sedimentierungsfächern identifiziert.

Die Zusammenschau der Ergebnisse aus den seismischen Messungen mit den hochauflösenden fernerkundlichen Beobachtungen der Hangoberfläche ermöglicht eine räumliche Abschätzung von seismischen Quellbereichen und liefert zusätzliche Informationen über mögliche Bruchmechanismen. Eine erste Interpretation legt nahe, dass die lokalisierten Brüche vor allem in den Grenzbereichen zwischen Rutschungsmaterial und bedeckten Festgesteinskämmen im Untergrund generiert werden.

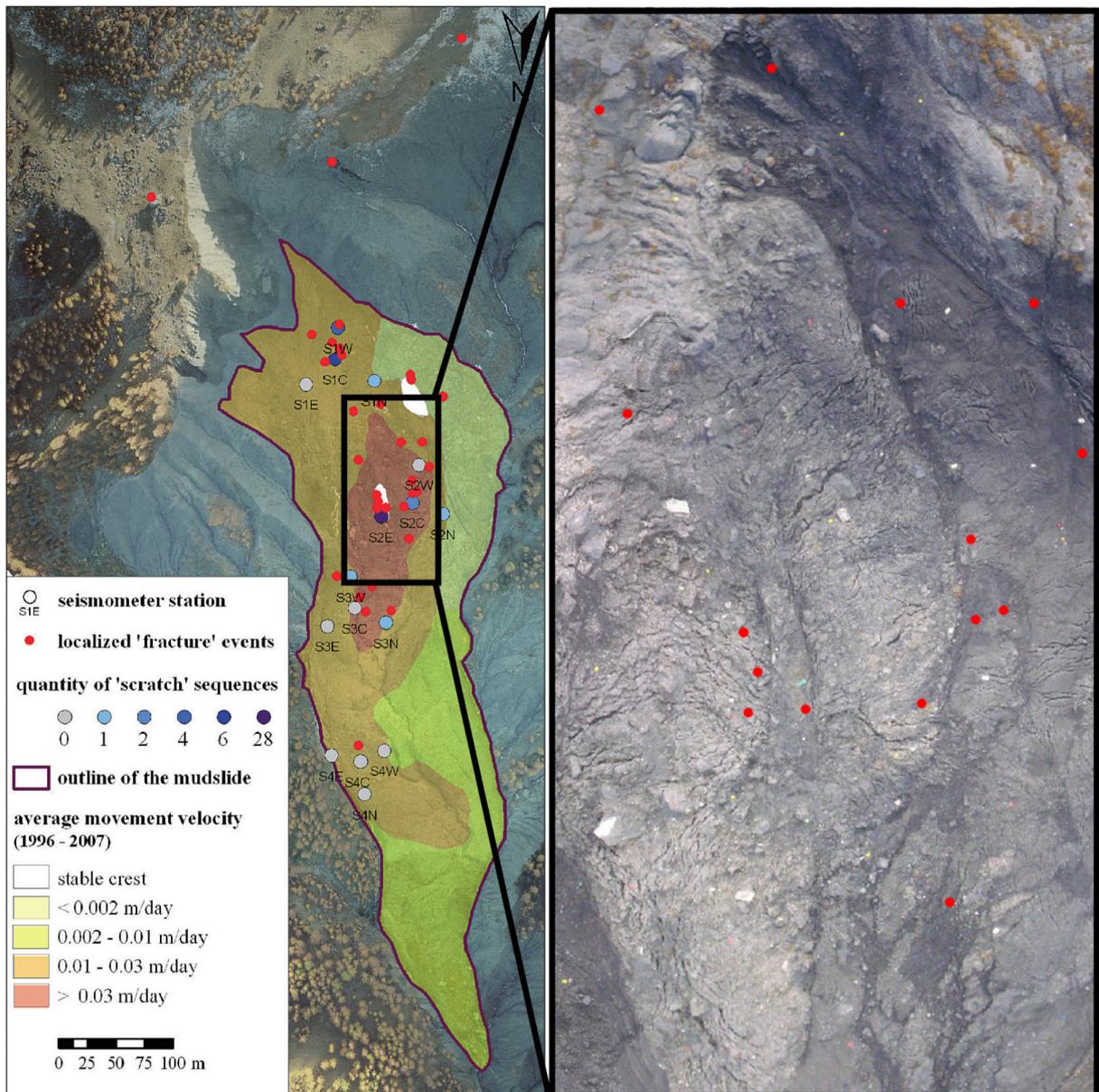


Abbildung 2.12.: Kombinierte Hangrutschungsanalyse, links: durchschnittliche Bewegungsraten zwischen 1996 - 2007 überlagert mit den Positionen der *Seismometer-Arrays*, Epizentren der lokalisierten Brüche und Anzahl der an den Seismometern gemessenen *Scratch-Sequenzen*. Rechts: Ausschnitt aus UAV-basiertem Ortho-Mosaik überlagert mit Epizentren der lokalisierten Bruchereignisse.

3. Diskussion und Ausblick

UAV-Systeme der M-Klasse unter 5 kg Abfluggewicht waren vor dem Jahre 2012 in der Bundesrepublik Deutschland ohne aufwendige Genehmigungsprozedur nach den Richtlinien des Betriebs von Modellflugzeugen einsetzbar. Zukünftige Luftbild-Befliegungen werden nach neuer Gesetzeslage jedoch genehmigungspflichtig, allerdings kann für UAV-Systeme unter 5 kg Abfluggewicht eine allgemeine Erlaubnis erteilt werden. Weiterhin sind autonome UAV-Flüge in vielen Ländern unzulässig und die manuelle UAV-Navigation erfordert einschlägige Flugerfahrung.

Im Bereich der aerogeophysikalischen Fernerkundung werden UAV-Systeme der M-Klasse bisher nur für aeromagnetische Erkundungen genutzt, da die eingeschränkte Nutzlast eine Integration größerer Sensor-Komponenten verhindert. Größere UAV-Systeme eignen sich grundsätzlich als aerogeophysikalische Erkundungsplattform (Hugenholtz et al., 2012). In der Bundesrepublik Deutschland sind Flüge mit UAV-Systemen über 5 kg Abfluggewicht jedoch problematisch, da UAV-Aufstiegs-Genehmigungen notwendig sind. Langwierige Genehmigungs-Prozeduren mit ungewissem Ausgang sind zu erwarten und eine flexible Datenerfassung ist nicht durchführbar. Somit verbleiben nur wenige Vorzüge im Vergleich zur bemannten Fernerkundung. UAV-Einsätze in der Bundesrepublik Deutschland lassen sich aufgrund dieser rechtlichen Hürden unter realistischen Gesichtspunkten nur mittels Systemen der M-Klasse realisieren.

In den kommenden Jahren kann mit einer weiteren technischen Miniaturisierung gerechnet werden. Vor allem im Bereich der UAV-basierten, geodätischen Laser-Fernerkundung zeigen neue Forschungsansätze brauchbare Ergebnisse, und so wird in der nächsten Zeit mit ersten UAV-basierten LiDAR-Erkundungen zu rechnen sein. Hierfür müssen jedoch zuverlässige Methoden der direkten und kontinuierlichen UAV-Georeferenzierung implementiert werden. Aerogravimetrische Untersuchungen werden aufgrund der Größe und der Empfindlichkeit der Messgeräte zukünftig weiter auf den Bereich der bemannten- und satellitengestützten Fernerkundung beschränkt bleiben. Aeroradiometrische Messungen können prinzipiell mit Hilfe von UAV-Systemen realisiert werden, jedoch sind in diesem Forschungsbereich eher großflächige Informationen von Interesse, und können aufgrund von luftrechtlichen Vorgaben in den seltensten Fällen mittels UAV gewonnen werden. Die aktiven geophysikalischen Verfahren der Aeroelektromagnetik und des Aero-Georadars

eignen sich zur Erfassung von oberflächennahen Hangparametern. Jedoch müssen auch hier zuverlässige Methoden der direkten und kontinuierlichen UAV-Georeferenzierung gefunden werden. Zusätzlich weist die Sensorik einen nicht zu vernachlässigenden Energiebedarf auf, und die Sensoren sind aufgrund von Größe und Gewicht bisher nicht in UAV-Systeme der M-Klasse unter 5 kg integrierbar.

Optische Erkundungen im VIS und NIR können mittels M-Klasse UAV-Systemen zuverlässig durchgeführt werden. Jedoch lassen sich in diesen Spektralbereichen nur unzureichende Oberflächenparameter zur multispektralen Hangrutschungsanalyse bestimmen. Whitworth et al. (2000) zeigten, dass spektrale Signaturen an Hangrutschungen vor allem für Wellenlängen oberhalb des nahen Infrarot zu erwarten sind. Obwohl seit einigen Jahren miniaturisierte Thermalsensoren in UAV-Systeme integrierbar sind, können mit diesen Systemen bisher nur niedrig auflösende Aufnahmen gewonnen werden. Eine mit der regulären luftgestützten Fernerkundung vergleichbare Multispektral-Erkundung ist mit UAV-Systemen der M-Klasse bisher nicht durchführbar, und der UAV-Einsatz im Bereich der Hangrutschungs-Forschung bleibt aktuell hauptsächlich auf die optischen Verfahren beschränkt.

Das optische Bildmaterial muss für aussagekräftige Analysen mittels photogrammetrischer Verfahren perspektivisch entzerrt werden. Ebene Entzerrungen sind aufgrund von systembedingten Abweichungen und zeitaufwendiger manueller Arbeit nicht das Mittel der Wahl, allerdings können mit Mosaiken der ebenen Entzerrungen beachtliche Ergebnisse erzielt werden. Anhand differenzieller 3D-Orthoprojektionen lassen sich UAV-basierte Luftbilder in der Regel gut entzerren. Hierfür werden jedoch hochauflösende 3D-Modelle benötigt. Grundsätzlich muss für UAV-basierte Erkundungen eine Balance zwischen unterschiedlichen Parametern gefunden werden: Hochauflösende Bildinformationen erfordern niedrige Flughöhen. Aus niedrigeren Flughöhen müssen deutlich mehr Luftbilder aufgenommen werden ($n \propto h^{-2}$), und große Bilddatensätze sind photogrammetrisch nur schwer prozessierbar. Zusätzlich ist die photogrammetrische Verarbeitung großer Datensätze sehr zeitaufwendig, eine automatische Prozessierung muss angestrebt werden.

Die Ergebnisse der UAV-Pilotstudien zeigen für unbewachsene Hänge unterschiedlichste Analysen-Möglichkeiten auf: Mit Hilfe der hochauflösenden Luftaufnahmen im VIS können Informationen über seismische Quellbereiche und mögliche Bruchmechanismen von Rutschungen gewonnen werden. Jedoch war diese mit seismischen Messungen gekoppelte Analyse an der Hangrutschung des Heumöser Hangs nicht möglich, da die ausgeprägte Vegetation eine Erfassung von Rissen im sichtbaren Spektralbereich verhinderte. Hochauflösende multispektrale Fernerkundungsverfahren lassen sich mit den entwickelten UAV-Systemen der M-Klasse bisher nicht umsetzen.

Weiter können anhand der hochauflösenden Orthofotos semi-automatische Kartierun-

gen von Oberflächenrissen erstellt werden. Großflächige Riss-Karten erlauben vertiefende Analysen über mechanische Prozesse in Größenordnungen der Hang-Skala. Die implementierten semi-automatische Algorithmen zeigen allerdings eine leichte Anfälligkeit gegenüber Beleuchtungs-Variationen in den zugrunde liegenden Luftbildern. Für weitere Analysen sollte die Bildakquise daher während diffuser Beleuchtungsverhältnisse durchgeführt werden, oder effektive Verfahren einer radiometrischen Angleichung des Bildmaterials implementiert werden. So könnten z. B. auch sichtbare Kontraste aus den Luftbildern für großflächige Durchfeuchtungs-Analysen der Hangrutschungs-Oberfläche genutzt werden.

An der Super-Sauze Hangrutschung können automatische Verschiebungsanalysen mit Hilfe von Bildkorrelation oder Merkmals-basierten Methoden nicht zuverlässig durchgeführt werden, da eine starke Sedimentierung sichtbare Merkmale an der Rutschungsoberfläche über längere Zeiträume verändert. Systembedingte Abweichungen der entzerrten Orthofotos erschweren zusätzlich hochauflösende Analysen innerhalb kürzerer Zeitabschnitte, und lange Bearbeitungszeiten verhindern eine kostengünstige Bearbeitung der Daten. Diese Einschränkungen stehen bisher im Widerspruch zu den gewünschten Vorteilen einer kostengünstigen, flexiblen und zeitlich hochauflösenden UAV-basierten Fernerkundung. Optimierungen zur Verbesserung der Genauigkeit und Beschleunigung der Verarbeitungsroutinen sind daher in weiteren Studien erforderlich. Allerdings können mit Hilfe von SfM-MVS Verfahren nun vollautomatische photogrammetrische Prozessierungen vollzogen werden. Abweichungen unter 0.25 m RMS versprechen für kleinere Hangbereiche hochauflösende 3D-Modelle. Hieraus können zur Hangrutschungsanalyse nutzbare Orthofotos erzeugt werden. Analysen großer Hang-Modelle zeigen jedoch, dass die vollautomatische SfM-basierte Bündel-Block-Prozessierung in den resultierenden 3D-Modellen zu signifikanten Abweichungen führen kann. Dies ist nach aktuellen Studien von James und Robson (2012) vor allem auf unzureichende Kamera-Modelle der automatischen Kalibrierungsroutinen zurückzuführen und muss anhand weiterer Studien verbessert werden.

Kombinierte Hangrutschungsanalysen mittels *Nanoseismic-Monitoring* und hochauflösender UAV-Erfassung ermöglichen Beobachtungen von Bruchprozessen im Untergrund, sowie sichtbarer Oberflächendeformationen des Rutschungskörpers. Erste Interpretationen legen nahe, dass die lokalisierten Brüche vor allem in den Grenzbereichen zwischen Rutschungsmaterial und den bedeckten Festgesteinskämmen im Untergrund generiert werden. Eine eindeutige Zuordnung zwischen Bruchereignissen und der sichtbaren Genese von Rissöffnungen ist bisher jedoch noch nicht gelungen. Hierfür wurde eine weitere, kombinierte Feldkampagne in Südfrankreich durchgeführt (Rothmund et al., 2013). Diese Forschungen sollen zukünftig vertiefende Informationen über Zusammenhänge zwischen Hangbewegung, Bruchprozessen, Riss-Entwicklung und des Porenwasserdrucks liefern.

Literaturverzeichnis

- Aber, J. S., Aber, S. W., und Pavri, F. (2002). Unmanned small-format aerial photography from kites for acquiring large scale, high-resolution, multiview-angle imagery. In *The International Archives of the Photogrammetry, Remote Sensing and Spatial Information Sciences, Pecora 15/Land Satellite Information*. IV/ISPRS Commission I/FIEOS, Denver, CO, USA., ISPRS. Zitiert auf Seite 36.
- Albertz, J. (2007). *Einführung in die Fernerkundung - Grundlagen der Interpretation von Luft- und Satellitenbildern*. WBG, Darmstadt, 3 edition. Zitiert auf Seite 19, 21, 22, 25.
- Altan, M. O., Celikoyan, T. M., Kemper, G., und Toz, G. (2004). Balloon photogrammetry for cultural heritage. In *International Archives of the Photogrammetry, Remote Sensing and Spatial Information Sciences, XX ISPRS Congress, Istanbul, Turkey*, volume XXXV-B5, pages 964–968. Zitiert auf Seite 34, 35.
- Arya, S., Mount, D. M., Netanyahu, N. S., Silverman, R., und Wu, A. Y. (1998). An optimal algorithm for approximate nearest neighbor searching fixed dimensions. *Journal of the ACM (JACM)*, 45(6):891–923. Zitiert auf Seite 46.
- van Asch, T. W., van Beek, L. P. H., und Bogaard, T. A. (2007). Problems in predicting the mobility of slow-moving landslides. *Engineering Geology*, 91(1):46–55. Zitiert auf Seite 17.
- Balsley, B. B., Jensen, M. L., und Frehlich, R. G. (1998). The use of state-of-the-art kites for profiling the lower atmosphere. *Boundary-Layer Meteorology*, 87(1):1–25. Zitiert auf Seite 36.
- Baltsavias, E. P. (1996). Digital ortho-images - a powerful tool for the extraction of spatial-and geo-information. *ISPRS Journal of Photogrammetry and Remote sensing*, 51(2):63–77. Zitiert auf Seite 21.
- Baran, I. (2009). Airborne InSAR and LiDAR compared, online e-book.
http://www.aoc.co.za/resources/pdf/publications/technical_papers/AirborneInSARandLiDARCompared_AOC.pdf. Zitiert auf Seite 27.

- de Bary, E. und Bullrich, K. (1962). Über den Anteil der Rayleigh-Streuung und den Einfluß der Aerosol-Größenverteilung auf Extinktion und spektrale Intensität der Streustrahlung eines Luftvolumens. *Theoretical and Applied Climatology*, 12(2):254–277. Zitiert auf Seite 21.
- Bäumker, M. und Przybilla, H.-J. (2011). Investigations on the accuracy of the navigation data of unmanned aerial vehicles using the example of the system mikrokopter. In *International Archives of Photogrammetry, Remote Sensing and Spatial Information Sciences*, volume XXXVIII-1/C22, Zürich, Switzerland. Zitiert auf Seite 40.
- Belardinelli, M. E., Sandri, L., und Baldi, P. (2003). The major event of the 1997 umbriamarche (Italy) sequence: what could we learn from DInSAR and GPS data? *Geophysical Journal International*, 153(1):242–252. Zitiert auf Seite 27.
- Bloomenthal, J. und Rokne, J. (1994). Homogeneous coordinates. *The Visual Computer*, 11(1):15–26. Zitiert auf Seite 154.
- Bouabdallah, S., Noth, A., und Siegwart, R. (2004). PID vs LQ control techniques applied to an indoor micro quadrotor. In *Proceedings of Intelligent Robots and Systems, IEEE/RSJ International Conference*, volume 3, pages 2451–2456. Zitiert auf Seite 32.
- Brenner, A. und Ender, J. (2006). Demonstration of advanced reconnaissance techniques with the airborne SAR/GMTI sensor PAMIR. *Radar, Sonar and Navigation, IEE Proceedings*, 153(2):152–162. Zitiert auf Seite 26.
- Bry, A., Bachrach, A., und Roy, N. (2012). State estimation for aggressive flight in GPS-denied environments using onboard sensing. In *Proc. of IEEE Conference on Robotics and Automation (ICRA 2012)*. Zitiert auf Seite 40.
- BuildMosaic (2013). Official build-mosaic software homepage. <http://build-mosaic.sourceforge.net>. Zitiert auf Seite 49.
- Canas, A. A. D. und Barnett, M. E. (1985). The generation and interpretation of false-colour composite principal component images. *International Journal of Remote Sensing*, 6(6):867–881. Zitiert auf Seite 22.
- Casagli, N., Fanti, R., Nocentini, M., und Righini, G. (2005). Assessing the capabilities of VHR satellite data for debris flow mapping in the Machu Picchu area (c101-1). In Sassa, K., Fukuoka, H., Wang, F., und Wang, G., editors, *Landslides: Risk Analysis and Sustainable Disaster Management*, pages 61–70. Springer. Zitiert auf Seite 23.

- Catani, F., Farina, P., Moretti, S., Nico, G., und Strozzi, T. (2005). On the application of SAR interferometry to geomorphological studies: estimation of landform attributes and mass movements. *Geomorphology*, 66(1-4):119–131. Zitiert auf Seite 26.
- Clark, A. F., Woods, J. C., und O., O. (2010). A low-cost airborne platform for ecological monitoring. *Int. Archives of Photogrammetry, Remote Sensing and Spatial Information Sciences*, XXXVIII(5):167–172. Com. V. Zitiert auf Seite 36, 37.
- Crosilla, F. (1999). Procrustes analysis and geodetic sciences. Technical report, Quo vadis geodesia...? Department of Geodesy and GeoInformatics, University of Stuttgart. Zitiert auf Seite 47.
- Cruden, D. M. und Varnes, D. J. (1996). Landslide types and processes. Technical report. Zitiert auf Seite 15, 16.
- Curran, P. (1980). Multispectral remote sensing of vegetation amount. *Progress in Physical Geography*, 4(3):315. Zitiert auf Seite 22.
- Damm, B. (2000). Hangrutschungen im Mittelgebirgsraum - Verdrängte „Naturgefahr“? *STANDORT*, 24(4):27–34. Zitiert auf Seite 15.
- Darvishzadeh, R. (2008). *Hyperspectral remote sensing of vegetation parameters using statistical and physical models*. PhD thesis, International Institute for Geo-information Science & Earth Observation. Zitiert auf Seite 23, 24.
- Davis, J. L. und Annan, A. P. (1989). Ground-penetrating radar for high-resolution mapping of soil and rock stratigraphy. *Geophysical Prospecting*, 37:531–551. Zitiert auf Seite 25.
- Dubois, P. C., van Zyl, J., und Engman, T. (1995). Measuring soil moisture with imaging radars. *IEEE Transactions on Geoscience and Remote Sensing*, 33(4):915–926. Zitiert auf Seite 26.
- Duranti, S., Conte, G., Lundström, D., Rudol, P., Wzorek, M., und Doherty, P. (2007). LinkMAV, a prototype rotary wing micro aerial vehicle. In *Proc. of the 17th IFAC Symposium on Automatic Control in Aerospace*, page 6. Zitiert auf Seite 32.
- Eeckhaut, M. V., Poesen, J., Verstraeten, G., Vanacker, V., Nyssen, J., Moeyersons, J., Beek, L. P., und Vandekerckhove, L. (2007). Use of LIDAR-derived images for mapping old landslides under forest. *Earth Surface Processes And Landforms*, 32(5):754–769. Zitiert auf Seite 25.

- Eisenbeiss, H. (2009). *UAV photogrammetry*. PhD thesis, Institute of Geodesy and Photogrammetry, ETH Zurich. Mitteilungen Nr. 105. Zitiert auf Seite 29, 30, 31, 38.
- Eisenbeiss, H., Lambers, K., und Sauerbier, M. (2005). Photogrammetric recording of the archaeological site of Pinchango Alto (Palpa, Peru) using a mini helicopter (UAV). In *Proc. of the 33rd CAA Conference*, pages 21–24. Zitiert auf Seite 31.
- Elachi, C. (1987). *Introduction to the physics and techniques of remote sensing*. Wiley. Zitiert auf Seite 20, 34.
- Enblend (2013). Official enblend software homepage. <http://enblend.sourceforge.net>. Zitiert auf Seite 49.
- Fan, Q., Efrat, A., Koltun, V., Krishnan, S., und Venkatasubramanian, S. (2005). Hardware-assisted natural neighbor interpolation. In *Proc. 7th Workshop on Algorithm Engineering and Experiments (ALENEX)*, volume 21. Zitiert auf Seite 47.
- Fischler, M. A. und Bolles, R. C. (1981). Random sample consensus: a paradigm for model fitting with applications to image analysis and automated cartography. *Communications of the ACM*, 24(6):381–395. Zitiert auf Seite 46.
- Fotinopoulos, V. (2004). Balloon photogrammetry for archaeological surveys. *International Archives of the Photogrammetry, Remote Sensing and Spatial Information Sciences, XXXV-B5 ISPRS Congress, Istanbul, Turkey*, pages 504–507. Zitiert auf Seite 34.
- Frulla, L. A., Milovich, J. A., Karszenbaum, H., und Gagliardini, D. A. (1998). Radiometric corrections and calibration of SAR images. In *Geoscience and Remote Sensing Symposium Proceedings, 1998. IGARSS'98. 1998 IEEE International*, pages 1147–1149. Zitiert auf Seite 25.
- Furukawa, Y. und Ponce, J. (2007). Accurate, dense, and robust multi-view stereopsis. In *Computer Vision and Pattern Recognition, CVPR'07 IEEE Conference*. Zitiert auf Seite 46.
- Furukawa, Y. und Ponce, J. (2013). Official PMVS2 open source homepage. <http://www.di.ens.fr/pmvs/>. Zitiert auf Seite 47.
- Goepfert, W. (1984). Methods, accuracy requirements and applications of digital image rectifications. In *Proc. of 39th Photogrammetric Week, Institute of Photogrammetry, Univ. of Stuttgart*, pages 179–185. Zitiert auf Seite 22.

- Golub, G. und Kahan, W. (1965). Calculating the singular values and pseudo-inverse of a matrix. *Journal of the Society for Industrial and Applied Mathematics*, 2(2):205–224. Zitiert auf Seite 153.
- Gomez-Lahoz, J. und Gonzalez-Aguilera, D. (2009). Recovering traditions in the digital era: the use of blimps for modelling the archaeological cultural heritage. *Journal of Archaeological Science*, 36(1):100–109. Zitiert auf Seite 36.
- Görner, K. und Hübner, K. (2001). *Abfallwirtschaft und Bodenschutz*. Springer-Verlag. Zitiert auf Seite 28, 29.
- Graham, L. C. (1974). Synthetic interferometer radar for topographic mapping. *Proceedings of IEEE*, 62:763–768. Zitiert auf Seite 26.
- Grosser, J. (2009). *Räumlich hochauflösende Aeromagnetik-Messungen unter Verwendung eines ferngelenkten Luftschiffes*. Dissertation, Institut für Geophysik und extraterrestrische Physik, Technische Universität Braunschweig, Braunschweig, Germany. Zitiert auf Seite 36.
- Gruen, A. (2012). Development and status of image matching in photogrammetry. *The Photogrammetric Record*, 27(137):36–57. Zitiert auf Seite 21.
- Gülch, E. (2012). Photogrammetric measurements in fixed wing uav imagery. *International Archives of Photogrammetry, Remote Sensing and Spatial Information Sciences*, XXXIX-B1:381–386. Zitiert auf Seite 33, 34.
- Gundelach, V., Blindow, N., Buschmann, U., Salat, C., und Krellmann, Y. (2010). Exploration of geological structures with GPR from helicopter and on the ground in the letzlinger heide (germany). In *Ground Penetrating Radar (GPR), 2010 13th International Conference on*, pages 1–6. IEEE. Zitiert auf Seite 28.
- Haala, N., Cramer, M., Weimer, F., und Trittler, M. (2011). Performance test on uav-based photogrammetric data collection. *Int. Arch. Photogram. Remote Sensing Spatial Info. Sci.*, 38:1–6. Zitiert auf Seite 33, 34.
- Hauck, G. (1883). Neue Konstruktionen der Perspektive und Photogrammetrie. (Theorie der trilinearen Verwandtschaft ebener Systeme, I. Artikel). *Journal für die reine und angewandte Mathematik*, 95:1–35. Zitiert auf Seite 21.
- Hecht, J. (1992). *The Laser Guidebook*. McGraw-Hill, 2 edition. Zitiert auf Seite 24.

- Hugenholtz, C. H., Moorman, B. J., Riddell, K., und Whitehead, K. (2012). Small unmanned aircraft systems for remote sensing and earth science research. *Eos, Transactions American Geophysical Union*, 93(25):236–236. Zitiert auf Seite 57.
- Jaeger, T. und Metzger, A. (2011). *Open Source Software*. Beck, 3 edition. Zitiert auf Seite 49.
- James, M. R. und Robson, S. (2012). Straightforward reconstruction of 3d surfaces and topography with a camera: Accuracy and geoscience application. *Journal of Geophysical Research*, 117(F03017):1–17. Zitiert auf Seite 59.
- Jolliffe, I. T. (1986). Principal component analysis. *Springer Series in Statistics*, Berlin. Zitiert auf Seite 22.
- Jordan, H. und Siemon, B. (2002). Die Tektonik des nordwestlichen Harzrandes - Ergebnisse der Hubschrauber-Elektromagnetik. *Zeitschrift der Deutschen Geologischen Gesellschaft*, 153(1):31–50. Zitiert auf Seite 29.
- Joswig, M. (2008). Nanoseismic monitoring fills the gap between microseismic networks and passive seismic. *First Break*, 26:121–128. Zitiert auf Seite 5, 7.
- Jütte, K. (2008). Vergleich verschiedener low-cost Luftbildaufnahmesysteme sowie Einsatz von Drohnen: Grenzen und Möglichkeiten. In *Der gepixelte Wald - Fachtagung zur Forstlichen Fernerkundung, Bayerische Landesanstalt für Wald und Forstwirtschaft*. Zitiert auf Seite 36.
- Kawano, H. (2011). Study of path planning method for under-actuated blimp-type uav in stochastic wind disturbance via augmented-mdp. In *Proc. of Advanced Intelligent Mechatronics (AIM), IEEE/ASME International Conference*, pages 180–185. Zitiert auf Seite 36.
- Kernighan, B. W. und Ritchie, D. M. (1990). *Programmieren in C*. Hanser Verlag. Zitiert auf Seite 43.
- Killinger, D. K. und Menyuk, N. (1987). Laser remote sensing of the atmosphere. *Science*, 235:37–45. Zitiert auf Seite 25.
- Kraus, K. (1997). *Photogrammetry, Volume 2*. Ferd. Dümmlers Verlag, Bonn, 4 edition. contributions by J. Jansa and H. Kager. Zitiert auf Seite 21.
- Kraus, K. und Schneider, W. (1988). *Fernerkundung. Band 1: Physikalische Grundlagen und Aufnahmetechniken*. Ferd. Dümmlers Verlag. Zitiert auf Seite 26.

- Krieger, G., Moreira, A., Fiedler, H., Hajnsek, I., Younis, M., Werner, M., und Zink, M. (2007). The TanDEM-X mission: A satellite formation for high resolution SAR interferometry. *IEEE Trans. Geosci. Remote Sens.*, 45(11):3317–3341. Zitiert auf Seite 27.
- Lanier, D. (2011). *Development of an Autonomous Blimp*. PhD thesis, Worcester Polytechnic Institute. Zitiert auf Seite 35.
- Lefsky, M. A., Cohen, W. B., Parker, G. G., und Harding, D. J. (2002). LIDAR remote sensing for ecosystem studies. *BioScience*, pages 19–30. Zitiert auf Seite 24.
- Lillesand, T. und Kiefer, R. (1987). *Remote Sensing and Image Interpretation*. John Wiley and Sons, 2 edition. Zitiert auf Seite 19.
- Lin, Y., Hyypä, J., und Jaakkola, A. (2011). Mini-UAV-borne LIDAR for fine-scale mapping. *IEEE Geoscience and remote sensing letters*, 8(3):426–430. Zitiert auf Seite 38.
- Lindenmaier, F. (2010). *Hydrology of a large unstable hillslope at Ebnet, Vorarlberg: Identifying dominating processes and structures*. PhD thesis, Institut für Geoökologie, Universität Potsdam. Zitiert auf Seite 15.
- Löffler-Mang, M. (2011). *Optische Sensorik: Lasertechnik, Experimente, Light Barriers*. Vieweg + Teubner Verlag. Zitiert auf Seite 20.
- Lowe, D. G. (2004). Distinctive image features from scale-invariant keypoints. *International journal of computer vision*, 60(2):91–110. Zitiert auf Seite 46.
- Luhman, T. (2010). *Erweiterte Verfahren zur geometrischen Kamerakalibrierung in der Nahbereichsphotogrammetrie*. Habilitationsschrift, Deutsche Geodätische Kommission. Zitiert auf Seite 21, 149.
- Luhmann, T. (2002). *Nahbereichsphotogrammetrie: Grundlagen, Methoden und Anwendungen*. Herbert Wichmann Verlag, 2 edition. Zitiert auf Seite 48.
- Malet, J.-P., van Asch, T., van Beek, R., und Maquaire, O. (2005). Forecasting the behaviour of complex landslides with a spatially distributed hydrological model. *Nat. Hazards Earth Syst. Sci.*, 5(1):71–85. Zitiert auf Seite 17.
- Marchand, W. D., Killingtveit, A., Wilén, P., und Wikström, P. (2003). Comparison of ground-based and airborne snow depth measurements with georadar systems, case study. *Nordic hydrology*, 34(5):427–448. Zitiert auf Seite 28.
- Massonet, D. und Feigl, K. L. (1998). Radar interferometry and its application to changes in the earth’s surface. *Reviews of Geophysics*, 36(4):441–500. Zitiert auf Seite 27.

- Massonnet, D., Rossi, M., Carmona, C., Adragna, F., Peltzer, G., Feigl, K., und T., R. (1993). The displacement field of the landers earthquake mapped by radar interferometry. *Nature*, 364(6433):138–142. Zitiert auf Seite 26.
- McCardle, A., Rabus, B., Ghuman, P., Rabaco, L. M. L., Amaral, C. S., und Rocha, R. S. (2007). Using artificial point targets for monitoring landslides with interferometric processing. In *Proc. of Anais XIII Simposio Brasileiro de Sensoriamento Remoto*, pages 21–26. Zitiert auf Seite 27.
- Metternicht, G., Hurni, L., und Gogu, R. (2005). Remote sensing of landslides: An analysis of the potential contribution to geo-spatial systems for hazard assessment in mountainous environments. *Remote sensing of Environment*, 98(2):284–303. Zitiert auf Seite 29.
- Mikrokooper-Developer (2013). Official mikrokooper open source quadrotor homepage. <http://www.mikrokooper.com>. Zitiert auf Seite 38.
- Militzer, H. und Weber, F. (1985). *Angewandte Geophysik Band 2: Geoelektrik - Geothermik- Radiometrie - Aerogeophysik*. Springer. Zitiert auf Seite 19, 28.
- Mumby, P. J., Green, E. P., Clark, C. D., und Edwards, A. J. (1998). Digital analysis of multispectral airborne imagery of coral reefs. *Coral Reefs*, 17:59–69. Zitiert auf Seite 23.
- Niethammer, U., James, M., Rothmund, S., Travelletti, J., und Joswig, M. (2012). UAV-based remote sensing of the Super-Sauze landslide: Evaluation and results. *Engineering Geology*, 128:2–11. Zitiert auf Seite 42, 52, 73.
- Niethammer, U., Rothmund, S., und Joswig, M. (2009). UAV-based remote sensing of the slow moving landslide Super-Sauze. In Malet, J.-P., Remaître, A., und Bogaard, T., editors, *Landslide Processes: Landslide mapping and geomorphologic characterization*, CERG Editions, pages 69–74, 352, Strasbourg, France. CERG. Proceedings of a conference held in Strasbourg, France, 6.-7. Feb. 2009. Zitiert auf Seite 38.
- Niethammer, U., Rothmund, S., Joswig, M., James, M., und Travelletti, J. (2010). UAV-based remote sensing of landslides. *Int. Arch. Photogramm. Remote Sens. Spatial Inf. Sci.*, XXXVIII Part 5:496–501. Zitiert auf Seite 41, 44, 73.
- Niethammer, U., Rothmund, S., Schwaderer, U., Zeman, J., und Joswig, M. (2011). Open source image-processing tools for low-cost UAV-based landslide investigations. *Int. Arch. Photogramm. Remote Sens. Spatial Inf. Sci.*, XXXVIII-1 C22:161–166. Zitiert auf Seite 41, 43, 73.

- nnc (2013). Official nn-c software homepage. <http://nn-c.googlecode.com/svn/nn/>. Zitiert auf Seite 47.
- von Norbert, H. B. (1991). Eine erste gesamte aeromagnetische Karte von Österreich und ihre Transformationen. *Mitteilungen der Österreichischen Geologischen Gesellschaft*, 84:185. Zitiert auf Seite 27.
- Okada, Y., Hirao, C., Horiuchi, T., Hara, Y., Yedidia, J. S., Azarbayejani, A., Oishi, N., Furuhashi, M., Kumagai, N., Morioka, S., und Kato, Y. (2007). Highly accurate DSM reconstruction using ku-band airborne InSAR. In *Proc. of IEEE International Geoscience and Remote Sensing Symposium (IGARSS 2007)*. Zitiert auf Seite 27.
- d'Oleire Oltmanns, S., Marzloff, I., Peter, K. D., und Ries, J. B. (2012). Unmanned aerial vehicle (UAV) for monitoring soil erosion in Morocco. *Remote Sensing*, 4(11):3390–3416. Zitiert auf Seite 34.
- Onuma, T. und Ohkawa, S. (2009). Detection of surface deformation related with CO₂ injection by DInSAR at In Salah, Algeria. *Energy Procedia*, 11(1):2177–2184. Zitiert auf Seite 27.
- Pepe, A., Sansosti, E., Berardino, P., und Lanari, R. (2005). On the generation of ERS/ENVISAT DInSAR time-series via the SBAS technique. *IEEE Geosci. Remote Sens. Lett.*, 2:265–269. Zitiert auf Seite 26.
- Przybilla, H.-J. und Wester-Ebbinghaus, W. (1979). Bildflug mit ferngelenktem Kleinflugzeug. *Bildmessung und Luftbildwesen, Zeitschrift fuer Photogrammetrie und Fernerkundung*, 47(5):137–142. Zitiert auf Seite 30, 34.
- Refice, A., Bovenga, F., Guerriero, L., und Wasowski, J. (2001). DInSAR applications to landslide studies. In *Proc. of the Geoscience and Remote Sensing Symposium, IGARSS '01*, volume 1, pages 144–146. IEEE. Zitiert auf Seite 27.
- Reiche, M., Roger Funk, Z., Hoffmann, C., Li, Y., und Sommer, M. (2012). Using a parafoil kite for measurement of variations in particulate matter-A kite-based dust profiling approach. *Atmospheric and Climate Sciences*, 2(1):41–51. Zitiert auf Seite 37.
- Remy, M. A., de Macedo, K. A., und Moreira, J. R. (2012). The first UAV-based P- and X-band interferometric SAR system. In *Proc. of Geoscience and Remote Sensing Symposium (IGARSS)*, pages 5041–5044. IEEE. Zitiert auf Seite 38.
- Ries, J. B. und Marzloff, I. (2003). Monitoring of gully erosion in the Central Ebro Basin by large-scale aerial photography taken from a remotely controlled blimp. *CATENA*, 50(2):309–328. Zitiert auf Seite 36.

- Roelofs, G. und Koman, R. (1999). *PNG: The Definitive Guide*. O'Reilly & Associates, Inc. Zitiert auf Seite 49.
- Rothmund, S. (2009). Photogrammetrische Auswertung zur morphometrischen Analyse der Super-Sauze-Hangrutschung (Französische Alpen). Diplomarbeit, Institut für Geophysik, Universität Stuttgart. Zitiert auf Seite 51.
- Rothmund, S., Niethammer, U., Malet, J.-P., und Joswig, M. (2013). Landslide surface monitoring based on UAV-and ground-based images and terrestrial laser scanning: accuracy analysis and morphological interpretation. *First Break*, 31(8). Zitiert auf Seite 59.
- Sabins, F. F. (1996). *Remote Sensing: Principles and Interpretation*. W. H. Freeman, New York, 3 edition. Zitiert auf Seite 24.
- Scheritz, M., Dietrich, R., Scheller, S., Schneider, W., und Boike, J. (2008). High resolution digital elevation model of polygonal patterned ground on Samoylov Island, Siberia, using small-format photography. In *Proc. of the 9th International Conference on Permafrost, University of Alaska*, pages 1589–1594. Zitiert auf Seite 34.
- Schowengerdt, R. A. (2007). *Remote sensing: Models and methods for image processing*. Academic Press, San Diego and Chestnut Hill, 3 edition. Zitiert auf Seite 20.
- Schwaderer, U. (2010). Luftbildgestützte Kartierung von Bodenfeuchte und Bruchdynamik am Heumöser Hang. Diplomarbeit, Institut für Geophysik, Universität Stuttgart. Zitiert auf Seite 51.
- Sherwin, C. W., Ruina, P., und Rawcliffe, R. D. (1962). Some early developments in synthetic aperture radar systems. *IRE Trans.*, MIL-6:111–115. Zitiert auf Seite 25.
- Sibson, R. (1981). *A brief description of natural neighbour interpolation*, pages 21–36. John Wiley & Sons. Zitiert auf Seite 47.
- Siemon, B. (2005). Ergebnisse der Aeroelektromagnetik zur Grundwasser-Erkundung im Raum Cuxhaven-Bremerhaven. *Angew Geol.*, 1:7–13. Zitiert auf Seite 29.
- Singh, V. und Ray, P. (2009). Interferometry SAR for landslide hazard assessment in Garhwal Himalaya, India. *International Journal of Earth Sciences and Engineering*, 2(5):389–395. Zitiert auf Seite 27.
- Snaveley (2013). Official Bundler open source homepage. <http://www.cs.cornell.edu/~snaveley/bundler/>. Zitiert auf Seite 46.

- Snavely, N., Seitz, S. M., und Szeliski, R. (2008). Modeling the world from internet photo collections. *International Journal of Computer Vision*, 80(2):189–210. Zitiert auf Seite 21, 46, 49.
- Sörgel, U., Jacobsen, K., Lohmann, P., und Schmidt, A. (2011). Nutzung der Satellitenfernerkundung für synoptische Vermessungen der Küstengewässer der Nordsee. Technical report, BfG. Zitiert auf Seite 21, 22, 24.
- Studinger, M., Bell, R., und Tikku, A. (2004). Estimating the depth and shape of subglacial Lake Vostok’s water cavity from aerogravity data. *Geophysical Research Letters*, 31(12):L12401. Zitiert auf Seite 28.
- Stumpf, A., Malet, J.-P., Kerle, N., Niethammer, U., und Rothmund, S. (2013). Image-based mapping of surface fissures for the investigation of landslide dynamics. *Geomorphology*, 186:12–27. Zitiert auf Seite 42, 53, 73.
- Swift, C. (1967). *A magnetotelluric investigation of an electrical conductivity anomaly in the southwestern United States*. PhD thesis, Princeton University, Department of Geology and Geophysics. Zitiert auf Seite 28.
- Thamm, H. und Judex, M. (2006). The „low cost drone“ - an interesting tool for process monitoring in a high spatial and temporal resolution. *International Archives of Photogrammetry, Remote Sensing and Spatial Information Sciences, Enschede, The Netherlands*, XXXVI(part 7):8–11. Zitiert auf Seite 36.
- Travelletti, J. und Malet, J.-P. (2012). Characterization of the 3D geometry of flow-like landslides: a methodology based on the integration of heterogeneous multi-source data. *Engineering Geology*, 128:30–48. Zitiert auf Seite 54.
- Ulaby, F. T., Moore, R., und Funs, A. (1982). Radar remote sensing and surface scattering and emission theory. *Microwave Remote Sensing: Active and Passive*, 2:609. Zitiert auf Seite 25.
- Walter, M., Arnhardt, C., und Joswig, M. (2012). Seismic monitoring of rockfalls, subsurface fracture processes, and superficial fissure development at the super-sauze, french alps, mudslide. *Engineering Geology*, 128:12–22. Zitiert auf Seite 5, 7.
- Walter, M., Niethammer, U., Rothmund, S., und Joswig, M. (2009). Joint analysis of the Super-Sauze (French Alps) mudslide by nanoseismic monitoring and UAV-based remote sensing. *First Break, EAGE*, 27(8):53–60. European Association of Geoscientist & Engineers (EAGE). Zitiert auf Seite 42, 55, 73.

- Watson, G. (2006). Computing helmert transformations. *Journal of Computational and Applied Mathematics*, 197(2):387–394. Zitiert auf Seite 47.
- Wehr, A. und Lohr, U. (1999). Airborne laser scanning - an introduction and overview. *ISPRS J. Photogr. Rem. Sensing*, 54(2/3):68–82. Zitiert auf Seite 24, 25.
- Wester-Ebbinghaus, W. (1980). Aerial photography by radio controlled model helicopter. *The Photogrammetric Record*, 10(55):85–92. Zitiert auf Seite 31.
- Whitworth, M., Giles, D., Murphy, W., und Petley, D. (2000). Spectral properties of active, suspended and relict landslides derived from airborne thematic mapper imagery. In *Landslides in Research, Theory and Practice. Proceedings of VIII International Symposium on Landslides June*, pages 1569–1674. Citeseer. Zitiert auf Seite 58.
- Wiesel, J. (1985). Digital image processing for orthophoto generation. *Photogrammetria*, 40(2):69–76. Zitiert auf Seite 22.
- Yu, C. C., Fan, Z. G., Wang, N. D., Xiong, S. Q., Wan, J. H., und Zhang, H. R. (2007). High-resolution aeromagnetic exploration methods and their application in Daye iron mines. *Progress in Geophysics*, 3:47. Zitiert auf Seite 27.
- Zhu, X. und Bamler, R. (2010). Very high resolution spaceborne SAR tomography in urban environment. *IEEE Trans. Geosci. Remote Sens.*, 48(12):4296–4308. Zitiert auf Seite 26.
- Zillmann, E. und Schnug, E. (2005). Untersuchung zum Informationspotenzial multispektraler Satellitendaten zur Aktualisierung großmaßstäbiger Bodenkarten. *Landbauforschung Völkenrode*, 286:121–128. Zitiert auf Seite 22.
- Zimble, D. A., Evans, D. L., Carlson, G. C., Parker, R. C., Grado, S. C., und Gerard, P. D. (2003). Characterizing vertical forest structure using small-footprint airborne lidar. *Remote Sensing of Environment*, 87(2):171–182. Zitiert auf Seite 25.
- Zoughi, R., Wu, L. K., und Moore, R. K. (1985). SOURCECAT - a very fine resolution radar scatterometer. *Microwave Journal*, 28:183–186. Zitiert auf Seite 25.

A. Anhang

A.1. Publikationen Niethammer

Die vorliegende Dissertation wurde als kumulative Arbeit eingereicht. Grundlage dieser Arbeit sind die folgenden fünf ausgewählten Publikationen. Eine Übersicht aller Publikationen befindet sich in Anhang A.4, Seite 160

Niethammer et al. (2011) in Anhang A.1.1 ab Seite 74

Niethammer et al. (2010) in Anhang A.1.2 ab Seite 80

Niethammer et al. (2012) in Anhang A.1.3 ab Seite 86

Stumpf et al. (2013) in Anhang A.1.4 ab Seite 104

Walter et al. (2009) in Anhang A.1.5 ab Seite 132

OPEN SOURCE IMAGE-PROCESSING TOOLS FOR LOW-COST UAV-BASED LANDSLIDE INVESTIGATIONS

U. Niethammer^{a,*}, S. Rothmund^a, U. Schwaderer^a, J. Zeman^a, M. Joswig^a

^a Institute for Geophysics, University of Stuttgart – uwe.niethammer@geophys.uni-stuttgart.de

Commission I, WG I/V

KEY WORDS: UAVs, quad-rotor, landslide, photogrammetry

ABSTRACT:

In recent years, the application of unmanned aerial vehicles (UAVs) has become more common and the availability of lightweight digital cameras has enabled UAV-systems to represent affordable and practical remote sensing platforms, allowing flexible and high-resolution remote sensing investigations. In the course of numerous UAV-based remote sensing campaigns significant numbers of airborne photographs of two different landslides have been acquired. These images were used for ortho-mosaic and digital terrain model (DTM) generation, thus allowing for high-resolution landslide monitoring. Several new open source image- and DTM-processing tools are now providing a complete remote sensing working cycle with the use of no commercial hard- or software.

1. INTRODUCTION

Remote sensing has been an integral method of landslide investigations for many decades, with several different techniques being used (Mantovani et al., 1995). Traditional airborne- and satellite-based remote sensing techniques are suitable for landslide detection over areas of multiple square kilometres (Henry et al., 2002). However, data acquired with these methods is of neither sufficient resolution nor repeat rate to resolve the evolution of small landslide features, such as fissure structures or small displacements, which can provide significant information on landslide dynamics. Scientists are now beginning to turn to unpiloted aerial vehicles (UAVs) as a low-cost alternative for high-resolution data acquisition. In recent studies it has been shown that such low-cost approaches can be sufficient for reliable landslide analysis (Niethammer et al., 2011). Here, we investigate a low-cost UAV-system and an image processing chain based on open source tools for generating ortho-mosaics and digital terrain models (DTMs).

1.1 Studied landslides

Two landslides have been focused on for UAV-based landslide investigations. The Super-Sauze landslide (figure 1) is located on the north-facing slope of the Barcelonnette Basin (Southern French Alps). It extends over a horizontal distance of 850 m and occurs between an elevation of 2105 m at the crown and 1740 m at the toe with an average slope of 25°. Its total volume is estimated to be 750,000 m³. Sliding velocities range up to 0.4 m per day (Malet and Maquaire, 2003). The Heumoes landslide (figure 1) is located in the eastern Vorarlberg Alps, Austria, 10 km south-east of Dornbirn. It is approximately 2000 m in west to east direction and about 500 m at its widest extent in north to south direction. It occurs between an elevation of 940 m in the east and 1360 m in the west, slope angles of more than 60 % can be observed as well as almost flat areas. Its total volume is estimated to be 9,400,000 m³ and average velocities amount to some cm per year (Lindenmaier et al., 2005).



Figure 1. Top: view onto the Super-Sauze landslide, bottom: view onto the Heumoes landslide

* Corresponding author

2. IMAGE ACQUISITION

2.1 Quad-rotor UAV

An open source quad-rotor UAV-system (Niethammer et al., 2009) was used for image acquisition (figure 2). The UAV was primarily controlled manually, since the use of autonomously controlled UAVs is tightly regulated by civil aviation and security authorities. However, manual flights require a good level of pilot skill and range restrictions are limiting the operational area to a few hundred meters.

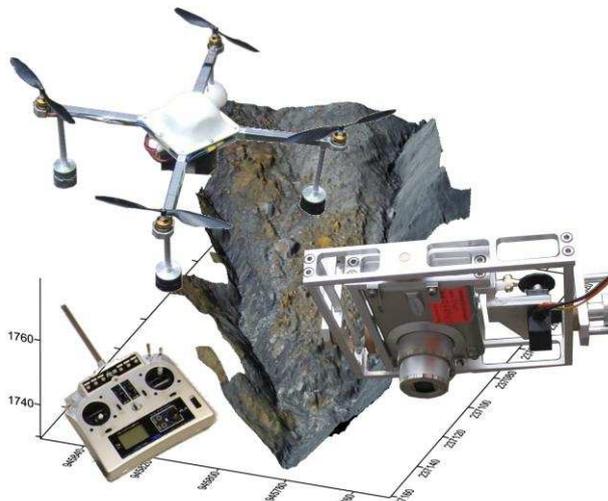


Figure 2. UAV-system for landslide investigations

2.2 Flight planning

Flight planning was carried out on site, where the area to be imaged was observed and suitable locations for take-off and landing could be identified. After launch, the quad-rotor was guided to the desired imaging flight altitude ~200 m to provide a ground resolution of approximately 0.06 m per pixel. However, manual control of the UAV often leads to deviations in flight altitude and deviation of the image resolution has to be accepted. At the imaging altitude the UAV was hovered for about 30 s before vertical landing is initiated. After each flight, the area covered by the acquired photographs was verified on the camera directly.

3. IMAGE PROCESSING

UAV-based images often have to be rectified and merged to an ortho-mosaic for further analysis. In general, best results can be achieved by photogrammetric processing. In a first step a digital terrain model (DTM) is generated and images can then be projected onto the surface of the DTM. In a final step orthographic re-projection of the texture can then be applied (Wiesel, 1985). However, if no regular image-block alignment for photogrammetric computation can be managed (e.g. when using manual controlled UAVs), single image processing can be a promising approach to handle such kind of data.

3.1 Single image rectification

In a first step, optical distortion has to be corrected, for example by applying a third degree polynomial approach (Niethammer et al., 2009). An open source correction tool 'fulla' can also be found in the public domain (<http://hugin.sf.net>). In a second step each image is rectified using a non-parametric rectification

approach (e.g. projective transformation, piecewise affine transformation, or polynomial transformation). Each rectification approach has to be selected in order to achieve the best result, which is dependent on the relief variation and the number of observed ground control targets (Niethammer et al., 2009). Nevertheless, in many cases the projective approach suggests to be an effective rectification method. Software tools for projective image rectification and geocoding are now available in the public domain (<http://rectif.sf.net>).

3.2 Mosaic processing

Rectified images can simply be merged to a large mosaic, but in most cases image borders remain visible (figure 3).

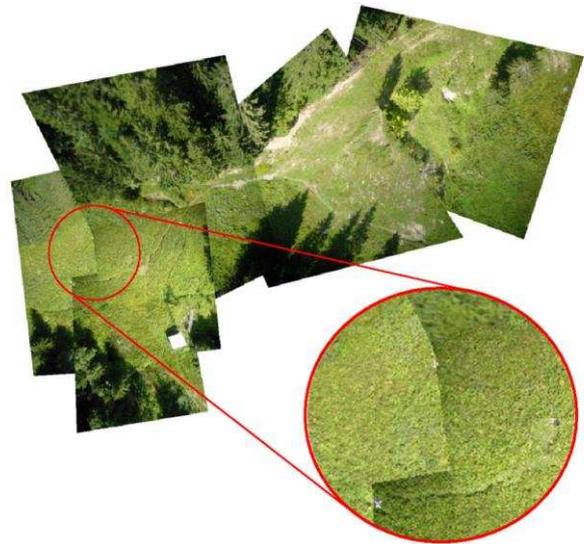


Figure 3. Mosaic of the Heumoes landslide with clearly visible image borders

However, this is not satisfying for further image analysis. Image blending can be a very effective method producing high quality mosaics, since radiometric variations of overlapping views often occur in UAV-acquired images.



Figure 4. Seamless mosaic of the Heumoes landslide

In recent studies novel approaches can be found for combining sets of registered images into a composite mosaic (Zomet et al., 2006; Pérez et al., 2003). Each image region keeps its own colour, brightness, and contrast and overlapping regions are blended with no seams (figure 4). An effective processing pipeline for geocoded ortho-mosaic blending is available in the public domain (<http://build-mosaic.sf.net>). This Linux bash-script is based on 'enblend', an open source tool available at <http://enblend.sf.net>.

3.3 Photogrammetric processing

Single image processing requires a significant amount of time and precision is limited when using plane rectified images for landslide analysis. Especially in irregular terrain approximate image transformation will not fully account for the effects of relief, and residual misalignments within the rectified image have to be accepted (Niethammer et al., 2011). However, misalignments can be avoided when using photogrammetry. Integrating DTM processing into the ortho-mosaic pipeline will significantly reduce errors in the final ortho-mosaic and additional three dimensional measurements can be made in a DTM. Currently, many commercial photogrammetry software packages are available, but most of them are expensive, yet not suitable for processing UAV-acquired photographs. In previous studies (Niethammer et al., 2011) photogrammetric processing of UAV-based images was made possible by using close-range VMS photogrammetry software (<http://www.geomsoft.com>) and 'GOTCHA' image matching from the University College London (Otto and Chau, 1989). Moreover, progress is also being made to streamline 3D-model processing (Niethammer et al., 2010) by using automated targetless structure-from-motion and multiview-stereo approaches to derive 3D models of the landslides topography (figure 5).

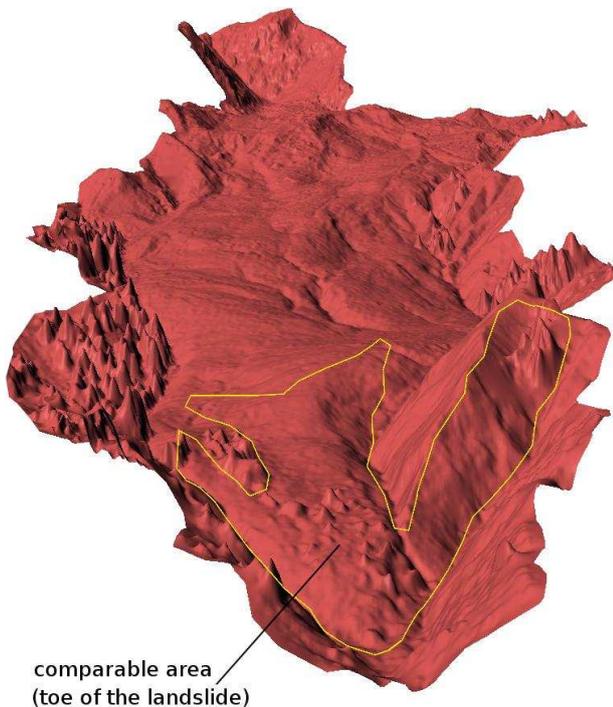


Figure 5. DTM of the entire Super-Sauze landslide (0.3 m grid)

These algorithms are also available in the public domain (Furukawa and Ponce, 2010; Snavely et al., 2008), providing an affordable basis for effective DTM processing, even if hundreds of images have to be processed. However, structure-from-

motion approaches do not consider ground control point information and the coordinate system of the final 3D point cloud remains indeterminate. The point cloud's alignment can be adjusted by applying a spatial similarity transformation to all points of the indeterminate 3D model (Niethammer et al., 2010). Seven parameters are required for transformation, which can be calculated from a set of corresponding 3D point locations between the generated point cloud and measured ground control points. Currently, best alignment precisions are achieved by computing preliminary rectified orthophotos for point digitising in the indeterminate point cloud. Precisions of the digitized points are then supported by the texture information within the 3D model. In a final processing step the whole point cloud is then transformed into the destination coordinate system. Different approaches for transformation parameter computation are possible (Watson, 2006; Crosilla, 1999). A software tool based on the Procrustes analysis can also be found in the public domain (<http://helmparms3d.sf.net>).

3.4 Photogrammetric precision analysis

In previous studies (Niethammer et al., 2010 and 2011) close-range photogrammetry, MVS and terrestrial laser scanning (TLS) approaches have been compared and analysed at the toe of the Super-Sauze landslide. An analysis of the entire landslide could not be managed since no comparable data of the interesting time period has been available.

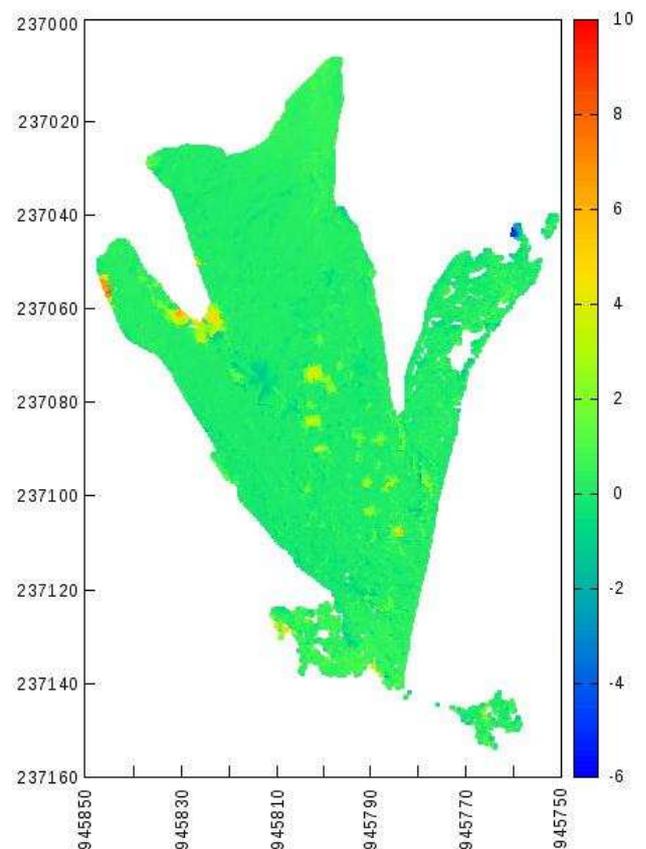


Figure 6. Altitude difference [m] at the toe (MVS -TLS)

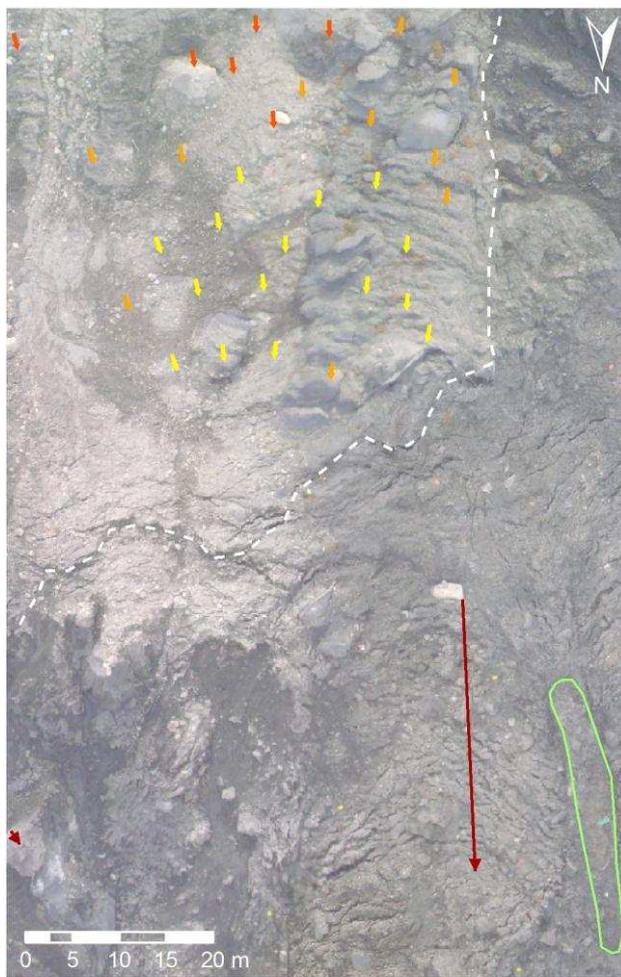
A comparison of the DGPS-measured ground control points and a derived orthophoto from the entire MVS-based model showed a significant planar misfit over the 815 m DTM-length of 6 m in west to east direction. This misfit can be explained by justification errors of the 3D Helmert-transformation, as well as

error propagation within the bundle-block processing of the very long and narrow model. Since the alignment of the entire landslide model could not be managed very precisely, an iterative closest point algorithm (Rusinkiewicz and Levoy, 2001) was applied. So the quality of the MVS-based model could easily be assessed by subtracting the elevations of two matched models. Here, a TLS of the toe of the Super-Sauze landslide (Travelletti et al., 2011) and the MVS-based point cloud of the toe of the landslide were compared. Both data sets were acquired at the same time period in order to avoid topographic changes of the landslide. In the vertical direction the RMS difference amounts 0.25 m. Deviations reach from -5.47 to +8.55 m (figure 6).

However, the most significant errors are induced by some small trees and bushes, the effects of which could not be reliably removed from the MVS-based point cloud.

The point density of the MVS-based digital surface model reaches up to 40 points per square meter and a separately processed model of the toe region with a point density of up to 70 points per square meter has been generated (Niethammer et al., 2010).

4. LANDSLIDES ANALYSIS



displacement vectors of the earthflow

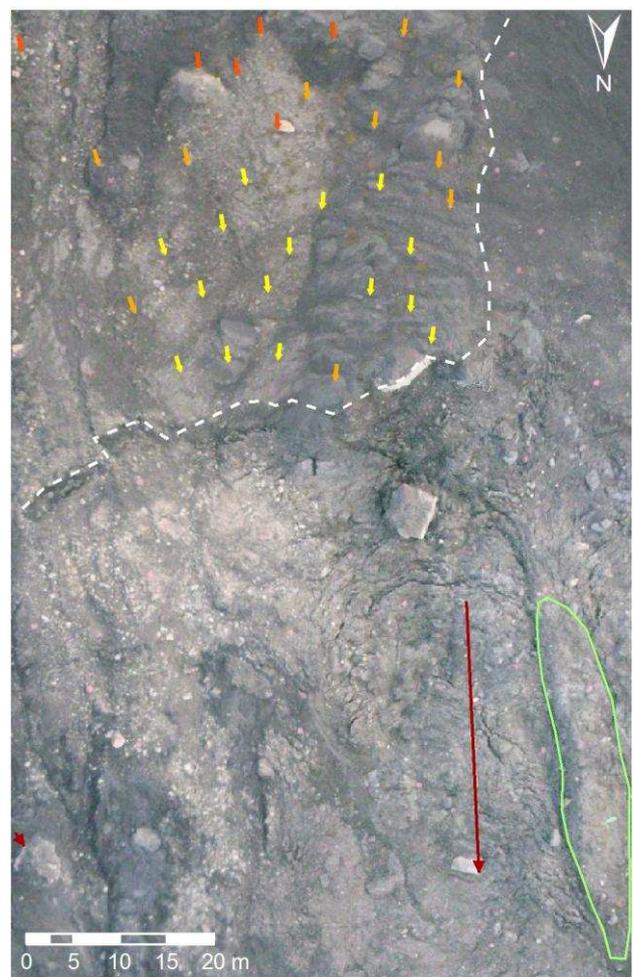
- ↓ 80,1 - 100,0 cm
- ↓ 60,1 - 80,0 cm
- ↓ 45,0 - 60,0 cm

Figure 7. Horizontal displacements and scarp within the Super-Sauze landslide in October 2008

4.1 Orthophoto analysis

Superficial displacements of landslides are of great interest and can be measured between orthophotos from different dates. Such measurements, for example, can be performed manually within a geographic information system (GIS) by identifying corresponding features and areas, such as rocks, stones and vegetation patches in different images (Niethammer et al., 2009) (figure 7, 8). Currently, many open source GIS software projects are available in the public domain. The most common projects are Qgis (<http://www.qgis.org>) and OpenJump (<http://www.openjump.org>) with a couple of software plugins which support many raster- and vector-based analysis- and processing tasks.

Displacement analysis can also be managed by applying automated image matching using correlation-based methods (Leprince et al., 2008) or by applying more sophisticated object- or feature-based matching techniques such as 'scale-invariant feature transform' (SIFT) (Lowe, 2004). However, analysis of orthophotos is only providing horizontal information of landslide displacements.



- ← displacement vectors of secondary movements
- secondary scarp
- emerging in-situ crest

Figure 8. Horizontal displacements and scarp within the Super-Sauze landslide in October 2009

4.2 DTM analysis



Figure 9. DTM of the upper part of the Super-Sauze landslide in October 2008



Figure 11. DTM of the upper part of the Super-Sauze landslide in October 2009

Digital terrain models are often used for mass-balancing in landslides research. This is commonly managed by computing the altitude difference between two different DTMs (figures 9, 10, 11). This technique only provides vertical information of the landslide, and it has to be emphasized that both horizontal and vertical surface information are not sufficient for representative mass-balancing of landslides, since additional subsurface displacements also have to be regarded. Currently such information cannot be acquired by remote sensing techniques and direct subsurface measurements have to be applied.

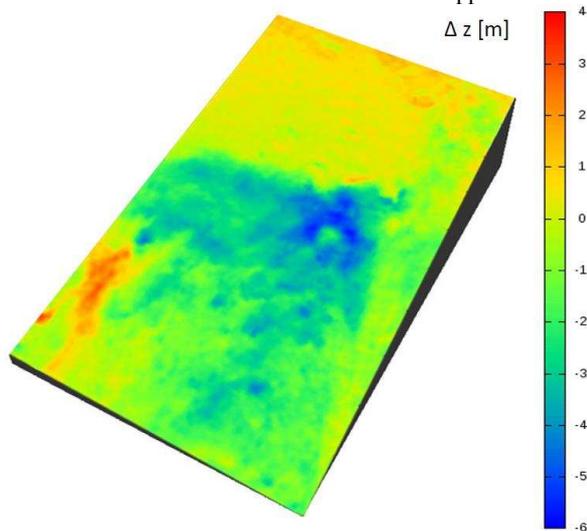


Figure 10. Altitude difference map between Oct. 2008 and Oct. 2009, upper part of the Super-Sauze landslide

Geotechnical, geological and hydrological soil parameters may provide enough information for the modelling of the subsurface displacements. In recent studies it is pointed out that some of the subsurface data (e.g. soil moisture (Niethammer et al., 2009) and medial soil grain size) may be gained from UAV-based high-resolution remote sensing data. UAV-based measurements of changes of landslide extension and topography may also provide interesting boundary conditions for modellers. These data can be used to verify the transferability of models into the real world with more realistic parameters than laboratory-based landslide experiments (Germer and Braun, 2011).

4.3 Geomatics in landslides research

Within the last decade a growing research interest for geomatics, a new discipline for many purposes of geographic knowledge discovery can be noticed (Gallerini et al., 2010).

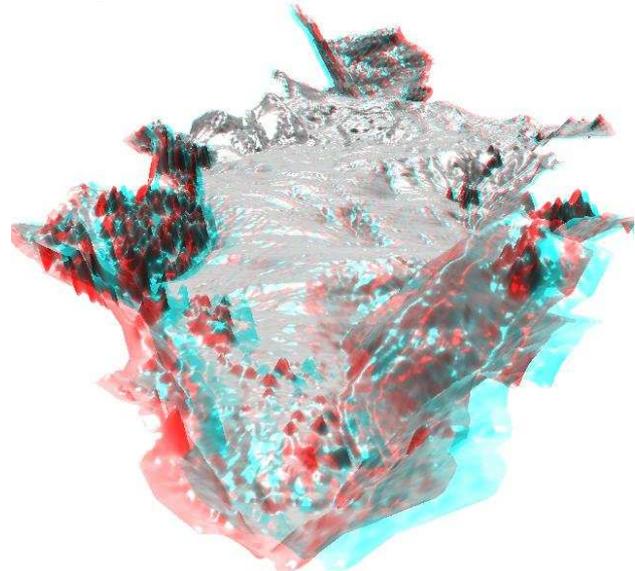


Figure 12. Virtual 3D anaglyph of the Super-Sauze landslide (red/cyan glasses are required for full 3D impression)

Geomatics has been defined as "the science of acquisition, management, modelling, analysis and representation of spatial data and processing with specific consideration of problems related to spatial planning, land use, land development and environmental issues" (Grun, 1998). Just in the field of landslides research many different spatial data sets have to be analysed from a global point of view. For example virtual UAV-based 3D models (figure 12), seismic 3D subsurface profiles, as well as different hydrological and morphological 3D variations may be visualized and analysed together in virtual space. In the future such new opportunities may lead to a better understanding of the interactions between many different landslide parameters that are supposed to be the main trigger mechanisms of landslide hazards. Landslide models may also be visualized and discussed, and consequences of different landslide event forecasts may be presented to the local

inhabitants in order to promote sensitivity against dangerous developments, such as deforestation, road works, or mining.

5. CONCLUSIONS

Within this study, a couple of public domain image processing tools for low-cost ortho-rectification and mosaic blending were used. Different open source GIS projects have also been made available, thus enabling analysis of the planar remote sensing data. Even photogrammetric processing of hundreds of UAV-based images acquired with uncalibrated cameras was managed by applying open source software tools. The used algorithms can easily handle unordered image collections and have provided digital surface models of landslides without any ground control point information. The density and accuracy of MVS-based models is comparable to common photogrammetric methods, but it has to be ensured that long and narrow models will not be twisted by error propagation within the bundle-block processing. Overall, it can be concluded that a complete remote sensing working cycle with no commercial hardware or software is now possible. However, many of these software-tools are only supplied in a very sparse command-line beta version. The user also has to prepare and convert input data between many different data formats. Especially some photogrammetric tools for registration and orthophoto processing are currently missing. Consequently, the development of such software-tools is advised in further studies.

REFERENCES

- Crosilla, F., 1999. Procrustes analysis and geodetic sciences. In: Krumm, F., Schwarze, V.S. (Eds.), *Technical Reports. Department of Geodesy and GeoInformatics*, University of Stuttgart, Part I, pp. 69-78.
- Furukawa, Y. and Ponce, J., 2010. Accurate, dense, and robust multi-view stereopsis. In: *IEEE transactions on pattern analysis and machine intelligence*, 32(8), pp. 1362-1376.
- Gallerini, G., Susini, S., Bruciatelli, L., De Donatis, M., 2010. Geomatics and geo-tourism: San Bartolo Natural Park case study (Pesaro, Italy). *Geology of the Adriatic area, Special Publication*, 3, pp. 167-178.
- Germer, K. and Braun, J., 2011. Effects of Saturation on Slope Stability: Laboratory Experiments Utilizing External Load. *Vadose Zone Journal*, 10(2), pp. 477-486.
- Grun, A., 1998. Geomatic Engineering and Environmental Engineering. *Geomatics Information Magazine*, 12, pp. 30-33.
- Henry, J.-B., Malet, J.-P., Maquaire, O., Grussenmeyer, P., 2002. The use of small-format and low-altitude aerial photos for the realization of high-resolution DEMs in mountainous areas: application to the Super-Sauze earth-flow (Alpes-de-Haute-Provence, France). In: *Earth Surf. Process. Landforms*, 27(12), pp. 1339-1350.
- Leprince, S., Berthier, E., Ayoub, F., Delacourt, C., Avouac, J.-P., 2008. Monitoring earth surface dynamics with optical imagery. *EOS Transactions, American Geophysical Union*, 89(1), pp. 1-2.
- Lindenmaier, F., Zehe, E., Dittfurth, A., Ihringer, J., 2005. Process identification at a slow-moving landslide in the Vorarlberg Alps. *Hydrological Processes*, 19, pp. 1635-1651.
- Lowe, D., 2004. Distinctive image features from scale-invariant keypoints. *International Journal of Computer Vision*, 60(2), pp. 91-110.
- Mantovani, F., Soeters, R., Van Westen, C.J., 1996. Remote sensing techniques for landslide studies and hazard zonation in Europe. *Geomorphology*, 15(3-4), pp. 213-225.
- Malet, J.P. and Maquaire, O., 2003. Black marl earthflows mobility and long-term seasonal dynamic in southeastern France. In: Picarelli, L. (ed.), *Proceedings of the International Conference on Fast Slope Movements: Prediction and Prevention for Risk Mitigation*, Bologna, Patron Editore, pp. 333-340.
- Niethammer, U., Rothmund, S., Joswig, M., 2009. UAV-based remote sensing of the slowmoving landslide Super-Sauze. In: Malet, J.-P., Rémaitre, A., Boogard, T. (Eds.), *Proceedings of the International Conference on Landslide Processes: From Geomorphologic Mapping to Dynamic Modelling*, CERG Editions, Strasbourg, pp. 69-74.
- Niethammer, U., Rothmund, S., James, M.R., Travelletti, J., Joswig, M., 2010. UAV-based remote sensing of landslides. In: *Int. Arch. Photogram. Rem. Sens. Spatial Inf. Sciences*, Vol. XXXVIII. ISPRS Comm. V., Newcastle-upon-Tyne, U.K, pp. 496-501.
- Niethammer, U., James, M.-R., Rothmund, S., Travelletti, J., Joswig, M., 2011. UAV-based remote sensing of the Super-Sauze landslide: Evaluation and results. *Eng. Geol.*, doi:10.1016/j.enggeo.2011.03.012.
- Otto, G.P., and Chau, T.K.W., 1989. Region-growing algorithm for matching of terrain images. *Image Vision Comp.*, 7, pp. 83-94.
- Pérez, P., Gangnet, M., Blake, A., 2003. Poisson image editing. In: *Proc. SIGGRAPH*, Jul. 2003, pp. 313-318.
- Rusinkiewicz, S. and Levoy, M., 2001. Efficient variants of the ICP algorithm. In: *Proc. of the third international conference on 3-D digital imaging and modelling*, doi: 10.1109 / IM.2001.924423, pp.145-152.
- Snaveley, N., Seitz, S.M., Szeliski, R., 2008. Modeling the World from Internet Photo Collections. *International Journal of Computer Vision*, 80(2), pp. 189-210.
- Travelletti, J., Malet, J.P., Delacourt, C., 2011. Multi-dates correlation of Terrestrial Laser Scanning data for the characterization of landslide kinematics. *Geophysical research abstracts, vol. 13, Vienna*.
- Watson, G.A., 2006. Computing Helmert transformations. *Journal of Computational and Applied Mathematics*, 197(2), pp. 387-394.
- Wiesel, J., 1985. Digital image processing for orthophoto generation. *Photogrammetria*, 40(2), pp. 69-76.
- Zomet, A., Levin, A., Peleg, S., Weiss, Y., 2006. Seamless Image Stitching by Minimizing False Edges. *IEEE image processing*, 15(4), pp. 969-977.

UAV-BASED REMOTE SENSING OF LANDSLIDES

U. Niethammer^a, S. Rothmund^a, M. R. James^b, J. Travelletti^c, M. Joswig^a

^a Institute for Geophysics, Universität Stuttgart, 70174 Stuttgart, Germany - uwe.niethammer@geophys.uni-stuttgart.de

^b Lancaster Environment Centre, Lancaster University, Lancaster, UK - m.james@lancaster.ac.uk

^c School and Observatory of Earth Science, University of Strasbourg, France - julien.travelletti@eost.u-strasbg.fr

KEY WORDS: UAV, Quad-rotor, Landslide, Photogrammetry, DEM, DSM

ABSTRACT:

In this study a low-cost remote sensing approach based on unmanned aerial vehicles (UAVs) and digital compact cameras will be presented. This approach enables high-resolution acquisitions of landslides. The concept of manual controlled quad-rotor helicopters has been investigated for photogrammetric applications, since quad-rotor systems have been proved to be well suited for landslide monitoring in difficult alpine terrain. During the UAV-based remote sensing campaigns significant numbers of airborne photographs of the Super-Sauze landslide (Southern France) have been acquired. These photographs were combined to an ortho-mosaic by applying plane image rectification methods. Digital surface models (DSMs) were generated using a new feature-based surface reconstruction approach which does not require any ground control point information.

1. INTRODUCTION

1.1 Study area

This study was carried out on the Super-Sauze landslide (Southern French Alps). The Super-Sauze landslide is located on the North-facing slope of the Barcelonnette Basin. It has developed in a torrential basin located in the upper part of Sauze torrent. The landslide is one of the persistently active landslides (since the 1970's). It extends over a horizontal distance of 850 m and occurs between an elevation of 2105 m at the crown and 1740 m at the toe with an average of 25° slope. Its total volume is estimated to be 750.000 m³ and velocities range from 0.01 m up to 0.4 m per day (Malet et al. 2003).



Figure 1. Super-Sauze landslide

1.2 Previous UAV-based remote sensing

UAV-based remote sensing studies have been carried out for many decades. In the late 1970's fixed wing remote controlled aircrafts have been investigated for first motorized UAV photogrammetry experiments (Przybilla and Wester-Ebbinghaus, 1979). A quarter century later Eisenbeiss et al. (2005) generated the first high-resolution digital elevation models (DEMs) using autonomously controlled helicopter

UAVs. Today there are many other UAV-systems like motorized paragliders (Jütte, 2008), blimps (Gomez-Lahoz and Gonzalez-Aguilera, 2009), kites (Aber et al., 2002) and balloons (Fotinopoulos, 2004) in use. But such systems are strongly affected by wind and often cannot be used in alpine terrain. Since 2006 quad-rotor systems are available as open source projects (Mikrokopter, 2009). When compared to commercially available UAV-systems, the costs of such open source systems are very low and all software source codes, as well as electronic schematics are available in the public domain.

1.3 UAV-based remote sensing in landslide research

Monitoring and analysis of active landslides involves both spatial and temporal measurements and requires continued assessment of landslide conditions, including the extent and rate of displacements as well as changes in the surface topography. Displacement rates are of great interest and can be directly achieved by the comparison of ortho-photographs as well as digital surface models (DSMs) from different dates. Such measurements can be performed manually or automatically, for example by image correlation algorithms (Leprince et al., 2008). UAV-acquired ortho-mosaics now allow for a detailed large scaled analysis of landslide materials and fissure structures (Walter et al., 2009). Such fissure structures have been clearly detected and could be related to fracture processes in the landslide material. Additionally, high-resolution textural information in UAV-acquired ortho-photographs could possibly permit a soil moisture analysis of the surface of landslides (Niethammer et al., 2009). Such analysis could be supported by multi-spectral analysis in the near- and thermal infrared spectrum. One major advantage of UAV-based remote sensing applications for hazardous environments like landslides, mudslides or rockfalls is the possibility to gain information in very dangerous areas of interest. Direct measurements in such area often are impossible.

1.4 UAV-based photogrammetry

Up to now UAV-based photogrammetric evaluations are still very difficult. UAV-acquired airborne photographs are required to be in an optimal block configuration alignment in order to

manage standard aerial photogrammetric processing. In addition the camera-systems are required to maintain a stable interior orientation, as well as reduced optical distortions and a lightweight but robust design. These requirements have been solved in the past by the usage of high-end fixed-lens SLR-cameras, as well as precise UAV navigation based on high-end autopilot- and UAV-systems and special developed photogrammetric software packages (Eisenbeiss et al., 2005).

Here we present a low-cost UAV-based remote sensing approach using new structure from motion algorithms which can reduce limitations when using manual controlled UAVs and digital low-cost compact cameras. These methods easily can handle unordered image collections and do not require any ground control point information. Therefore this approach is very suitable in the field of landslide research.

2. UAV-SYSTEM

2.1 Quad-rotor UAV

When compared to conventional helicopters, quad-rotor systems are more stable in flight with reduced vibration and have the mechanical advantage of not requiring a large, variable pitch rotor-unit. Our in-house developed quad-rotor system is stabilized by inertial measurement units (IMU), including three acceleration sensors, three gyroscopes, a three-axis compass, a pressure sensor, and is regulated by basic PID (proportional integral differential) loops. A quad-rotor open source project (Mikrokopter, 2009) has been used and improved by modifications of the software and the electronic circuit in order to comply with the requirements for landslide studies.



Figure 2. Modified Mikrokopter-system

2.2 Autonomous versus manual flight

Autonomously controlled UAVs have been proved to be successful for first remote sensing applications but they do not benefit from the intelligence of a human operator and, currently, are less able to cope with unpredictable conditions such as gusty winds. In addition, the use of autonomously controlled UAVs is tightly regulated by civil aviation and security authorities, preventing their practical deployment.

In this study radio-controlled UAVs have been used. This requires a good level of pilot skill, and range restrictions limit the operational area to a few hundreds of meters. There are also

further issues related to the relatively small payloads and UAV-reliability. However, the advantages of using manual controlled quad-rotor UAVs currently are significant.

2.3 Camera-system

The quad-rotor UAVs are equipped with lightweight low-cost digital compact cameras, which support manual camera settings. For all flights the camera settings were fixed to ISO 200 at F2.8 and a focus of 6.2 mm. These settings enabled an average shutter speed of 1/800 s which was necessary to avoid blurred photographs.



Figure 3. UAV camera-system

3. IMAGE ACQUISITION

In October 2008 a set of 1486 UAV-acquired photographs covering the whole sliding area of 850 m x 250 m were taken. The achievable altitude over ground was in the range between 20 m and 250 m. All photographs were taken in an automatic image series mode shooting one photo every three seconds. In a first in-situ flight planning step, the desired area and suitable locations for starting and landing were chosen. Then the quad-rotor was launched to the maximum flight altitude of about 200 m. At this position the UAV was hovered for about 30 seconds. Vertical landing was then initiated by the pilot. After each flight the covered area of the acquired photographs was checked on the camera directly.

4. DIGITAL SURFACE MODEL PROCESSING

The field of computer vision now offers methods for extraction of 3D surface models from overlapping digital images as an efficient alternative to commercial photogrammetry software. Immense progress has been made on algorithms for multiple view reconstruction. Such multi view stereo (MVS) algorithms are now robust and accurate and do not require any ground control point information or tie points as usually required for standard photogrammetric processing. Additionally, an optimized initial block alignment for the photogrammetric processing is not required.

The proposed MVS method consists of a structure from motion algorithm (Snavely et al., 2008) for automated camera calibration and bundle block computation, as well as a patch based multi view stereo algorithm for the generation of dense 3D point cloud models (Furukawa and Ponce, 2007).

4.1 Structure from motion algorithm

The structure from motion algorithm (Snavely et al., 2008) computes a set of parameters for each of the supplied photographs (extrinsic and intrinsic camera parameters, as well as a sparse 3D point cloud). It does not rely on a previous camera calibration or any other information to provide location, orientation, or geometry. Instead this information is computed from the images themselves. For all images, SIFT key-point

descriptors (Lowe, 2004) are matched, using an approximate nearest neighbour algorithm (ANN) (Arya et al., 1998). After matching features a robust fundamental matrix is estimated for each image pair using the RANSAC algorithm (Fischler and Bolles, 1981). Finally a set of camera parameters and the relative 3D locations between all supplied images is calculated (e.g. rotation, translation, focal length and radial distortion parameters), as well as a new set of undistorted photographs.

4.2 Patch-based multi view stereo algorithm

The patch-based multi view stereo algorithm (Furukawa and Ponce, 2007) computes a dense set of small rectangular patches covering the surfaces visible in the images using the supplied parameters from the structure from motion algorithm. Stereopsis is implemented as a match, expand, and filter procedure, starting from a sparse set of matched key points, and repeatedly expanding these before using visibility constraints to filter away false matches. The keys to the performance of the algorithm are effective techniques for enforcing local photometric consistency and global visibility constraints.

4.3 Alignment adjustment of the point cloud

Since the investigated algorithms do not consider any ground control point information the coordinate system of the final 3D point cloud remains indeterminate. This is the major disadvantage of this approach, but can be solved applying a spatial similarity transformation to all points of the computed 3D model:

$$X_i = T + sRX \quad (1)$$

where X_i = transformed coordinate vector
 X = initial coordinate vector
 T = translation vector
 R = rotation matrix including r_x, r_y, r_z
 r_x, r_y, r_z = rotations around the coordinate axes
 s = scale factor

Seven parameters are required for this kind of transformation and were calculated from a set of three well known prominent locations which were visible in a computed hillshading of the generated point cloud. However, this strategy is susceptible to misalignments of the final DSM, because of the limited precision possible when registering ground control points using only a shaded relief model.

4.4 Processing

30 photographs of the landslide toe-region, as well as 285 photographs of the entire landslide (manually pre-selected by criteria like image quality and covered area size) were computed to two digital surface models, one of the toe and one of the entire landslide.

First, all photographs were processed using the structure from motion algorithm. This computation supplied a set of camera parameters and the relative 3D locations between all supplied images, as well as a new set of undistorted images. In a second step these data were supplied to the patch based multi view stereo algorithm which finally computed a dense point cloud for all supplied photographs.

4.5 Ortho-mosaic computation

Since the proposed photogrammetric methods do not directly generate an ortho-mosaic, a straightforward plane image rectification method as described in Niethammer et al. (2009) has also been used (figure 9). In a first step, optical barrel distortion of the camera was corrected. In a second processing step, each image was rectified manually onto DGPS-measured ground control point (GCP) coordinates using plane image rectification approaches. In a final step all rectified photographs with a ground resolution in the range of 3 to 8 cm have been merged to a high-resolution ortho-mosaic. However, this approach requires a significant amount of manual processing and the presence of residual misalignments has to be accepted.

4.6 DSM precision analysis

In order to assess the quality of the generated digital surface models, the surface model of the landslide toe-region (figure 4) was compared to the result of a previously performed photogrammetric investigation (James et al., 2010) (figure 5) using a GOTCHA region-growing algorithm (Otto and Chau, 1989). Both surface reconstructions were computed using the same photographs.

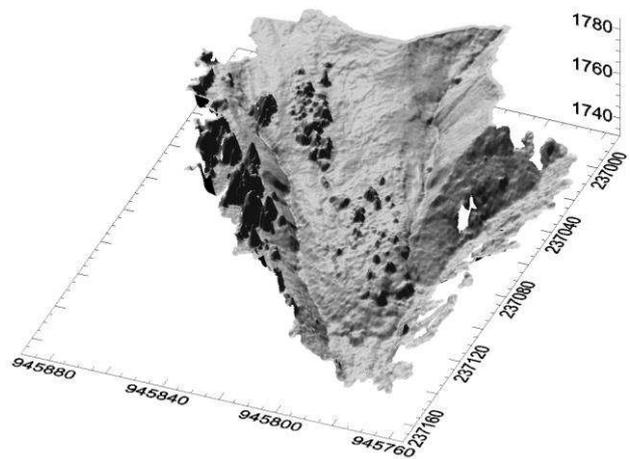


Figure 4. DSM for precision analysis of the toe region, generated using the proposed MVS algorithms

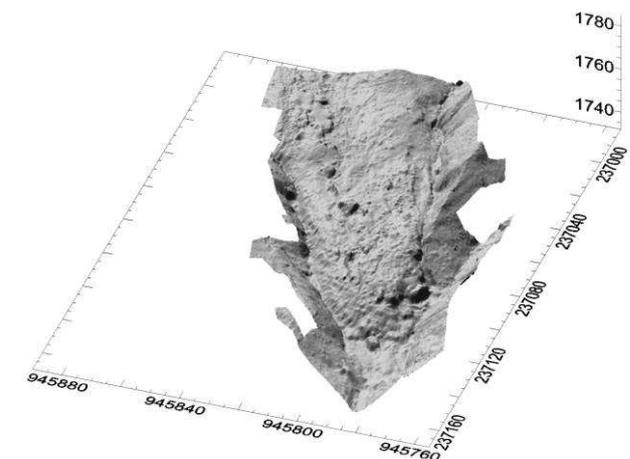


Figure 5. DEM of the toe region, generated using a GOTCHA region growing algorithm (James et al., 2010)

The surface model of our proposed method (figure 4) shows a little denser point cloud (figure 6B) compared to the other model (figure 6A), especially in the middle part of the investigated area.

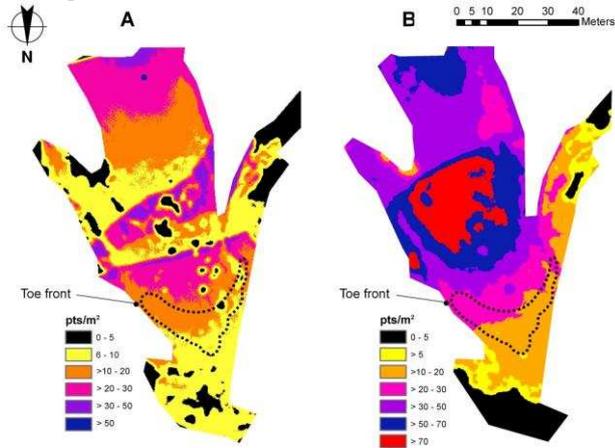


Figure 6. Comparison of the point density. A: DEM generated using a GOTCHA region-growing algorithm. B: DSM generated using the proposed MVS approach.

In figure 8 the point density of the surface model of the entire landslide is illustrated. Some sparse areas can be observed (illustrated by yellow and white) as a result of supplying too few photographs of this areas to the algorithms. Additionally an analysis of the alignment was done by subtracting the elevation of both models of the toe-region (figure 7). In the vertical direction deviations reach from -3 m to +4 m. These significant deviations reflect the presence of vegetation which was removed in only one of the investigated models (figure 5). Further sizable differences of about one meter from north to south direction can be observed. These differences can be explained by misalignments when using a shaded relief for the registration of the GCPs and it is anticipated that they can be significantly reduced in further work. In general it can be concluded that both photo-based methods provide consistent surface models.

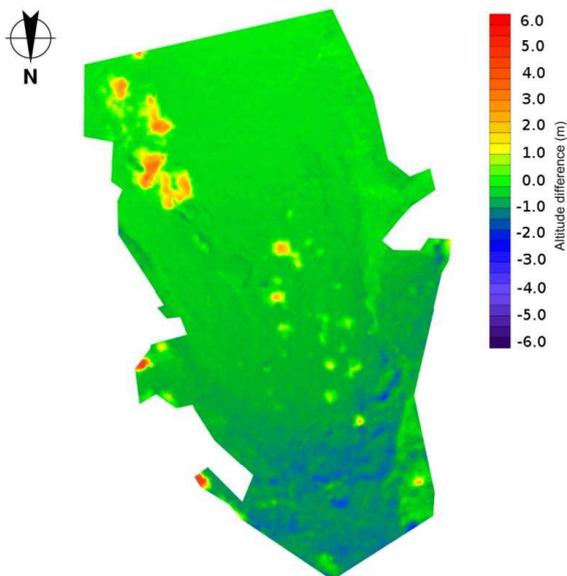


Figure 7. Altitude differences between the GOTCHA- and the MVS-generated DEM of the toe-region

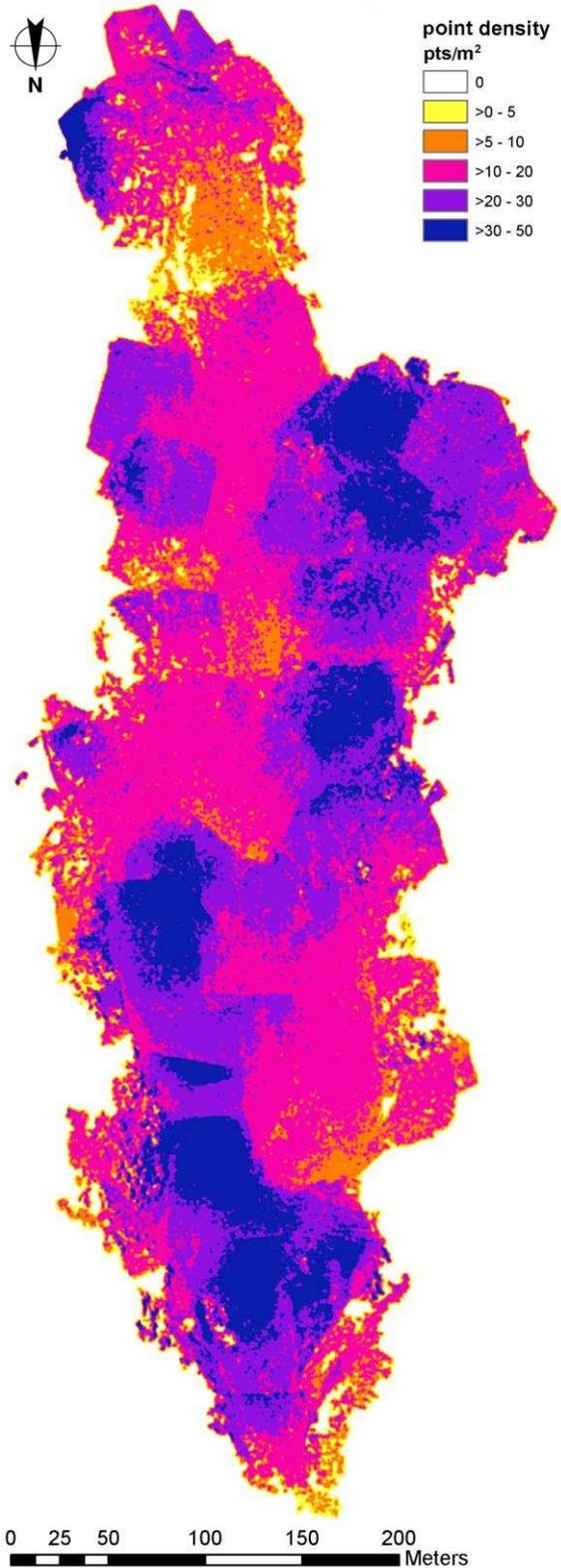


Figure 8. Point density of the entire landslide surface model

5. RESULTS

In figure 9 an ortho-mosaic of the Super-Sauze landslide is illustrated. Figure 10 shows a hillshading of the generated digital surface model. These results are showing a good agreement and are suitable for high-resolution investigations of the entire Super-Sauze landslide.

5.1 Resulting ortho-mosaic

59 UAV-acquired photographs have been merged to an ortho-mosaic by using plane image rectification methods. The generated ortho-mosaic covers the entire sliding area of the Super-Sauze landslide (figure 9), with a spatial resolution in the range of 3 cm to 8 cm. Within the ortho-mosaic some misalignments are present. The maximum deviation within the boundary of the sliding area reaches 3.9 m and the mean error can be quantified to be 0.5 m.

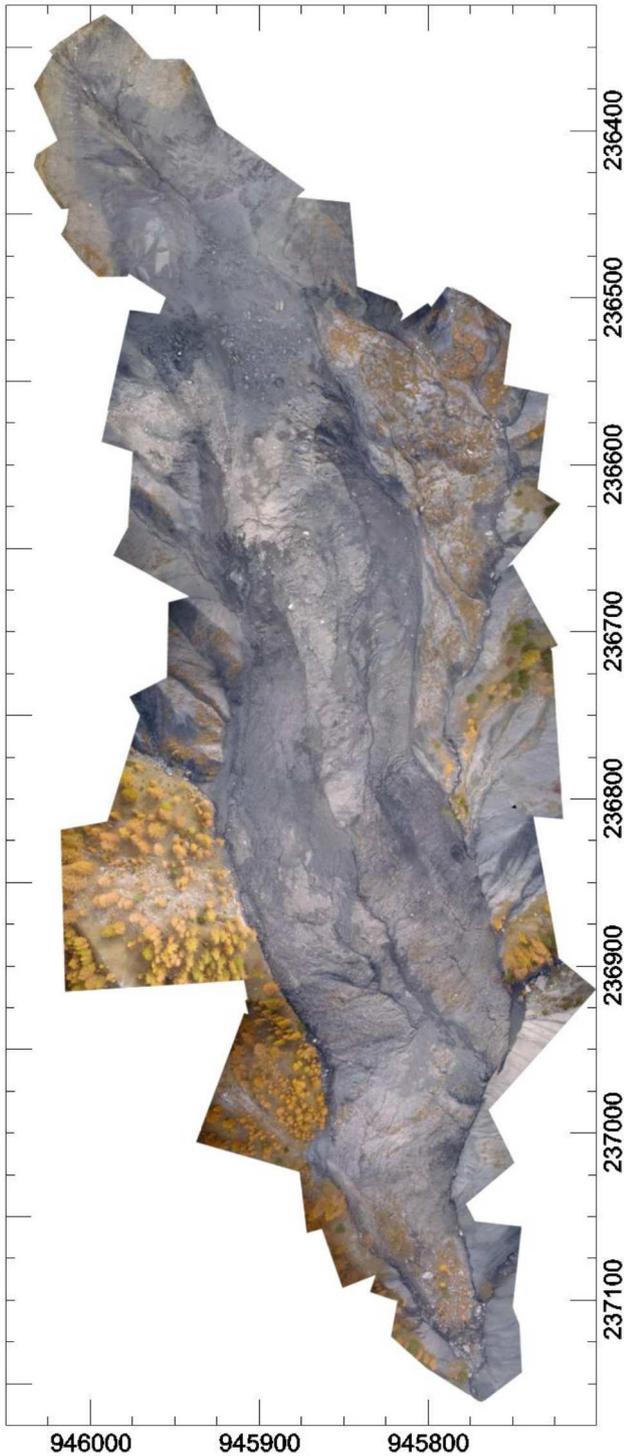


Figure 9. Ortho-mosaic of the entire Super-Sauze landslide

5.2 Resulting digital surface model

285 pre-selected photographs were computed to a digital surface model of the entire landslide. The point density of the achieved model varies between 0 and 40 points per square meter. A grid size of 30 cm was chosen in order to avoid interpolation artefacts in sparse areas of the point cloud (the maximum point density would allow a grid size of 20 cm). The achieved digital surface model shows clearly the details of the shape of the landslide but a misalignment up to several meters is present.

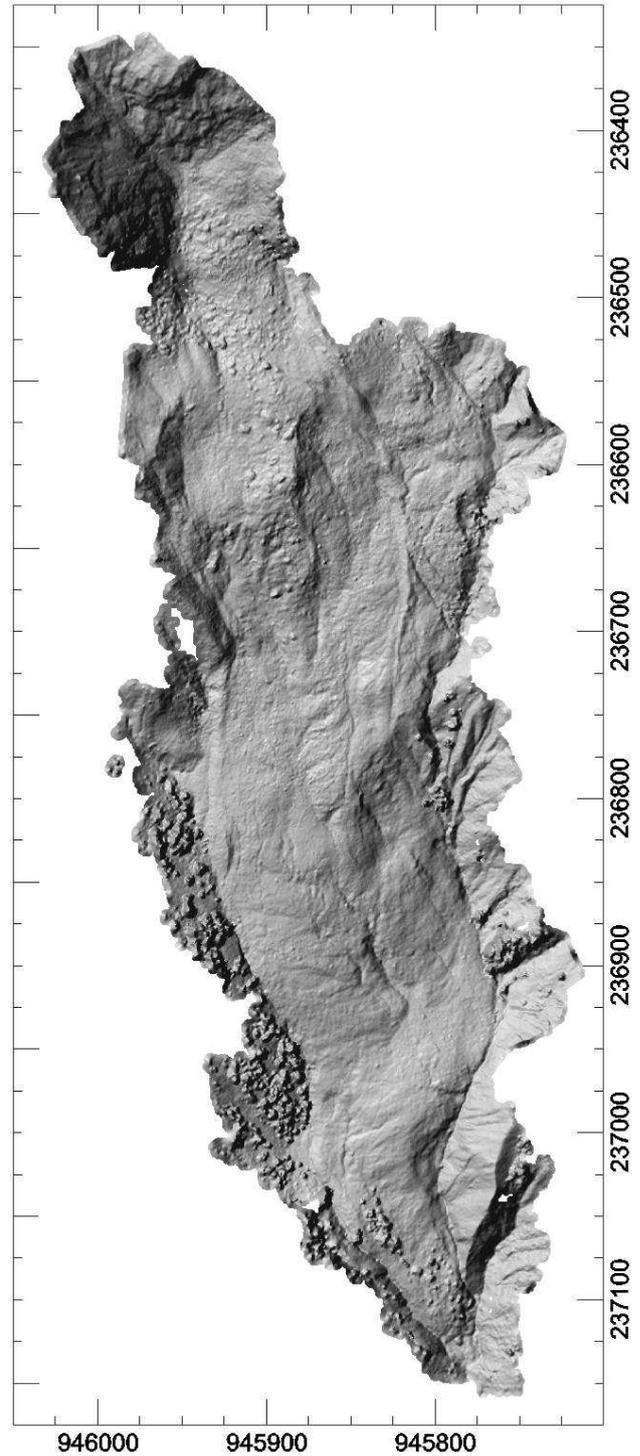


Figure 10. Hillshading of the entire landslide surface model

6. CONCLUSIONS

In this study it was shown that a low-cost UAV-based remote sensing approach reveals high-resolution digital surface models of landslides. The proposed structure from motion method can easily handle unordered image collections and has provided a consistent digital surface model of the Super-Sauze landslide that is consistent with results from a more traditional photogrammetric approach. This approach does not require any ground control point information and enables surface models to be generated from UAV-based remote sensing without ground-based measurements. In many cases the area of interest cannot be directly measured because of hazardous environment. The proposed approach is therefore very well suitable in the field of landslide research. The point densities of the achieved digital surface models reach up to 70 points per square meter and are comparable to a previously generated DEM using a GOTCHA region-growing algorithm (Otto and Chau, 1989). Since the proposed algorithms do not consider any ground control point information the coordinate system of the final 3D point cloud remains indeterminate and has to be aligned in a separate processing step. Here, sizable misfits of the aligned models were observed and reducing them will be the focus of further work, for example by applying a 3D surface matching algorithm in order to match the digital surface model onto stable parts of a previously acquired DEM.

ACKNOWLEDGMENTS

We thank all colleagues from the OMIV project (Observatoire des Instabilités de Versants) for the helpful discussions and their support in the field. The authors are grateful to Jean-Philippe Malet (School and Observatory of Earth Sciences, University of Strasbourg) for providing several datasets. Our thanks also go to Eberhard Claar (Institute for Geophysics, Universität Stuttgart) who built significant components of the quad-rotor systems. The work was supported by the DFG within the project FOR 581 'Natural Slopes'.

REFERENCES

Aber, J. S., Aber, S. W. and Pavri, F., 2002. Unmanned small-format aerial photography from kites for acquiring large scale, high-resolution, multiview-angle imagery. In: *International Archives of the Photogrammetry, Remote Sensing and Spatial Information Sciences*, Pecora 15/Land Satellite Information IV/ISPRS Commission I/FIEOS, Denver, CO, USA.

Arya, S., Mount, D. M., Netanyahu, N. S., Silverman, R., Wu, A. Y., 1998. An optimal algorithm for approximate nearest neighbor searching fixed dimensions. *Journal of the ACM*, 45(6), pp. 891–923.

Eisenbeiss, H., Lambers, K., Sauerbier, M., 2005. Photogrammetric recording of the archaeological site of Pinchango Alto (Palpa, Peru) using a mini helicopter (UAV). In: *Proc. of the 33rd CAA Conference*, Tomar, Portugal.

Fischler, M. A. and Bolles, R. C., 1981. Random sample consensus: A paradigm for model fitting with applications to image analysis and automated cartography. *Communications of the ACM*, 24(6), pp. 381–395.

Fotinopoulos, V., 2004. Balloon photogrammetry for archaeological surveys. In: *International Archives of the Photogrammetry, Remote Sensing and Spatial Information*

Sciences, XX ISPRS Congress, Istanbul, Turkey, XXXV-B5, pp. 504-507.

Furukawa, Y. and Ponce, J., 2007. Accurate, dense, and robust multi-view stereopsis. In: *Conference on Computer Vision and Pattern Recognition, IEEE Computer Society*

Gomez-Lahoz, J. and Gonzalez-Aguilera, D., 2009. Recovering traditions in the digital era: the use of blimps for modelling the archaeological cultural heritage. *Journal of Archaeological Science*, 36(1), pp. 100-109.

James, M. R., Niethammer, U., Traveletti, J., 2010. Topographic reconstruction of landslide surfaces using images from an unmanned aerial vehicle. In: *ISPRS Commission V Mid Term Symposium*, Newcastle, UK.

Jütte, K., 2008. Vergleich verschiedener low-cost Luftbildaufnahmesysteme sowie Einsatz von Drohnen: Grenzen und Möglichkeiten. In: Bayerische Landesanstalt für Wald und Forstwirtschaft. Der gepixelte Wald - Fachtagung zur Forstlichen Fernerkundung.

Leprince, S., Berthier, E., Ayoub, F., Delacourt, C., Avouac, J.-P., 2008. Monitoring earth surface dynamics with optical imagery. *EOS Transactions, American Geophysical Union*, 89(1), pp. 1-2.

Lowe, D., 2004. Distinctive image features from scale-invariant keypoints. *International Journal of Computer Vision*, 60(2), pp. 91–110.

Mikrokopter, 2010. Official Mikrokopter open source quad-rotor homepage. <http://www.mikrokopter.com> (accessed 10 April 2010).

Malet, J. P. and Maquaire, O., 2003. Black marl earthflows mobility and long-term seasonal dynamic in southeastern France. In: *Proceedings of the International Conference on Fast Slope Movements: Prediction and Prevention for Risk Mitigation*, Picarelli L. (ed.), Bologna, Patron Editore, pp. 333-340.

Niethammer, U., Rothmund, S., Joswig, M., 2009. UAV-based remote sensing of the slow-moving landslide Super-Sauze. In: *Malet, J.-P., Remaître, A., Boogard, T. (Eds) Proceedings of the International Conference on Landslide Processes: from geomorphologic mapping to dynamic modelling*, Strasbourg, CERG Editions, pp. 69-74.

Otto, G. P., and T. K. W. Chau (1989), Region-growing algorithm for matching of terrain images. *Image Vision Comp.*, 7, pp. 83-94.

Snively, N., Seitz, S. M., Szeliski, R., 2008. Modeling the World from Internet Photo Collections. *International Journal of Computer Vision*, 80(2), pp. 189-210.

Przybilla, H.-J. and Wester-Ebbinghaus, W., 1979. Bildflug mit ferngelenktem Kleinflugzeug. *Bildmessung und Luftbildwesen, Zeitschrift fuer Photogrammetrie und Fernerkundung*, 47(5), pp. 137-142.

Walter, M., Niethammer, U., Rothmund, S., Joswig, M., 2009. Joint analysis of the Super-Sauze (French Alps) mudslide by nanoseismic monitoring and UAV-based remote sensing. *EAGE First Break* 27(8), pp. 75-82.

UAV-based remote sensing of the Super-Sauze landslide: Evaluation and results

U. NIETHAMMER^{a,*}, M.R. JAMES^b, S. ROTHMUND^a, J. TRAVELLETTI^c, M. JOSWIG^a

^aInstitute for Geophysics, University of Stuttgart, Germany

^bLancaster Environment Centre, Lancaster University, UK

^cSchool and Observatory of Earth Science, University of Strasbourg, France

Abstract

Unmanned aerial vehicles (UAVs) equipped with digital compact cameras can be used to map landslides quickly and at a high ground resolution. Images taken by a radio-controlled mini quad-rotor UAV of the SuperSauze, France landslide have been used to produce a high-resolution ortho-mosaic of the entire landslide and digital terrain models (DTMs) of several regions. The UAV capability for imaging fissures and displacements on the landslide surface has been evaluated, and the subsequent image processing approaches for suitably georectifying the data have been assessed. For Super-Sauze, horizontal displacements of 7 to 55 m between a high-resolution airborne ortho-photo of May 2007 and a UAV-based ortho-mosaic of October 2008 have been measured. Fixed areas of persistent deformation have been identified, producing fissures of different distributions and orientations comparable to glacial crevasses, and relating directly to the bedrock topography. The UAV has demonstrated its capability for producing valuable landslide data but improvements are required to reduce data processing time for the efficient generation of ortho-mosaics based on photogrammetric DTMs, in order to minimise georeferencing errors.

1 Introduction

In order to monitor hazards from active landslides and to understand the processes involved, both spatial and temporal measurements such as displacement rates and extents and changes in the surface topography are required. For these, remote sensing has been an integral method of landslide investigations for many decades, with several different techniques being used. For example, differential InSAR (Interferometric Synthetic Aperture Radar) enables detailed displacement analysis (Belardinelli et al., 2003), although signal decorrelation due to vegetation changes and sedimentological processes can prevent its use on active landslide surfaces. Passive space-borne imaging is becoming increasingly useful for landslide studies; panchromatic QuickBird satellite images can provide data at a ground resolution of 0.61 m and a repeat acquisition interval of down to 3-4 days (Niebergall et al., 2007).

Airborne and terrestrial geodetic LIDAR-scans (Light Detection and Ranging) are powerful tools for rapidly collecting high densities of precise and high-resolution 3D surface point coordinates. The quality of such point clouds is mainly influenced by the roughness and reflectivity of the surface, the measurement incidence angle and the observation range (Cheok et al., 2002; Lichti et al., 2005). From point clouds, high-resolution digital terrain models (DTMs) can be derived with accuracies in the submetre range and, in many cases, surface topography can be determined even in vegetated environments (Carter et al., 2007; van den Eeckhaut et al., 2007). Airborne images can provide important surface textural data, but photogrammetric DTMs are not usually as accurate and precise as airborne LIDAR-based DTMs (Baltsavias, 1999) and topography covered by dense vegetation cannot be reconstructed. Traditional airborne- and satellite-based remote sensing techniques are suitable

*Corresponding author: uwe.niethammer@geophys.uni-stuttgart.de

for landslide detection over areas of multiple square kilometres (Henry et al., 2002). For the Super-Sauze landslide studied here, the geomorphological evolution between 1950 and 1995 has been previously reconstructed from 6 airborne ortho-photographs (1 m ground resolution) and the 6 corresponding DTMs (15 m grid) (Weber and Herrmann, 2000). However, these data were of neither sufficient resolution nor repeat rate to resolve the evolution of small landslide features, such as fissure structures or small displacements, which can provide significant information on landslide dynamics.

Here, we investigate the use of radio controlled unmanned aerial vehicles (UAVs) for making such high-resolution measurements of landslides. The mini-UAV used has the advantage over traditional methods of allowing flexible deployments capable of acquiring both high-temporal and spatial resolution data. Radio controlled UAVs are less expensive with significantly lower operational costs than manned aircraft and, in recent years, mapping and remote sensing applications of UAV-systems have become more common (Everaerts, 2008). In the late 1970s the use of fixed wing remote controlled aircraft was investigated for motorised UAV photogrammetry experiments (Przybilla and Wester-Ebbinghaus, 1979) and, a quarter century later, Eisenbeiss et al. (2005) generated the first high-resolution digital terrain models (DTMs) using autonomously controlled helicopter UAVs.

Currently, a range of UAV-systems are in use, for example, motorised paragliders (Jütte, 2008), blimps (Gomez-Lahoz and Gonzalez-Aguilera, 2009), kites (Aber et al., 2002) and balloons (Fotinopoulos, 2004). However, many such systems are strongly affected by wind and could only be used infrequently or with difficulty in mountainous terrain. The availability of small high-quality digital cameras has now enabled radio controlled UAV-systems to represent affordable and practical remote sensing platforms, but data analysis challenges remain. For example, in order to utilise standard aerial photogrammetric processing software, UAV-acquired photographs should be ac-

quired in an optimal block configuration alignment, with internally stable camera-systems and minimal optical distortion. These restrictions have previously required the use of fixed-lens SLR cameras, expensive autopilot UAV navigation systems, and driven the development of dedicated photogrammetric software packages (Eisenbeiss et al., 2005).

In 2006, relatively stable quad-rotor helicopter systems became available as open source public domain projects (Mikrokooper, 2010). These systems are suitable for adaptation for use in alpine terrain and are low-cost when compared to commercially available UAV-systems. The goal of this study was to evaluate a UAV-system developed inhouse for landslide research. Here, we report on the potential and limitations of such a system, with preliminary results acquired from the Super-Sauze landslide, France. For Super-Sauze, a specific aim was to consider the UAV capability for imaging fissures and displacements on the landslide surface and to assess the subsequent image processing approaches for suitably georectifying the data. Fissures on the Super-Sauze landslide have not been mapped in detail in the past and, although this could be carried out by traditional surveying techniques, the large area of the landslide makes remote sensing an appealing technique for this task. With most fissures around 0.1 m in width, they are not resolvable in satellite data and only imaged infrequently by manned airborne systems. Thus, a UAV-system could offer the opportunity for regular data at a suitable resolution to detect changes in the fissure systems.

For full coverage of the landslide area, a plane-rectified orthomosaic of UAV imagery has been constructed and comparisons were made with a previously acquired traditional aerial ortho-photo. However, the use of plane-rectification can result in significant errors in regions of rugged topography, so we explore the application of close range photogrammetry software to enhance the results with a photogrammetric DTM. The close range software can handle convergent imagery from non-metric cameras much more readily than tradi-



Fig. 1. Quad-rotor system for remote sensing and its main characteristics.

tional aerial photogrammetry applications, facilitating DTM generation from UAV imagery. The quality of the digital terrain model is assessed by comparison with data from a terrestrial laser scanner (TLS).

2 UAV-system

The UAV-system developed in-house is a low-cost quad-rotor (Figure 1) that has been previously demonstrated to be capable of flying in difficult alpine terrain. When compared to conventional helicopters, quad-rotor systems are more stable with less in-flight vibration and have the mechanical advantage of not requiring a large, variable pitch rotor-unit. Our system was derived from an open source project (Mikrokopter, 2010) and enhanced for landslide studies. A robust aluminium flight frame was developed and the payload of the UAV-system was increased by using more powerful motors and some modifications of the flight control software. The UAV is stabilised by inertial measurement units (IMUs), including three acceleration sensors, three gyroscopes, a three-axis compass, and a pressure sensor, regulated by basic PID (proportional integral differential) loops. Flight endurance (hovering time of the UAV-system) is up to 12 min using a lithium polymer battery with a capacity of ~ 5.0 Ah. Overall UAV-development took about one man year in order to meet all the requirements for

operation in difficult alpine terrain. For image acquisition, a light weight low-cost digital compact camera (Praktica Luxmedia 8213) which supports manual camera settings was used. For all flights the sensitivity, zoom and the aperture were set to fixed values in order to achieve exposure times $< 1/800$ s and the largest visual angle. Without an auto-pilot navigation system to control image acquisition, all photographs were taken in an automatic image-series mode, acquiring one image every 3 s to ensure full coverage.

Our choice of a radio controlled UAV requires the presence of a highly skilled pilot and limits the operational area to the control range of a few hundreds of metres. There are also challenges related to the relatively small payloads, UAV-reliability and the restricted radiobandwidth for ground communication (Colomina et al., 2007). Although the use of an autonomously controlled UAV could significantly increase the operational area, autonomous control is less able to cope with unpredictable conditions such as gusty winds than an experienced operator. Furthermore, the use of autonomous UAVs is tightly regulated by civil aviation and security authorities, preventing their practical deployment. Our experience is that, particularly in alpine terrain, UAV-based image acquisition requires significant technical skill and a good UAV pilot.

3 Study area and data acquisition

The study was carried out on the Super-Sauze landslide (Figure 2), located on the north-facing slope of the Barcelonnette Basin (Southern French Alps). The landslide has developed in a torrential basin located in the upper part of Sauze torrent, on the left side downstream of the Ubaye valley and is one of several that have been persistently active since the 1970s. The landslide extends over a horizontal distance of 850 m between elevations of 2105 m at the crown, and 1740 m at the toe, with an average slope of 25° . The landslide mainly consists of



Fig. 2. Location of the study area and upward view of the Super-Sauze landslide. Picture was taken in summer 2006.

Jurassic black marls and has a total volume estimated at $750,000 \text{ m}^3$. Displacement velocities of the unstable slope range from 0.01 m to 0.4 m per day (Malet et al., 2002; Malet et al., 2005).

In October 2008 a UAV flight campaign was carried out covering the whole sliding area ($850 \times 250 \text{ m}$) of the Super-Sauze landslide, acquiring 1486 airborne photographs. Flight planning was carried out in-situ, where the area to be imaged could be observed and suitable locations for takeoff and landing could be identified. After launch, the quad-rotor was guided to an imaging flight altitude of $\sim 200 \text{ m}$ to provide a ground resolution of approximately 0.06 m per pixel. However, manual control of the UAV led to deviations in flight altitude between 100 m and 250 m, with corresponding ground resolutions between 0.03 m and 0.08 m. At the imaging altitude the UAV was hovered for about 30 s before vertical landing was initiated. After each flight, the area covered by the acquired photographs was verified on the camera directly. To enable the images to be georeferenced, 199 targets ($\sim 0.4 \times 0.6 \text{ m}$ rectangular coloured sheets to ensure visibility) were deployed over the landslide as ground control points (GCPs), and their centroid locations determined with differential GPS (DGPS). Deploying such a number of GCPs requires significant effort but was deemed an appropriate precaution for the initial assessment of UAV use over the landslide. Although long-term DGPS observations of these targets could al-

low for accurate displacements analysis at each GCP without the need for any UAV flight, such point data could potentially miss areas of interest and would not provide opportunity for the analysis of surface features such as fissures.

To enable a comparison of the UAV results with ground-based data, the topography of the toe-region of the slide was also mapped with a terrestrial laser scanner (TLS). The TLS instrument, an Optech ILRIS-3D, was used from a single site at a mean distance of 150 m from the toe (Figure 3A), producing an average data density of 23,000 points per m^2 in the image plane perpendicular to the line of sight, and a total of 3×10^6 points. The laser logged the last return from each line of sight in order to minimise undesired returns from vegetation. A stable area outside of the landslide was also included within the scanned area in order to georeference the TLS data. This georeferencing was carried out using a DTM acquired by airborne LIDAR on 22 May, 2007 and supplied by the company SINTEGRA. A traditional aerial ortho-photo from the same overflight, with a ground resolution of 0.2 m, was also provided by SINTEGRA and this has been used to determine displacements in conjunction with our UAV imagery.

4 Data processing

To allow comparison of the UAV data with these other sources, two processing procedures were carried out; generation of an orthomosaic and DTM construction of selected areas using close range photogrammetry techniques.

4.1 Ortho-mosaic

Previous work has shown that a straightforward plane image rectification approach can be used to produce ortho-mosaics suitable for displacement analysis, analysis of soil moisture, as well as an analysis of fissure structures (Niethammer et al., 2009). Here, the best 59 suitable UAV-acquired images were selected for mosaic processing. In a first step, optical (barrel) distortion was corrected using the

common third degree polynomial approach (Niethammer et al., 2009). In a second processing step, each image was rectified onto the plane GCP coordinates using one of four non-parametric rectification approaches (projective transformation, piecewise affine transformation and polynomial transformations of the 2nd and 3rd order). For each image, the rectification approach was selected in order to achieve the best result and depended on the relief variation and the number of observed ground control points. In irregular terrain these approximate transformations will not fully account for the effects of relief and residual misalignments within the ortho-mosaic have to be accepted. Finally, all rectified photographs were merged to a uniform high-resolution ortho-mosaic with a spatial resolution of 0.04 m. Automatic colour correction was carried out within OrthoVista software (OrthoVista, 2010) by applying a global tiling adjustment function which compares overlapping areas of images and then computes radiometric adjustment parameters for each image. All images were then merged into a seamless mosaic by an adaptive feathering image blending algorithm within OrthoVista (Figure 3A).

4.2 Photogrammetric DTM

DTM generation was carried out using VMS close range photogrammetry software (VMS, 2010) and an image matching algorithm, GOTCHA (Gruen Otto-Chau) from the University College London (Otto and Chau, 1989). Three regions of the Super-Sauze landslide were analysed (Figure 3), representing the areas best covered by multiple images. Two of these cover the upper reaches (DTM 1 and 2, Figure 3B and C, from 10 and 6 images respectively) and one covers the toe-region (DTM 3, Figure 3D, from 30 images). With TLS data only covering the toe-region, the DTM analysis was restricted to DTM 3 of the toe-area.

For DTM creation, observations of ground control points in the selected images were used

to calculate initial camera orientations (positions and pointing directions) using a preliminary estimated camera model defining principal distance only. The photogrammetric network produced was densified by incorporating additional tie points generated with GOTCHA. GOTCHA is a dense matching algorithm capable of generating patch-based (rather than featurebased) matches for each pixel of an image. The output was then reduced to a few thousand matches distributed over the images and a self-calibrating network adjustment was carried out in which the errors in the GCP positions, camera orientations and the camera model (principal distance, two radial and two tangential distortion components, principal point offsets and an affinity term) were simultaneously minimised. The optimised locations for the 16 GCPs in the toe-region (Figure 3A) showed RMS position residuals (from the original GCP coordinates) of 0.023, 0.018 and 0.019 m in x , y , and z . As is standard in rigorous close range photogrammetry procedures, VMS calculates the measurement precision within the photogrammetric network (Cooper and Robson, 2001). Average precisions for all the GCPs were 0.079, 0.079 and 0.185 m in x , y , and z , reflecting mean image residuals of 1.4 pixels in both x and y . Such precisions and residual magnitudes are poorer than it is possible to achieve with oblique photogrammetric networks of environmental scenes; for example, over similar observation distances, Chandler et al. (2002) obtained control point measurement precisions that were generally <20 mm for monitoring river channel change. However, such results generally require careful image acquisition planning and the use of an SLR camera, options that are not available when using small, manually controlled UAVs. Nevertheless, compact cameras have been shown to have sufficiently stable imaging geometries for photogrammetric work (Wackrow et al., 2007) and precisions of 20 mm may exceed the requirements of remote sensing of mass-movement phenomena.

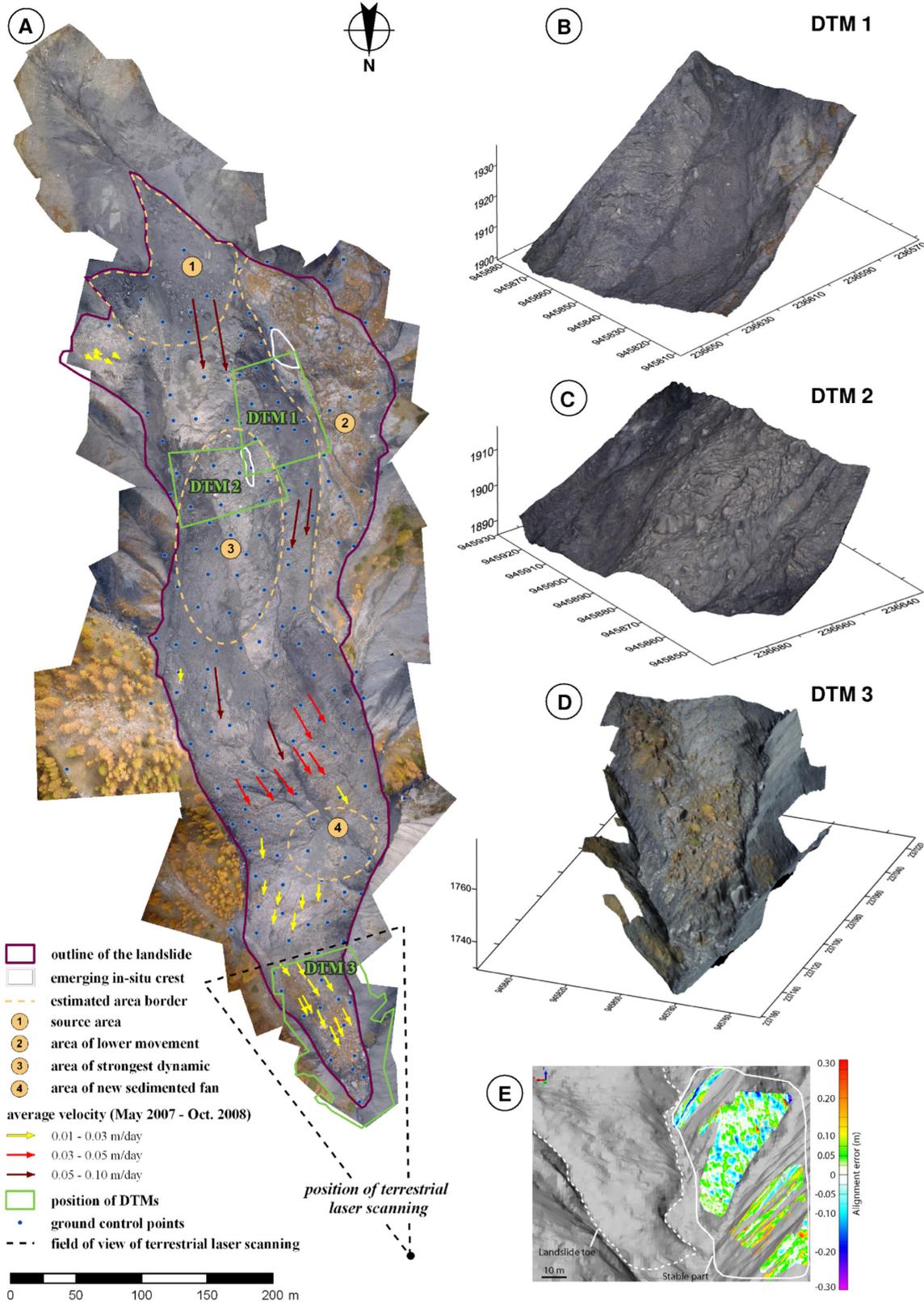


Fig. 3. A: Ortho-mosaic of the Super-Sauze landslide of October 2008 with ground control points (GCPs), horizontal surface displacement vectors colour coded by average movement velocity (May 2007-October 2008), different areas of dynamics and sedimentation, locations of the DTMs and the position and field of view of the terrestrial laser scanner survey. B-D: DTM 1-3 overlain with an ortho-image. E: Alignment error between the TLS DTM (October 2008) and airborne LIDAR DTM (May 2007) of the stable topography adjacent to the toe-region of the landslide.

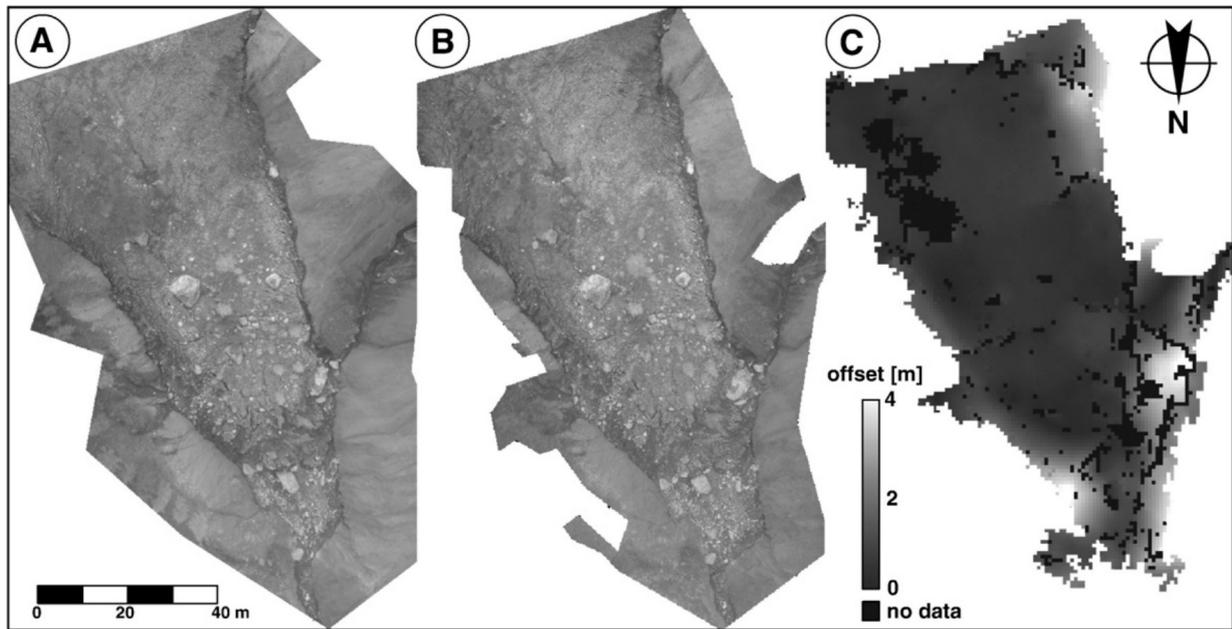


Fig. 4. Comparison between the ortho-mosaic (A) and a DTM-derived ortho-photo (B) of the toe-region. (C) Horizontal offsets determined by GOTCHA image matching.

For example, the precisions here are better than those required and achieved by James et al. (2007) who used a ground-based SLR for assessing lava flows. In future work, one of the easiest ways to increase the precision of the UAV-based DTMs would be to reduce the size of the GCP targets, which were not originally selected for use with VMS. The algorithms in VMS to automatically locate control target centroids are optimised for use with circular retroreflective targets (Robson and Shortis, 1998) and perform best when targets are 5 to 10 pixels across in images. Consequently, centres of the large, rectangular GCPs are not as accurately located within the images as they could be, and GCP residual errors would probably be reduced if smaller, circular targets were employed.

For the creation of DTM 3, 17 of the 30 images in the network overlapped suitably to contribute to the final surface model. After image matching, the output was refined by eliminating outliers, weak matches (e.g. points with significant residuals, poor precisions or matched in only two images) and points clearly influenced by vegetation cover. The resulting point clouds were then interpolated over a 0.2 m grid

using kriging in Surfer software (Surfer, 2010).

4.3 Terrestrial laser DTM

TLS data processing was performed using Polyworks software (Polyworks, 2010). The landslide surface is nearly free of vegetation. Trees, stumps and bushes were easily identifiable in the TLS point clouds and could be removed manually without any automatic filtering. In some minor parts of the landslide toe, sparse vegetation, such as grass (less than 0.1 m high) was present. Its effect on the elevation accuracy is smoothed by a 0.2 m grid interpolation, thus leading to a maximum error less than 0.1 m in elevation. However, many automatic filtering methods can be used to remove vegetation (Prokop and Panholzer, 2009). They are useful when vegetation is dense and the affected point cloud covers a large area which was not the case in the present study. Georeferencing was achieved by aligning stable topography adjacent to the landslide to equivalent data in the 2007 airborne LIDAR DTM (Figure 3E). This was carried out using an automated iterative closest point algorithm (ICP), with an initial manual alignment to ensure that the ICP did

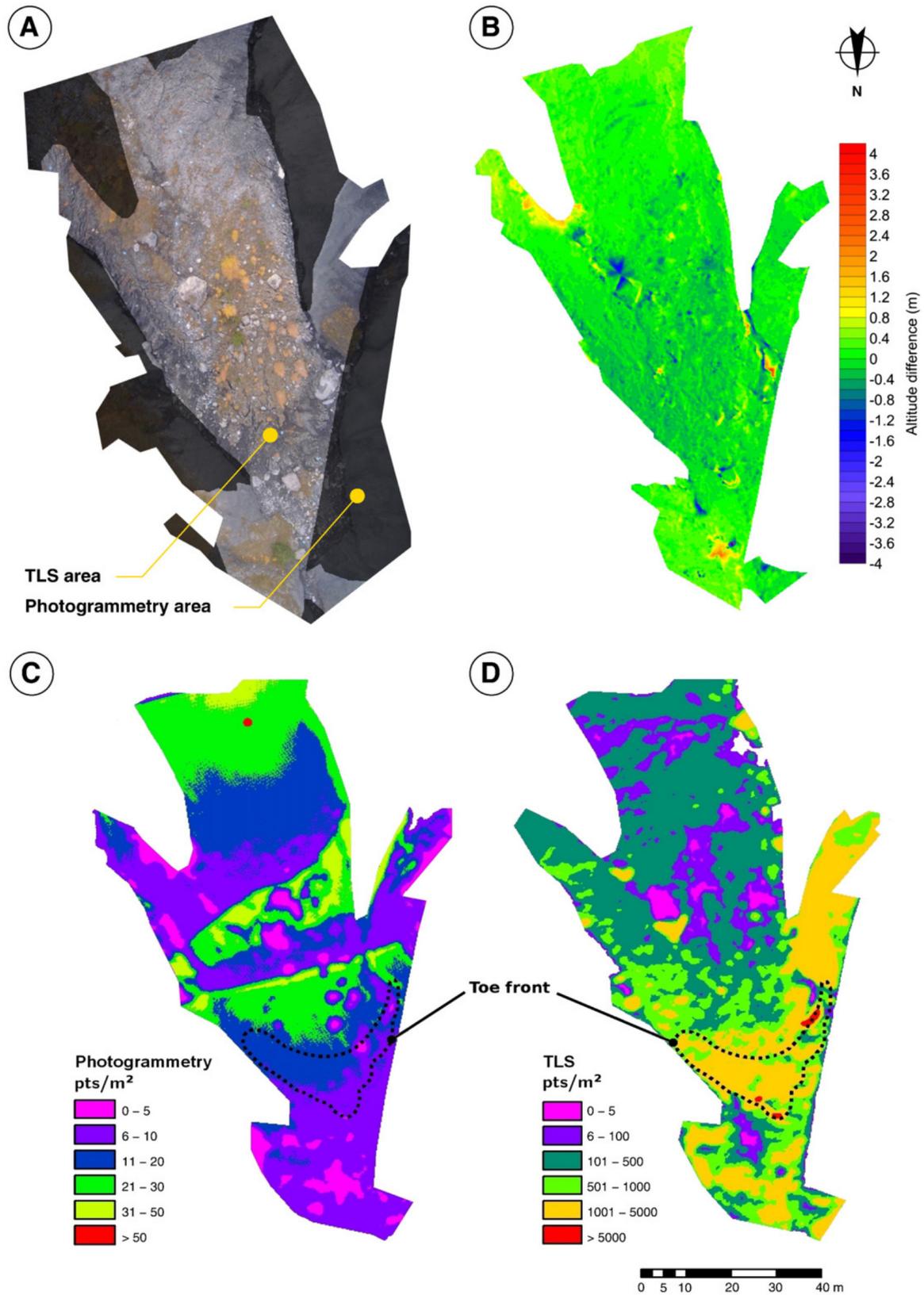


Fig. 5. DTM precision analysis at the toe-region; A: texture of the toe-region, B: elevation differences between TLS and photogrammetric DTM, C: point-density of the photogrammetry data, and D: point-density of the TLS data.

not converge on a local minimum (Lee et al., 1999). This georeferencing method is often applied in areas where access is difficult and where precise GCP reflectors cannot be readily installed, issues typical of landslide areas where slopes of more than 60° can be present (Travelletti et al., 2008; Oppikofer et al., 2009). After alignment, the mean 3D misfit in the stable area was quantified to be 0.05 m with a standard deviation of 0.16 m. The TLS data were then resampled and interpolated to generate a DTM with a 0.2 m grid.

5 Results and discussion

5.1 Ortho-mosaic and DTM quality

Errors within the georeferencing of the ortho-mosaic were quantified by comparison of all 199 GCP locations to their DGPS-measured locations. Within the boundary of the sliding area the mean error was 0.5 m, with a standard deviation of 0.57 m and a maximum misalignment of 3.9 m. However, large misalignments between 2.0 m and 3.9 m were only located at the margins of the landslide and, away from the boundary, accuracies can be considered to be ~ 0.5 m. In the toe-region, the ortho-mosaic could also be compared with UAV images ortho-rectified within VMS software using the photogrammetry-derived DTM 3 (Figure 3D). Horizontal offsets were determined by image matching (using GOTCHA) and show similar magnitudes to those of the full ortho-mosaic GCPs (Figure 4A), with the largest values located near the slide boundary.

The quality of the photogrammetric DTM was assessed by subtracting the overlapping TLS DTM (Figure 5A and B). In the vertical direction the RMS difference is 0.31 m although maximum deviations reach +3.44 to -4.08 m. The most significant errors are induced by some small trees and bushes, the effects of which could not be reliably removed from the photogrammetric DTM. However, vegetation correction on landslides has been managed by applying non-uniform vegetation-height surfaces (Martha et al., 2010), but such proce-

dures were not warranted in this work because the most significant vegetation errors were localised and occurred only at the margins of the DTMs. Further sizable differences occur on the steepest sides of large blocks. On the northern faces, where the block surface is nearly perpendicular to the TLS line of sight (Figure 3A), the TLS point cloud is much denser than the photogrammetric one. For example, Figure 5C and D shows that in the steep front of the toe, the point cloud of the TLS is two orders of magnitude denser than the point cloud of the photogrammetry.

However, the TLS can only observe one side of a block and the other, shadowed, side has to be interpolated. In shadow areas, the zero point density results in predicted elevations that reflect the interpolation technique used rather than any real measurements (Figure 6C). Nevertheless, such regions are observed fully by the UAV.

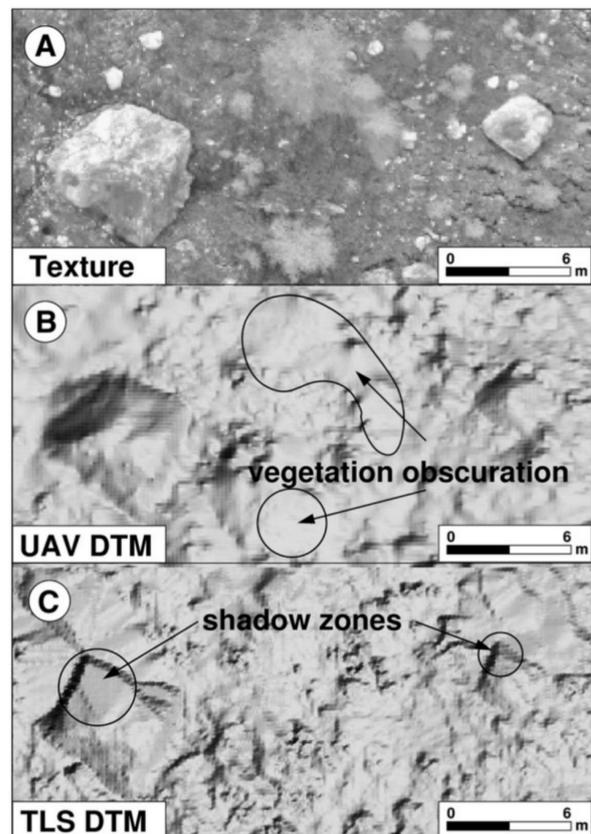


Fig. 6. DTM artefacts resulting from shadow zones in TLS data and vegetation obscuration in the UAV-based DTM.

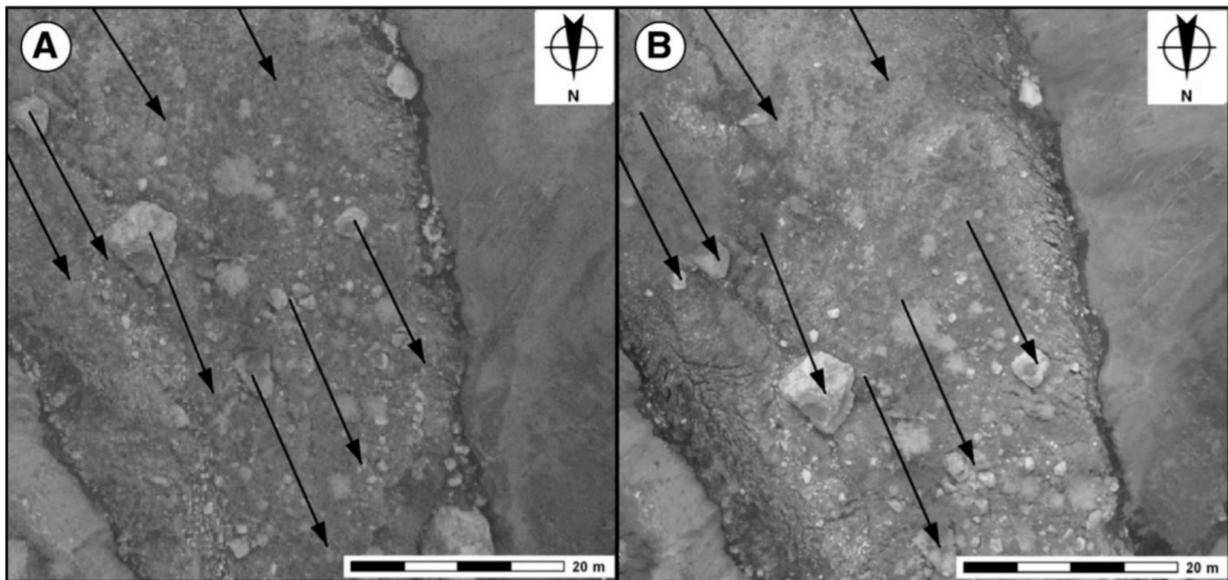


Fig. 7. Horizontal displacement analysis of the toe-region between the airborne ortho-photo of May 2007 (A) and the UAV-based ortho-mosaic of October 2008 (B).

In regions of low vegetation, such as grass or small shrubs, it is difficult to completely remove vegetation returns from the TLS point cloud and this can lead to some small artefacts in the TLS DTM (Figure 6A and C). On the other hand the photogrammetric approach can fail in areas of low image contrast or shadowing (for example, on some large blocks, Figure 6A and B). Dense vegetation cannot be penetrated and can give poor or no results during image matching (Figure 6A and B). It can be concluded that both DTMs must be regarded with caution. Each set of data and method can have advantages and limitations (Kerle, 2002).

5.2 Surface displacements

Our UAV-based displacement analysis of the Super-Sauze landslide was carried out by comparing the ortho-mosaic from October 2008 with the aerial ortho-photo from May 2007 in a geographical information system (GIS). Horizontal displacements were measured by identifying corresponding features and areas, such as rocks, stones and parts of vegetation patches in both images (Figure 7A and B). In principle, such analysis could be attempted by automated image matching (e.g. using correlation-based methods), but due to the resurfacing changes over the 17-month interval, this would be inef-

fective with the available image pair. However, automated image matching should be possible between UAV-derived orthomosaics acquired at shorter interval periods, and the use of more sophisticated object- or feature-based matching like scale-invariant feature transform (SIFT) could also be investigated (Lowe, 2004; Leprieux et al., 2008).

Horizontal displacements between 7 and $55 \text{ m} \pm 0.5 \text{ m}$, as well as varying displacement directions were detected (Figure 3A). However, several regions could not be successfully analysed due to a lack of clear surface features in both image sets (area 3 in Figure 3A). Comparisons were also prevented in areas of resurfacing by either new fine-grained sediments (the left part of area 3 and area 4, Figure 3A) or the rapid accumulation of both boulders and sediments (particularly in the source region, area 1, Figure 3A). Area 2 (Figure 3A) is characterised by very low velocities, and displacements could not be resolved in this area. Converting all identified displacements to daily average displacement rates gives the range of $0.01 \text{ to } 0.1 \text{ m} \pm 1 \text{ mm}$ per day for the period between May 2007 and October 2008. In the source area, displacement rates are up

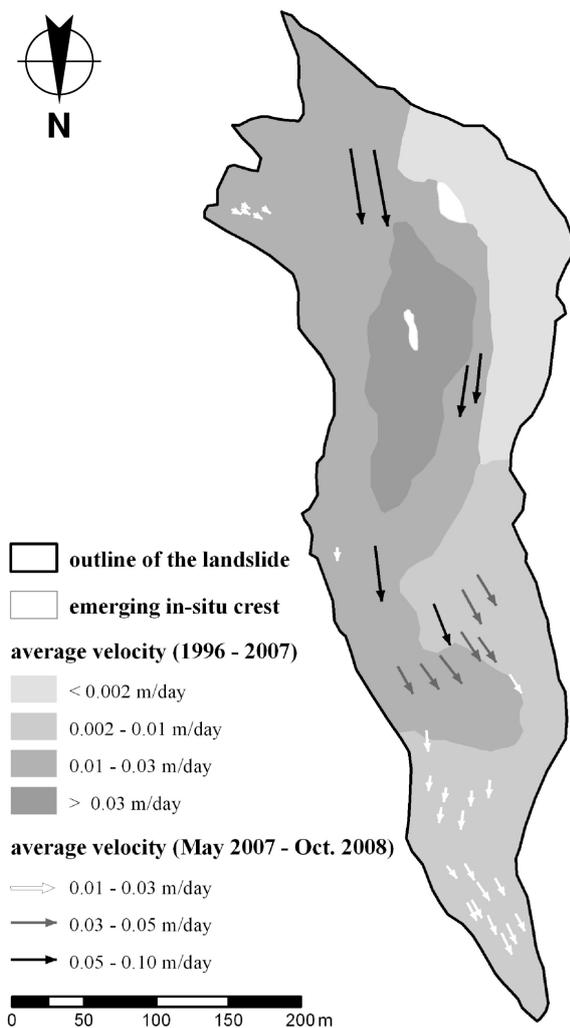


Fig. 8. Horizontal surface displacement vectors (May 2007-October 2008), colour coded by average movement velocity and long-term average movement velocity map (1996-2007), (Amitrano et al., 2007).

to three times greater than to the long-term average (Amitrano et al., 2007) (Figure 8) and approximately two times greater than the average in other regions of the landslide. This suggests that the May 2007 to October 2008 period represented (or encompassed) a period of significantly greater dynamics than normal for the Super-Sauze landslide.

Displacements of the Super-Sauze landslide have been measured on the ground since 1991 by GPS, geodetic and strain instruments (Amitrano et al., 2007). Between 1996 and 2004, average velocities were in the range of 0.002 to 0.03 m per day, but velocities up to 0.4 m per

day may be observed each year in the spring season (Amitrano et al., 2007). Monitoring of continuous displacements and pore water pressure have demonstrated that seasonal landslide accelerations are controlled by hydro-climatic conditions and that the long-term behaviour is characterised by continuous movements with a seasonal trend of two acceleration periods (spring and autumn) and two deceleration periods in summer and in winter (Malet and Maquaire, 2003). Such seasonal movement differences cannot be resolved over a 17 month-period. With the capability for providing regular surveys, UAVs could significantly assist in the spatial assessment of landslide displacement. However, despite the high-resolution of the imagery, the general georeferencing accuracy here of ~ 0.5 m (resulting from the use of plane-rectification approximations in constructing the ortho-mosaic), could restrict the usefulness of UAV mosaics collected over intervals much shorter than a year. Consequently, effort is required to streamline photogrammetric DTM creation from the UAV images, so that the full landslide area can be efficiently reconstructed and used to increase the accuracy of the orthorectification process.

5.3 Fissures

Many tension- and desiccation cracks and fissures are present on the surface of the Super-Sauze landslide. Tension fissures can be ~ 20 m long, up to 0.4 m wide and reach 1 m in depth (Grandjean et al., 2007). In October 2008 most of the fissures were ~ 0.1 m in width and are observable in the UAV ortho-mosaic (Figure 9).

Inspection of the fissures in the ortho-mosaic was carried out in a GIS. Despite the downhill movement of the landslide, superficial fissures arise in the same regions of the landslide each year, demonstrating that their locations are controlled by interactions with the paleotopography of the buried bedrock. At the Super-Sauze landslide, longitudinal, transverse, shear, and cross-shaped fissures (Figure 10) have been classified as the principal fissure types (Walter et al., 2009), with their positions

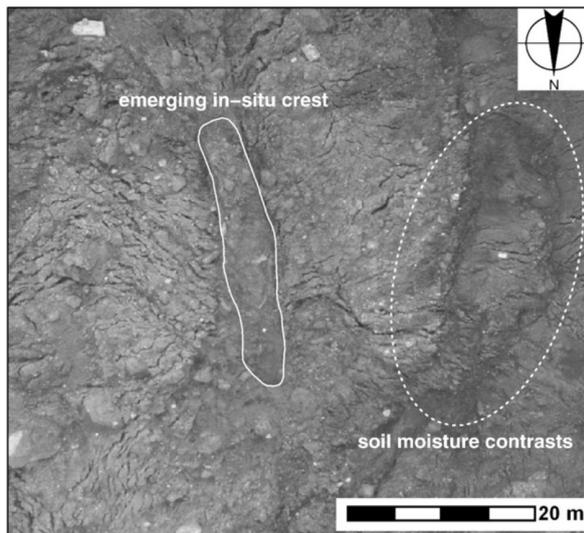


Fig. 9. Emerging in-situ crest, fissures (e.g. shear fissures) and soil moisture contrasts (detail of UAV-based ortho-mosaic of October 2008).

and orientations indicating different styles of deformation and development (Parise, 2003).

Similarities between the observed fissure patterns and those of glacial crevasses suggest a comparable genesis. Landslide dynamics may also be analogous to those of glaciers, resulting from either, or both, sliding and flowing (Kääb, 2002, Malet et al., 2005, Amitrano et al., 2007). Glacial dynamics and crevasses have been well studied (Wilhelm, 1975; Hambrey and Alean, 1994; Hambrey and Lawson, 2000) and crevasse distribution linked to changes in bedrock topography and the lateral bedrock boundaries. For example, longitudinal fissures occur in the direction of movement where an extension of the pathway is initiated. Transverse fissures occur in regions of changes in the decline of the subsurface bedrock slope (Wilhelm, 1975; Varnes, 1978; Hambrey and Alean, 1994). Marginal or shear fissures mostly occur at lateral boundaries between bedrock and the landslide material as result of the velocity gradient (Wilhelm, 1975). In Super-Sauze, such fissures also appear within the landslide material along emerging in-situ bedrock crests (Figures 9 and 10). More intricate fissures, such as crossshaped, may result from a combination of dynamics induced by complex bedrock topography.

Our observations support previous work indicating that stable buried bedrock crests directly affect the behaviour and dynamics of the entire landslide, and that sliding material is 'canalised' by the gullies between crests (Flageollet et al., 2000; Malet, 2003).

Regularly acquired UAV-derived fissure maps could provide valuable spatial data to augment ground-based studies aimed at understanding the links between the sliding material and the bedrock. For example, nano-seismic monitoring can now resolve the low amplitude signals of fracture processes within sedimentary landslide material (Walter et al., 2009 and this issue). Combining these data with high-resolution UAV-based snapshots of fissure distributions and their temporal development could provide valuable insights into the flow dynamics. Furthermore, soil moisture changes suggest to be detectable in contrast variations in UAV images of the landslide surface (Figure 9). This may indicate a promising new approach for high spatial resolution assessment of surface soil moisture, capable of assisting in the quantification of preferred infiltration pathways (for example through fissures), that remains a challenging problem (Krzeminska et al., 2009).

6 Conclusions

In this study it has been shown that radio controlled low-cost UAVs can deliver high-resolution remote sensing data on landslides. The proposed UAV-based remote sensing approach shows significant potential for the production of high-resolution ortho-mosaics and DTMs that enable the analysis of fissures and surface displacements. The manual data acquisition and processing procedures used require a significant amount of time, but progress is already being made to streamline data processing by using automated targetless structure-from-motion and multiview-stereo approaches to derive the topographic surface (Niethammer et al., 2010). Integrating such DTM generation (which includes camera model re-

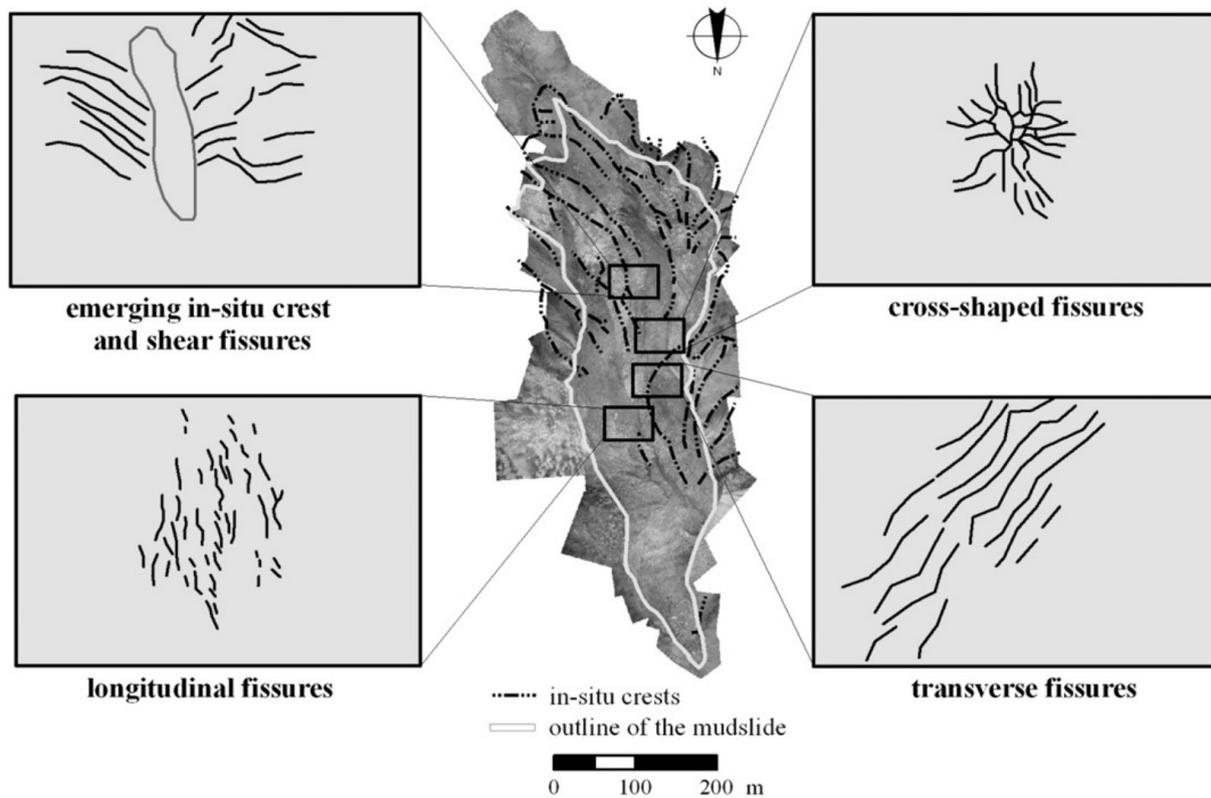


Fig. 10. Principal fissure types: shear fissures, cross-shaped fissures, longitudinal fissures and transverse fissures identified in the ortho-mosaic 2008 of Super-Sauze landslide.

finement), and possibly also vegetation removal, into the ortho-mosaic pipeline, will significantly reduce errors in the final ortho-mosaic of the Super-Sauze landslide.

The high-resolution of the UAV images and the resulting orthomosaic allowed analysis of fissure patterns and different arrangements (longitudinal, transverse, shear and cross-shaped fissure distributions) were identifiable. The fissures are comparable to glacial crevasses where similar dynamics take place and their patterns reflect the interactions between the sliding material and the bedrock. The UAV imagery thus supports prior observations that buried bedrock crests directly affect the behaviour and dynamics of the entire landslide (Malet, 2003).

The comparison between the plane-rectified UAV ortho-mosaic and an earlier ortho-photo revealed horizontal displacements between 7 and $55 \text{ m} \pm 0.5 \text{ m}$, representing daily average displacements rates in the range of 0.1 to

$0.01 \text{ m} \pm 1 \text{ mm}$ per day, between May 2007 and October 2008. Despite the high-resolution of the imagery, errors resulting from the plane-rectification degrade the georeferencing accuracy to $\sim 0.5 \text{ m}$ over most of the landslide. Although acceptable when calculating displacement rates over periods of a year, errors of this magnitude would be restrictive for analyses over shorter intervals, and hence could limit the usefulness of the UAV's capability to regularly acquire data.

Consequently, ortho-rectification using photogrammetric DTMs is advised. A DTM of the toe-region of the Super-Sauze landslide, constructed using close range photogrammetry software, has been compared with TLS data of the same area giving an RMS of height difference values of 0.31 m. Although TLS-based point clouds are denser than photogrammetric derived point clouds, TLS data are subject to shadowing due to the oblique view point. Such shadows are minimised in nadir UAV-acquired

images and a large scale data acquisition can be obtained more effectively by UAV.

Acknowledgements

We thank all colleagues from the OMIV project (Observatoire des Instabilités de Versants) for the helpful discussions and their support in the field. The authors are grateful to Jean-Philippe Malet (School and Observatory of Earth Sciences, University of Strasbourg) for providing several datasets. Our thanks also go to Eberhard Claar (Institute for Geophysics, Univer-

sität Stuttgart) who built significant components of the quad-rotor systems. The work was supported by the DFG within the project FOR 581 'Natural Slopes' and by the European Commission within the Marie Curie Research Training Network Mountain Risks: from prediction to management and governance (MCRTN-035798). Prof. S. Robson and Prof. J. P. Muller (UCL, London) are thanked for ongoing support through the use of VMS and the Gotcha stereo matching engine respectively. We also like to thank the reviewers for their constructive comments and suggestions.

References

- Aber, J.S., Aber, S.W., Pavri, F., 2002. Unmanned small-format aerial photography from kites for acquiring large scale, high-resolution, multiview-angle imagery. Proceedings of Pecora 15, Land Satellite Information IV/ISPRS Conference Commission I/FIEOS, Denver, CO, USA.
- Amitrano, D., Gaffet, S., Malet, J.-P., Maquaire, O., 2007. Understanding mudslides through micro-seismic monitoring: the Super-Sauze (South-East French Alps) case study. Bull. Soc. Géol. Fr. 178 (2), 149-157.
- Baltsavias, E.P., 1999. A comparison between photogrammetry and laser scanning. ISPRS J. Photogramm. Remote Sensing 54, 83-94.
- Belardinelli, M.E., Sandri, L., Baldi, P., 2003. The major event of the 1997 UmbriaMarche (Italy) sequence: what could we learn from DInSAR and GPS data? Geophys. J. Int. 153 (1), 242-252.
- Carter, W.E., Shrestha, R.L., Slatton, K.C., 2007. Geodetic laser scanning. Phys. Today 60 (12), 41-47.
- Chandler, J., Ashmore, P., Paola, C., Gooch, M., Varkaris, F., 2002. Monitoring riverchannel change using terrestrial oblique digital imagery and automated digital photogrammetry. Ann. Assoc. Am. Geogr. 92, 631-644.
- Cheok, G.S., Leigh, S., Rukhin, A., 2002. Technical report: calibration Experiments of a Laser Scanner. US National Institute of Standards and Technology, Report No NISTIR, p. 6922.
- Colomina, I., Aigner, E., Agea, A., Pereira, M., Vitoria, T., Jarauta, R., Pascual, J., Ventura, J., Sastre, J., Brechbühler, G.P., Derani, A., Hasegawa, J., 2007. The uVISION project for helicopter UAV photogrammetry and remote-sensing. Proceedings of the 7th Geomatic Week, Barcelona, Spain.
- Cooper, M.A.R., Robson, S., 2001. Theory of close range photogrammetry. In: Atkinson, K.B. (Ed.), Close Range Photogrammetry and Machine Vision. Whittles Publishing, Caithness, p. 371.

Van den Eeckhaut, M.V., Poesen, J., Verstraeten, G., Vanacker, V., Nyssen, J., Moeyersons, J., Beek, L.P., Vandekerckhove, L., 2007. Use of LIDAR-derived images for mapping old landslides under forest. *Earth Surf. Process. Landforms* 32 (5), 754-769.

Eisenbeiss, H., Lambers, K., Sauerbier, M., 2005. Photogrammetric recording of the archaeological site of Pinchango Alto (Palpa, Peru) using a mini helicopter (UAV). *Proceedings of the 33rd CAA Conference, Tomar, Portugal, 21-24 March 2005*.

Everaerts, J., 2008. The use of unmanned aerial vehicles (UAVs) for remote sensing and mapping. *The International Archives of the Photogrammetry. Remote Sensing Spatial Information Sciences XXXVII Part B1, Beijing 2008*.

Flageollet, J.-C., Malet, J.-P., Maquaire, O., 2000. The 3D structure of the Super Sauze earthflow: a first stage towards modelling its behaviour. *Phys. Chem. Earth* 25 (9), 785-791.

Fotinopoulos, V., 2004. Balloon photogrammetry for archaeological surveys. *International Archives of the Photogrammetry. Remote Sensing and Spatial Information Sciences, XX ISPRS Congress, Istanbul, Turkey, XXXV-B5, pp. 504-507*.

Gomez-Lahoz, J., Gonzalez-Aguilera, D., 2009. Recovering traditions in the digital era: the use of blimps for modelling the archaeological cultural heritage. *J. Archaeol. Sci.* 36 (1), 100-109.

Grandjean, G., Malet, J.-P., Bitri, A., Méric, O., 2007. Geophysical data fusion by fuzzy logic for imaging the mechanical behaviour of mudslides. *Bull. Soc. Géol. Fr.* 178 (2), 127-136.

Hambrey, M., Alean, J., 1994. *Glaciers*. Cambridge University Press, New York.

Hambrey, M.J., Lawson, W.J., 2000. Structural styles and deformation fields in glaciers: a review. In: Maltman, A.J., Hubbard, B., Hambrey, M.J. (Eds.), *Deformation of Glacial Materials: Geol. Soc. Spec. Publ.*, 176, pp. 59-83.

Henry, J.-B., Malet, J.-P., Maquaire, O., Grussenmeyer, P., 2002. The use of small-format and low-altitude aerial photos for the realization of high-resolution DEMs in mountainous areas: application to the Super-Sauze earth-flow (Alpes-de-Haute-Provence, France). *Earth Surf. Process. Landforms* 27 (12), 1339-1350.

James, M.R., Pinkerton, H., Robson, S., 2007. Image-based measurement of flux variation in distal regions of active lava flows. *Geochem. Geophys. Geosyst.* 8, Q03006. doi:10.1029/2006GC001448.

Jütte, K., 2008. Vergleich verschiedener low-cost Luftbildaufnahmesysteme sowie Einsatz von Drohnen: Grenzen und Möglichkeiten. Bayerische Landesanstalt für Wald und Forstwirtschaft, *Der gepixelte Wald - Fachtagung zur Forstlichen Fernerkundung*.

Kääb, A., 2002. Monitoring high-mountain terrain deformation from repeated air- and spaceborne optical data: examples using digital aerial imagery and ASTER data. *ISPRS J. Photogrammetry Remote Sensing* 57, 39-52.

- Kerle, N., 2002. Volume estimation of the 1998 flank collapse at Casita volcano, Nicaragua: a comparison of photogrammetric and conventional techniques. *Earth Surf. Process. Landforms* 27, 759-772.
- Krzeminska, D.M., Bogaard, T.A., Debieche, T.-H., Marc, V., Ponton, J., Malet, J.-P., 2009. Quantitative analysis of preferential flow during small scale infiltration tests on an active mudslide, French Alps. In: Malet, J.-P., Remaitre, A., Boogard, T. (Eds.), *Proceedings of the International Conference on Landslide Processes: From Geomorphologic Mapping to Dynamic Modelling*. CERG Editions, Strasbourg, pp. 151-156.
- Lee, B.U., Kim, C.M., Park, R.H., Nurre, J.H., Corner, B.R., 1999. Error sensitivity of rotation angles in the ICP algorithm. *SPIE Proc. A* 3640, 146-156.
- Leprince, S., Berthier, E., Ayoub, F., Delacourt, C., Avouac, J.-P., 2008. Monitoring earth surface dynamics with optical imagery. *EOS Transactions American Geophysical Union* 89 (1).
- Lichti, D.D., Gordon, S.J., Tipdecho, T., 2005. Error models and propagation in directly georeferenced terrestrial laser scanner networks. *J. Surv. Eng.* 131 (4), 135-142.
- Lowe, D., 2004. Distinctive image features from scale-invariant keypoints. *International J. Computer Vision* 60 (2), 91-110.
- Malet, J.-P., Maquaire, O., Calais, E., 2002. The use of Global Positioning System techniques for the continuous monitoring of landslides: application to the Super-Sauze earthflow (Alpes-de-Haute-Provence, France). *Geomorphology* 43 (1-2), 33-54.
- Malet, J.-P., 2003. Les glissements de type écoulement dans les marnes noires des Alpes du Sud. Morphologie, fonctionnement et modélisation hydro-mécanique. Phd thesis, Université Louis Pasteur, Strasbourg, 364 pp.
- Malet, J.-P., Maquaire, O., 2003. Black marl earthflows mobility and long term seasonal dynamic in southeastern France. In: Picarelli, L. (Ed.), *Proceedings of the International Conference on Fast Slope Movements: Prediction and Prevention for Risk Mitigation*. Bologna, Patron Editore, pp. 333-340.
- Malet, J.-P., van Asch, Th.W.J., van Beek, R., Maquaire, O., 2005. Forecasting the behaviour of complex landslides with a spatially distributed hydrological model. *Nat. Hazards Earth Syst. Sci.* 5 (1), 71-85.
- Martha, T.R., Kerle, N., Jetten, V.G., van Westen, C.J., Kumar, V., 2010. Landslide volumetric analysis using Cartosat-1-derived DEMs. *IEEE Geosci. Remote Sensing Lett.* 7 (3), 582-586.
- Mikrokopter, 2010. Mikrokopter Open Source Quad-Rotor Homepage. <http://www.mikrokopter.com>. (accessed 01.08.2010).
- Niebergall, S., Loew, A., Mauser, W., 2007. Object-orientated analysis of very highresolution QuickBird data for mega city research in Delhi/India. *Proceedings of the Urban Remote Sensing Joint Event, Paris*. ISBN: 1-4244-0712-5. 8 pp., IEEE 07EX1577.

Niethammer, U., Rothmund, S., Joswig, M., 2009. UAV-based remote sensing of the slowmoving landslide Super-Sauze. In: Malet, J.-P., Remaitre, A., Boogard, T. (Eds.), Proceedings of the International Conference on Landslide Processes: From Geomorphologic Mapping to Dynamic Modelling. CERG Editions, Strasbourg, pp. 69-74.

Niethammer, U., Rothmund, S., James, M.R., Travelletti, J., Joswig, M., 2010. UAV-based remote sensing of landslides. *Int. Arch. Photogram. Rem. Sens. Spatial Inf. Sciences*, vol. XXXVIII. ISPRS Comm. V., Newcastle-upon-Tyne, U.K.

Oppikofer, T., Jaboyedoff, M., Blikra, L., Derron, M.-H., Metzger, R., 2009. Characterization and monitoring of the Aknes rockslide using terrestrial laser scanning. *Nat. Hazards Earth Syst. Sci.* 9 (3), 1003-1019.

OrthoVista, 2010. Official OrthoVista Software Homepage. <http://www.orthovista.com>. (accessed 01.08.2010).

Otto, G.P., Chau, T.K.W., 1989. Region-growing algorithm for matching of terrain images. *Image Vision Comput.* 7 (2), 83-94.

Parise, M., 2003. Observation of surface features on an active landslide, and implications for understanding its history of movement. *Nat. Hazards Earth Syst. Sci.* 3, 569-580.

Polyworks, 2010. Official Invometric Software Homepage. <http://www.inovmetric.com>. (accessed 01.08.2010).

Prokop, A., Panholzer, H., 2009. Assessing the capability of terrestrial laser scanning for monitoring slow moving landslides. *Nat. Hazards Earth Syst. Sci.* 9, 1921-1928.

Przybilla, H.-J., Wester-Ebbinghaus, W., 1979. Bildflug mit ferngelenktem Kleinflugzeug. *Bildmessung und Luftbildwesen Zeitschrift fuer Photogrammetrie Fernerkundung* 47 (5), 137-142.

Robson, S., Shortis, M.R., 1998. Practical influences of geometric and radiometric image quality provided by different digital camera systems. *Photogrammetric Record* 16(92),225-248.

Surfer, 2010. Golden Software Homepage. <http://goldensoftware.com>. (accessed 01.08.2010).

Travelletti, J., Oppikofer, T., Delacourt, C., Malet, J.-P., Jaboyedoff, M., 2008. Monitoring landslide displacements during a controlled rain experiment using a long-range terrestrial laser scanning (TLS). *Int. Arch. Photogramm. Remote Sens.* 37 (Part B5), 485-490.

Varnes, D.J., 1978. Slope movement types and processes. In: Schuster, R.L., Krizek, R.J. (Eds.), *Landslides – Analysis and Control: Rep. Natl. Res. Council. Transp. Res. Board*, vol. 176, pp. 11-33.

VMS, 2010. Official VMS Software Homepage. <http://www.geomsoft.com>. (accessed 01.08.2010).

Wackrow, R., Chandler, J.H., Bryan, P., 2007. Geometric consistency and stability of consumer-grade digital cameras for accurate spatial measurement. *Photogrammetric Record* 22 (118), 121-134.

Walter, M., Niethammer, U., Rothmund, S., Joswig, M., 2009. Joint analysis of the SuperSauze (French Alps) mudslide by nanoseismic monitoring and UAV-based remote sensing. *EAGE First Break* 27 (8), 75-82.

Walter, M., Arnhardt, C., Joswig, M., this issue. Seismic monitoring of rockfalls, subsurface fracture processes, and superficial fissure development at the SuperSauze, French Alps, mudslide. *Eng. Geol.*

Weber, D., Herrmann, A., 2000. Contribution of digital photogrammetry in spatiotemporal knowledge of unstable slopes: the example of the Super-Sauze landslide (Alpes-de-Haute-Provence, France). *Bull. Soc. Géol. Fr.* 171 (6), 637-648.

Wilhelm, F., 1975. *Schnee- und Gletscherkunde*. Walter de Gruyter Press, Berlin, New York.

Image-based mapping of surface fissures for the investigation of landslide dynamics

A. STUMPF^a, J-P. MALET^{b*}, N. KERLE^c, U. NIETHAMMER^d, S. ROTHMUND^d

^aLaboratoire Image, Ville, Environnement, University of Strasbourg, France

^bSchool and Observatory of Earth Science, University of Strasbourg, France

^cFaculty of Geo-Information Science and Earth Observation, University of Twente, NL

^dInstitute for Geophysics, University of Stuttgart, Germany

Abstract

The development of surface fissures is an important indicator for understanding and forecasting slope movements. Landslide investigations therefore frequently include the elaboration and interpretation of maps representing their spatial distribution, typically comprising intensive field work and instrumentation. It is only recently that aerial photography with sub-decimetre spatial resolution is becoming more commonly available and opens a window to analyse such features from a remote sensing perspective. While these data are in principle helpful to elaborate maps from image interpretation techniques, there is still no image processing technique available to extract efficiently these geomorphological features. This work proposes a largely automated technique for the mapping of landslide surface fissures from very-high resolution aerial images. The processing chain includes the use of filtering algorithms and post-processing of the filtered images using object-oriented analysis. The accuracy of the resulting maps is assessed by comparisons with several expert maps in terms of affected area, fissure density and fissure orientation. Under homogenous illumination conditions, true positive rates up to 65% and false positive rates generally below 10% are achieved. The resulting fissure maps provide sufficient detail to infer mechanical processes at the slope scale and to prioritize areas for more detailed ground investigations or monitoring.

1 Introduction

Observations of features and structural patterns of earth surface landforms can reveal information on the origin and mechanisms controlling the geomorphological processes. Structural geology and geomorphology have developed comprehensive concepts to delineate geomorphological units and structure types from remote sensing images, and infer about mechanical processes without necessarily measuring displacement, deformation or the applied forces directly (Melton, 1959; Davis and Reynolds, 1996; Passchier and Trouw, 2005; Pollard and Fletcher, 2005). Surface discontinuities observed in rocks and sediments have proven to be valuable indicators of the deformation history and stress pattern of the slope. For landslide analysis, their observation and inter-

pretation can contribute to a better understanding of the controlling physical processes and help in the assessment of the related hazards (McCalpin, 1984; Fleming and Johnson, 1989; Parise, 2003). In hard-rock slopes, the analysis of structural discontinuities (faults, bedding planes, joints, and fractures) allows us to characterize potentially unstable areas (Hoek and Bray, 1981; Matheson, 1983; Priest, 1993; Selby, 1993; Günther et al., 2004; Jaboyedoff et al., 2004; Glenn et al., 2006). In soft-rock slopes and sediments, the analysis of surface fissures may indicate the development of future failures (Krauskopf et al., 1939; Shreve, 1966; Chowdhury and Zhang, 1991; Abramson et al., 2001; Khattak et al., 2010) and is often considered as a geo-indicator of the activity stage of a landslide. In sediments, the surface fissure characteristics also influence water in-

*Corresponding author: jeanphilippe.malet@unistra.fr

filtration and drainage, which in turn affect the ground-water system and the kinematic response of slopes to hydrological events (Malet et al., 2003, 2005a; van Asch et al., 2009).

Maps of surface deformation features can be obtained by extensive field surveys either through the direct visual observation of the topography (Fleming et al., 1999; Meisina, 2006) or through the indirect measure of seismic wave propagation in tomography setups (Grandjean et al., 2011; Bièvre et al., 2012). Relatively large fissures on landslides may also be discernible in Very-High-Resolution (VHR) spaceborne images (Glenn et al., 2006; Youssef et al., 2009), but typically, those structures reach widths in the decimetre-range and at present only airborne photographs provide sufficient detail for their detection in the centimetric range. Recent studies (Eisenbeiss, 2009; Niethammer et al., 2011a) have shown that VHR images acquired from unmanned aerial vehicles (UAVs) are cost-efficient data sources for the monitoring of landslide surfaces with subdecimetric image resolution. Especially small UAVs with payloads below 5 kg and operating altitudes below 2000 m are expected to be employed much more frequently in coming years (Frost and Sullivan Co., 2007) though more specific regulations for their operational use are being discussed at national and international levels (Prats et al., 2012; Watts et al., 2012).

Visual interpretation of VHR imagery is a classical method in geomorphology, but it remains subjective, and rather impractical for repetitive observations or the inspection of large areas. An increasing number of studies therefore targeted the development of automated techniques to extract relevant features from imagery (Graham et al., 2010; Martha et al., 2010; Stumpf and Kerle, 2011). Although the detection and extraction of linear features is a fundamental operation in digital image processing (Quackenbush, 2004; Mendonca and Campilho, 2006; Papari and Petkov, 2011), relatively few studies have explored the application of automatic approaches for the mapping of geomorphologically relevant linear features (Baruch and Filin, 2011; Shruthi et al., 2011).

Considering the increasingly widespread availability of subdecimetre resolution images from UAVs and other airborne platforms, this study targeted the development of a semi-automatic image analysis technique to support geomorphologists in the detection, mapping and characterization of landslide surface fissures from VHR aerial images. In this context, the term "semi-automatic" expresses that the technique requires user input to be adapted for different image types and environmental settings. The developed method is based on a combination of Gaussian directional filters, mathematical morphology and objectoriented image analysis (OOA) and was tested on a set of multitemporal VHR images acquired at the Super-Sauze landslide (southeast French Alps). The obtained results were compared to manual mappings carried out by experts combining image interpretation and field surveys.

2 Types of surface fissure observed on landslides

Detailed observations of landslide surface fissures were provided by Krauskopf et al. (1939) who adapted analogies from structural geology for their interpretation and distinguished between strike-slip structures, normal faults, graben structures and compression structures. In addition, Ter-Stephanian (1946) noticed the mechanical significance of surface fissures and elaborated a classification scheme relating fissure morphology and location within the landslide mass to corresponding mechanical processes. This included a first-order differentiation between upper extension, side friction, central compression, and lower creep-on cracks. Although some authors used similar classification schemes (Bombard, 1968), the adopted terminology varies among different authors and affected lithologies (Fleming and Johnson, 1989; Cruden and Varnes, 1996; Fleming et al., 1999; Walter et al., 2009), and the terms crack and fissure are often used synonymously to refer to a variety of surface discontinuities.

Here, fissure is adopted as a generic term for open fractures on the topographic surface of a natural slope. At first instance, transversal, longitudinal and diagonal fissures are distinguished according to their main orientation axes relative to the dip of the slope. This terminology can be used ad hoc to classify fissures solely based on geometric properties observed in the field or in an image. A more refined mechanical classification such as provided in Ter-Stephanian (1946) will generally require considerations of the fissure patterns, the involved material and the local geometry of the slip surface. The term crack is used in this manuscript when referring to genetic processes described within classical fracture mechanics (Anderson, 2005). It should be noted that the term crack is also often adopted to refer to shrinking-swelling induced fractures (Malet et al., 2003) which are not the objective of this study.

Classical fracture mechanics postulates tensile opening, sliding and tearing as the three basic modes for crack propagation (Fig. 1a). The concept has been developed for brittle material but is also adopted to explain fracturing of plastic materials at high deformation rates (Schulson and Duval, 2009). Surface fissures may develop from a combination of all three modes, whereas in practice, considering the relatively low tensile fracture toughness of most geomaterials (Backers, 2004; Ke et al., 2008; Schulson and Duval, 2009), tensile fracturing can be expected to dominate the formation of fissures at the free surfaces of a landslide. However, interpreting tension cracks as a direct indicator for a purely tensile stress regime may often fall too short. In fact, tensile fracturing may also result from relaxation of tensile stresses that originate from deformation induced by shearing and compression as well (Wang and Shrive, 1995). A mechanical interpretation and classification of the fissures must therefore consider the fissure pattern, material and landslide geometry.

Fig. 1b-d illustrates three typical fissure patterns that are frequently used as geoindicators of specific deformation processes in the above-cited studies. One commonly observed

example for such patterns is the formation of en-echelon fissure arrays (Fig. 1c), often also termed Riedel shears (Riedel, 1929). They accommodate tensile stress and shear stress typically resulting from shear in the bounding zone of blocks moving with different displacement rates. Certain patterns such as arrays of transversal fissures (Fig. 1b) are typically associated with tension in the steeper upper slopes, whereas fissures resulting from compression and lateral extension (Fig. 1d) are more typically associated with gentler slopes in the transit and accumulation zones of landslides (Sowers and Royster, 1978). For landslides with a complex geometry, the position of those fissure patterns may however deviate considerably from this simple scheme (Niethammer et al., 2011a).

3 Study site and data

The Super-Sauze mudslide is an active slow-moving landslide located in the Barcelonnette Basin in the Southern French Alps (Fig. 2) that developed in weathered black marls in the 1960s, and features highly variable displacement rates (from 0.01 to 0.40 m day⁻¹) controlled by the local hydrological conditions (Malet et al., 2005a). The landslide measures 950 m from the main scarp to the toe, and is up to 150 m wide. The moving mass has a clay-rich matrix containing up to 30% coarse gravel as well as larger boulders and blocks (Malet et al., 2005a). The surface displays the signs of deformation in the form of ridges, bulges, lobes and fissures but also markers of surface erosion such as rills and small gullies. Unlike surrounding stable areas the landslide surface is largely bare and only at a few locations, especially at its toe, cushion plants form small vegetation patches. Fissure widths of 0.01-0.40 m, lengths of more than 1.0 m and depths of up to 1.5 m (Espinosa, 2009) can be observed in the field (Fig. 4b). During the last 15 years, the landslide has been investigated through numerous monitoring campaigns including in-situ geophysical measurements, terrestrial and airborne LiDAR (light detection and ranging) and the acquisition of VHR optical imagery.

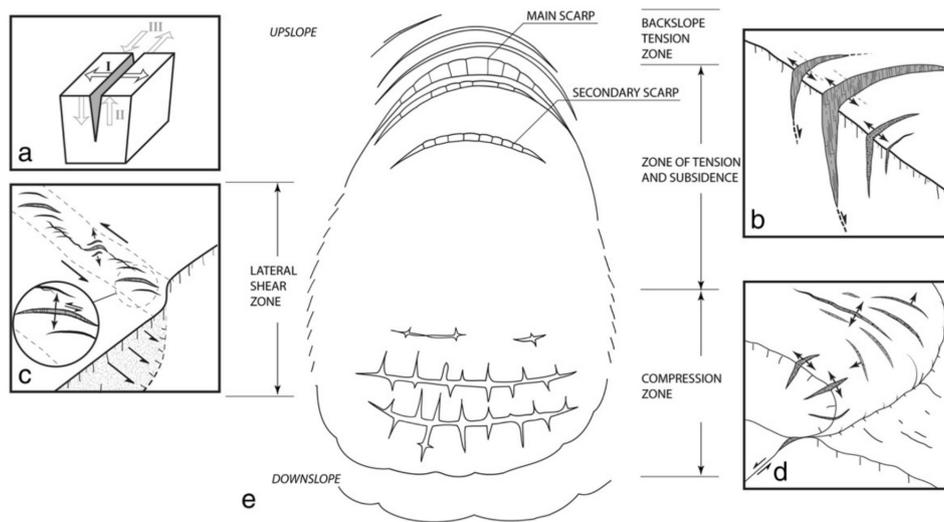


Fig. 1. Generic types of surface fissures and their typical spatial occurrence within a landslide mass. (a) Modes of fracture propagation: mode I (opening), mode II (sliding) and mode III (tearing). (b) Fissures developing predominately in mode I and resulting from tensile stress. (c) Fissures developing predominately in mode I and resulting from shear stress. (d) Fissures developing predominately in mode I resulting from compressive stress and lateral expansion. (e) Division of a landslide mass (Sowers and Royster, 1978).

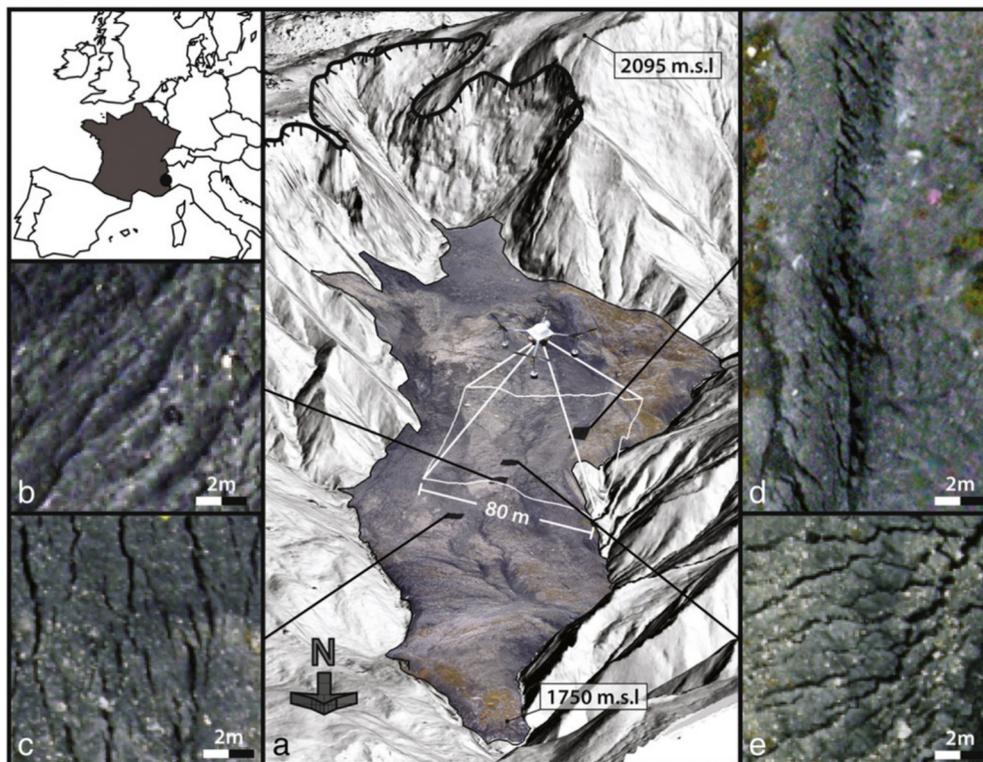


Fig. 2. Oblique view of the Super-Sauze landslide combining a hillshade image derived from an airborne LiDAR DTM (July 2009) and a UAV image (October 2008). (a) Main scarp (hashed black line), transport and accumulation zone (black outline), and area of interest for the multi-temporal analysis (white square). UAV image subsets show (b) compression ridges, (c) longitudinal fissures, (d) diagonal fissures at the boundary of the active part, and (e) transversal fissures.

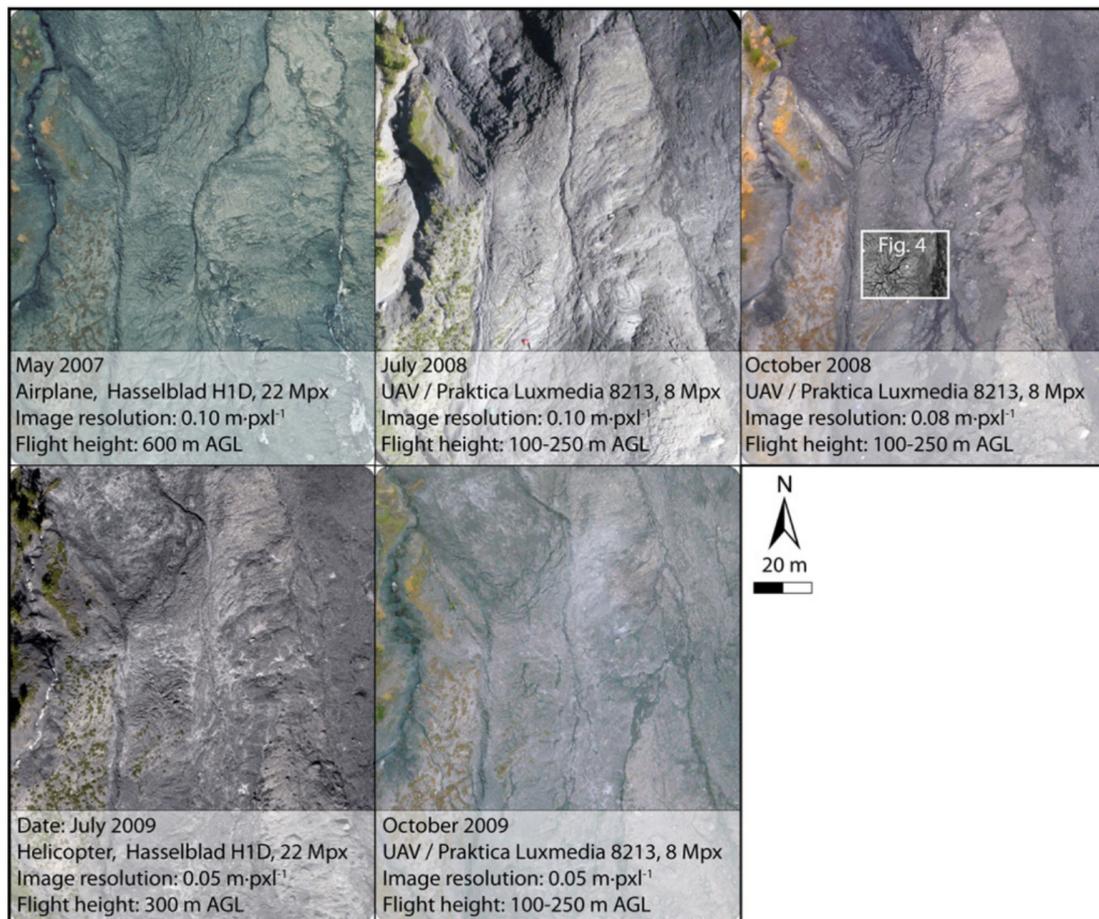


Fig. 3. Subsets of orthophotographs (see location in the white bounding box in Fig. 2a) acquired at five different dates with details of the acquisition systems and image ground resolutions.

In the VHR airborne optical images, the fissures can be recognized as dark curvilinear structures (Fig. 2c-e) as soon as their width approaches one pixel in size. Previous studies (Malet, 2003; Niethammer et al., 2011a; Walter et al., 2012) already discussed relationships between the observed fissure patterns (Fig. 2c-e) and strain resulting from a spatially heterogeneous displacement field and interactions between moving mass and the stable bedrock. However, a full reconstruction of the complex bedrock geometry that may allow for a more detailed characterisation of the underlying deformation mechanisms has been conducted only recently (Travelletti and Malet, 2012).

3.1 Airborne acquisitions of VHR optical imagery at the Super-Sauze landslide

Between April 2007 and October 2009, diverse imaging systems and airborne platforms were used to acquire VHR images of the landslide at five different dates (Fig. 3). In July 2008, October 2008, and October 2009, a low-cost UAV system equipped with compact camera was operated at flight heights between 100 and 250 m yielding images of the surface with a ground resolution between 0.03 and 0.10 m. The individual images were corrected for barrel lens distortion, rectified according to ground control points (GCPs) measured with differential GPS (DGPS), and finally merged into one large orthomosaic. Further details on the

image acquisition and processing were provided by Niethammer et al. (2010, 2011b) who quantified the residual positional error (x-y) for the October 2008 images with 0.5 ± 0.57 m within the boundaries of the sliding area. The UAV images for July 2008 and October 2009 are expected to provide better positional accuracies because they were orthorectified using elevation models that were generated from a photogrammetric analysis of the images.

During the two airborne LiDAR surveys in May 2007 and July 2009 (see Section 3.2), two orthomosaics of optical images with full coverage of the landslide were recorded using medium format cameras (Fig. 3) mounted on, respectively an airplane and a helicopter. The surveys used fully integrated systems for direct georeferencing and orthorectification with LiDAR surface models (see Section 3.2), which in general provide sub-decimetres positional accuracy in the x-y plane (Vallet, 2007).

For the study presented here, additionally 60 homologous tie points on stable areas were manually selected in the available images and showed a mean relative alignment error of 0.76 ± 0.82 m among the different acquisitions. Further details on the adopted camera systems and the resolutions of the images resulting from the five surveys are summarized in Fig. 3. The figure also illustrates the considerable radiometric differences among the five images originating from illumination changes, seasonal variations and the distinct characteristics of the sensors. The scenes for May 2007, October 2008 and October 2009 were acquired under cloudy conditions with diffuse sky radiation and consequently show a more homogeneous illumination of the surface. The scenes for July 2008 and July 2009 in contrast were recorded under sunny sky yielding strong contrast and many cast shadows. The latter are more prominent in the image for July 2008 which was recorded in the morning hours, at a relatively low sun angle. Although available methods for absolute and relative radiometric correction can be employed for the radiometric alignment of satellite images (Hong and Zhang, 2008; Vicente-Serrano et al., 2008), to the best of our knowledge, no approach exists to accu-

rately align the radiometry of sub-decimetres images from different sensors, with substantial changes in illumination, a complex topography and changing surface characteristics. Initial test using histogram-matching, linear-regression (Schott et al., 1988) and iteratively re-weighted regression (Canty and Nielsen, 2008) did not provide satisfactory results. Consequently, no radiometric normalization was performed and the image analysis technique was designed and tested with radiometric diverse imagery.

In order to calibrate adjustable parameters of the detection algorithm to the targeted fissures and the variable scene characteristics, the processing was first tested on a subset of the terrain covering $14,000 \text{ m}^2$ in the central part of the landslide (Figs. 2a and 3). This section was characterized by different fissure patterns and recorded during all surveys (including July 2008 and October 2009 which did not yield full coverage of the surface). Subsequently, the developed workflow was applied on the full scenes for a comprehensive mapping and analysis of the fissure distribution. Corresponding results for the full extent of the Super-Sauze landslide and their mechanical significance are discussed in Section 5.2.

3.2 LiDAR DTM

Two airborne LiDAR surveys were conducted in May 2007 and July 2009, respectively. The first survey used a Riegl LMS-Q560 laser scanner mounted on an airplane flying 600 m above the ground and resulted in a mean point density of 0.9 pts m^{-2} after vegetation filtering. The residual 3D positional error of the ground points was quantified as 0.12 m. The second survey was conducted with a Riegl Q240i laser scanner mounted on a helicopter and after vegetation filtering resulted in a mean point cloud density of 3.2 pts m^{-2} . The residual 3D positional error of the ground points was 0.07 m. Continuous surface rasters with a pixel size of 0.5 m were interpolated from the respective point clouds using Delaunay triangulation. The resulting surface was then adopted for the extraction of the principal hydrological drainage lines.

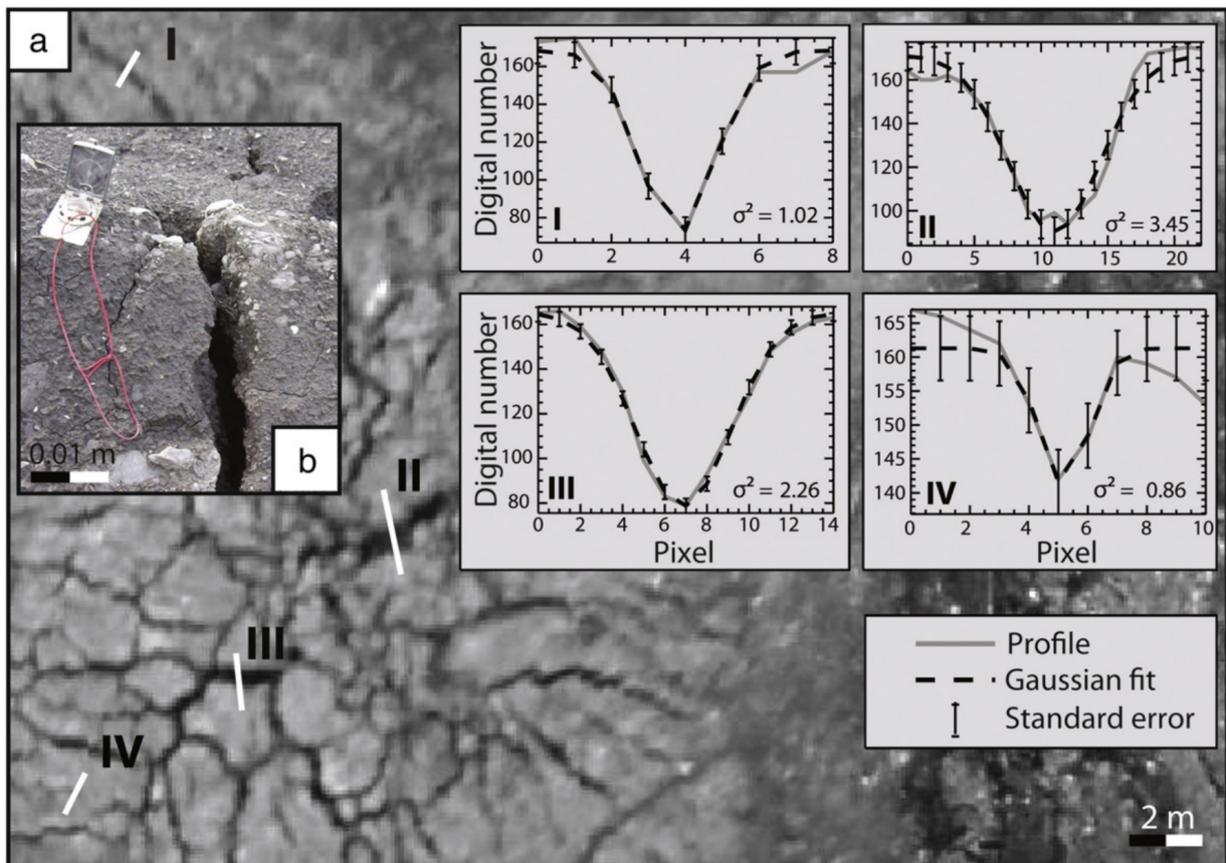


Fig. 4. Images of surface fissures. (a) Subset (see extent in Fig. 3) of the UAV image from October 2008 showing typical fissure patterns and (I-IV) grey-value profiles (green channel) approximated with Gaussian curves. (b) Field photograph taken in October 2009.

3.3 Reference datasets: expert maps of surface fissures

Reference mappings of the fissure characteristics (type and distribution) were elaborated by an expert geomorphologist familiar with the study site. The fissures were first identified on-site during a field survey carried out in October 2009 at the same time as the acquisition of the UAV images. The position of the fissures was mapped using a dGPS survey and terrestrial photographs. Then image interpretation rules were defined to identify and digitize the fissures on the images as polyline vectors using a 2D view and at a scale of 1:250. The image interpretation rules were then applied to the four other images in order to elaborate an expert fissure map for each date. The resulting five maps were adopted as a reference to assess the performance of the semi-automatic method.

4 Image processing methods

While first generic edge detection operators were already proposed in the 1980s (Marr and Hildreth, 1980; Canny, 1986), the extraction of linear features from imagery remains a challenging task in many disciplines such as medical research (Mendonca and Campilho, 2006), earth science (Shao et al., 2011; Shruthi et al., 2011) or signal processing (Lampert and O’Keefe, 2011). For our focus, the specific challenges posed for an automation of fissure detection can be summarized as follows:

- The approach should be scalable to apply for variable fissure sizes and image resolutions, and as insensitive as possible to variable radiometric image characteristics;

- The technique should not respond to edges but enable the detection of dark curvilinear structures that may be oriented at any direction. Classical techniques such as Sobel operator and the Canny detectors (González and Woods, 2008) have been designed specifically for edge detection and are not directly applicable;
- The complex micro-topography, the presence of rock blocks and gravels as well as small patches of vegetation yield highly textured images. Consequently, the approach should enable us to smooth out spurious signals from the noisy background while still retaining small partially disconnected linear features of interest. Contextual scene information should be taken into account to resolve ambiguities of the local features.

Considering these challenges, a processing workflow including three main stages was developed. Firstly, a set of scalable Gaussian filters is applied to detect fissure candidates and suppress responses at edges. Secondly, a set of morphological filters is used to close small gaps along the extracted candidates. Thirdly, an object-oriented procedure is followed to eliminate some of the false positives exploiting higher-level scene information with contextual rules.

4.1 Stage 1: extraction of fissure candidates using a Gaussian matched filtering algorithm

A particularly well-studied example for the detection of dark curvilinear structures is the extraction of dark blood vessels in photographs of the human retina. Based on the observation that the cross-profiles of the vessels resembles a Gaussian distribution, Chaudhuri et al. (1989) proposed the use of a matched filter (*MF*) that is essentially a Gaussian convolution kernel subtracted by its own mean value. As illustrated in Fig. 4a, the cross-sections of surface

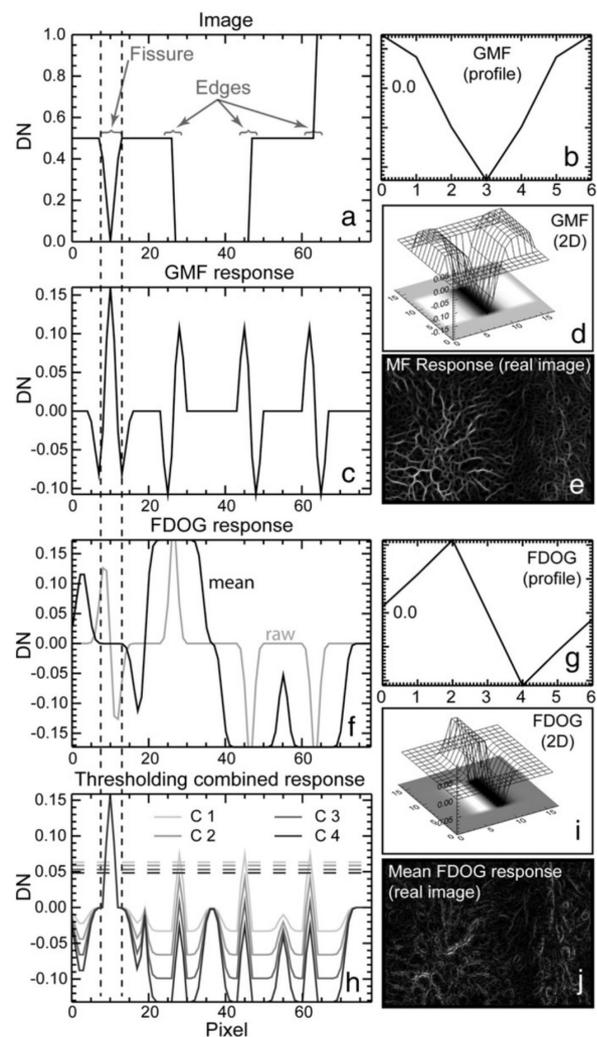


Fig. 5. Illustration of the principles of the Gaussian filtering for (a-c and f-h) a simplified 1-D case, (d and i) a 3D visualization of 2D filters and (e and j) the filter responses for the image subset in Fig. 4a. See text for details.

fissures can be approximated with a Gaussian distribution and an *MF* scaled to the size of the fissure will give a peak response when crossing the fissure at an angle of approximately 90° . Because the *MF* still yields errors such as false detections at step edges (Fig. 5a, c) numerous extensions (Hoover et al., 2000; Sofka and Stewart, 2006) and alternative approaches (Mendonca and Campilho, 2006; Soares et al., 2006) have been developed. Recently, Zhang et al. (2010) proposed modification to the original *MF* filtering approach integrating a first order derivative of a Gaussian function (FDOG) to locally adapt the thresholds separating dark lines from non-target features. Compared to

other state-of-the-art algorithms their approach provided competitive accuracies while being a computationally efficient and hence easier to apply on the large images resulting from VHR remote sensing.

For this study, a similar approach was implemented in ENVI-IDL 4.8 (ITT Visual Information Solutions). The algorithm and its parameterization are detailed below.

The *MF* is a two dimensional kernel defined in the *x*-direction by an inverted Gaussian profile (Fig. 5b), and in the *y*-direction by replicates of the same profile (Fig. 5d). It may be denoted as:

$$MF = g(x; y; \sigma) = -\frac{1}{\sqrt{2\pi}\sigma} e^{-\frac{x^2}{2\sigma^2}} - m \quad (1)$$

$$\text{for } |x| \leq 3\sigma, |y| \leq L/2$$

where σ denotes the standard deviation of the Gaussian functions and relates to the width of the targeted feature. To centre the kernel on zero, it is subtracted by its own mean m . The extent of the kernel in the *x*-direction is typically constrained to 3σ , whereas L defines the extent of the kernel in the *y*-direction and can be related to the length of the fissures. Because the matched filter still yields false responses at dark and bright step edges (Fig. 5c) Zhang et al. (2010) proposed to use the response of the FDOG to locally adjust the thresholds which are applied to classify the *MF* response into fissure and non-fissure structures. In analogy to Eq. (1), the first order derivative filter may be denoted as:

$$FDOG = g'(x; y; \sigma) = -\frac{1}{\sqrt{2\pi}\sigma^3} e^{-\frac{x^2}{2\sigma^2}} \quad (2)$$

$$\text{for } |x| \leq 3\sigma, |y| \leq L/2$$

Fig. 5f illustrates that the FDOG responds with a single peak to edges but with a zero crossing at the centre of the idealized fissure. A simple mean filter can be applied to broaden the zero crossing into a plateau covering the whole width of the fissure (Fig. 5f). Subtracting

the smoothed FDOG response from the *MF* response will attenuate the signal at edges while at the position of the fissure the full response is retained (Fig. 5h).

Since the orientation of the fissures is a priori unknown, multiple rotated versions of the Gaussian filters are applied to the image and for each pixel only the maximum response value is retained. This corresponds to finding the angle $\theta_{\max(x,y)}$ which maximizes the filter response at a given position in the image $I_{(x,y)}$ using:

$$\theta_{\max(x,y)} = \arg \max \left(I_{(x,y)} \otimes MF_{\theta} \right) \quad (3)$$

$$\text{for } 0 \leq \theta_i, |y| \leq \pi$$

where \otimes denotes the convolution operator and θ the orientation of the *MF*.

The calculation of the maximum response image R can then be obtained with:

$$R_{(x,y)} = \left[I_{(x,y)} \otimes MF_{\theta_{\max(x,y)}} \right] > 0 \quad (4)$$

where all negative response values are automatically set to zero and only values greater than zero are retained. The FDOG filter is rotated according to the determined $\theta_{\max(x,y)}$ and the corresponding response image D can be derived by:

$$D_{(x,y)} = \left| I_{(x,y)} \otimes FDOG_{\theta_{\max(x,y)}} \otimes m \right| \quad (5)$$

where M denotes the above-mentioned mean filter used to broaden the zero crossing to the width of the fissures.

While Zhang et al. (2010) used a very broad mean filter with a fixed size, we suggest to use a kernel size that matches the width of the Gaussian kernel (6σ) and is thereby related to the width of the targeted features (Fig. 5a, f). In contrast to early studies where the FDOG response was used to locally adapt the threshold (Zhang et al., 2010) the final response image \bar{R} is obtained by subtracting the FDOG from the GMF response using:

$$\bar{R}_{(x,y)} = R_{(x,y)} - Ct * D_{(x,y)} \quad (6)$$

where Ct denotes a user defined trade off parameter to adjust the sensitivity of the detection with typical range of values between 3 and 4. A threshold T is defined by:

$$T = \mu_{\bar{R}} + 2\sigma_{\bar{R}} \quad (7)$$

where $\mu_{\bar{R}}$ is the mean of the response image \bar{R} and $\sigma_{\bar{R}}$ is the respective standard deviation.

A binary fissure candidate map F_{map} is obtained by applying the threshold T on the response image \bar{R} using:

$$\begin{aligned} \overline{R_{(x,y)}} \geq T_{(x,y)} : F_{map} = 1 \\ \overline{R_{(x,y)}} < T_{(x,y)} : F_{map} = 0 \end{aligned} \quad (8)$$

The thresholding after subtraction of the FDOG response was found to provide a generally more robust attenuation of undesired edge responses than the technique previously applied by Zhang et al. (2010).

In summary, the user needs to specify four simple parameters, namely (1) the scale of the filter kernels in terms of σ , (2) the length L of the kernel, (3) the constant Ct of the thresholding sensitivity and (4) the number of orientations n_{θ} at which the filters are calculated. In this study, n_{θ} was kept constant at 36 for all experiments, whereas, if computational time becomes an issue, the angular resolution may be reduced to 12 steps without major losses of accuracy. To determine σ a tool was created, which allows drawing profiles on the image and automatically estimates the fitting Gaussian function (Fig. 4). Cross-profiles of the smallest fissures visible in the image with the coarsest resolution (0.1 m pixel^{-1}) were best fitted by Gaussian curves with $\sigma \approx 0.6$. To ensure a homogenous scale of the detected features among all images, the kernel can be scaled by changing σ relative to the image resolution. If, for instance, the image resolution is increased to $0.08 \text{ m pixel}^{-1}$, a value of $\sigma \approx 0.75$ yields a kernel with the same physical size (Table 1). The same applies to the filter length L which was estimated at 1 m corresponding to the typical minimum length of the fissures. Resampling of the images can thereby be avoided. In our experience, σ establishes the

lower bound for the width of the targeted features, whereas the filters still remain sensitive to features which are up to 5 times larger. For the choice of σ it is also helpful to note that the discrete kernel cannot represent FDOG functions with $\sigma \leq 0.5$.

To assess the sensitivity of the parameters and to determine a suitable threshold parameter Ct , a sensitivity analysis was carried out on a subset of the October 2008 image. Based on a visual assessment, values of $L = 1 \text{ m}$ and $\sigma = 0.75$ were found suitable for the detection of the fine fissure structures. The preliminary analysis also showed that increasing the parameters L and σ directs the detection towards more elongated and broader features, whereas in general the sensitivity of those parameters is rather low compared to the influence of the threshold Ct . Values of $Ct = \{0.0, 1.0, 2.0, 3.0, \text{ and } 4.0\}$ were tested and based on a visual assessment of the outputs, a value of $Ct = 3$ was established for an optimal trade-off between detection rate and the amount of false positives. The final parameter set is summarized in Table 1.

Table 1
Parameter set of the Gaussian filters scaled according to the respective image resolution.

Image date	May 2007	July 2008	October 2008	July 2009	October 2009
Pixel size [m]	0.10	0.10	0.08	0.05	0.05
σ [pixel]	0.60	0.60	0.75	1.20	1.20
L [pixel]	10	10	12	20	20
n_{θ}	36	36	36	36	36
Ct	3.0	3.0	3.0	3.0	3.0

4.2 Stage 2: connection of broken lines using structuring elements

The highly textured surface of the landslide constitutes a noisy background that affects the detection especially at section where the fissures are very thin or partially occluded. While a human operator can easily interpolate broken lines through perceptual grouping (Metzger, 1975), this needs special attention for a semi-automated mapping technique.

To close small gaps between broken line segments of the detected candidates, a hit-or-miss transform algorithm (Serra, 1982) was used. The transform assigns a value of 1 to each pixel whose local neighbourhood fulfils the criteria

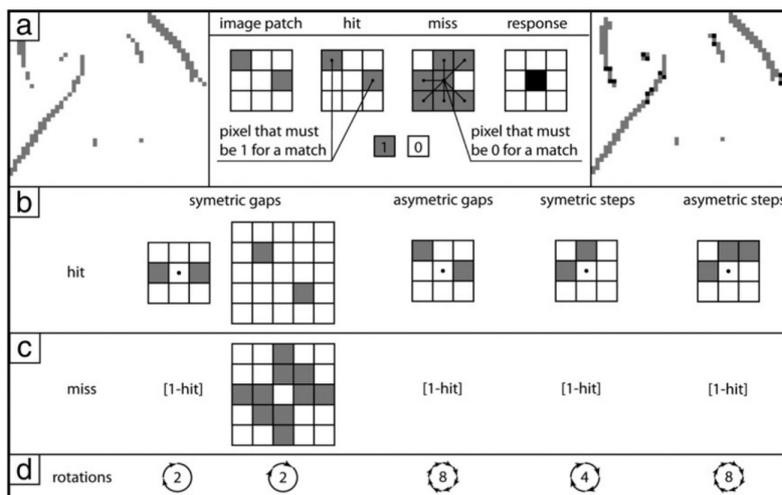


Fig. 6. Strategy used to connect broken line segments. (a) Working principle of the hit- and miss transform, (b) hit structures, (c) miss structures and (d) respective rotations used for the plausible pixel neighbourhoods.

defined by hit-and-miss structures (Fig. 6a), also known as structuring elements. They were defined to address all plausible 3-by-3 neighbourhoods representing small gaps in the detection starting from four prototype hit-structures shown in Fig. 6b. The respective miss-structures (Fig. 6c) are typically derived by simply inverting the prototype hit-structures, and both elements were rotated (Fig. 6d) to test for a total number of 24 possible neighbourhood arrangements. Exceptional cases were thereby the structuring elements for closing directly diagonal gaps, where an extended neighbourhood was used for the hit-and-miss structures (Fig. 6b, c) to prevent connections of lines running parallel to each other.

The connectivity of the line segments was also particularly important for the subsequent object-oriented post-processing, where objects constitute from pixels groups connected in a Von Neumann neighbourhood (four adjacent pixels at each side), and small isolated objects could be disregarded as noise.

4.3 Stage 3: object-oriented analysis for false positive removal

Due to visually similar objects, such as linear erosion features (rills and small gullies) and elongated shadows induced by the microtopog-

raphy, the fissure candidates resulting from the described filtering routine may still comprise numerous false positive detections. While a human interpreter can differentiate most of the false positives assessing the geospatial context of the scene, the efficient use of such information with automated systems is a challenge for object-oriented image analysis.

To exploit the contextual scene information for an automatized refinement of the extracted fissure candidate maps, an object-oriented routine that integrates spatial reasoning into an explicit form was elaborated and implemented using eCognition 8.64 (Trimble, 2011). The routine included the following steps:

1. The ratio of shadow around the detections is evaluated and candidates with a ratio of shadow pixels in their smallest enclosing circle above 33% are regarded as false detections induced by shadings of the micro-topography. This ratio threshold was determined empirically through visual inspection of the candidate fissures, and selected to capture elongated false detections with one side lying fully in shaded zones. The threshold for shadow can thereby be adjusted

according to the illumination conditions and the dynamic range of the image (Table 2).

2. Further false detections may result from vegetation which typically shows a lower reflectance in the green and red channel compared to the blue. The blue ratio in the sum of all channels is consequently typically below one third for vegetated areas. The suitable value varies slightly with the illumination conditions and the season, and Otsu's method (Otsu, 1979) was employed to automatically adapt to such changes. Through an iterative testing of all possible values, Otsu's method determines threshold value that maximizes variance between two classes in an image. Hence, constraining the search space to all pixels with a ratio blue below 33%, the algorithm was used to determine the thresholds that maximize the contrast between vegetation and the background (Fig. 7). Fissure candidates covered by the resulting vegetation class, or having a relative border length larger than 0.15, were subsequently removed.
3. Another class of frequent false detections resulted from linear objects such as rills, gullies and nearly vertical steps at the landslide flanks, which may locally obtain similar characteristics as the targeted fissures. To test for the presence of larger linear features and evaluate their relationship with fissure candidates, a strategy to suppress additional false positives was required. For the mapping of the larger linear elements, two sources were adopted. First drainage lines were extracted from the LiDAR DTMs using hydrological standard tools (Tarboton et al., 1991) and enlarged with a surrounding buffer of 0.5 m. A second approach was to repeat the Gaussian filtering with the parameter set indicated in Table 1, but with a two times increased scale σ and a five times coarser image resolu-

tion (resampled with bilinear interpolation). This is equivalent to a search with a 10 times larger scale providing a sufficiently large scale difference to assure that none of the detected linear features would correspond to fissures. The linear objects extracted with both approaches were virtually overlaid with the fissure candidates, and the difference of the orientations of their respective centre lines was adopted as criteria to evaluate if the fissure candidate was in fact part of a larger linear object or constitutes an independent structure (Fig. 8). Image-based measurements of the angular offset of the fissured indicated a minimum offset of about $\pm 13^\circ$. Considering that the lowest effective friction angle values measured for the landslide material are $\alpha' = 26^\circ$ (Malet et al., 2005b), the thresholds are consistent with the orientation of $\alpha'/2$ that the Coulomb criterion predicts for the orientation of shear fissures at the landslide boundary (Tchalenko, 1970).

4. A last filtering step was implemented by removing all candidates with length not longer than 0.4 m and an area smaller than 0.1 m^2 . Finally, all fissure candidates falling in areas with a fissure class density lower than 1% in a surrounding neighbourhood of 10 m^2 were considered as noise and also removed.

Table 2 displays that most adopted thresholds were kept the same among all the images and only the classification rule for the shadow areas was adapted in order to compensate radiometric differences in the input images.

Table 2
Summary of the thresholds adopted in the object-oriented post-processing routine. See text for details.

Feature	Thresholds
Shadow	Red < 100*, 40**
Shadow ratio	≤ 0.33
Vegetation	Ratio blue $\leq 0.33 + \text{Otsu}$
Relative border to vegetation	≤ 0.15
Minimum angular difference	$> 13^\circ$
Minimum length (clean up)	$\geq 0.4 \text{ m}$
Minimum area (clean up)	$> 0.1 \text{ m}^2$
Minimum fissure density (clean up)	$> 1\% \cdot 10 \text{ m}^{-2}$

* For May 2007, July 2008 and October 2008.

** For July 2009 and October 2009.

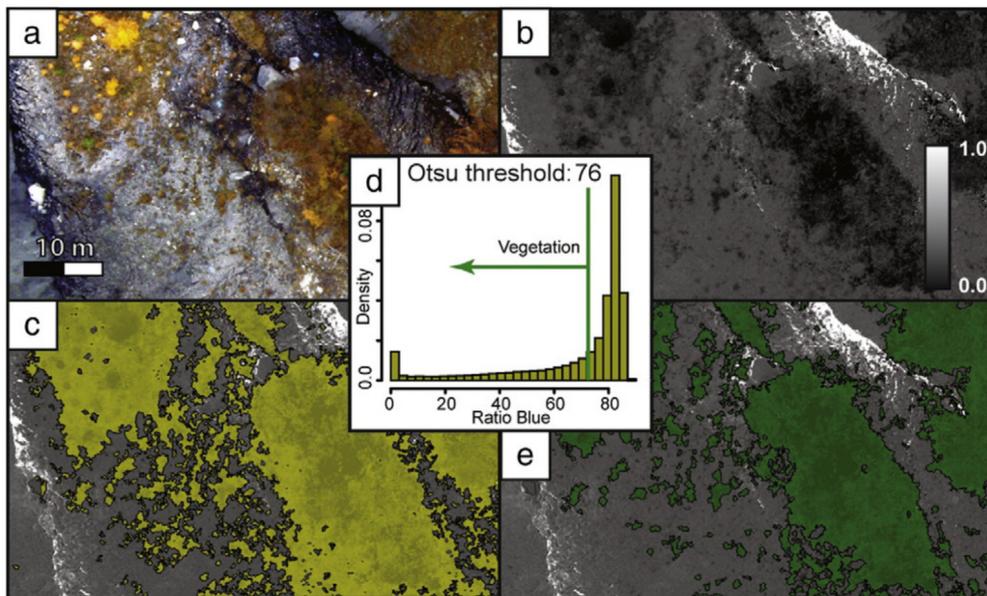


Fig. 7. Illustration of the automatic threshold detection for the intermediate mapping of vegetation. (a) Subset of the October 2008 image at the toe of the landslide. (b) Ratio blue. (c) Initial thresholding at ratio blue 0.33 to obtain vegetation candidates (yellow). (d) Histogram of the vegetation candidates with the automatically selected threshold. (e) Final map of the vegetation (green).

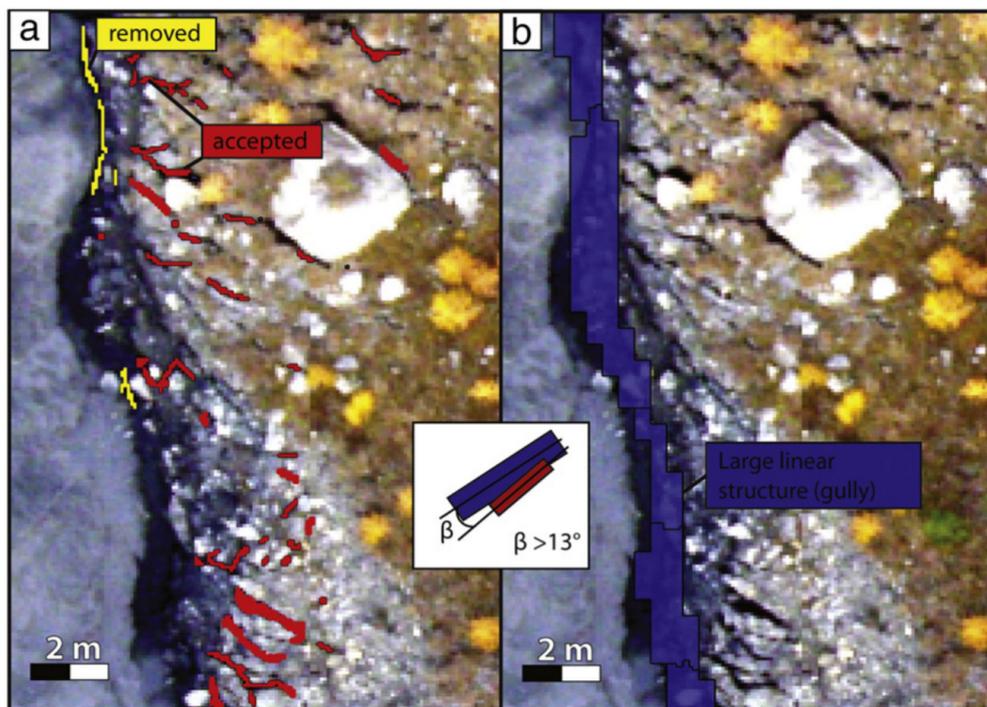


Fig. 8. Illustration of the object-oriented post-processing routine. (a) Fissure candidates that overlapped with linear structures. (b) Linear structure detected at a ten times greater filter scale. The fissure candidates aligned with the linear structures at angles below $\pm 13^\circ$ were removed.

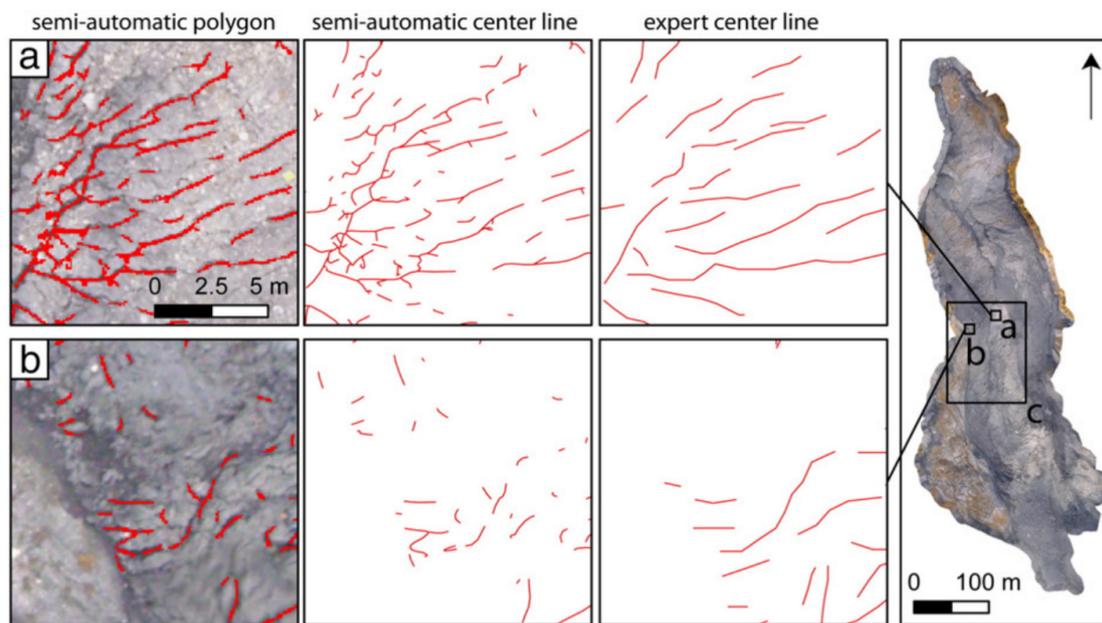


Fig. 9. Example of comparison of the obtained fissure maps with the expert mapping for October 2010 (fissures in red). (a) Area with relatively high agreement of the mapped fissure patterns. (b) Area with relatively high rate of false negatives and false positives. The scale of the representations corresponds approximately to the scale used for the expert mapping (1:250).

5 Results and discussion

5.1 Comparison with multi temporal manual mappings

The primary output of the developed processing routine is a map of the detected fissures represented by polygons. Applying a Delaunay triangulation that extracts the skeleton of those polygons (Trimble, 2011), a 2D line representation, which enables a more immediate comparison with expert mappings, can be obtained.

Fig. 9 displays an example of comparison between an expert map and the result of the semi-automatic detection. A first visual assessment of the obtained maps suggested better agreement of the fissure patterns in areas with high contrast and low texture (Fig. 9a), whereas false positives and false negatives concentrated in sections with low contrast and increased surface texture (Fig. 9b).

For a quantitative assessment of the mapping accuracy, the obtained results were compared with the expert mappings in the central part of the landslide (Fig. 9c) at all five

dates. While several accuracy measures for geographic line datasets have been already proposed, there is still no consensus about one generally applicable technique and the metrics should be selected according to the problem at hand (Ariza-López and Mozas-Calvache, 2012). Here, we focus on three crucial aspects of the map accuracy that may have direct implications for their further use, namely the size of the affected (e.g. fissured) area, the length and density of the fissures, and their orientation.

5.1.1 Size of the fissured area

Tveite and Langaas (1999) suggested an accuracy measure for line datasets based on repeated buffering and overlay operations of detected and reference line datasets. A similar strategy was adopted in this study by repeatedly calculating true positive and false positives rates from two raster data representing the detections and the expert mapping at increasingly coarser resolutions. The raster data were calculated at 10 cm steps for resolutions between 0.1 and 1.0 m, and each pixel was assigned as fissured or non-fissured area accord-

ing to the presence or absence of a fissure in the detections and the reference map, respectively. The resulting receiver operating characteristics (ROC) plots are presented (Fig. 10). The analysis showed a correspondence with the expert maps at true positive rates typically above 40% and up to 65%. The false positive rates were below 5% except for the scenes recorded with full sunlight where false positive rates up to 9% could be observed (Fig. 10).

5.1.2 Fissure length and density

Hydrological models that integrate the influence of surface fissures on infiltration and preferential flow have demonstrated that the fraction of fissures per unit area is an important parameter with considerable influence on the modelled water storage (Malet et al., 2005a; Krzeminska et al., 2011). Such models are typically generated at slope scale with grid resolutions below 10 m. To assess the accuracy of the

extracted maps with respect to this potential application, the fissure density was calculated as the line length in circular sliding windows with diameters between 2 and 10 m, and compared among automated detection and expert mappings.

The regression plots in Fig. 11 illustrate the correlation of the fissure density estimates with a 5 m circular sliding window yielding coefficient of determination (R^2) typically above 0.5. The regression analysis further indicated generally higher densities resulting from the semi-automatic detection originating from false positive detections but also from a stronger generalization of the fissure line drawings within the expert mapping. Exceptions from this general trend are the results obtained from the image of July 2008 which was recorded at a low sun incidence angle leading to a relatively low $R^2_{5m} = 0.36$. The bar plots in Fig. 11 display generally higher R^2 values at increasing resolutions of the density raster. This is a well-known

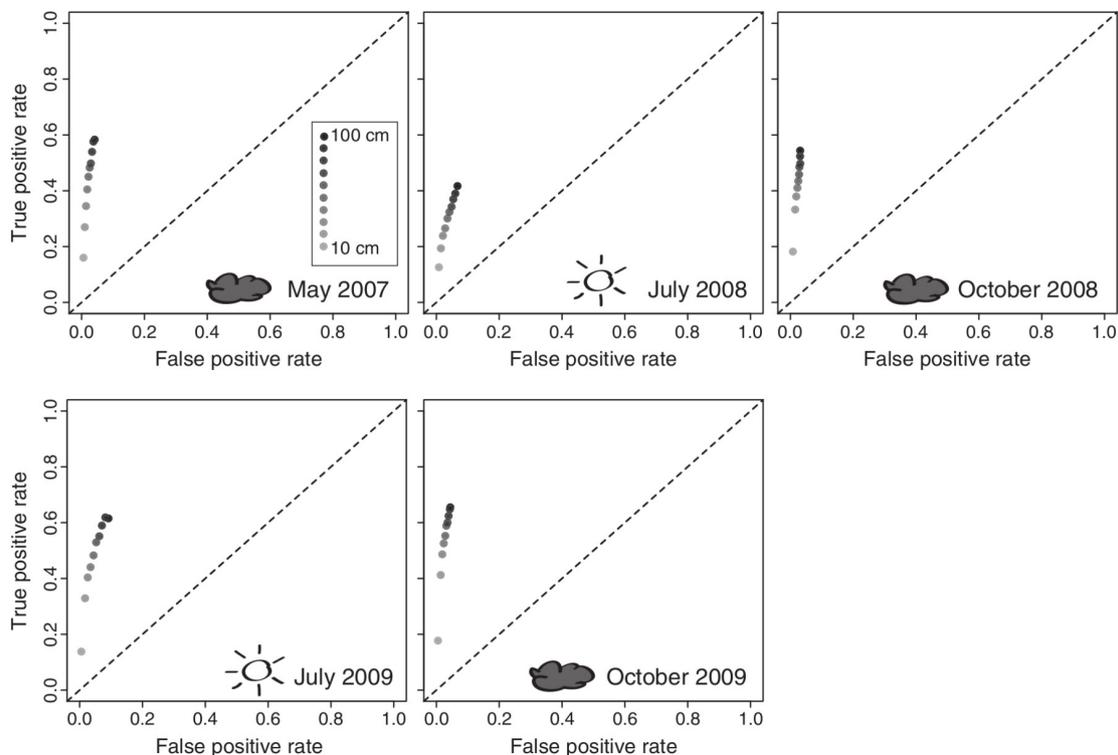


Fig. 10. Receiver operating characteristics (ROC) plots for the fissured area at different map resolutions. The sky conditions for the five different dates are indicated.

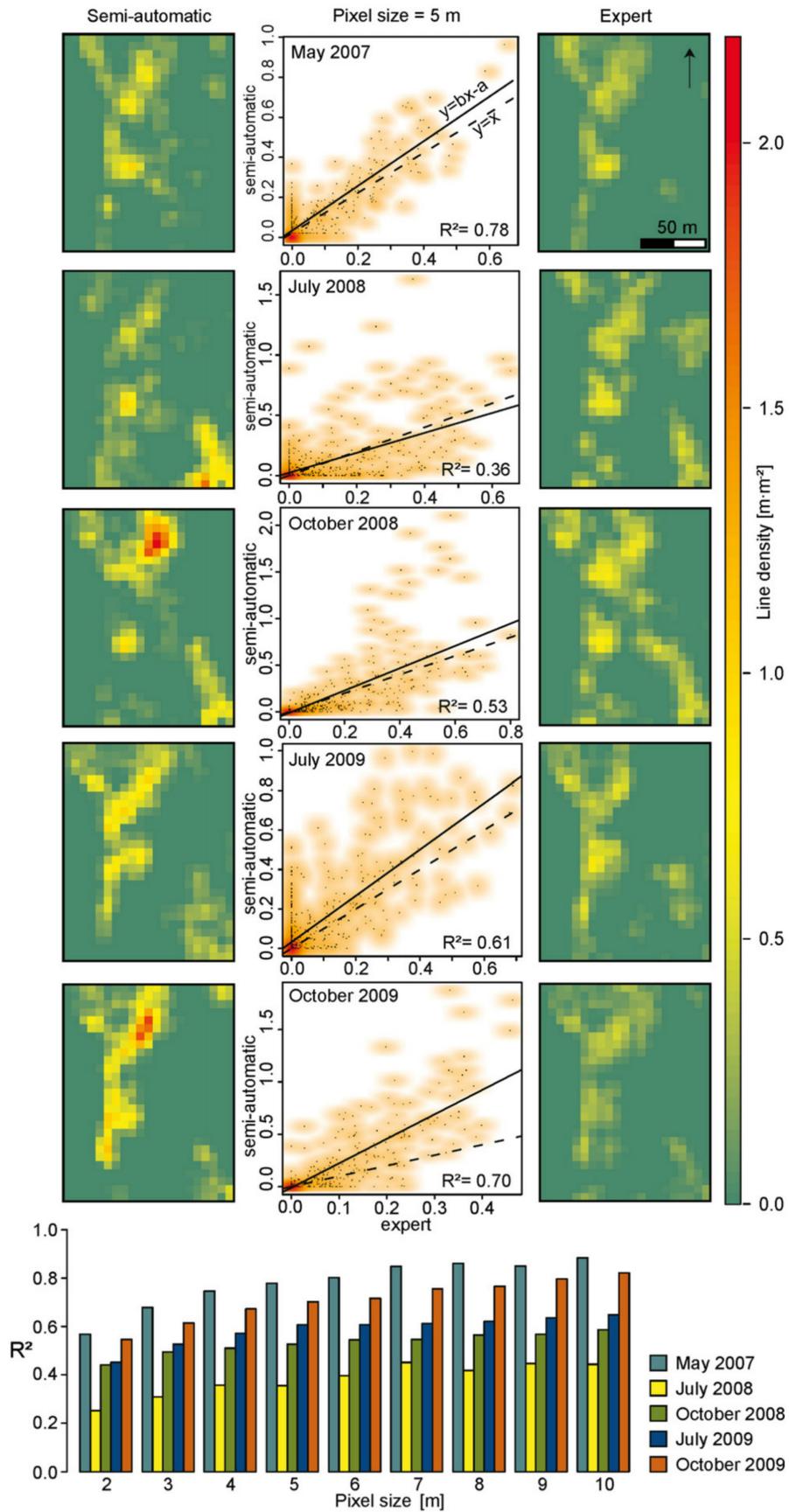


Fig. 11. Correlation between fissure density estimates at 5 m raster resolution based on semi-automatic detections and expert mappings from the five images. The bar plots at the bottom display the R^2 coefficient at different raster resolutions.

effect of spatial aggregation on correlation statistics (Gotway and Young, 2002) but also reflects the contrast between stronger discrepancies of local details and a better correspondence of the global fissure pattern pictured in the respective maps. The highest correlation was observed among the mappings for May 2007 with $R_{10m}^2 = 0.88$ indicating that the lower resolution of the corresponding input image was not an important factor for the accuracy of the detection.

5.1.3 Fissure orientation

As outlined in the Introduction section, different fissure patterns may signal respective mechanical processes, and statistics of the principal fracture orientation often allow us to estimate the directions of the principal stresses (Pollard and Fletcher, 2005). The fissure orientations were quantified as a third factor to assess the accuracy of the extracted maps using rose diagrams frequently employed for the analysis and interpretation of two dimensional orientation data (Jammalamadaka and SenGupta, 2001). Rose diagrams with a bin width of 10° were computed on a 10 m regular grid for the semi-automatic detections and the expert mappings at all five dates. Considering the length and direction of each bin expressed as a respective vector the preferred fissure orientation within a grid cell can be calculated by summing the vectors over all bins. Taking into account all cells containing fissures in both the expert map and the semi-automatic detection, the mean absolute error (MAE) of the mean orientations provides a quantitative measure for the orientation accuracy.

The rose diagrams plots and error statistics in Fig. 12 depict MAE values between 9.7° and 22.5° for the five dates. The detections on the three scenes recorded under cloudy sky resulted in MAE not larger than 10.7° , whereas the error rate clearly exceeded 20° with the scenes of July 2008 and 2009 recorded with full sunlight at the surface. The lower orientation accuracies are largely consistent with the relatively low accuracies in terms of area (see Section 5.1.1) and density (see Section 5.1.2)

resulting from the detection at the latter two dates.

5.2 Fissure patterns as possible geoindicators of deformation processes

For a comprehensive interpretation of the detected fissure patterns at the scale of the entire slope, the scenes of May 2007, October 2008 and July 2009 offering a full coverage of the landslide, have been analysed. However, considering the relatively low detection accuracy on the sunlit images of July 2009, the interpretation was focused essentially on the scenes of 2007 and 2008 spanning also over a period with displacement rates significantly above the average annual rates (Travelletti, 2011).

Comparing the detection results of May 2007 (Fig. 13a) and October 2008 (Fig. 13b), a significant increase in the abundance of fissures could be noted for the entire landslide. This can be attributed to a phase of strongly increased displacement rates (up to 3.5 m day^{-1}) in early June 2008 (Travelletti, 2011) preceding the UAV survey in October 2008. However, in October 2008, the displacement rates already consolidated again at average rates between 0.01 and 0.03 m day^{-1} , most of the fissures induced in June were preserved and evolved at the surface until October. This view is supported by the results obtained for the test area with the five scenes (Figs. 10 and 11) picturing rather a transient evolution than a complete reorganization of the fissure patterns. Despite partially strong disagreement in the absolute measured fissure density, both expert maps and semi-automatic mapping showed an increase in fissure density after May 2007, with higher values in October 2008 (Fig. 11) than directly after the peak displacement in spring. Pluviometric records for the area in 2008 show the relatively dry summer season with a cumulative rainfall of 110 mm for the month of July, August and September, suggesting that the increased fissure density in October is partially caused by an increased brittleness of the upper soil layer that dried out during summer.

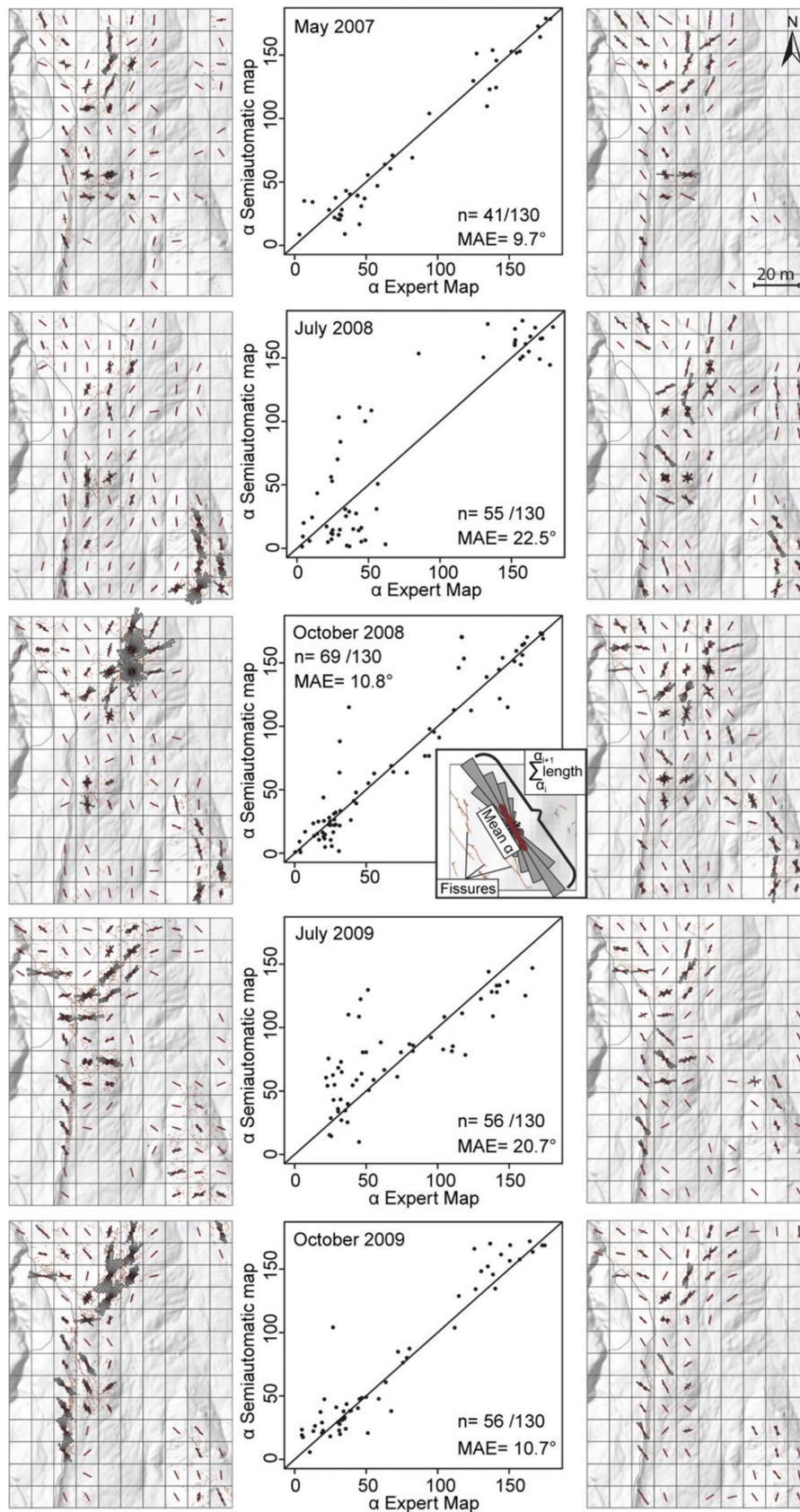


Fig. 12. Rose diagram plots with mean orientation (red line) and error statistics for the mean fissure orientation per 10 m grid cell for the test area at the five different dates. For visualization, the rose diagrams were plotted over a hillshade of the landslide surface and the scatterplot angles were centred at 90° .

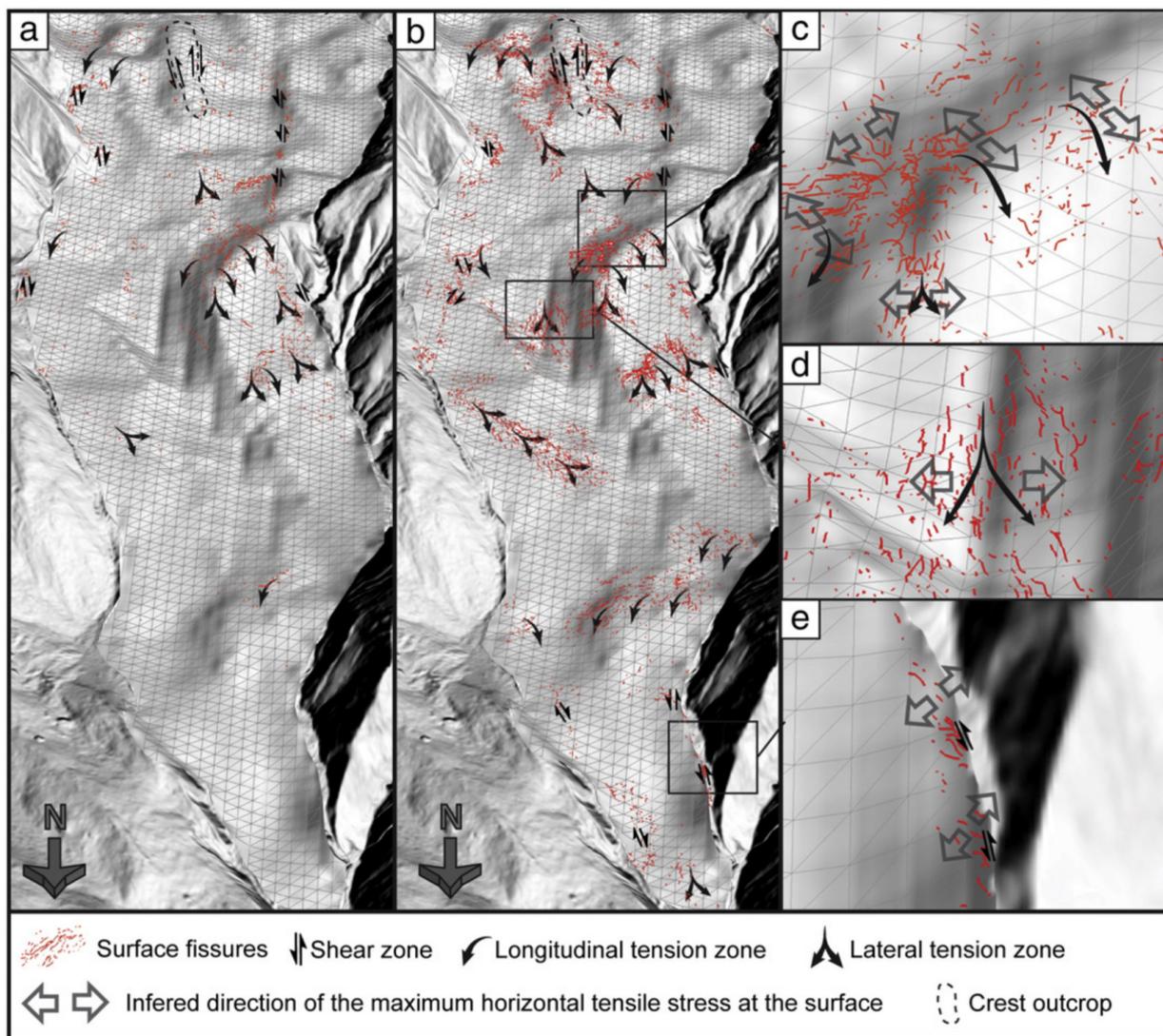


Fig. 13. Pseudo 3D view showing the landslide dynamics inferred from the fissure patterns detected in the aerial images of (a) May 2007 and (b) October 2008. (c, d, and e) Close up views for October 2008 showing inferred landslide dynamics and stress vectors. The results are overlaid on a hillshade model of the topography of the stable bedrock proposed by Travelletti and Malet (2012).

Besides the general increase in the amount of fissures, it is intriguing to observe that at several local plots, similar fissure patterns can be observed at approximately the same positions through time (Figs. 12 and 13a,b), despite maximal displacements of up to 55 m between October 2008 and October 2009 (Niethammer et al., 2011a). This indicates the recurrent continuous in-situ formation where the fissures provide a close representation of the local strain field, similar as observed for the evolution of glacier crevasses (Harper et al., 1998).

Previous studies (Malet, 2003; Niethammer et al., 2011a; Walter et al., 2012) already observed close relationships between the occurrence of fissures and the geometry of the stable bedrock at the Super-Sauze landslide. They also noted a general contrast between higher water content and rather ductile behaviour in the lower subsurface (< 1 m) and typically lower water content of the topsoil yielding more brittle behaviour at the surface. The surface fissures can therefore be understood as the response to stresses induced in the top-

soil through coupling with ductile strain in the deeper subsurface. A similar model was already described by Fleming and Johnson (1989) and adopted as a basis to qualitatively estimate the patterns of flow and stresses from a joint-interpretation (Fig. 13) of the detected fissure patterns and a geometrical model of the stable bedrock (Travelletti and Malet, 2012).

Considering the bedrock geometry and a formation of the open fissures normal to the direction of the least compressive stress (Pollard and Fletcher, 2005), three different flow field patterns leading to the fissure formation at the Super-Sauze landslide can be suggested. First, lateral shear at external and internal landslide boundaries aligned with the general flow field leads to the formation of diagonal shear fissure arrays (Fig. 13e). Second, longitudinal compressive and tensile strain related to abrupt changes in the slope of the sliding surface induces tensile stresses at the surface that results in transversal fissure arrays (Fig. 13c). Third, divergence of the flow field over topographic ridges and at the outlets of confining topographic channels induces lateral extension and tensile stresses resulting in longitudinal fissure arrays (Fig. 13d). At several locations, those processes overlap and lead to the formation of mixed structures such as a radial fissure patterns displayed in Figs. 4 and 13c, resulting from lateral shear and longitudinal strain, and from a divergent stress field, respectively.

5.3 Accuracy and related uses

Deformation patterns at the surface of landslides are important indicators for the mechanical processes, whereas the elaboration of detailed maps of such features remains a challenging and time-consuming task. While Sowers and Royster (1978) still argued that aerial photographs do not reach sufficient resolution for such mappings, modern digital sensors and new aerial platforms such as UAVs today provide the necessary level of detail. Furthermore, this study demonstrated the possible use of a semi-automatic image processing chain for the extraction of surface fissure maps.

The accuracy of the method was assessed by comparisons with expert maps and demonstrated heterogeneous areal accuracies with true positive rates of up to 65% and false positive rates generally below 10%. In addition, the orientation accuracy showed a variable quality of the resulting maps with mean deviations between 9.7° and 22.5° . The fissure densities derived from both maps have significant correlations ($R^2 = 0.36-0.78$), whereas the semi-automatic detections yield typically higher estimates. Interestingly, this difference is more pronounced with the images of 2009 (Fig. 10) reflecting the contrast between increased semi-automatic detection rates at higher resolutions and the fixed scale of the expert mapping. Contrariwise, the best agreement among detection and expert maps was measured for the scene of May 2007 showing that the lower resolution does not necessarily yield lower accuracies. Generally, lower accuracies were observed for the scenes recorded with full sunlight at the surface in July 2008 and 2009, and the worst results were obtained for July 2008 when images were recorded at a relatively low sun incidence angle. Since the direct sunlight induces shading that affects the local contrast and global image normalization methods cannot alleviate this problem, image acquisition with diffuse skylight appears to be the generally better option.

In the initial stage of the processing chain, a low-level linear feature detector is used. Similar techniques yield competitive results in medical image analysis (Zhang et al., 2010), whereas the accuracies achieved with aerial images in this study are still significantly lower. This must be attributed to the generally higher complexity of outdoor scenes and at the moment still requires additional steps and parameters to take the contextual scene information into account. The use of an OOA heuristic-based post-processing technique proved useful for the removal of false positives and helped to objectify the image analysis by transferring expert knowledge in an explicit form. The analysis still relies on a number of fixed thresholds which may hinder an easy transfer of

the entire processing chain to a different geographic area. This concerns especially parameters that require knowledge of the local processes (e.g. minimum fissure length and effective friction angle), while thresholds that can be determined directly from the image (e.g. shadows and vegetation) may be adjusted more effortlessly.

The development of surface fissures precedes and accompanies especially slow- and very slow-moving landslides (Cruden and Varnes, 1996) making the developed technique particularly applicable to such types of landslides and to potentially unstable slopes. However, the spatial resolution of the acquired images must at least match, or should ideally exceed, the width of the targeted fissures, and the vegetation must be sufficiently sparse to permit direct view on the bare ground. The results of this study demonstrate that if those requirements are met, the obtained fissure maps can already provide sufficient accuracy to infer the landslide dynamics and mechanical processes at the slope scale (see Section 5.2). Density maps from both semi-automatic and expert mappings show a strong spatial and temporal variability of the fissure abundance pointing toward important local and temporal contrasts in the infiltration capacity which may need considerations in the design of hydro-mechanical models. An analysis of the evolution and mechanics of individual fissures will however require higher temporal resolution and terrestrial cameras have recently been installed at the surface of the landslide to record imagery for further research in this direction. It would also be desirable to test the developed technique for the investigation of other landslides with different characteristics in order to validate a more general applicability of the approach and the mechanical interpretation of the observed fissure dynamics.

The OOA heuristics already considers multi-scale information to some degree (see Section 4.3), whereas for further methodological improvements an explicit integration of an automatic scale selection technique at the low-level filtering stage appears as a promis-

ing approach to further reduce heuristics and tuneable parameters (Stumpf et al., 2012). The first and second stages of the proposed method are generic for the detection of dark linear features, and could in principle also be applied to detect other geomorphological and geological structures with similar characteristics. The proposed technique might be of interest for the mapping of gullies (Shruthi et al., 2011), geological lineaments (Mallast et al., 2011), ice-glacier crevasses (Vaughan, 1993) or tectonically induced fractures (Allmendinger and González, 2010), sufficiently larger to be depicted in sub-metre satellite images.

Considering the intrinsic disagreement in expert mappings of linear features, especially in the inter- and extrapolation of lines (Sander et al., 1997), further studies should also include an assessment of the uncertainties of reference maps since their quality can strongly bias the evaluation of different alternative approaches (Lampert et al., submitted for publication).

6 Conclusions

This study developed an image processing chain to extract surface fissures from heterogeneous sets of VHR aerial images and tested the approach with a challenging multi-temporal set of images recorded at the Super-Sauze landslide for five different dates. The first two stages of the developed workflow combine families of Gaussian matched filters and morphological filters, and are followed by an object-oriented analysis to reduce the amount of false positive detection using contextual information and auxiliary topographic information. The detection results can be represented in raster maps or optional by centre skeleton lines.

Under homogenous illumination conditions a comparison of the results with expert mapping demonstrated detection rates of up to 65% and orientation errors below 10°. Contrary, the technique is relatively sensitive to shading effects at full sunlight and prone to errors especially at low sun incidence angle. A joint-interpretation of obtained fissure maps

and of a 3D geometrical model of the stable bedrock demonstrated their complementary use for a better understanding of the geomorphological and geomechanical processes, such that the detected fissure pattern may be used for first approximation for mechanical processes in the recent deformation history of a slope. Possible directions for further research are the reduction of tuneable parameters and a more immediate exploitation of multi-scale information, as well as an adaption of the technique to other linear features with geomorphological and geological relevance.

Acknowledgements

The work was supported by the project SafeLand "Living with landslide risk in Europe: assessment, effects of global change, and risk management strategies" funded by the 7th Framework Programme of the European Com-

mission (grant agreement no. 226479), the project SISCA 'Système Intégré de Surveillance de Crises de Glissements de Terrain' funded by the French Research Agency (contract ANR Risk-Nat, 2009-2012), the project FOSTER 'Spatio-temporal data mining: application to the understanding and monitoring of soil erosion' funded by the French Research Agency (contract ANR Cosinus, 2011-2013), and the project Grosshang "Coupling of Flow and Deformation Processes for Modeling the Movement of Natural Slopes" funded by the Deutsche Forschungsgemeinschaft (DFG). The authors would like to acknowledge Alexandre Mathieu (University of Strasbourg) for his assistance in the field and for the expert mapping of the different fissure patterns, and Julien Travalletti for discussion on the recent dynamics of the landslide. The IDL code implementing the first two detection stages and the eCognition rule set implementing the object-oriented analysis are available on demand.

References

- Abramson, L.W., Lee, T.S., Sharma, S., Boyce, G.M., 2001. *Slope Stability and Stabilization Methods*, 2nd edition. Wiley, Chichester.
- Allmendinger, R.W., González, G., 2010. Invited review paper: Neogene to Quaternary tectonics of the coastal Cordillera, northern Chile. *Tectonophysics* 495, 93-110.
- Anderson, T.L., 2005. *Fracture Mechanics: Fundamentals and Applications*, 3rd edition. Taylor & Francis.
- Ariza-López, F., Mozas-Calvache, A., 2012. Comparison of four line-based positional assessment methods by means of synthetic data. *GeoInformatica* 16, 221-243.
- Backers, T., 2004. *Fracture Toughness Determination and Micromechanics of Rock Under Mode I and Mode II Loading*. PhD, Universität Potsdam, Potsdam.
- Baruch, A., Filin, S., 2011. Detection of gullies in roughly textured terrain using airborne laser scanning data. *ISPRS Journal of Photogrammetry and Remote Sensing* 66, 564-578.
- Bièvre, G., Jongmans, D., Winiarski, T., Zumbo, V., 2012. Application of geophysical measurements for assessing the role of fissures in water infiltration within a clay landslide (Trièves area, French Alps). *Hydrological Processes* 26, 2128-2142.

Bombard, J.-P., 1968. Une approche des problèmes posés par l'étude des mouvements de terrains. Thèse de Géologie, Faculté des Sciences de Grenoble, Grenoble, (in French).

Canny, J., 1986. A computational approach to edge detection. *IEEE Transactions on Pattern Analysis and Machine Intelligence* 8, 679-698.

Canty, M.J., Nielsen, A.N., 2008. Automatic radiometric normalization of multitemporal satellite imagery with the iteratively re-weighted MAD transformation. *Remote Sensing of Environment* 112, 1025-1036.

Chaudhuri, S., Chatterjee, S., Katz, N., Nelson, M., Goldbaum, M., 1989. Detection of blood vessels in retinal images using two-dimensional matched filters. *IEEE Transactions on Medical Imaging* 8, 263-269.

Chowdhury, R.N., Zhang, S., 1991. Tension cracks and slope failure. In: Chandler, R.J. (Ed.), *Proceedings of the International Conference on Slope Stability Engineering: Developments and Applications*. Institution of Civil Engineers, Isle of Wight, pp. 27-32.

Cruden, D.M., Varnes, D.J., 1996. Landslides types and processes. In: Turner, A.K., Schuster, R.L. (Eds.), *Landslides: Investigation and Mitigation*. Transportation Research Board, Special Report, 247. National Academy of Sciences, Washington, DC, pp. 36-75.

Davis, G.H., Reynolds, S.J., 1996. *Structural Geology of Rocks and Regions*. Wiley, Chichester.

Eisenbeiss, H., 2009. *UAV Photogrammetry*. PhD, ETH Zürich, Zürich.

Espinosa, A., 2009. *Analysis and Quantification of Preferential Flow on the Super-Sauze Landslide*. MSc, Delft University of Technology, Delft, Netherlands. (80 pp.).

Fleming, R.W., Johnson, A.M., 1989. Structures associated with strike-slip faults that bound landslide elements. *Engineering Geology* 27, 39-114.

Fleming, R.W., Baum, R.L., Giardino, M., 1999. Map and description of the active part of the slumgullion landslide, Hinsdale County, Colorado. *Geologic Investigations Series Map I-2672*. U.S. Geological Survey, Denver, Colorado.

Frost & Sullivan Co., 2007. *Study analysing the current activities in the field of UAV*. European Commission Enterprise and Industry Directorate-General.

Glenn, N.F., Streutker, D.R., Chadwick, D.J., Thackray, G.D., Dorsch, S.J., 2006. Analysis of LiDAR-derived topographic information for characterizing and differentiating landslide morphology and activity. *Geomorphology* 73, 131-148.

González, R.C., Woods, R.E., 2008. *Digital Image Processing*, 3rd edition. Prentice Hall, Upper Saddle River.

Gotway, C.A., Young, L.J., 2002. Combining incompatible spatial data. *Journal of the American Statistical Association* 97, 632-648.

- Graham, D.J., Rollet, A.-J., Piégay, H., Rice, S.P., 2010. Maximizing the accuracy of imagebased surface sediment sampling techniques. *Water Resources Research* 46 [http:// dx.doi.org/10.1029/2008WR006940](http://dx.doi.org/10.1029/2008WR006940).
- Grandjean, G., Bitri, A., Krzeminska, D.M., 2011. Characterisation of a landslide fissure pattern by integrating seismic azimuth tomography and geotechnical testing. *Hydrological Processes* 26, 2120-2127.
- Günther, A., Carstensen, A., Pohl, W., 2004. Automated sliding susceptibility mapping of rock slopes. *Natural Hazards and Earth System Sciences* 4, 95-102.
- Harper, J.T., Humphrey, N.F., Pfeffer, W.T., 1998. Crevasse patterns and the strain-rate tensor: a high-resolution comparison. *Journal of Glaciology* 44, 68-76.
- Hoek, E., Bray, J.W., 1981. *Rock Slope Engineering*. The Institution of Mining and Metallurgy, London.
- Hong, G., Zhang, Y., 2008. A comparative study on radiometric normalization using high resolution satellite images. *International Journal of Remote Sensing* 29, 425-438.
- Hoover, A.D., Kouznetsova, V., Goldbaum, M., 2000. Locating blood vessels in retinal images by piecewise threshold probing of a matched filter response. *IEEE Transactions on Medical Imaging* 19, 203-210.
- Jaboyedoff, M., Baillifard, F., Couture, R., Locat, J., Locat, P., 2004. Toward preliminary hazard assessment using DEM topographic analysis and simple mechanical modeling by means of sloping local base level. In: Lacerda, W.A., Ehrlich, M., Fontoura, A.B., Sanyal, A. (Eds.), *Landslides: Evaluation and Stabilization*. Taylor & Francis Group, London, pp. 199-205.
- Jammalamadaka, S.R., SenGupta, A., 2001. *Topics in Circular Statistics*. World Scientific, Singapore.
- Ke, C.C., Chen, C.S., Tu, C.H., 2008. Determination of fracture toughness of anisotropic rocks by boundary element method. *Rock Mechanics and Rock Engineering* 41, 509-538.
- Khattak, G.A., Owen, L.A., Kamp, U., Harp, E.L., 2010. Evolution of earthquake-triggered landslides in the Kashmir Himalaya, northern Pakistan. *Geomorphology* 115, 102-108.
- Krauskopf, K.B., Feitler, S., Griggs, A.B., 1939. Structural features of a landslide near Gilroy, California. *Journal of Geology* 47, 630-648.
- Krzeminska, D.M., Bogaard, T.A., van Asch, T.W.J., van Beek, L.P.H., 2011. A conceptual model of the hydrological influence of fissures on landslide activity. *Hydrology and Earth System Sciences* 8, 11039-11073.
- Lampert, T.A., O'Keefe, S.E.M., 2011. A detailed investigation into low-level feature detection in spectrogram images. *Pattern Recognition* 44, 2076-2092.
- Lampert, T.A., Stumpf, A., Gancarski, P., submitted for publication. An empirical study into

expert agreement and ground truth estimation. IEEE Conference on Computer Vision and Pattern Recognition, Portland, USA.

Malet, J.P., 2003. Les 'glissements de type écoulement' dans les marnes noires des Alpes du Sud. Morphologie, fonctionnement et modélisation hydro-mécanique. PhD, Université Louis Pasteur, Strasbourg (in French).

Malet, J.-P., Auzet, A.-V., Maquaire, O., Ambroise, B., Descroix, L., Esteves, M., Vandervaere, J.-P., Truchet, E., 2003. Soil surface characteristics influence on infiltration in black marls: application to the Super-Sauze earth flow (southern Alps, France). *Earth Surface Processes and Landforms* 28, 547-564.

Malet, J.P., van Asch, T.W.J., van Beek, R., Maquaire, O., 2005a. Forecasting the behaviour of complex landslides with a spatially distributed hydrological model. *Natural Hazards and Earth System Sciences* 5, 71-85.

Malet, J.P., Laigle, D., Remaître, A., Maquaire, O., 2005b. Triggering conditions and mobility of debris flows associated to complex earthflows. *Geomorphology* 66, 215-235.

Mallast, U., Gloaguen, R., Geyer, S., Rödiger, T., Siebert, C., 2011. Semi-automatic extraction of lineaments from remote sensing data and the derivation of groundwater flowpaths. *Hydrology and Earth System Sciences Discussions* 8, 1399-1431.

Marr, D., Hildreth, E., 1980. Theory of edge detection. *Proceedings of the Royal Society of London, Series B: Biological Sciences* 207, 187-217.

Martha, T., Kerle, N., van Westen, C.J., Kumar, K., 2010. Characterising spectral, spatial and morphometric properties of landslides for semi-automatic detection using object-oriented methods. *Geomorphology* 116, 24-36.

Matheson, G.D., 1983. Rock Stability Assessment in Preliminary Site Investigations – Graphical Methods. Transport and Road Research Laboratory, Crownthorne.

McCalpin, J., 1984. Preliminary age classification of landslides for inventory mapping. 21st Annual Engineering Geology and Soils Engineering Symposium, Moscow, Idaho, pp. 99-111.

Meisina, C., 2006. Characterisation of weathered clayey soils responsible for shallow landslides. *Natural Hazards and Earth System Sciences* 6, 825-838.

Melton, F.A., 1959. Aerial photographs and structural geomorphology. *Journal of Geology* 67, 351-370.

Mendonca, A.M., Campilho, A., 2006. Segmentation of retinal blood vessels by combining the detection of centerlines and morphological reconstruction. *IEEE Transactions on Medical Imaging* 25, 1200-1213.

Metzger, W., 1975. *Gesetze des Sehens*, 3. Auflage. Waldemar Kramer, Frankfurt am Main.

- Niethammer, U., Rothmund, S., James, M.R., Travelletti, J., Joswig, M., 2010. UAV-based remote sensing of landslides. *ISPRS Commission V Mid Term Symposium XXXVIII, Part 5*, pp. 496-501.
- Niethammer, U., James, M.R., Rothmund, S., Travelletti, J., Joswig, M., 2011a. UAV-based remote sensing of the Super-Sauze landslide: evaluation and results. *Engineering Geology* 128, 2-11.
- Niethammer, U., Rothmund, S., Schwaderer, U., Zeman, J., Joswig, M., 2011b. Open source image-processing tools for low cost UAV-based landslide investigations. *The International Archives of the Photogrammetry, Remote Sensing and Spatial Information Sciences XXXVIII-1/C22*.
- Otsu, N., 1979. A threshold selection method from gray-level histograms. *IEEE Transactions on Systems, Man, and Cybernetics* 9, 62-66.
- Papari, G., Petkov, N., 2011. Edge and line oriented contour detection: state of the art. *Image and Vision Computing* 29, 79-103.
- Parise, M., 2003. Observation of surface features on an active landslide, and implications for understanding its history of movement. *Natural Hazards and Earth System Sciences* 3, 569-580.
- Passchier, C.W., Trouw, R.A.J., 2005. *Microtectonics*. Springer, Berlin Heidelberg.
- Pollard, D.D., Fletcher, R.C., 2005. *Fundamentals of Structural Geology*. Cambridge University Press, New York. Third printing with corrections.
- Prats, X., Ramiírez, J., Delgado, L., Royo, P., 2012. Regulations and requirements. In: Angelov, P. (Ed.), *In Sense and Avoid in UAS: Research and Applications*. Wiley, Chichester, pp. 87-117.
- Priest, S.D., 1993. *Discontinuity Analysis for Rock Engineering*. Chapman & Hall, London.
- Quackenbush, L.J., 2004. A review of techniques for extracting linear features from imagery. *Photogrammetric Engineering and Remote Sensing* 70, 1383-1392.
- Riedel, W., 1929. Zur Mechanik geologischer Brucherscheinungen. *Zentralblatt für Mineralogie, Geologie und Paläontologie B* 354-368.
- Sander, P., Minor, T.B., Chesley, M.M., 1997. Ground-water exploration based on lineament analysis and reproducibility tests. *Ground Water* 35, 888-894.
- Schott, J.R., Salvaggio, C., Volchok, W.J., 1988. Radiometric scene normalization using pseudoinvariant features. *Remote Sensing of Environment* 26, 1-16.
- Schulson, E.M., Duval, P., 2009. *Creep and Fracture of Ice*. Cambridge University Press, New York.
- Selby, M.J., 1993. *Hillslope Materials and Processes*, 2nd edition. Oxford University Press, Oxford.
- Serra, J., 1982. *Image Analysis and Mathematical Morphology*. Academic Press, Orlando.
- Shao, Y., Guo, B., Hu, X., Di, L., 2011. Application of a fast linear feature detector to road extraction

from remotely sensed imagery. *IEEE Journal of Selected Topics in Applied Earth Observations and Remote Sensing* 4, 626-631.

Shreve, R.L., 1966. Sherman landslide, Alaska. *Science* 154, 1639-1643.

Shruthi, R.B.V., Kerle, N., Jetten, V., 2011. Object-based gully feature extraction using high spatial resolution imagery. *Geomorphology* 134, 260-268.

Soares, J.V.B., Leandro, J.J.G., Cesar, R.M., Jelinek, H.F., Cree, M.J., 2006. Retinal vessel segmentation using the 2-D Gabor wavelet and supervised classification. *IEEE Transactions on Medical Imaging* 25, 1214-1222.

Sofka, M., Stewart, C.V., 2006. Retinal vessel centerline extraction using multiscale matched filters, confidence and edge measures. *IEEE Transactions on Medical Imaging* 25, 1531-1546.

Sowers, G.F., Royster, D.L., 1978. Field investigation. In: Schuster, R.L., Krizek, R.J. (Eds.), *Landslides: Analysis and Control*. Transportation Research Board, Special Report, 176. National Academy of Science, Washington, DC, pp. 81-111.

Stumpf, A., Kerle, N., 2011. Object-oriented mapping of landslides using Random Forests. *Remote Sensing of Environment* 115, 2564-2577.

Stumpf, A., Lampert, T.A., Malet, J.-P., Kerle, N., 2012. Multi-scale line detection for landslide fissure mapping. *International Geoscience and Remote Sensing Symposium*, Munich, Germany, p. 4.

Tarboton, D.G., Bras, R.L., Rodriguez-Iturbe, I., 1991. On the extraction of channel networks from digital elevation data. *Hydrological Processes* 5, 81-100.

Tchalenko, J.S., 1970. Similarities between shear zones of different magnitudes. *Geological Society of America Bulletin* 81, 1625-1640.

Ter-Stephanian, G., 1946. On the landslide cracks classification. *Bulletin of the Academy of Sciences of the Armenian SSR* 10, 65-80 (in Russian with abstracts in Armenian and English).

Travelletti, J., 2011. *Imagerie multi-paramètres et multi-résolutions pour l'observation et la caractérisation des mécanismes de glissements-coulées*. PhD, Université de Caen Basse-Normandie, Strasbourg.

Travelletti, J., Malet, J.P., 2012. Characterization of the 3D geometry of flow-like landslides: a methodology based on the integration of heterogeneous multi-source data. *Engineering Geology* 128, 30-48.

Trimble, 2011. *eCognition Developer 8.64.0*. Reference Book. Trimble Documentation, München.

Tveite, H., Langaas, S., 1999. An accuracy assessment method for geographical line data sets based on buffering. *International Journal of Geographical Information Science* 13, 27-47.

Vallet, J., 2007. GPS/IMU and LiDAR integration to aerial photogrammetry: development and practical experiences with Helimap System(R), 27. *Wissenschaftlich-Technische Jahrestagung der DGPF, Dreiländertagung, Muttenz.*

van Asch, T.W.J., van Beek, L.P.H., Bogaard, T.A., 2009. The diversity in hydrological triggering systems of landslides. *The First Italian Workshop on Landslides, Napoli, Italy*, pp. 151-156.

Vaughan, D.G., 1993. Relating the occurrence of crevasses to surface strain rates. *Journal of Glaciology* 39, 255-266.

Vicente-Serrano, S.M., Pérez-Cabello, F., Lasanta, T., 2008. Assessment of radiometric correction techniques in analyzing vegetation variability and change using time series of Landsat images. *Remote Sensing of Environment* 112, 3916-3934.

Walter, M., Niethammer, U., Rothmund, S., Joswig, M., 2009. Joint analysis of the SuperSauze (French Alps) mudslide by nanoseismic monitoring and UAV-based remote sensing. *First Break* 27, 53-60.

Walter, M., Arnhardt, C., Joswig, M., 2012. Seismic monitoring of rockfalls, slide quakes, and fissure development at the Super-Sauze mudslide, French Alps. *Engineering Geology* 128, 12-22.

Wang, E.Z., Shrive, N.G., 1995. Brittle fracture in compression: mechanisms, models and criteria. *Engineering Fracture Mechanics* 52, 1107-1126.

Watts, A.C., Ambrosia, V.G., Hinkley, E.A., 2012. Unmanned aircraft systems in remote sensing and scientific research: classification and considerations of use. *Remote Sensing* 4, 1671-1692.

Youssef, A., Maerz, N., Hassan, A., 2009. Remote sensing applications to geological problems in Egypt: case study, slope instability investigation, Sharm El-Sheikh/ Ras-Nasrani area, southern Sinai. *Landslides* 6, 353-360.

Zhang, B., Zhang, L., Zhang, L., Karray, F., 2010. Retinal vessel extraction by matched filter with first-order derivative of Gaussian. *Computers in Biology and Medicine* 40, 438-445.

Joint analysis of the Super-Sauze (French Alps) mudslide by nanoseismic monitoring and UAV-based remote sensing

M. WALTER^{a,*}; U. NIETHAMMER^a, S. ROTHMUND^a, M. JOSWIG^a

^aInstitute for Geophysics, University of Stuttgart, Germany

Abstract

Marco Walter, Uwe Niethammer, Sabrina Rothmund and Manfred Joswig report on how the study of landslide dynamics at locations like the Super-Sauze mudslide in the French Alps have benefited from emerging methods such as nanoseismic monitoring and unmanned aerial vehicle remote sensing by resolving surface fractures and mudslide-bedrock interaction.

Introduction

Due to global climate change and the fact that mountain areas will become inhabited at a progressive rate, landslides pose a huge threat to the environment, the infrastructure and the people living in the vicinity of affected areas. In inhabited regions landslides can cause enormous economic damage and unfortunately human losses as well. Slope instabilities are caused by the non-linear interaction of geological, hydrological, morphological, and soil mechanical processes on many scales in time and space. Models for the prediction of landslides are very vulnerable because the influencing parameters are still incompletely or unsatisfactorily observed. Therefore the observation of landslides by multiple disciplines is the challenge of recent studies. Integrated analysis should reveal further insights into the process interactions and the complex behaviour of landslides.

Our research is highly motivated by newly improved measuring techniques that can resolve specific landslide parameters at higher resolution, and in repeat observations. We can determine landslide dynamics using nanoseismic monitoring (Joswig, 2008) and UAV-based

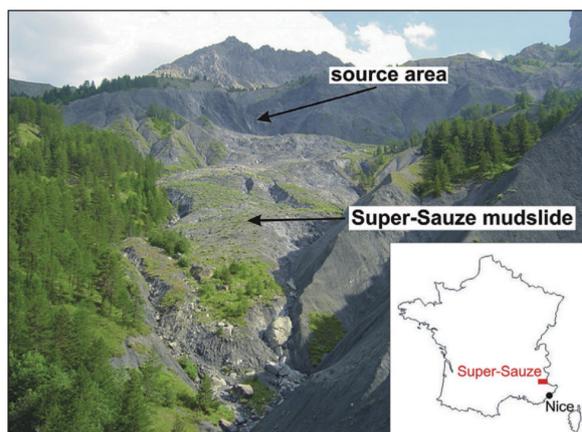


Figure 1 Location of Super-Sauze and upward view of the mudslide and its source area. Picture was taken in summer of 2006.

(unmanned aerial vehicle) high-resolution remote sensing (Niethammer et al., 2009). With the former, one can resolve fracture processes in the shallow subsurface (Walter and Joswig, 2008; Walter and Joswig, 2009). The latter technique is especially suited for mapping the corresponding photo-lineaments at the slope's surface. Our geophysical investigations were carried out at the Super-Sauze, French Alps mudslide (Figure 1) and the Heumoes, Austrian Alps slope. They are part of the research project 'Coupling of flow and deformation processes for modelling the movement of natural slopes' (www.grosshang.de).

*Corresponding author: marco.walter@geophys.uni-stuttgart.de

Applying geophysical methods like active seismics, ground penetrating radar, and geo-electrical mapping and sounding, Grandjean et al. (2007) inferred dynamic processes and static properties for the mudslide in Super-Sauze. Single fracture processes during the movement of landslides consisting of hard rock (fragments) have been seismically monitored in the Alps (e.g., Brückl and Mertl, 2006; Spillmann et al., 2007) and in Norway (Roth et al., 2005). Fracturing within creeping landslides consisting of weak sediments radiates signals of much smaller energy; it has first been observed, to our knowledge, by Walter and Joswig (2008) applying the nanoseismic monitoring method.

Here we describe how the seismic moni-

toring of the slope's subsurface is combined with the UAV-based remote sensing of the surface. By remotely sensing the active slope, its dimensions and surface structures can be characterized (Niethammer et al., 2009). Aerial images taken by satellites or airplanes have spatial resolutions of metres to decimetres. They can be used for landslide detection and to determine deformations on a large scale (Henry et al., 2002). UAV-based remote sensing is suited to map surface structures with high spatio-temporal resolution, e.g., fissure patterns on landslides with centimetre resolution and monthly overflight. In particular, it is possible to detect and analyze dislocation vectors on landslides from these data (Niethammer et al., 2009).

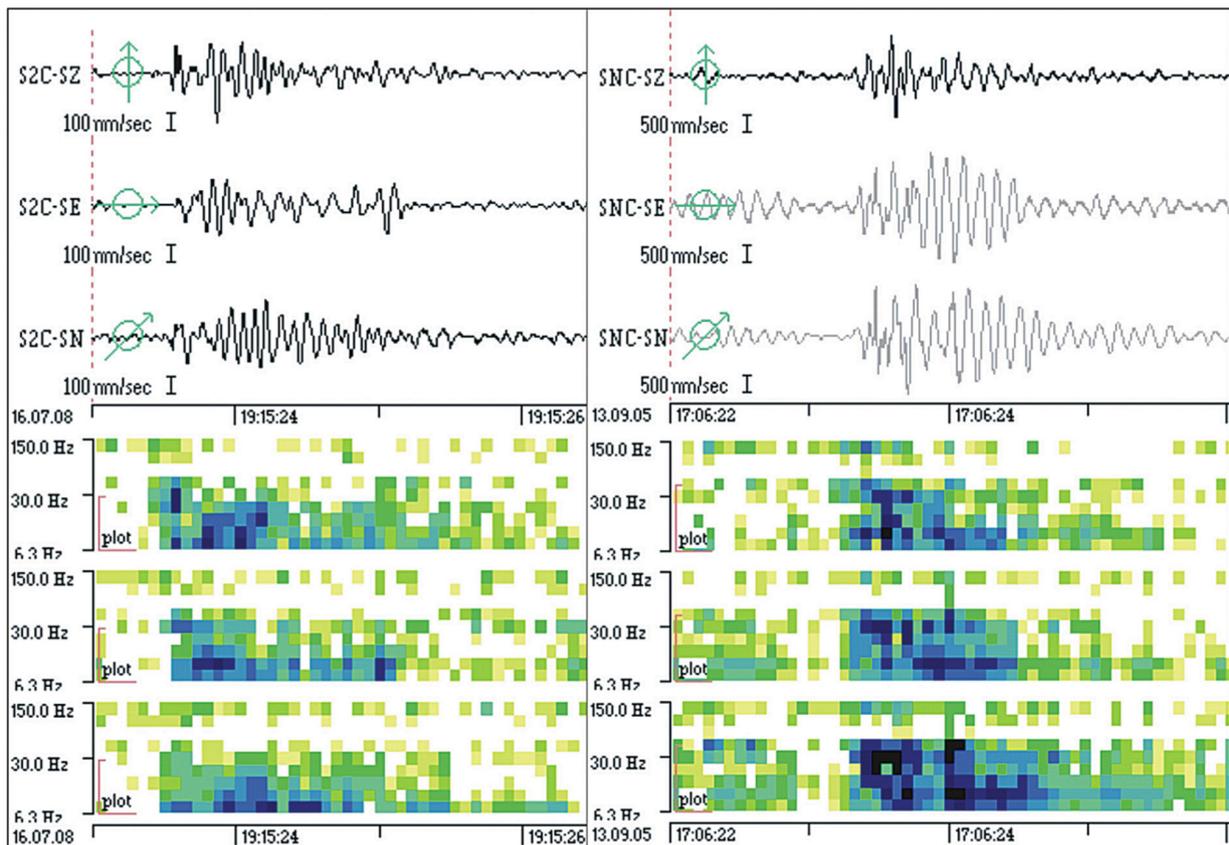


Figure 2 Typical seismograms and sonograms of deformation processes caused by softrock-landslides, recorded with a 3c-seismometer: Left: 'fracture' event, $M_L = -2.2$ in ~ 120 m distance, recorded at the Super-Sauze mudslide Right: fracture process of $M_L = -1.2$ in ~ 100 m distance observed at the Heumoes slope. Modified after Walter and Joswig 2008, 2009.

Observation of slope dynamics by nanoseismic monitoring

Nanoseismic monitoring acts as a seismic ‘microscope’ to detect small impulsive signals in the subsurface, and was first applied to map sinkholes in Israel (Wust-Bloch and Joswig, 2006). We used the method to monitor fracture processes at the Heumoes slope, Austria (Walter and Joswig, 2008). Like the Super-Sauze mudslide, the Heumoes slope consists of weak sediments. The existence of impulsive seismic signals wasn’t expected due to the presumed lack of brittle material that could generate impulse fracture release. The increased sensitivity available from nanoseismic monitoring was needed to discover these local fracture processes in sediments at all.

Data acquisition/data processing

In Super-Sauze, the seismic data was acquired during a 10-day field campaign in July 2008 deploying four tripartite seismic mini arrays on the mudslide (Figure 4). Each mini array, so-called seismic navigating system (SNS) consists of one three-component and three vertical, short-period seismometers installed with an aperture of 30-40 m. Data was recorded in continuous mode with a sampling rate of 400 Hz. The observation period was limited to 10 days because nanoseismic monitoring resembles more a campaign of refraction seismics, than a permanent seismic network installation. It achieves its superior sensitivity by not compromising in site selection (e.g., demands for shelter, power, communications) or on cost of increased vulnerability by extended array cabling. The data set was processed using the software HypoLine, an interactive, graphical jack knife tool which displays the most plausible solution for low-SNR (signal to noise ratio) signals, resolving the influence of individual parameters on the event localization in real-time (Joswig, 2008).

Signal classification

From seismic data analysis, we could detect different types of events caused by the dynamics in the source area of the mudslide, and within the slope itself. The signals vary in duration, amplitude, frequency content, and consequently in sonogram patterns (Walter and Joswig, 2009). We could distinguish three principal types of events: The ‘rockfall’ events occur in the source area of the mudslide while the events of type ‘fracture’ and type ‘scratch’ are caused within the mudslide body during its deformation. The classification of the observed signals is described in detail by Walter and Joswig (2009). For the joint analysis of the mudslide dynamics in Super-Sauze by nanoseismic monitoring and UAV-based remote sensing, we focus on the characteristics and locations of the ‘fracture’ and ‘scratch’ events.

Seismic signals caused by failure of the slope material

We could detect 34 ‘fractures’, which show clear phase onsets (Figure 2), allowing for their localization by standard seismological procedures. The duration of these events lies between 2-5 seconds, the maximum amplitude varies between 40 and 200 nm/s (peak to peak) and the frequency content is concentrated between 10-80 Hz. The signals had to be recorded on at least 2 SNS for being localized, where the distance range for reliable detection was within some 200 m. The emergent onset, the lack of higher frequencies above 80 Hz, and the signal incoherency indicate intense scattering caused by the high heterogeneity of slope material (Figure 2). Comparable signals have been observed on the Heumoes slope, which consists of soft rock material as well (Walter and Joswig, 2008). The magnitudes of ‘fractures’ at Super-Sauze vary between $-3.2 \leq ML \leq -1.3$. This range is about one magnitude lower than at Heumoes slope ($-2.2 \leq ML \leq -0.7$) indicating a 10 times lower ambient noise level in Super-Sauze.

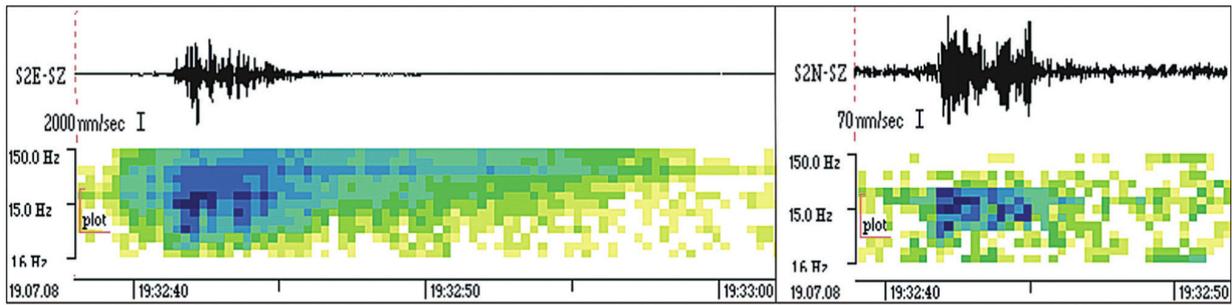


Figure 3 Typical waveforms and sonogram patterns of one 'scratch' sequence, recorded with a 1c-station close to the source location (left) and with a 1c-station in a distance of ~ 25 m (right). Modified after Walter and Joswig 2009.

The localized fractures are mainly clustered in the middle part of the mudslide (Figure 4). The cluster correlates with the part of the slope showing the highest velocities at the surface. The three events located in the south, outside of the slope catchment, are probably generated by material failure in the hard rock mass in the source area of the mudslide (Figure 4). Another cluster of 'fractures' is located directly at the boundary between the mudslide material and one of the emerging in-situ crests in the middle part of the slope. The estimated detection threshold for these events is $ML = -2.6$ for a slant distance of about 140 m. The estimated localization accuracy is about 10% of the epicentral distance. As the source depth could not be determined due to the sparse station distribution, it is not possible to estimate at which depth nor along which material interface the source processes took place.

Furthermore, we recorded 44 signals showing significant differences compared to the 'fracture' impulses. They occur as sequences lie barely above the ambient noise level and could not be observed at Heumoos slope due to the tenfold higher noise level there. These 'scratch' events haven't been expected previously. Their duration varies between 2-20 seconds, and the small amplitudes were only recorded at one single SNS. Compared to 'fractures', signal energy is prevailing at higher frequencies up to 150 Hz (Figure 3). Enormous attenuation effects can be seen within one single SNS with decay of signal amplitude by a factor of thirty. No distinct phase onsets could be identified, thus we just estimated the source area close

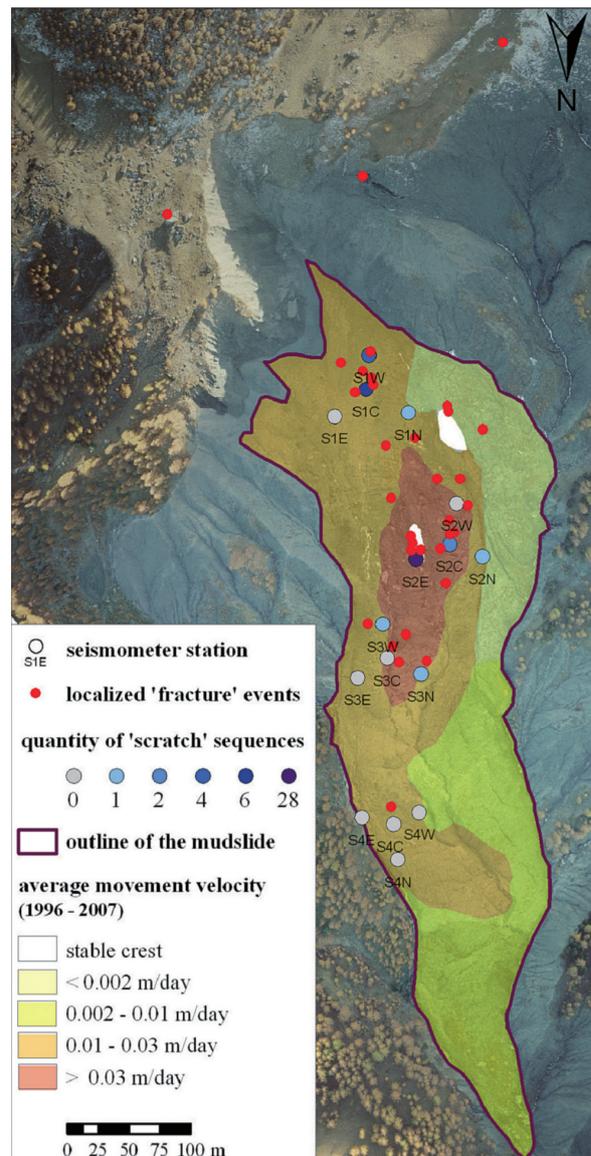


Figure 4 Location of the installed seismometer stations (circles), epicentres of the located 'fractures' (red) and the quantity of 'scratch' sequences recorded at each station (blue colour scale). Underlayment is the map of the average movement velocities of the mudslide (1996-2007).

to the station with highest amplitude. Figure 4 shows the quantity of these 'scratch' events at each station. Like the 'fracture' locations, most of the 'scratch' events occurred in the middle part of the slope. The source area of 64% of these events is estimated to be close to the station S2E, at the boundary of the slope material and one of the emerging in-situ crests.

UAV-based remote sensing of the mudslide

The Super-Sauze mudslide was imaged in October 2008 using a self-designed quad-rotor remote sensing platform. The achievable flight height over ground is 20 m to 200 m, resulting in ground resolutions between 1-8 cm per pixel. This high resolution is essential to detect small fissure patterns at the surface. Quad-rotor systems basically enable close-range photographs of any desired area. Compared to conventional helicopters, quad-rotor systems do not require mechanical steering of the rotors and are stabilized by inertial measurement sensors (IMU). Especially in alpine terrain, like at the mudslide in Super-Sauze, such robust and reliable UAV-systems have considerable advantages. Open source projects are available to provide quad-rotor software and hardware (UAVP, 2008; Mikrocopter, 2008).



Figure 5 Quad-rotor system for remote sensing and its main characteristics. Here in use at the mudslide in Super-Sauze.

The quad-rotor system and its main features are illustrated in Figure 5.

Image acquisition/image processing

The installed compact camera suffers from optical distortion in the wide-angle range (barrel distortion). In a first processing step this distortion of all acquired photographs was corrected by a polynomial correction approach. In a second step, plane image rectification was applied to all images. The necessary ground information was gained by 199 ground control points (GCP) on the surface of the mudslide, measured by a differential GPS system with an accuracy of a few cm. This information was also necessary for the further geocoding of the pictures. In a third step, 59 rectified photographs were combined to one high resolution ortho-mosaic. Errors could be identified by comparison of the visible GCP locations in the photograph to the DGPS-measured locations, using a geographic information system (GIS). Areas which still showed ineligible errors in rectification were cut out manually before the final assembly of the rectified images was performed. The uniformly coloured mosaic was gained by colour balance correction in conjunction with an image-blending algorithm.

Displacement analysis

In May 2007 an aerial LIDAR scan of the Super-Sauze mudslide was acquired, and on this basis another DTM and orthophotograph were created. The spatial resolution of the DTM data is 1.0 m, the resolution of the ortho-photograph is about 0.25 m. The image analysis was carried out by the comparison of the geocoded ortho-photograph from 2007 and the geocoded ortho-mosaic of our UAV-based campaign in October 2008 (Niethammer et al., 2009).

Superficial displacement rates were identified directly, comparing the locations of rocks, stones, and parts of vegetation patches between the ortho-photograph from 2007 and our acquired ortho-mosaic from 2008. These measurements were performed manually within a GIS. Hence, between May 2007 and October

2008, displacements of 7.1 m - 55.4 m were detected. The maximum deviation reaches 3.9 m, the mean error can be quantified to be 0.5 m.

However, areas which were characterized by extremely high displacement rates couldn't be compared, since no clear detectable features were left on the surface. In some areas it is likely that fine-grained sediments originating from debris flows cover the main features. The crown of the slope, the source area, is characterized by enormous dynamics, e.g., rockfalls, which cover these structures as well.

The identified displacement vectors were converted to daily displacement rates and compared to long-term displacement measurements between 1996-2007, acquired by laser scanning and DGPS measurements (Amitrano et al., 2007, Figure 6).

The displacement rates of our studies are up to ten times higher in the source area, and in the remaining part of the landslide approximately two times higher than the average movement rates. This deviation might be explained by higher dynamics in recent years, but the location of the strongest dynamics did not change.

Analysis of fissure patterns

The spatial resolution of the acquired UAV-based ortho-mosaic allows for detailed analysis of fissure structures. The hard rock boundaries of the Super-Sauze mudslide are very complex caused by the diversified former topography, comparable to badlands, consisting of buried crests and gullies. As the dynamics of the mudslide are high, the behaviour of the slope can be compared to glaciers, with similar fissure structures observed at the surface. Fissure structures on glaciers have been thoroughly investigated (Hambrey and Alean, 1994; Hambrey and Lawson, 2000; Wilhelm, 1975). In our context, fissure patterns on glaciers can be compared to the ones we observed at Super-Sauze. From their spatio-temporal occurrences one can learn about their development, and consequently about the behaviour of the entire mudslide.

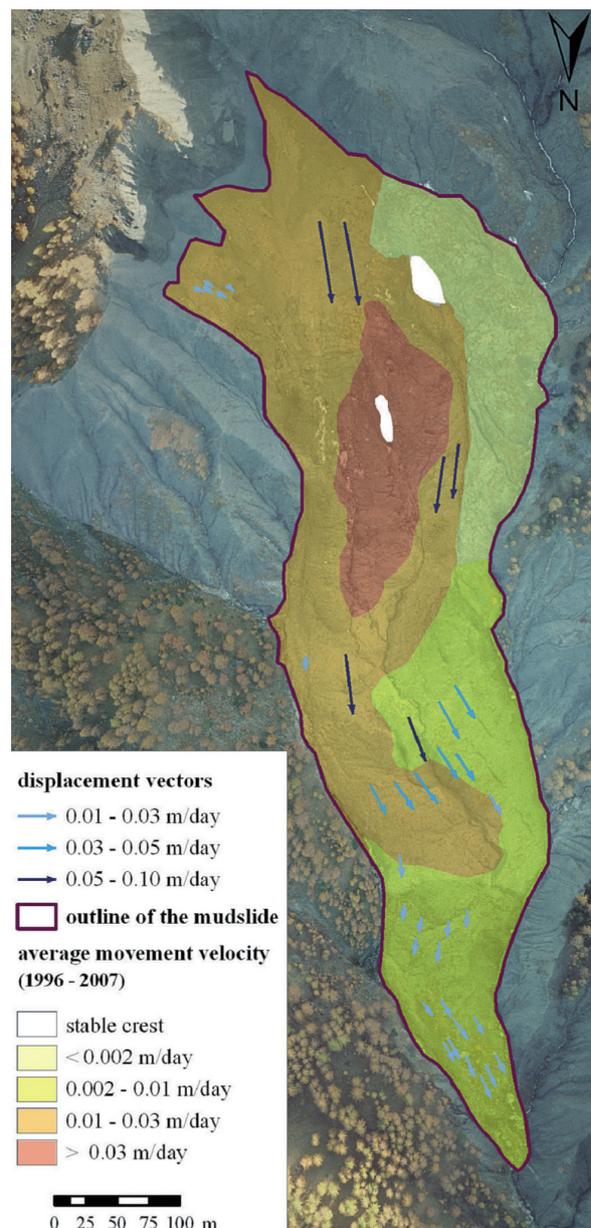


Figure 6 Displacement vectors (blue colours) between May 2007 - October 2008 plotted on top of the average movement velocity map (1996-2007).

As shown in Figure 7, there are several structures at the mudslide's surface which differ in shape and orientation. The structures could be identified as longitudinal fissures, transversal fissures, shear fissures, and cross-shaped fissures. The occurrence of those tension cracks depend on the bedrock topography, as well as on the lateral hard rock boundary, cavity, and extension in the longitudinal direction of movement, and changes in the decline

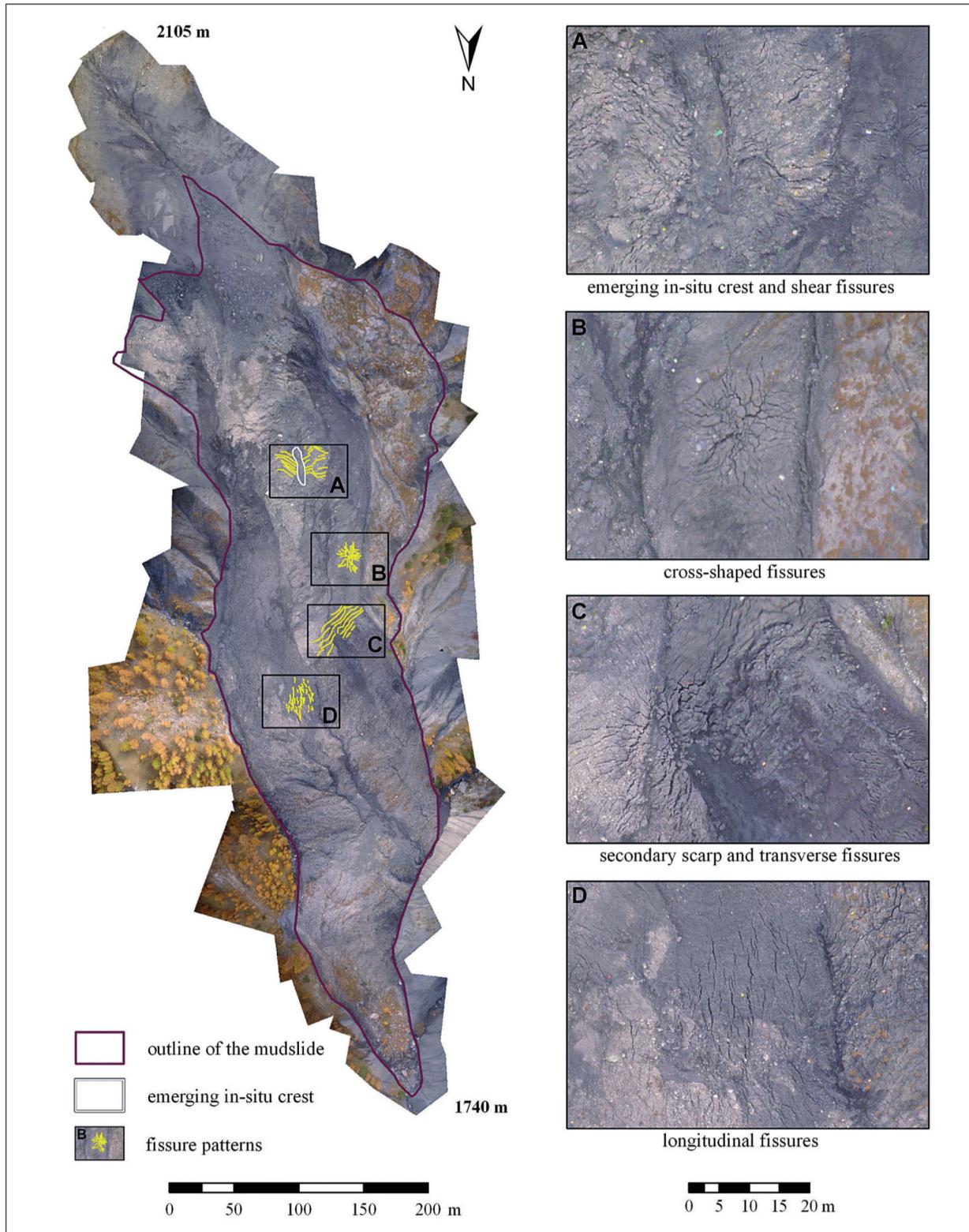


Figure 7 Ortho-mosaic from pictures taken in October 2008 with locations of observed fissure patterns.

of the slope (Wilhelm, 1975). Longitudinal fissures mostly occur after a cavity in the longitudinal direction of the movement, where an increased extension is initiated (Hambrey and Alean, 1994); such structures are shown in Figure 7d. The cavity of the stream can be explained by a curved crest in this area hidden by the mudslide material today (Figure 8). Transversal fissures often can be observed in areas where changes in the decline of the slope are present (Varnes, 1978; Hambrey and Alean, 1994; Wilhelm, 1975); comparable structures on the mudslide are shown in Figure 7c. In this particular case, the change of the decline of the slope can be explained by the secondary scarp in this area.

Marginal or shear fissures mostly occur at the boundary area between solid rock margins and the landslide material, resulting in a velocity transition (Wilhelm, 1975). These fissures run in accordance with the shear-strain conditions and start from the solid rock boundary with an angle of 30° - 45° up the slope in the direction of the sliding body (Wilhelm, 1975; Hambrey and Alean, 1994, Figure 7a). Beside these patterns we observed 'cross-shaped' fissures, which are probably caused by an unknown combination of these dynamics (Figure 7b). Despite an apparent movement of the sliding surface, fissures linger on the same place. These cross-shaped fissures are obviously a result of tension changes caused by the change of the bedrock-topography in form of in-situ crests within the mudslide material (Figure 8).

Joint interpretation

The observation of mudslide subsurface dynamics by nanoseismic monitoring and the mapping of fissure patterns at surface by UAV-based remote sensing can be combined in a joint interpretation that compensates for inherent weaknesses of each method. In the given field lay out, nanoseismic monitoring cannot precisely determine the depth of the seismically observed events. They could occur within the mudslide, or along the mudslide bedrock

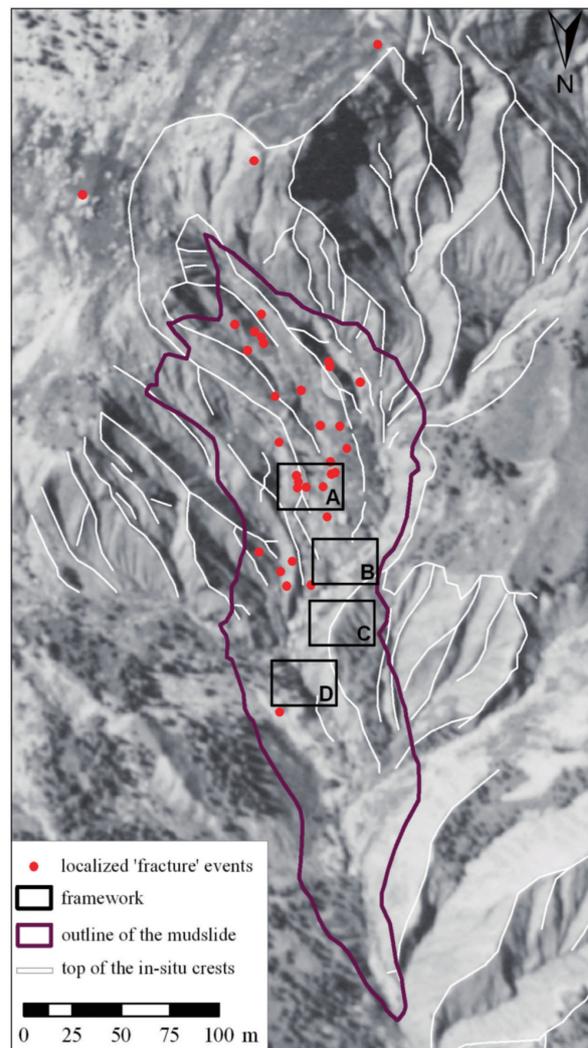


Figure 8 Epicentres of the localized 'fractures', determined displacement vectors (May 2007 - October 2008) and locations of remarkable fissure patterns (see figure 7) mapped on an airborne picture from 1956.

interface. Remote sensing maps fissures but does not directly relate to the time history of generating processes. By chance, one of our seismometers dropped into a newly opened fissure on 22 July 2008. In the few hours before, we had observed four 'fracture' events close by, indicating recent fissure development. We therefore assume that 'fracture' signals are typically generated by fissure development in the shallow subsurface. This assumption is supported by observations of UAV-based remote sensing where fissure patterns could be observed for all cases where subsurface fracture propagated to surface rupture. Only in

the uppermost section, the continuous drop of new material fills fissures shortly after opening. The process of rockfalls can be observed by 'rockfall' or impact signals in nanoseismic monitoring (Walter and Joswig, 2009).

More support of our hypothesis on source processes comes from field and lab observations. Below a depth of some one metre, the mudslide material is permanently water-saturated, but above, water saturation varies seasonally (Malet, 2003). For our observations of impulsive stress relief and fissure patterns, the material must deform in a brittle manner. The mudslide material shows highest shear strength in a range of 15-18% water saturation (Malet, 2003). Once the snow melting period took place, the surface material dries out in summer, and the necessary material properties can be observed.

Our observations at the Super-Sauze mudslide also support prior investigations suggesting that the topography of the bedrock below the mudslide material plays a key role regarding the dynamic of the entire slope instability. By nanoseismic monitoring, we could observe numerous 'scratch' sequences that are generated within the shallow subsurface. Their energetic signature in the frequency-time domain is completely different to the impulsive 'fracture' signals. The vast majority of 'scratch' is bound to in-situ crests indicating scratching and grinding of single rock particles within the mudslide along the crests. Most sequences occur at emerging crests close to or above surface where rock particles are embedded in a shear resistant matrix of dried mud. Our hypothesis is supported by UAV-based remote sensing where several cross-shaped and shear fissures indicating dynamics according to in-situ crests are co-located to 'scratch' sites.

Conclusions

Applying the nanoseismic monitoring method we observed different seismic signals caused by the varying slope dynamics. Our preliminary hypothesis is that the 'fracture' events are

caused by impulsive fracture processes within the unstable material. Similar signals have been observed at Heumoes slope consisting of weak sediments as well (Figure 2, Walter and Joswig, 2008). By contrast, we assume that the 'scratch' sequences are caused by 'scratching' and 'grinding' of single rocks in the slope material against the (emerging) in-situ crests (Walter and Joswig, 2009). Both processes are constrained by the uppermost metre where mudslide material dries out in summer to consolidate with sufficient shear resistance. Our ideas are supported by the existence of fissure patterns at the surface which could be observed by UAV-based remote sensing.

The joint observations by nanoseismic monitoring and UAV-based remote sensing in 2008 indicate that the varying tempo-spatial dynamics of the mudslide in Super-Sauze match the long-term observations. These dynamics are controlled by the fixed topography of the bedrock and the lateral hard rock boundaries where gullies between the crests 'canalize' the sliding material (Malet, 2003). Different fissure patterns at the surface are linked to abrupt changes of in-situ crest orientation in the shallow subsurface (Figure 8). Fissure patterns could be identified by comparison to glaciers where similar dynamics take place.

The joint observations of the mudslide in Super-Sauze indicate that the variations of tempo-spatial dynamics in 2008 are similar to the dynamics within the recent years. We can support prior observations (Malet, 2003) that the stable, buried in-situ crests at the bedrock of the mudslide directly affect the behaviour of the entire mudslide, and that gullies between the crests 'canalize' the sliding material. Several fissure patterns at the surface are linked to an abrupt change of the in-situ crests' orientation in the shallow subsurface (Figure 8).

Acknowledgements

We thank all colleagues from the OMIV project (Observatoire des Instabilités de Versants) for the helpful discussions and their support in

the field. The authors are especially grateful to Jean-Philippe Malet (School and Observatory of Earth Sciences, University of Strasbourg) for providing several airborne pictures (Figures 4, 6, and 8) and datasets. Many thanks to

Eberhard Claar (Institute for Geophysics, Universität Stuttgart) who built significant components of the quad-rotor system. The work is funded by the DFG within the project FOR 581 'Natural Slopes'.

References

Amitrano, D., Gaffet, S., Malet, J.-P. and Maquaire, O. [2007] Understanding mudslides through micro-seismic monitoring: the Super-Sauze (SouthEast French Alps) case study. *Bulletin de la Société Géologique de France* 178(2), 149-157.

Brückl, E. and Mertl, S. [2006] Seismic Monitoring of Deep-Seated Mass Movements. INTER-PRAEVENT International Symposium 'Disaster Mitigation of Debris Flows, Slope Failures and Landslides.' Universal Academy Press, Tokyo, Japan, 571-580.

de Montety, V., Marc, V., Emblanch, C., Malet, J.-P., Bertrand, C., Maquaire, O. and Bogaard, T.A. [2007] Identifying the origin of groundwater and flow processes in complex landslides affecting black marls: Insights from a hydrochemical survey. *Earth Surface Processes and Landforms*, 32(1), 32-48.

Flageollet, J.-C., Malet, J.-P., Maquaire, O. and Schmutz, M. [2004] Integrated investigations on landslides: example of the Super-Sauze earthflow. In: Casale, R., Margottini, C. (Eds) *Natural Disasters and Sustainable Development*, Springer-Verlag, Berlin, 213-238.

Flageollet, J.-C., Malet, J.-P. and Maquaire, O. [1999] The 3D structure of the Super-Sauze earthflow: a first stage towards modelling its behaviour. *Physics and Chemistry of the Earth*, 25(9), 785-791.

Flageollet, J.-C., Maquaire, O., Martin, B. and Weber, D. [1999] Landslides and climatic conditions in the Barcelonnette and Vars basins (Southern French Alps, France). *Geomorphology*, 30, 65-78.

Grandjean, G., Malet, J.-P., Bitri, A. and Méric, O. [2007] Geophysical data fusion by fuzzy logic for imaging the mechanical behaviour of mudslides. *Bulletin de la Societe Geologique de France*, 178(2), 127-136.

Hambrey, M. and Alean, J. [1994] *Glaciers*. Cambridge University Press, 208pp.

Hambrey, M. J. and Lawson, W. J. [2000] Structural styles and deformation fields in glaciers: a review. In: Maltman, A. J., Hubbard, B. and Hambrey, M. J. (Eds) *Deformation of Glacial Materials*, Geol. Soc. Spec. Publ., 176, 59-83.

Henry, J.-B, Malet, J.-P., Maquaire, O. and Grussenmeyer, P. [2002] The use of small-format and low-altitude aerial photos for the realization of high-resolution DEMs in mountainous areas: application to the Super-Sauze earthflow (Alpes-de-Haute-Provence, France) *Earth Surface Processes and Landforms*, 27(12), 1339-1350.

Joswig, M. [2008] Nanoseismic Monitoring fills the gap between microseismic networks and passive seismic, *First Break*, 26(6) 121-128.

Malet, J.-P. and Maquaire, O. [2003] Black marl earthflows mobility and long-term seasonal dynamic in southeastern France. In: Picarelli, L. (Ed) *International Conference on Fast Slope Movements: Prediction and Prevention for Risk Mitigation*, Patron Editore, Bologna, 333-340.

Malet, J.-P. [2003] *Les glissements de type écoulement dans les marnes noires des Alpes du Sud. Morphologie, fonctionnement et modélisation hydromécanique*. Thèse de Doctorat, Université Louis Pasteur, Strasbourg, 364pp.

Malet, J.-P., Maquaire, O. and Calais, E. [2002] The use of Global Positioning System for the continuous monitoring of landslides. Application to the Super-Sauze earthflow (Alpes-de-Haute-Provence, France). *Geomorphology*, 43, 33-54.

Mikrocopter 2008. <http://www.mikrocopter.de>.

Niethammer, U., Rothmund, S. and Joswig, M. 2009. UAV-based remote sensing of the slow-moving landslide Super-Sauze. In: Malet, J.-P.,

Remaitre, A., Boogard, T. (Eds) *Proceedings of the International Conference on Landslide Processes: from geomorphologic mapping to dynamic modelling*, Strasbourg, CERG Editions: 69-74.

Roth, M., Dietrich, M., Blikra, L.H. and Lecomte, I. [2005] Seismic monitoring of the unstable rock slope at Aknes, Norway. *NORSAR Report for the International Centre for Geohazards*.

Spillmann, T., Maurer, H., Green, A. G., Heincke, B., Willenberg, H. and Husen, S. [2007] Microseismic investigations of an unstable mountain slope in the Swiss Alps. *J. Geophys. Res.*, 112, B07301.

UAVP [2008] <http://www.uavp.ch>.

Varnes, D.J. [1978] Slope movement types and processes. In: Schuster, R. L. and Krizek, R. J. (Eds) *Landslides—Analysis and Control*. Rep. Natl. Res. Council. Transp. Res. Board, 176, 11-33.

Walter, M. and Joswig, M. [2008] Seismic monitoring of fracture processes generated by a creeping landslide in the Vorarlberg Alps. *First Break*, 26(6), 131-135.

Walter, M. and Joswig, M. [2009] Seismic characterization of slope dynamics caused by softrock-landslides: The Super-Sauze case study. In: Malet,

J.-P., Remaitre, A., Boogard, T. (Eds) *International Conference on Landslide Processes: from geomorphologic mapping to dynamic modelling*, Strasbourg, CERG Editions, 215-220.

Wilhelm, F. [1975] *Schnee- und Gletscherkunde*. Walter de Gruyter Press, 434pp.

Wust-Bloch, G. H. and Joswig, M. [2006] Pre-collapse identification of sinkholes in unconsolidated media at Dead Sea area by Nanoseismic Monitoring, *Geophys. J. Int.*, 167, 1220-1232.

A.2. Entwickelte UAV-Systeme

A.2.1. Flugplattform

Im Rahmen der Forschungen wurden Quadrotor- und Oktokopter-Systeme entwickelt (Abbildung A.1) und Abbildung A.2). Die Quadrotor-Systeme sind mit vier *Brushless*-Motoren ($P_{max} = 4 \times 200 \text{ W}$) ausgestattet, der Achsabstand beträgt 600 mm (Abbildung A.3). Mit einem Eigengewicht von 2100 g können die Quadrotor-Systeme ca. 500 g Nutzlast tragen. Die Flugzeit beträgt ca. 12 min. Die Rahmenkonstruktion wurde aufgrund der geforderten Robustheit aus Aluminium gefertigt. Im Vergleich zu Kohlefaser-Profilen besitzen Aluminium-Profile kein Sprödbruch-Verhalten. Das vergrößerte Abfluggewicht erweist sich zusätzlich vorteilhaft für einen stabilen Flugbetrieb bei Wind.

Für den Einsatz mehrerer Kameras (RGB, NIR und TIR) wurden Oktokopter-Prototypen entwickelt. Diese Systeme sind mit acht Motoren ($P_{max} = 8 \times 200 \text{ W}$) ausgestattet. Der maximale Achsabstand beträgt 1150 mm. Mit einem Eigengewicht von 3200 g kann dieses System eine Nutzlast bis ca. 1500 g tragen. Die Flugzeit beträgt ca. 12 min.

A.2.2. Steuerung (Flight-Ctrl)

Als Steuerungselektronik kommen *Open-Source* Module (Flight-Ctrl¹, und die zugehörigen Sensor-Komponenten) zum Einsatz (Abbildung A.4). Die Steuerungsplatine wird bereits SMD-vorbestückt geliefert. Dennoch müssen bedrahtete Bauelemente und die komplette Verkabelung angelötet werden. Damit das UAV-System die Gier-Ausrichtung halten kann, ist der Einsatz eines Magnetkompasses nötig. Hierzu wird ein MK3Mag¹ eingesetzt. Ein Navi-Ctrl¹ Modul dient dazu, Positionsdaten auszuwerten, und entsprechende Steuerungssignale an die Flight-Ctrl¹ weiterzugeben. Kombiniert mit einem MK-GPS¹ bietet das Modul die Möglichkeit, die aktuelle Position zu halten und zum Startpunkt zurückzukehren oder Wegpunkte abzufliegen.

A.2.3. Fernsteuerung

Als Fernsteuerungsanlage kommt ein 35 MHz Handsender *Robbe*² FX-18 zum Einsatz. Um den gesamten Funktionsumfang der UAVs nutzen zu können, ist ein Umbau der Steuerung notwendig. Neben den beiden Steuerknüppeln (5, 8) wurden weitere Schalter (3, 4, 10, 11) und einen Linearschieber (9) integriert (Abbildung A.5).

¹<http://www.mikrokoetter.de>

²<http://www.robbe.de>



Abbildung A.1.: Quadrotor-System, Befliegung der Super-Sauze Hangrutschung



Abbildung A.2.: Prototyp des entwickelten Oktokopter UAV-Systems

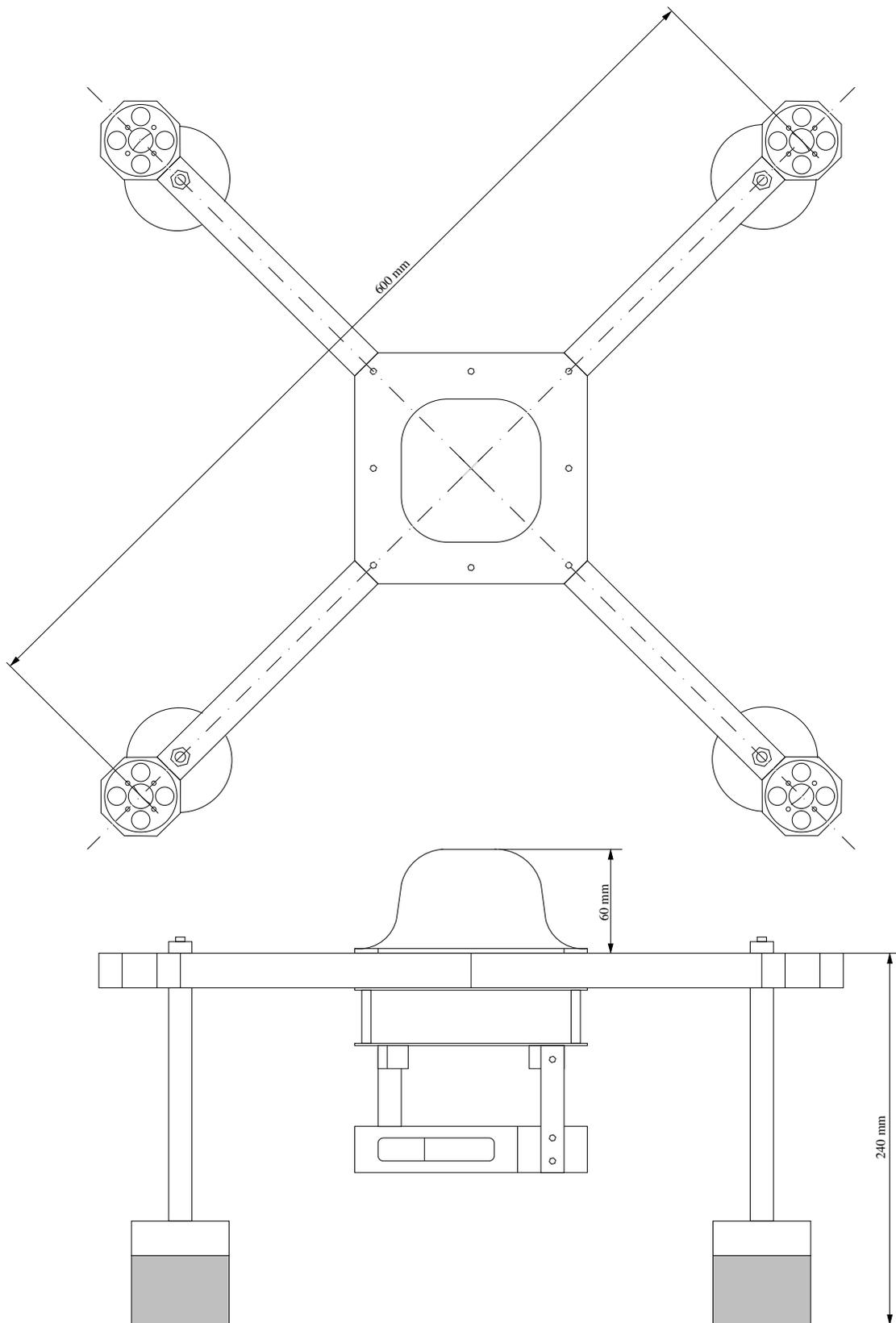


Abbildung A.3.: Konstruktionszeichnung und Übersicht zur Rahmenkonstruktion des Quadrotor-Systems.

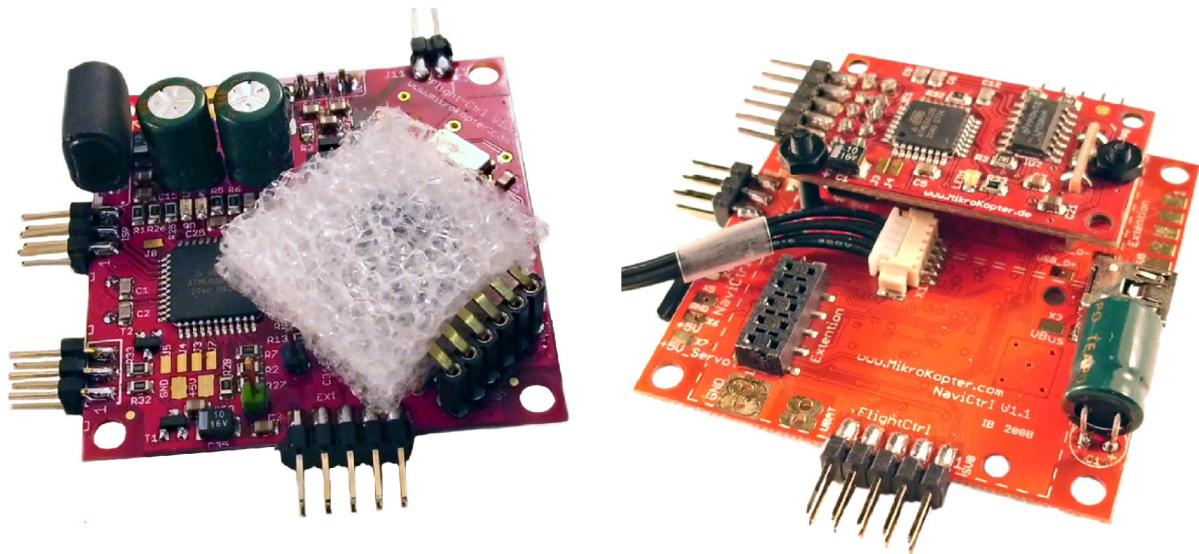


Abbildung A.4.: Steuerungselektronik: links Flight-Ctrl, rechts Navi-Ctrl und MK3Mag.

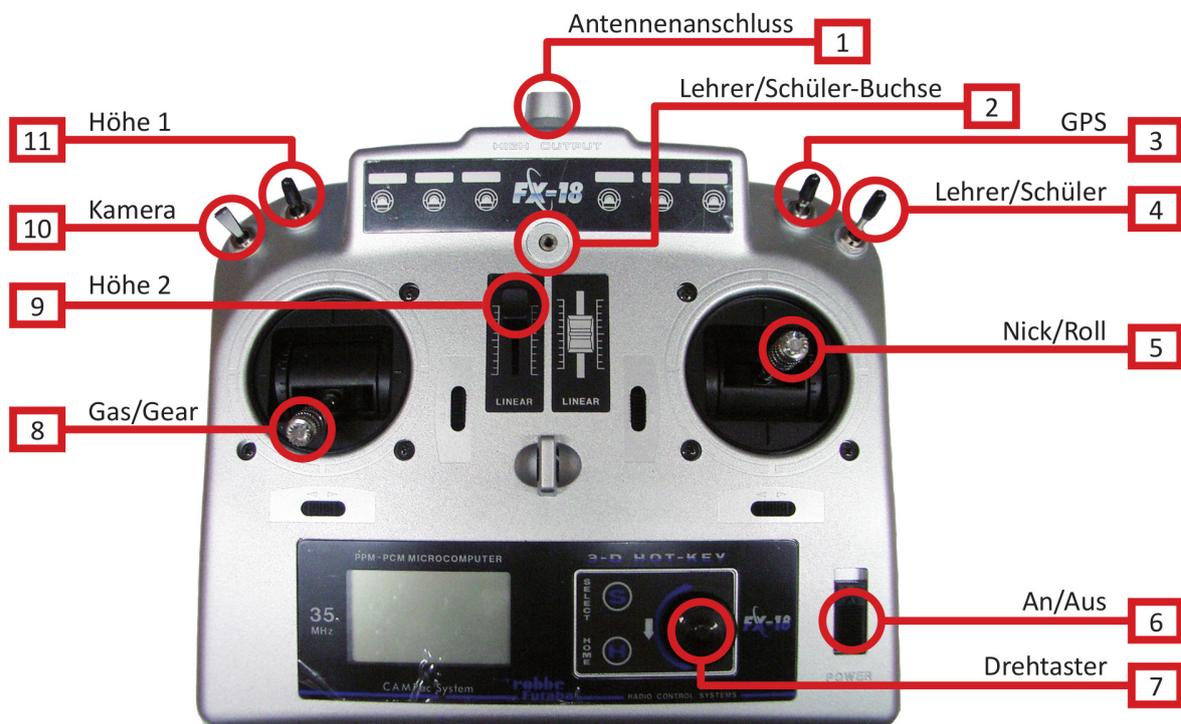


Abbildung A.5.: Fernsteuerungsanlage und Belegung der einzelnen Funktionen.

A.2.4. Kamera

Zur Bilderfassung kommen handelsübliche Kompaktkameras zum Einsatz. Bisher wurde das Modell *Praktica*³ luxmedia 8213 verwendet, da es eine brauchbare Bildqualität und manuelle Einstellungsmöglichkeiten zu einem günstigen Preis bietet. Inzwischen kommt auch ein Nachfolgemodell luxmedia 8403 zum Einsatz. Beide Modelle erlauben den Austausch des integrierten Infrarotfilters durch einen Sperr-Filter des visuellen Bereiches, sodass Luftaufnahmen im Spektralbereich des NIR durchgeführt werden können. Eine mechanische Auslösung per Servomotor erwies sich im Feldeinsatz als anfällig, die Kamera wird daher elektronisch ausgelöst (Abbildung A.6).



Abbildung A.6.: Modifizierte Kamera Praktica Luxmedia mit elektronischer Fernauslösung.

³<http://www.praktica.de>

A.3. Photogrammetrische Verfahren und Berechnungen

A.3.1. 3D-Helmert-Transformation

Die 3D-Helmert Transformation wird nach folgender Form definiert:

$$\mathbf{X}_d = \mathbf{T} + s\mathbf{R}\mathbf{X}_s \quad (\text{A.1})$$

\mathbf{X}_d = Vektor im Ziel-Koordinatensystem ($\mathbf{X}_d \in \mathbb{R}^3$)

\mathbf{T} = Vektor der Translation ($\mathbf{T} \in \mathbb{R}^3$)

s = Skalierungsfaktor ($s \in \mathbb{R}$)

\mathbf{R} = 3×3 Rotationsmatrix

\mathbf{X}_s = Vektor im Ausgangs-Koordinatensystem ($\mathbf{X}_s \in \mathbb{R}^3$)

n = Anzahl von gegebenen 3D-Punktkorrespondenzen $\mathbf{X}_s \iff \mathbf{X}_d$ ($n \in \mathbb{Z} \wedge n \geq 3$).

\mathbf{A} = $n \times 3$ Matrix der Ausgangs-Koordinatenvektoren \mathbf{X}_s

\mathbf{B} = $n \times 3$ Matrix der Ziel-Koordinatenvektoren \mathbf{X}_d

\mathbf{E} = $n \times n$ Einheitsmatrix, Diagonalelemente 1, sonst alle Elemente 0,

\mathbf{F} = $n \times n$ Hilfsmatrix, alle Elemente 1

\mathbf{G} = Hilfsvektor, alle Elemente 1, ($\mathbf{G} \in \mathbb{R}^n$)

Eine Hilfsmatrix \mathbf{K} wird anhand der folgenden Beziehung errechnet:

$$\mathbf{K} = \mathbf{E} - \frac{1}{n}\mathbf{F} \quad (\text{A.2})$$

Die Matrix \mathbf{C} kann nach folgender Gleichung berechnet werden:

$$\mathbf{C} = \mathbf{B}^t\mathbf{K}\mathbf{A} \quad (\text{A.3})$$

\mathbf{C} lässt sich mit Hilfe einer Singulärwertzerlegung in ein Matrizenprodukt aufspalten. Man erhält hieraus die Matrizen \mathbf{U} , \mathbf{S} und \mathbf{V} :

$$\mathbf{C} = \mathbf{U}\mathbf{S}\mathbf{V}^t \quad (\text{A.4})$$

Mit den nachfolgenden Berechnungsvorschriften erhält man die gesuchten Transformationsparameter:

$$\mathbf{R} = \mathbf{V}\mathbf{U}^t \quad (\text{A.5})$$

$$s = \frac{\text{Spur}(\mathbf{B}^t\mathbf{K}\mathbf{A}\mathbf{R})}{\text{Spur}(\mathbf{A}^t\mathbf{K}\mathbf{A})} \quad (\text{A.6})$$

$$\mathbf{T} = \frac{1}{n}(\mathbf{B} - s\mathbf{A}\mathbf{R})^t\mathbf{G} \quad (\text{A.7})$$

A.3.2. Photogrammetrische Abbildungsgleichungen

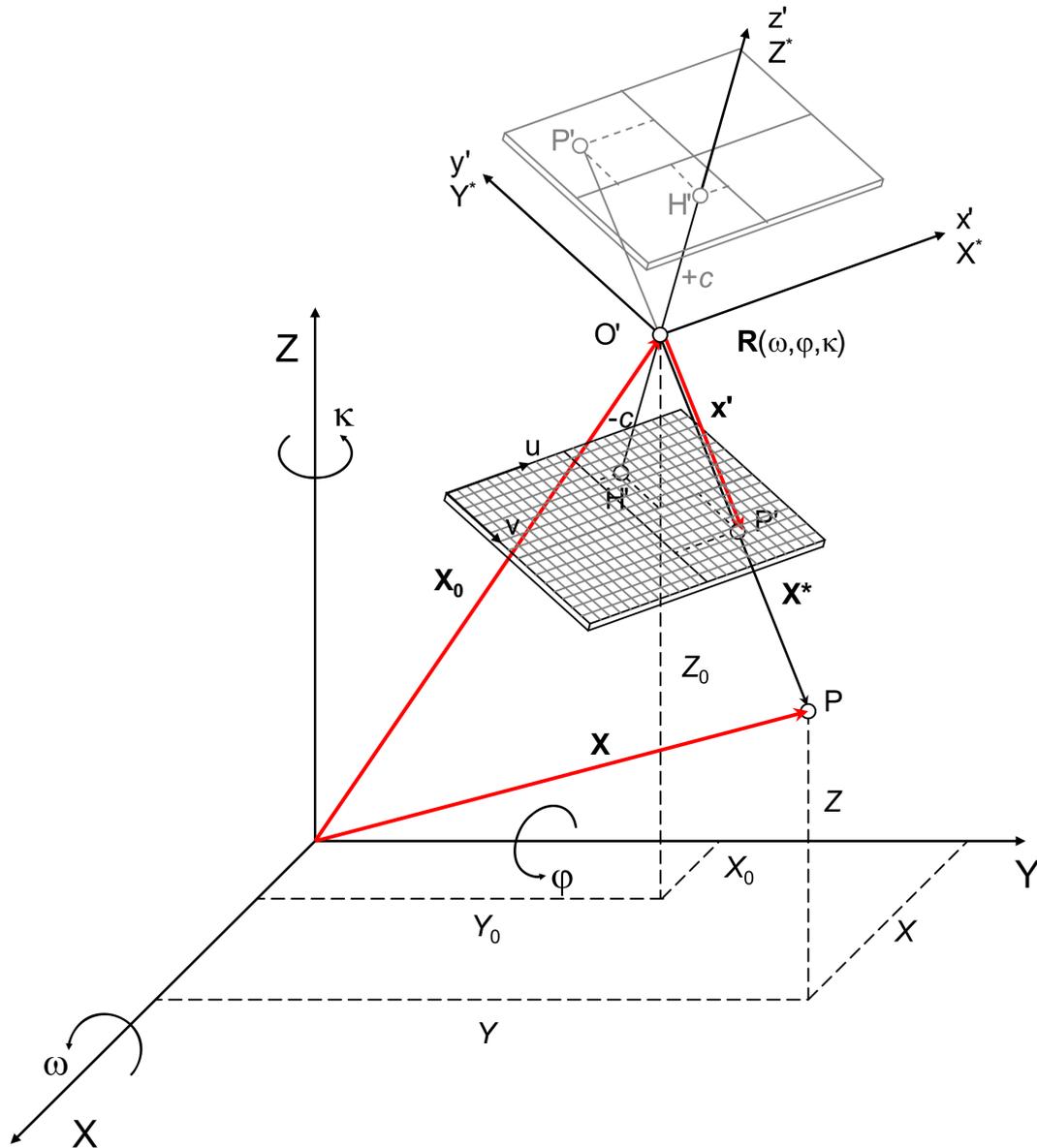


Abbildung A.7.: Koordinatensysteme des Bild- und Objektraums, modifiziert nach Luhman (2010).

Die zentral-perspektivischen Abbildungen vom Bildraum in den Objektraum (räumlicher Vorwärtsschnitt) und umgekehrt (räumlicher Rückwärtsschnitt) werden im Folgenden mathematisch durch Translation, Rotation und eine Skalierung beschrieben (Abbildung A.7).

\mathbf{X}	Objektkoordinatenvektor ($\mathbf{X} \in \mathbb{R}^3$)
\mathbf{X}_0	Koordinaten des Projektionszentrums c im Objektraum ($\mathbf{X}_0 \in \mathbb{R}^3$)
c	Projektionszentrum
\mathbf{x}	Bildkoordinatenvektor ($\mathbf{x} \in \mathbb{R}^3 \wedge x_z = 0$)
\mathbf{x}_0	Bildkoordinaten des Hauptpunktes ($\mathbf{x}_0 \in \mathbb{R}^3 \wedge x_{0z} = f$)
\mathbf{R}	3×3 Rotationsmatrix
s	Skalierungsfaktor ($s \in \mathbb{R}$)

Der räumliche Vorwärtsschnitt wird durch folgende Gleichung aufgestellt:

$$\mathbf{X} = \mathbf{X}_0 + s\mathbf{R}(\mathbf{x} - \mathbf{x}_0) \quad (\text{A.8})$$

In ausgeschriebener Form soll folgende Notation für den räumlichen Vorwärtsschnitt gelten:

$$\begin{pmatrix} X \\ Y \\ Z \end{pmatrix} = \begin{pmatrix} X_0 \\ Y_0 \\ Z_0 \end{pmatrix} + s \begin{pmatrix} r_{11} & r_{12} & r_{13} \\ r_{21} & r_{22} & r_{23} \\ r_{31} & r_{32} & r_{33} \end{pmatrix} \begin{pmatrix} x - x_0 \\ y - y_0 \\ -c \end{pmatrix} \quad (\text{A.9})$$

Die einzelnen Komponenten des räumlichen Vorwärtsschnittes:

$$X = X_0 + s(r_{11}(x - x_0) + r_{12}(y - y_0) - r_{13}c) \quad (\text{A.10})$$

$$Y = Y_0 + s(r_{21}(x - x_0) + r_{22}(y - y_0) - r_{23}c) \quad (\text{A.11})$$

$$Z = Z_0 + s(r_{31}(x - x_0) + r_{32}(y - y_0) - r_{33}c) \quad (\text{A.12})$$

Die Z-Komponente (Gl. (A.12)) lässt sich nach s auflösen:

$$s = \frac{Z - Z_0}{r_{31}(x - x_0) + r_{32}(y - y_0) - r_{33}c} \quad (\text{A.13})$$

Mit Gleichungen (A.10), (A.11) und (A.13) erhält man schließlich die Gleichungen des räumlichen Vorwärtsschnittes:

$$X = X_0 + (Z - Z_0) \frac{r_{11}(x - x_0) + r_{12}(y - y_0) - r_{13}c}{r_{31}(x - x_0) + r_{32}(y - y_0) - r_{33}c} \quad (\text{A.14})$$

$$Y = Y_0 + (Z - Z_0) \frac{r_{21}(x - x_0) + r_{22}(y - y_0) - r_{23}c}{r_{31}(x - x_0) + r_{32}(y - y_0) - r_{33}c} \quad (\text{A.15})$$

Die Gleichung des räumlichen Rückwärtsschnittes berechnet sich aus Gl. (A.8) zu:

$$\mathbf{x} = \mathbf{x}_0 + \frac{1}{s} \mathbf{R}^{-1} (\mathbf{X} - \mathbf{X}_0) \quad (\text{A.16})$$

Die Rotationsmatrix \mathbf{R} ist orthogonal und kann durch einfaches Transponieren invertiert werden. In ausgeschriebener Form erhält man für den räumlichen Rückwärtsschnitt:

$$\begin{pmatrix} x \\ y \\ 0 \end{pmatrix} = \begin{pmatrix} x_0 \\ y_0 \\ c \end{pmatrix} + \frac{1}{s} \begin{pmatrix} r_{11} & r_{21} & r_{31} \\ r_{12} & r_{22} & r_{32} \\ r_{13} & r_{23} & r_{33} \end{pmatrix} \begin{pmatrix} X - X_0 \\ Y - Y_0 \\ Z - Z_0 \end{pmatrix} \quad (\text{A.17})$$

Die einzelnen Komponenten des räumlichen Rückwärtsschnittes:

$$x = x_0 + \frac{1}{s} (r_{11}(X - X_0) + r_{21}(Y - Y_0) + r_{31}(Z - Z_0)) \quad (\text{A.18})$$

$$y = y_0 + \frac{1}{s} (r_{12}(X - X_0) + r_{22}(Y - Y_0) + r_{32}(Z - Z_0)) \quad (\text{A.19})$$

$$0 = c + \frac{1}{s} (r_{13}(X - X_0) + r_{23}(Y - Y_0) + r_{33}(Z - Z_0)) \quad (\text{A.20})$$

Die Z-Komponente aus Gleichung (A.20) wird nach $\frac{1}{s}$ umgestellt:

$$\frac{1}{s} = \frac{-c}{r_{13}(X - X_0) + r_{23}(Y - Y_0) + r_{33}(Z - Z_0)} \quad (\text{A.21})$$

Mit Gleichungen (A.18), (A.19) und (A.21) erhält man schließlich die Gleichungen des räumlichen Rückwärtsschnittes:

$$x = x_0 - c \frac{r_{11}(X - X_0) + r_{21}(Y - Y_0) + r_{31}(Z - Z_0)}{r_{13}(X - X_0) + r_{23}(Y - Y_0) + r_{33}(Z - Z_0)} \quad (\text{A.22})$$

$$y = y_0 - c \frac{r_{12}(X - X_0) + r_{22}(Y - Y_0) + r_{32}(Z - Z_0)}{r_{13}(X - X_0) + r_{23}(Y - Y_0) + r_{33}(Z - Z_0)} \quad (\text{A.23})$$

A.3.3. Projektive Entzerrung

Im Anhang A.3.2 wurden die Gleichungen des räumlichen Vorwärtsschnittes hergeleitet:

$$X = X_0 + (Z - Z_0) \frac{r_{11}(x - x_0) + r_{12}(y - y_0) - r_{13}c}{r_{31}(x - x_0) + r_{32}(y - y_0) - r_{33}c} \quad (\text{A.24})$$

$$Y = Y_0 + (Z - Z_0) \frac{r_{21}(x - x_0) + r_{22}(y - y_0) - r_{23}c}{r_{31}(x - x_0) + r_{32}(y - y_0) - r_{33}c} \quad (\text{A.25})$$

Weitere Vereinfachungen werden vorgenommen:

- Das Projektionszentrum c liege senkrecht über dem Ursprung des Objektraums ($X_0 = 0$ und $Y_0 = 0$).
- Die abzulichtende Fläche im Objektraum sei eben, und liege ohne Verkippung im Objektkoordinatensystem ($Z = \textit{konstant}$). Weiterhin ist dann $Z - Z_0 = k = \textit{konstant}$.
- Der Bildhauptpunkt liege in der Sensormitte ($x_0 = 0$ und $y_0 = 0$).

Die Gleichungen (A.14) und (A.15) können mit diesen Vereinfachungen in nachfolgender Form dargestellt werden:

$$X = k \frac{r_{11}x + r_{12}y - r_{13}c}{r_{31}x + r_{32}y - r_{33}c} \quad (\text{A.26})$$

$$Y = k \frac{r_{21}x + r_{22}y - r_{23}c}{r_{31}x + r_{32}y - r_{33}c} \quad (\text{A.27})$$

Mit dem Ziel einer Reduktion der unbekannt Parameter sei $k = 1$, zusätzlich werden die Gleichungen (A.26) und (A.27) durch $-r_{33}c$ dividiert:

$$X = \frac{\frac{r_{13}}{r_{33}} + \frac{r_{11}}{-r_{33}c}x + \frac{r_{12}}{-r_{33}c}y}{\frac{r_{31}}{-r_{33}c}x + \frac{r_{32}}{-r_{33}c}y + 1} \quad (\text{A.28})$$

$$Y = \frac{\frac{r_{23}}{r_{33}} + \frac{r_{21}}{-r_{33}c}x + \frac{r_{22}}{-r_{33}c}y}{\frac{r_{31}}{-r_{33}c}x + \frac{r_{32}}{-r_{33}c}y + 1} \quad (\text{A.29})$$

Es werden nun folgende Substitutionen durchführt:

$$a_0 = \frac{r_{13}}{r_{33}}; \quad a_1 = -\frac{r_{11}}{r_{33}c}; \quad a_2 = -\frac{r_{12}}{r_{33}c}; \quad (\text{A.30})$$

$$b_0 = \frac{r_{23}}{r_{33}}; \quad b_1 = -\frac{r_{21}}{r_{33}c}; \quad b_2 = -\frac{r_{22}}{r_{33}c}; \quad (\text{A.31})$$

$$c_1 = -\frac{r_{31}}{r_{33}c}; \quad c_2 = -\frac{r_{32}}{r_{33}c} \quad (\text{A.32})$$

Man erhält die Projektionsgleichungen mit 8 unbekanntem Parametern:

$$X_i = \frac{a_0 + a_1x_i + a_2y_i}{c_1x_i + c_2y_i + 1} \quad (\text{A.33})$$

$$Y_i = \frac{b_0 + b_1x_i + b_2y_i}{c_1x_i + c_2y_i + 1} \quad (\text{A.34})$$

Eine Linearisierung des Gleichungssystems wird durch Multiplikation mit dem Nennerterm $(c_1x_i + c_2y_i + 1)$ vollzogen :

$$a_0 + a_1x_i + a_2y_i - X_i - c_1x_iX_i - c_2y_iX_i = 0 \quad (\text{A.35})$$

$$b_0 + b_1x_i + b_2y_i - Y_i - c_1x_iY_i + c_2y_iY_i = 0 \quad (\text{A.36})$$

Das gefundene Gleichungssystem $\mathbf{A}\vec{a} = \vec{x}$ ist mit acht Gleichungen und acht Unbekannten anhand von vier 2D-Punkt-Korrespondenzen eindeutig lösbar:

$$\begin{pmatrix} 1 & x_1 & y_1 & 0 & 0 & 0 & -x_1X_1 & -y_1X_1 \\ 0 & 0 & 0 & 1 & x_1 & y_1 & -x_1Y_1 & -y_1Y_1 \\ 1 & x_2 & y_2 & 0 & 0 & 0 & -x_2X_2 & -y_2X_2 \\ 0 & 0 & 0 & 1 & x_2 & y_2 & -x_2Y_2 & -y_2Y_2 \\ 1 & x_3 & y_3 & 0 & 0 & 0 & -x_3X_3 & -y_3X_3 \\ 0 & 0 & 0 & 1 & x_3 & y_3 & -x_3Y_3 & -y_3Y_3 \\ 1 & x_4 & y_4 & 0 & 0 & 0 & -x_4X_4 & -y_4X_4 \\ 0 & 0 & 0 & 1 & x_4 & y_4 & -x_4Y_4 & -y_4Y_4 \end{pmatrix} \begin{pmatrix} a_0 \\ a_1 \\ a_2 \\ b_0 \\ b_1 \\ b_2 \\ c_1 \\ c_2 \end{pmatrix} = \begin{pmatrix} X_1 \\ Y_1 \\ X_2 \\ Y_2 \\ X_3 \\ Y_3 \\ X_4 \\ Y_4 \end{pmatrix} \quad (\text{A.37})$$

$$\mathbf{A}\vec{a} = \vec{x} \implies \vec{a} = \mathbf{A}^{-1}\vec{x} \quad (\text{A.38})$$

Im überbestimmten Fall kann eine Ausgleichslösung mit Hilfe einer Pseudoinversen \mathbf{A}^+ gefunden werden (Golub und Kahan, 1965):

$$\mathbf{A}\vec{a} = \vec{x} \implies \vec{a} \approx \mathbf{A}^+\vec{x} \quad (\text{A.39})$$

A.3.4. Projektionsmatrix

Im Bereich der computergestützten 3D-Bildverarbeitung kommen zur interaktiven Bild-darstellung homogenen Koordinaten zum Einsatz (Bloomenthal und Rokne, 1994). Der räumlicher Rückwärtsschnitt (Abbildung vom Objektraum in den Bildraum) wird im Fol-genden mit Hilfe von homogenen Koordinaten dargestellt. Eine räumliche Abbildung wird dann durch Multiplikation mit der Projektionsmatrix \mathbf{P} vollzogen. Optische Fehler, und Fehler der inneren Orientierung sollen im Folgenden vernachlässigt werden.

$$\mathbf{U} = \begin{pmatrix} X \\ Y \\ Z \\ 1 \end{pmatrix} \quad \text{Homogener Vektor im Objektkoordinatensystem.} \quad (\text{A.40})$$

$$\mathbf{u} = \begin{pmatrix} u \\ v \\ w \end{pmatrix} = w \begin{pmatrix} x \\ y \\ 1 \end{pmatrix} \quad \text{Homogener Vektor im Bildkoordinatensystem.} \quad (\text{A.41})$$

$$\mathbf{K} = \begin{pmatrix} -c & 0 & x_0 \\ 0 & -c & y_0 \\ 0 & 0 & 1 \end{pmatrix} \quad \text{Die Parameter der inneren Orientierung.} \quad (\text{A.42})$$

$$\mathbf{R}^{-1} = \begin{pmatrix} r_{11} & r_{21} & r_{31} \\ r_{12} & r_{22} & r_{32} \\ r_{13} & r_{23} & r_{33} \end{pmatrix} \quad \text{Rotationsmatrix (Gleichung (A.3.2)).} \quad (\text{A.43})$$

$$\mathbf{L} = \begin{pmatrix} 1 & 0 & 0 & -X_0 \\ 0 & 1 & 0 & -Y_0 \\ 0 & 0 & 1 & -Z_0 \end{pmatrix} \quad \text{Lage des Projektionszentrums im Objektraum.} \quad (\text{A.44})$$

Die Projektionsmatrix wird aus den obigen Matrizen mit folgender Rechenvorschrift kon-struiert:

$$\mathbf{P} = \mathbf{K}\mathbf{R}^{-1}\mathbf{L} = \begin{pmatrix} p_{11} & p_{12} & p_{13} & p_{14} \\ p_{21} & p_{22} & p_{23} & p_{24} \\ p_{31} & p_{32} & p_{33} & p_{34} \end{pmatrix} \quad (\text{A.45})$$

In ausgeschriebener Form erhält man für \mathbf{P} :

$$\mathbf{P} = \begin{pmatrix} x_0 r_{13} - cr_{11} & x_0 r_{23} - cr_{21} & x_0 r_{33} - cr_{31} & -X_0(x_0 r_{13} - cr_{11}) - Y_0(x_0 r_{23} - cr_{21}) - Z_0(x_0 r_{33} - cr_{31}) \\ y_0 r_{13} - cr_{12} & y_0 r_{23} - cr_{22} & y_0 r_{33} - cr_{32} & -X_0(y_0 r_{13} - cr_{12}) - Y_0(y_0 r_{23} - cr_{22}) - Z_0(y_0 r_{33} - cr_{32}) \\ r_{13} & r_{23} & r_{33} & -r_{13}X_0 - r_{23}Y_0 - r_{33}Z_0 \end{pmatrix}$$

Der räumliche Rückwärtsschnitt wird nun mit Hilfe einer Matrixmultiplikation berechnet:

$$\mathbf{u} = \mathbf{P}\mathbf{U} \quad (\text{A.46})$$

$$\mathbf{u} = \begin{pmatrix} x_0 (r_{13}(X - X_0) + r_{23}(Y - Y_0) + r_{33}(Z - Z_0)) - c(r_{11}(X - X_0) + r_{21}(Y - Y_0) + r_{31}(Z - Z_0)) \\ y_0 (r_{13}(X - X_0) + r_{23}(Y - Y_0) + r_{33}(Z - Z_0)) - c(r_{12}(X - X_0) + r_{22}(Y - Y_0) + r_{32}(Z - Z_0)) \\ r_{13}(X - X_0) + r_{23}(Y - Y_0) + r_{33}(Z - Z_0) \end{pmatrix}$$

Nach vollendeter Transformation müssen die Komponenten aus \mathbf{u} durch w dividiert werden. Man erhält somit x und y im Bildkoordinatensystem. Ein Vergleich mit Gleichungen (A.22) und (A.23) bestätigt äquivalente Gleichungen zur Berechnung des räumlichen Rückwärtsschnittes:

$$x = \frac{u}{w} = x_0 - c \frac{r_{11}(X - X_0) + r_{21}(Y - Y_0) + r_{31}(Z - Z_0)}{r_{13}(X - X_0) + r_{23}(Y - Y_0) + r_{33}(Z - Z_0)} \quad (\text{A.47})$$

$$y = \frac{v}{w} = y_0 - c \frac{r_{12}(X - X_0) + r_{22}(Y - Y_0) + r_{32}(Z - Z_0)}{r_{13}(X - X_0) + r_{23}(Y - Y_0) + r_{33}(Z - Z_0)} \quad (\text{A.48})$$

A.3.5. Differenzielle Entzerrung

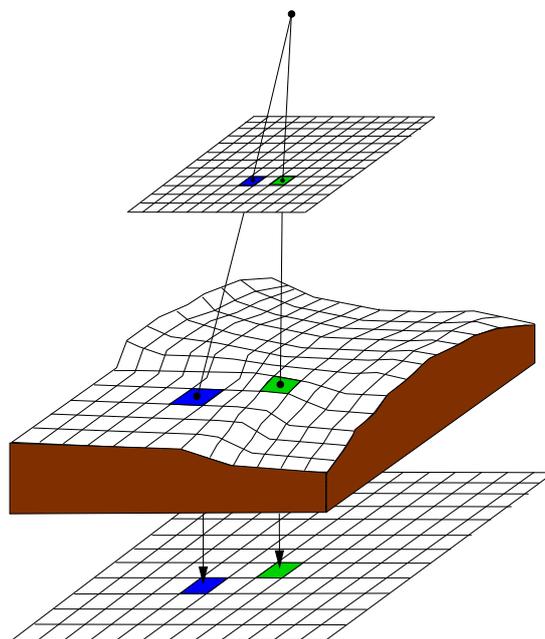


Abbildung A.8.: Parallelprojektion zur Luftbildentzerrung.

Die Texturinformation wird in einem ersten Schritt mit Hilfe der zum Luftbild zugehörigen Projektionsmatrix (siehe Anhang A.3.4) auf das zugrunde liegende 3D-Oberflächenmodell projiziert. Die Projektion errechnet sich nach Gleichung (A.46) zu:

$$w \begin{pmatrix} x \\ y \\ 1 \end{pmatrix} = \begin{pmatrix} p_{11} & p_{12} & p_{13} & p_{14} \\ p_{21} & p_{22} & p_{23} & p_{24} \\ p_{31} & p_{32} & p_{33} & p_{34} \end{pmatrix} \begin{pmatrix} X \\ Y \\ Z \\ 1 \end{pmatrix} \quad (\text{A.49})$$

Mit den normierten Komponenten aus \mathbf{u} erhält man folgende Transformationsgleichungen:

$$\begin{aligned} x &= \frac{p_{11}X + p_{12}Y + p_{13}Z + p_{14}}{p_{31}X + p_{32}Y + p_{33}Z + p_{34}} \\ y &= \frac{p_{21}X + p_{22}Y + p_{23}Z + p_{24}}{p_{31}X + p_{32}Y + p_{33}Z + p_{34}} \end{aligned} \quad (\text{A.50})$$

Die Farbwerte des 3D-Modells an der Stelle $(X \ Y \ Z)^t$ werden aus dem ursprünglichen Bild an der Stelle $(x \ y)^t$ ermittelt. Anschließend wird die gewünschte Entzerrung durch einfache Parallelprojektion $Z = 0$ vollzogen. Man erhält somit das entzerrte Bild.

A.3.6. Parametrisierbare Glättungsfiler

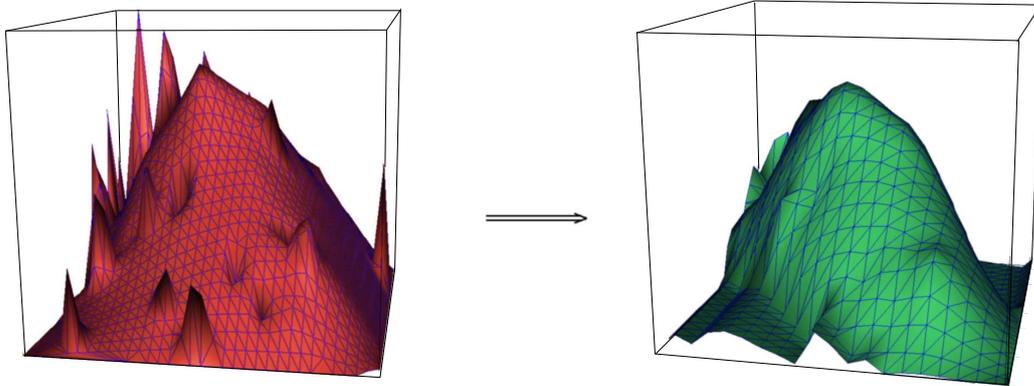


Abbildung A.9.: Beispiel Filterung einer 3D-Punktvolke. Links: 3D-Punktvolke mit Rauschartefakten, rechts: gefiltertes Modell.

Bildverarbeitungsoperationen lassen sich in vielen Fällen allgemein durch eine zweidimensionale diskrete Faltungsoperation aufstellen. Folgende Konvention wird zur Glättung von dreidimensionalen gerasterten Punktvolken anhand eines fixen 3×3 Kerns \mathbf{K} getroffen:

$$\tilde{z}(x, y) = \sum_{j=1}^3 \sum_{i=1}^3 z(x+i-2, y+j-2)k_{ij} \quad (\text{A.51})$$

Wobei der funktionelle Faltungskern \mathbf{K} mit den einzelnen Elementen k_{ij} beliebig parametrisierbar ist:

$$\mathbf{K} = \begin{pmatrix} k_{11} & k_{12} & k_{13} \\ k_{21} & k_{22} & k_{23} \\ k_{31} & k_{32} & k_{33} \end{pmatrix} \quad (\text{A.52})$$

Die Elemente des 3×3 Faltungskerns eines Rechteck-Mittelwert Glättungsfilters:

$$\mathbf{K} = \frac{1}{9} \begin{pmatrix} 1 & 1 & 1 \\ 1 & 1 & 1 \\ 1 & 1 & 1 \end{pmatrix} \quad (\text{A.53})$$

Der 3×3 Faltungskern eines Gaussfilters:

$$\mathbf{K} = \frac{1}{16} \begin{pmatrix} 1 & 2 & 1 \\ 2 & 4 & 2 \\ 1 & 2 & 1 \end{pmatrix} \quad (\text{A.54})$$

A.4. Lebenslauf

seit 10/2007

Institut für Geophysik, Universität Stuttgart, wissenschaftlicher Mitarbeiter im Bereich der Fernerkundung mit Drohnen

05/2006 - 02/2007

TimeTech GmbH Stuttgart, Systemingenieur im Bereich Raumfahrtsysteme und Zeitmesstechnik

01/2004 - 05/2006

SYNARGOS GmbH Stuttgart, Systementwickler im Bereich Kryptographie für Zahlungssysteme

12/2003

Diplomarbeit, Thema: Entwicklung eines Hohlleiterdiplexers basierend auf dem Talboteffekt im Winkelraum

10/1996 - 12/2003

Studium der Elektro- und Informationstechnik, Universität Stuttgart, Vertiefungsrichtung: Systemtheorie, Abschluss: Diplom-Ingenieur für Elektro- und Informationstechnik

08/1994 - 07/1996

Technische Oberschule Stuttgart, Abschluss: Fachgebundene Hochschulreife

06/1994 - 07/1994

NINNELT GmbH Stuttgart, Waagenbauer im Bereich Anlagentechnik

03/1993 - 05/1994

Zivildienst, Werkstattbetreuer für körperlich- und geistig Behinderte, Diakonie Stetten

09/1991 - 02/1993

NINNELT GmbH Stuttgart, Waagenbauer im Bereich Anlagentechnik

09/1988 - 07/1991

Berufsausbildung, Robert-Bosch GmbH Stuttgart, Abschluss: Industriemechaniker der Fachrichtung Produktionstechnik

08/1982 - 07/1988

Lindenrealschule Stuttgart, Abschluss: Mittlere Reife

Publikationen

Beckenbach, E., Niethammer, U., und Seyfried, H. (2013). Spätmittelalterliche Starkregeneignisse und ihre geomorphologischen Kleinformen im Schönbuch (Süddeutschland): Erfassung mit hochauflösenden Fernerkundungsmethoden und sedimentologische Interpretation. *Jahresberichte und Mitteilungen des Oberrheinischen Geologischen Vereins*, 95:421–438.

Joswig, M., Niethammer, U., Rothmund, S., und Walter, M. (2010). Mudslide-bedrock interaction at Super-Sauze (French Alps) by UAV-based remote sensing and Nanoseismic Monitoring. In *EAGE Near Surface - 16th European Meeting of Environmental and Engineering Geophysics, Zürich, Switzerland*.

Niethammer, U., James, M., Rothmund, S., Travelletti, J., und Joswig, M. (2012). UAV-based remote sensing of the Super-Sauze landslide: Evaluation and results. *Engineering Geology*, 128:2–11.

Niethammer, U. und Joswig, M. (2012). Analysis of UAV-based DTMs generated by Multi-View-Stereo approaches. In *Proc. of EAGE/GRSG Remote Sensing Workshop, Paris*. EAGE.

Niethammer, U., Rothmund, S., und Joswig, M. (2009). UAV-based remote sensing of the slow moving landslide Super-Sauze. In Malet, J.-P., Remaître, A., und Bogaard, T., editors, *Landslide Processes: Landslide mapping and geomorphologic characterization*, CERG Editions, pages 69–74, 352, Strasbourg, France. CERG. Proceedings of a conference held in Strasbourg, France, 6.-7. Feb. 2009.

Niethammer, U., Rothmund, S., Joswig, M., James, M., und Travelletti, J. (2010). UAV-based remote sensing of landslides. *Int. Arch. Photogramm. Remote Sens. Spatial Inf. Sci.*, XXXVIII Part 5:496–501.

Niethammer, U., Rothmund, S., Schwaderer, U., Zeman, J., und Joswig, M. (2011). Open source image-processing tools for low-cost UAV-based landslide investigations. *Int. Arch. Photogramm. Remote Sens. Spatial Inf. Sci.*, XXXVIII-1 C22:161–166.

Plaum, B., Niethammer, U., und Holzhauer, E. (2004). Characterization of diplexers based on the Talbot effect in rectangular waveguides. In *Infrared and Millimeter Waves, 2004 and 12th International Conference on Terahertz Electronics, 2004. Conference Digest of the 2004 Joint 29th International Conference on*, pages 473–474. IEEE.

Rothmund, S., Niethammer, U., Malet, J.-P., und Joswig, M. (2013). Landslide surface monitoring based on UAV-and ground-based images and terrestrial laser scanning: accuracy analysis and morphological interpretation. *First Break*, 31(8).

Stumpf, A., Malet, J.-P., Kerle, N., Niethammer, U., und Rothmund, S. (2013a). Image-based mapping of surface fissures for the investigation of landslide dynamics. *Geomorphology*, 186:12–27.

Stumpf, A., Niethammer, U., Rothmund, S., Mathieu, A., Malet, J.-P., und Joswig, M. (2011). Mapping and monitoring landslide surface features through object-oriented analysis of unmanned aerial vehicle (UAV) imagery. In *second world landslide forum WLF2 2011 Rome*.

Stumpf, A., Niethammer, U., Rothmund, S., Mathieu, A., Malet, J.-P., Kerle, N., und Joswig, M. (2013b). Advanced image analysis for automated mapping of landslide surface fissures. In *Landslide Science and Practice*, pages 357–363. Springer.

Walter, M., Niethammer, U., Rothmund, S., und Joswig, M. (2009). Joint analysis of the Super-Sauze (French Alps) mudslide by nanoseismic monitoring and UAV-based remote sensing. *First Break, EAGE*, 27(8):53–60. European Association of Geoscientist & Engineers (EAGE).

Walter, M., Rothmund, R., Niethammer, U., Malet, J.-P., und Joswig, M. (2013). Investigation of landslide kinematics derived from UAV-and ground-based imagery-precision analysis of 3D point clouds. In *Near Surface Geoscience 2013*.